Investigations of Daytime Thermospheric Wave Dynamics Over Low-Latitudes Using Ground-Based Optical Techniques

A thesis submitted in partial fulfilment of

the requirements for the degree of

Doctor of Philosophy

by

Deepak Kumar Karan

(Roll No. 11330025)

Under the guidance of

Prof. Duggirala Pallamraju
Space and Atmospheric Sciences Division
Physical Research Laboratory, Ahmedabad, India.

DISCIPLINE OF PHYSICS

INDIAN INSTITUTE OF TECHNOLOGY, GANDHINAGAR

2017

to

My Parents

Its all about your love and blessings

and

My Teachers

I am blessed to have teachers like you

Declaration

I declare that this written submission represents my ideas in my own words and where others' ideas or words have been included, I have adequately cited and referenced the original sources. I also declare that I have adhered to all principles of academic honesty and integrity and have not misrepresented or fabricated or falsified any idea/data/fact/source in my submission. I understand that any violation of the above can cause disciplinary action by the Institute and can also evoke penal action from the sources which have thus not been properly cited or from whom proper permission has not been taken when needed.

(Signature)

(Name: Deepak Kumar Karan)

(Roll No: 11330025)

Date: October 16, 2017

Thesis Approval

The thesis entitled

Investigations of Daytime Thermospheric Wave Dynamics Over Low-Latitudes Using Ground-Based Optical Techniques

by

Deepak Kumar Karan
(Roll No. 11330025)

is approved for the degree of

Doctor of Philosophy

Examiner

Examiner

Examiner

Examiner

Supervisor

Date:

Place:

Acknowledgments

The guidance, support, advice, motivation, and encouragement from my supervisor, colleagues, teachers, friends, family members and my well wishers had made this thesis work possible. Its indeed a great pleasure for me to acknowledge them all.

At first, with due respect, I would like to express my sincere thanks and gratitude to my thesis supervisor Prof. Duggirala Pallamraju for introducing me to this subject. I am delighted to have a supervisor like him, who could recognize my potentials very well from the beginning and had given me the freedom of investigating the research problems and for scientific discussions with no time bound. His enormous patience of listening and discussing the scientific problems; and during experimental observations and analysis, always inspired and motivated me towards the research work. His vast knowledge and depth understanding on various aspects of the subject helped me to bring clarity in my understanding the field. During confusion and upset hours of my research work, a short discussion with him would bring my focus back to the research. I am thankful for his countless support and invaluable guidance throughout the duration of this thesis work. Thank you sir. I would like to extend my thanks to Bhuvaneswari ma'am, Ananth, and Samba for their affection. Thank you so much ma'am for those tasty dishes, specially Dahivada.

I am thankful to my Doctoral Studies Committee (DSC) members Dr. D. Chakrabarty and Dr. Varun Sheel for evaluating my progress reports and suggesting improvements through out all the semesters. I thank them for critically going through the thesis and making valuable suggestions. The scientific input during discussions with Dr. D. Chakrabarty has increased my understanding the field better. I also thank the academic committee members of PRL for their inputs during review seminars.

I am obliged to Department of Space, Govt. of India for the research grant offered to me during my tenure at PRL. I extend my thanks to Dr. Anil Bhardwaj, Director, PRL, Ahmedabad and Prof. Sudhir K. Jain, Director, IIT, Gandhinagar for providing me with timely administrative help and necessary facilities to carry out my research work. I am also thankful to Prof. P. Janardhan, Dean, PRL and Dr. Bhushit Vaishnav, Head Academic Services for their support with academic matters. My sincere thanks to Prof. Nithin V George, Associate Dean, Prof. Vinod Chandra, Co-ordinator, Discipline of Physics, and the officials at the Academic section of IIT Gandhinagar for their help and cooperation with regard to the submission and evaluation process of my thesis.

I am highly obliged to Prof. R. Sridharan and Prof. R. Sekar for their encouragements, discussions and critical questions during the seminars, which were very helpful during my research. I always felt motivated after the inspiring discussions with Prof. R. Sridharan. I express my sincere thanks to Prof. S. Ramachandran, Chairman, Space and Atmospheric Sciences division, PRL. I also extend my thanks to Dr. L. K. Sahoo, Dr. S. K. Sharma, Dr. A. Guharay, Dr. H. Gadhvi, Mr. S. Venkataramani, Mr. T. A. Rajesh, Mr. A. A. Manke, Mr. M. B. Bhavsar, Mr. T. K. S. Kumar, Malai, Aditya, Anil, Vishnu, Hetal, Sourita, and Mahipath for providing nice atmosphere in the office.

The primary data set for this thesis work is obtained using MISE which is installed at Jawaharlal Nehru Technological University, Hyderabad (JNTUH) under the PRL-JNTUH collaboration. In this regard, I am thankful to the Vice Chancellor, JNTUH, Prof. A. Reddy, Director, University Foreign Relation, and Dr. T. Vijayalakshmi, Head, Center for Environment, IST, JNTUH for enabling smooth operation of this project. I would like to thank Samba bhai, Moid and Abhilash for the logistic support during my field trips to JNTUH.

I sincerely acknowledge the Director, Indian Institute of Geomagnetism, Mumbai, for making the magnetic data available. The geomagnetic indices are made available by ISGI collaborating institutes from data collected at magnetic observatories. I thank all those involved with ISGI (isgi.unistra.fr) and INTERMAGNET network. The GUVI data has been obtained from guvitimed.jhuapl.edu. I thank the GUVI team.

I thank all the staff members of PRL computer center for providing excellent computational facilities. I also appreciate the co-operation by the library staff members.

I am thankful to colleagues of my group F. I. Laskar, Kedar A. Phadke, R. P. Singh, Sneha Yadav, Subir Mandal, and Pradip S., who are always helpful and cooperative. I thank Fazlul bhaiya and R. P. sir for giving me their invaluable time for scientific discussions. I thank Subir and Pradip for making friendly environment in the lab. In particular, I am happy to have a lab mate and colleague like Subir, to have involved scientific discussions besides endless plans for good and tasty food. I am extremely happy to have a colleague, collaborator cum friend like Kedar. I fondly recollect his companionship during the scientific discussions, field trips to Hyderabad, over breakfast-lunch-snacks-dinner, on playground etc. I thank Sneha Nair and Kedar, for their mind relaxing gossips and encouragements, which used to motivate me to work hard. Thank you Sneha, for bringing those tasty food for the two other musketeers and you are a true inspiration.

I thank all my sweet batch mates (Dipti, Bivin, Lalit, Venky, Sukanya, Ritwik, *Chandana, Apurv, Pankaj, Rahul, Newton, Ashim, and Jinia), caring seniors (Susanta Bhai, Nigam Bhai, Priyanka, Arko, Tanmoy, Shweta, Monojit, Dilip, Naveen, Gaurav(T), Bhavya, Gaurav(J), Girish Kumar, Arun, Devrup, Damu, Ikshu, Anirban, Shraddha, Manu, Avdesh), loving juniors (Rukmani, Navpreet, Rupa, Kuldeep, Chandan, Prahlad, Satish, Kumar, Bhavesh, Pradeep, Niharika, Anil, Archita, Aarthy, Richa, Ranadeep, Kaustav, Nidhi, Shefu, Varun, Rahul, Shivangi, Arvind, Naman, Deepika, Sushree, Nisha, Sandeep, Soamdutta, Avik, Ayan, Harish, Abdur, Surendra, Priyank, Deepali, Sana, Ashwin), and many more for making my stay in hostel homely. The friendly and funny activities in the hostel used to refresh my thoughts and continue the research work with more zeal. I remember those memorable days of late night talks near the thinking tree in front of our hostel, going for bird watching in early morning of winter with seniors, playing various games, unique way of celebrating the festivals with you all. Thank you Subir, Aarthy, and Archita for planning those delicious cooking parties in hostel. I must thank Kuldeep, Prahlad, Archita, Subir, and Dipti for their valuable scientific and non-scientific inputs during my rehearsal presentations in hostel. Specially, I would like to thank Deepika and Sushree for making a true homely environment. Thank you Richa for the motivational and supportive discussions. I am extremely happy and thankful to you all for your help and support. Thank you all for being so supportive and kind to me. I would like to thank my friend Diptiranjan Rout who is there with me from the very beginning of the journey.*

I would like to take this opportunity to thank my dear friends Pankaj, Pradip, Gautam, Mitun, Ajay, Tiku, Subhanand, Uppu, and Manish Bhai for their encouragement. Specially, I thank Kadambinee for her continuous support, inspiration, and motivation throughout the journey. I fondly recollect the time I spent with Mr. Dharmananda Sahoo and his family. Thank you Nani and Moni for fueling the aspiration inside me. My heart felt thank to late Ajaa who took care of food during my college days. His love and affection is unforgettable. I extend my thanks to Mr. Haladhar Panda and his family to be always my well wisher.

My sincere thanks to my teachers, Mr. Shudarsana Mohapatra, Jalinani, Gitanani, Sabitrinani, Mr. Brajabandhu Karan, Debananda Sir, Bai Sir, Shiba Sir, Bada Didi, Mr. Rameshchandra Dalua, Mr. Padmanava Satpathy, Mrs. Suchismita Mohanty, Mr. Pranab Das, Mr. Anirudha Senapati, Mrs. Rita Paikray, and Prof. Gananath Dash who have enlightened me with their vast knowledge at each step of my academic life.

Last, but not the least, I express my indebtedness, love, and gratitude to the four pillars upon which the base of this journey stands. My deepest gratitude and respect to Mr. Pradeep Kumar Sahoo and Mr. Rajesh Moharana sir for whatever *you both have done for me. This long journey would not have possible without you. I fall short of words to express my thanks and appreciation to you and your family members. Thank you, for always being there with me.*

Finally, my sincere respect and biggest thank to my parents whose moral support and encouragement has always been a great source of inspiration to me. Thank you Bapa and Bou. This is the result of your blessing. I express my heartfelt thanks to all my family members (Late grand parents, Badabapa, Late Badabou, Sujibhai, Bhauja, Dudu, Samibhai, Babinani, Mitanani, Gitanani, Manashbhai, Puchun, Kajal, Tumpul, Gugu, Ritanani, Babulibhai, Prachi, Pilu, Late Badadata, Badakhudi, Lipu, Anitanani, Bedudata, Sanadata, Sanakhudi, Papu, Puja, and Bapu) for your love and support.

Deepak Kumar Karan

GUJARAT SCIENCE ACADEMY

॥ विज्ञानसारथिर्जयति ॥

CHAROTAR UNIVERSITY OF SCIENCE AND TECHNOLOGY, CHANGA INSPIRED

BEST PH. D. THESIS AWARD – PHYSICAL SCIENCES

For The Year 2017

Awarded To

Dr. Deepak Kumar Karan

of IIT, Gandhinagar

IN RECOGNITION OF THE CONTENT AND THE PRESENTATION OF HIS THESIS

Prof. A. K. Singhvi
PRESIDENT

Prof. P. N. Gajjar
SECRETARY

Abstract

The equatorial- low-latitude ionosphere-thermosphere system (ITS) hosts several inter-coupled process during the daytime. Various dynamical effects due to winds and waves affect the ITS. Further, solar forcing and geomagnetic storm effects also modulate the low-latitude ITS coupling. The varying nature of these dynamics in response to different geophysical conditions bring in complexities in these coupled processes, which result small and large scale variations in the behavior of the ITS, both in temporal and spatial domain. Even though, investigations of the wave characteristics in spatial domain of the ITS have been carried out over several decades for nighttime conditions, such investigations during the daytime are in a state of infancy. Therefore, systematic investigations of the wave characteristics for daytime conditions are essential in order to gain a comprehensive understanding of the ionospheric and thermospheric system.

The optical dayglow emission intensity variations can be used as tracers of the neutral dynamical variations that exist at the altitudes of their origin. In the present thesis work, by using a high spectral resolution large field-of-view spectrograph, MISE, we have obtained the neutral oxygen dayglow emission intensities at three wavelengths (OI 557.7, 630.0, and 777.4 nm) from Hyderabad, a low-latitude location in India. These emissions are considered to originate from altitudes around 130, 230 and 300 km. The dayglow emissions are used as the primary data set for the investigations carried out in this thesis work.

The dayglow emission intensity patterns showed both symmetric and asymmetric diurnal behavior with respect to local noon. Considering purely photochemical nature of the production mechanisms of the dayglow, the asymmetric diurnal behavior is not expected and hence, it is clear that transport processes play a role. The extent of asymmetric behavior in the dayglow emission intensity is characterized in terms of Asymmetricity in Time (AT), which is the product of difference in time of occurrence of peak intensity and local noon and the ratio of intensities at the peak and local noon. The days with AT $\leq$ 0.4 h and AT $>$ 0.4 h are considered to be the days with symmetric and asymmetric diurnal behavior in the emission intensities, respectively. Comparing the roles of neutral

winds and the EEJ strengths on the days with AT > 0.4 h, it is conclusively shown that the dayglow emission intensities over the off-equatorial thermosphere are predominantly affected by the equatorial electrodynamics. It is also noted that this asymmetric diurnal behavior in the neutral emission intensities has a solar cycle dependence with more number of days during high solar activity period showing larger AT values as compared to those during the low solar activity epoch.

Periodogram analyses of the dayglow emission intensity have been carried out at all the three emission wavelengths in three distinctly different directions (west, zenith and east) which are separated by 3^0-8^0 depending on the altitude of dayglow emissions. Presence/absence of the time periods with similar values in these three directions indicates the non-existence/existence of longitudinal differences in the gravity wave (GW) features suggesting to a common/different source driving the waves at these locations. The non-existence of the similar time periods on the days with asymmetric diurnal behavior was attributed to the stronger equatorial electrodynamics. Moreover, GW features in terms of the zonal scale sizes and propagation directions also show different behavior on the days with and without the existence of longitudinal differences in the equatorial processes. Thus, our results show, for the first time, that there exist longitudinal variations in the equatorial electrodynamics in as small separations as 3^0-8^0.

Variations in the dayglow emission intensities have been investigated for three geomagnetic disturbances that occurred in different seasons. It is found that the dayglow variations showed similarity with the variation of O/N_2 during geomagnetic disturbances that occurred in solstices. However, during the equinox, the dayglow showed similar variations with that of the EEJ strengths. Taken together, this shows the dominance of the equatorial electric field over the storm influenced neutral wave dynamics on low-latitude ITS during equinox times, and the effect of neutral wave dynamics from high-latitude during solstices. Moreover, contrasting distributions of the GW zonal scale sizes are observed on geomagnetically quiet and disturbed days in different seasons. This shows that changes are brought-in in the zonal GW scale sizes during geomagnetic disturbances irrespective of the season of the storm occurrence.

Near-simultaneous measurements of the spatial varying dayglow along both the zonal and meridional directions are obtained. From the wave number spectral analysis of these data, the zonal and meridional component of the horizontal waves are obtained. These values are used to calculate the horizontal scale sizes and their propagation angles. Such measurements on the horizontal scale sizes (in two dimensions) are first results of their kind. Moreover, these measured values have been used in conjunction with the GW dispersion relation to calculate the plausible wave features in the vertical direction. Thus, the first three dimensional GW characteristics in the daytime upper atmosphere has been derived. This technique opens up new possibilities in the investigations of the daytime wave dynamics.

Keywords: Dayglow, Ionosphere, Thermosphere, Upper atmosphere, Equatorial electrodynamics, Ionospheric-Thermospheric coupling, Gravity waves, Geomagnetic storm, Latitudinal coupling, Three dimensional gravity waves.

Contents

List of Figures

List of Tables

Chapter 1

Introduction

1.1 Background

Nature is extremely beautiful to observe, though not simple to explain. Thinking of the universe with our closed eyes, creates enormous excitement and avidness to explore and understand it thoroughly. Meanwhile, Life is an integral part of the nature, which is yet a mystery amongst all. In the explored part of the universe, our Earth is the only planet where the existence of life is known. This makes the Earth very special and unique among other planets. The Earth has a well-disposed and absolutely balanced internal as well as external structure. Its surface, atmosphere, and internal structures are perfectly arranged to make life sustainable on this planet since billions of years. Like water, the role of the Earth's atmosphere is invaluable for the existence of life on this planet.

The excitement to understand and explore the planet Earth motivates our scientific communities to carry out thorough investigations on its different aspects. Scientists and researchers are always fascinated by the Earth's atmosphere and focus their interest in rigorous and in-depth study of it. The study of Earth's upper atmosphere has always been challenging for scientists because of its highly complex behavior. Existence of both neutral and ionized species in the upper atmosphere and their varying response to the solar forcing, lower atmospheric dynamics, and geomagnetic disturbances bring complexities in the upper atmospheric behavior. Studies have been carried out to understand the upper atmospheric processes and their variations during different geophysical conditions. Nonetheless, there are many intricacies which need further investigation. In this chapter, we will discuss the structure of Earth's atmosphere (focus will be on thermosphere and ionosphere), various dynamics (e.g. winds, waves), and the related phenomena which occur in the low-latitude upper atmosphere during both geomagnetically quiet and disturbed periods.

1.2 Structure of Earth's Atmosphere

The atmosphere surrounds the Earth from all directions. It contains 78% nitrogen, 21% oxygen and 1% other constituents. The effect of gravity and temperature makes the atmosphere, to the first order, horizontally stratified. Based on the composition and mixing, the atmosphere is divided into two parts. The lower one, below 100 km is the *homosphere*. The varying temperature gradients in the atmosphere within this altitude range cause different turbulences with scales larger than the mean free path, which, in turn, make the homosphere a well-mixed part of the atmosphere. The atmosphere above 100 km altitude is called the *heterosphere*. A positive temperature gradient is maintained in the heterosphere till an altitude of around 500 km. Above this altitude, temperature remains almost constant. As a result, the neutrals separate and tend toward diffusive equilibrium, wherein, each species is distributed in altitude according to its weight. Thus, the lower/upper heterosphere is dominated mostly by molecular/atomic species. For example, at ~300 km altitude the O_2 concentration is $\sim 10^7$ cc^{-3}, whereas, the concentration of O is $\sim 10^9$ cc^{-3}. At a lower altitudes around 100 km, the concentrations of O_2 and O are $\sim 10^{13}$ and $\sim 10^{11}$ cc^{-3}, respectively. The layer that separates the homosphere from the heterosphere is called the *turbopause*, which is at an altitude of around 100 km (Figure 1.1).

Earth's atmosphere stretches to altitudes of several hundred kilometers. If a column with unit surface area is considered in the atmosphere, then its weight on the surface at the base of this column is called the atmospheric pressure. The gas number density of the atmosphere near the surface of Earth is $\sim 10^{19}$ cm^{-3} and

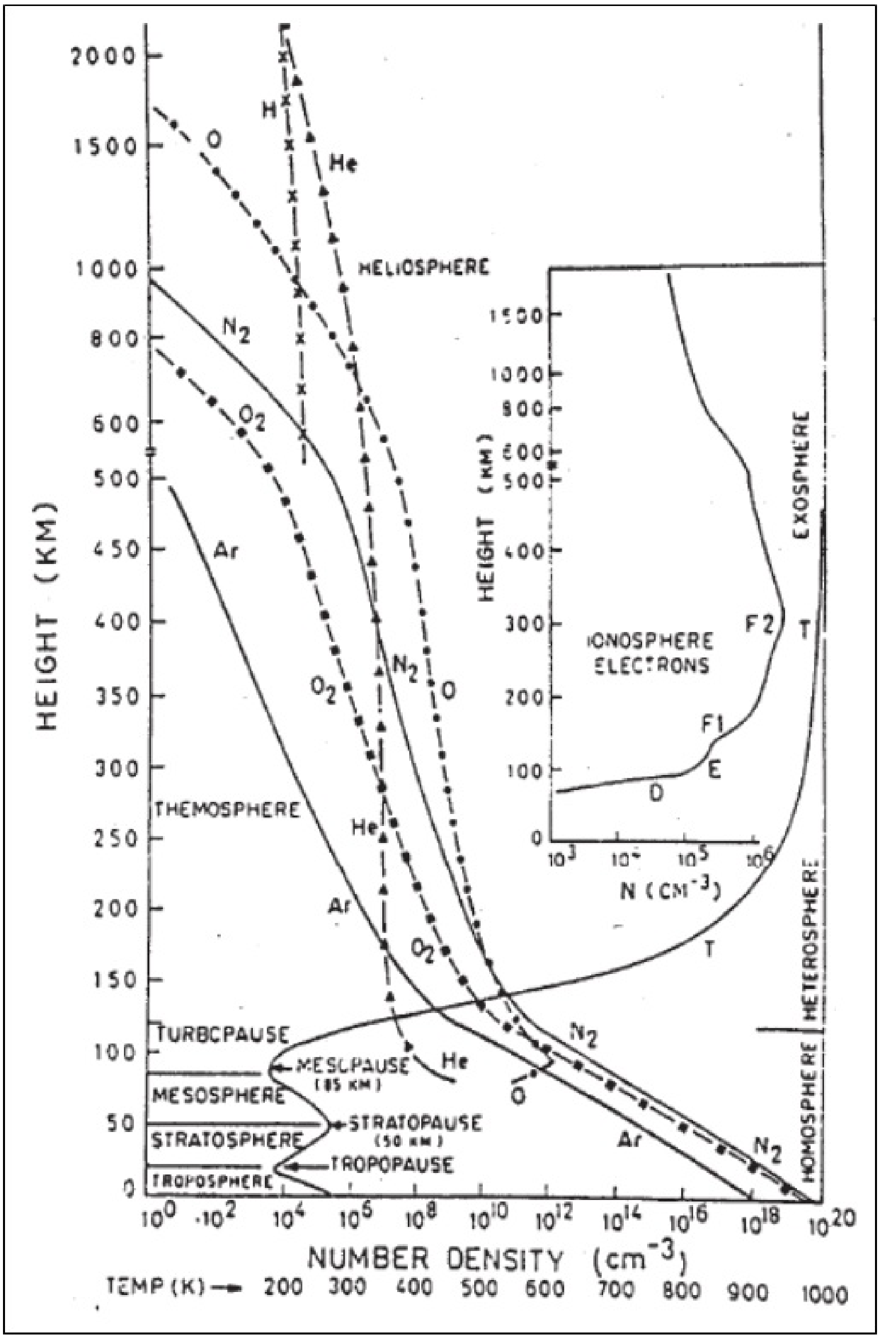

Figure 1.1: Classification of Earth's atmosphere showing variations of neutral temperature, number densities of different atomic and molecular species. The inscribed figure shows the electron density variations with altitude. After *Pallamraju* [1996].

it decreases exponentially with altitude near the surface. Earth's gravity attracts the atmosphere with a downward force. At the same time, the atmospheric pressure gradually decreases with altitude. Thus a hydrostatic equilibrium is attained due to the balance of gravitational force by the pressure gradient force.

The atmospheric temperature does not vary in the same manner at all the altitudes. The physical and chemical properties of the ambient constituents, transport mechanisms and dynamics decide the variation of the temperature gradient at a given altitude. According to the altitudinal gradients of neutral temperature, the atmosphere is broadly divided into five layers, i.e. *troposphere*, *stratosphere*, *mesosphere*, *thermosphere*, and *exosphere* (Figure 1.1). The troposphere constitutes the *lower atmosphere*; the stratosphere and a part of the mesosphere constitute the *middle atmosphere*; and the upper part of the mesosphere, thermosphere and exosphere constitute the *upper atmosphere*.

Troposphere is the bottom-most layer of the atmosphere, which covers from the surface of Earth up to around 12 km altitude. This layer gets heated up by the Earth's surface. Sunlight enters from the space to the atmosphere and strikes the surface of the Earth and heats the surface. Then, the surface radiates the heat into the adjacent atmosphere. At higher altitudes, where less heat from the surface warms the air, the temperature decreases. Due to the negative temperature gradient, convection sets up in the troposphere and equilibrium is maintained. Thus, the troposphere is known to be in convective-radiative equilibrium. Typically, the temperature drops around 6.5 K with each increase of 1 km altitude in the troposphere. This is called *lapse rate*. The decrease of temperature pauses at an altitude of around 10 to 15 km, which is called the *tropopause* region. Tropopause is the boundary layer between the troposphere and the stratosphere. The height of this boundary varies between about 15 km at the equator to 8 km at the Polar regions.

An increase in temperature occurs in the **stratosphere** (around 12 to ∼50 km) due to the absorption of solar ultraviolet (UVB, 253-300 nm) radiation by the stratospheric ozone. The stratosphere plays a protective role since harmful UV radiations are absorbed by the ozone layer that peaks at an altitude of around 25 km. The increase in temperature in the stratosphere reaches a maximum at about 50 km due to the combined effect of absorption of UVB by ozone and photodissociation of O_2 by the solar radiation (∼ 180-230 nm). Above this altitude, temperature again starts decreasing. The boundary that separates the stratosphere from the mesosphere (at about 50 km altitude) is called the *stratopause*.

Moving up to the next layer is the **mesosphere** (around 50 to ∼90 km). In this layer, the temperature decreases due to chemical and dynamical processes like radiative cooling of species like CO_2 in infrared and visible wavelengths. Absorption of solar radiation by ozone and molecular oxygen is the source of heating in the mesosphere. The boundary that separates the mesosphere from the thermosphere is called the *mesopause*, which is the coldest region (∼180 K) in the Earth's atmosphere. The Mesopause lies at an altitude of around 90 km.

The layer above mesopause is called the **thermosphere**, which extends to around 800 km. The temperature rises sharply from ∼200 to ∼1000 K from the lower to upper thermosphere due to photodissociation of O_2 by the solar radiation in the Schumann-Runge continuum (∼135-175 nm), which results oxygen atoms at different excited metastable states. The de-excitation of these excited states due to collisions cause local heating of the lower thermosphere. These energetic photoelectrons collide with the ambient neutrals and ions, thereby distribute the energy in the medium and contribute to the thermospheric heat content. The magnitudes of EUV and X-ray radiations from the sun are highly solar activity dependent, which vary up to a factor of 2 between the two extrema of the solar cycle [*Roble and Dickinson*, 1973; *Stolarski et al.*, 1975; *Hinteregger*, 1976]. The vertical propagating atmospheric waves (discussed in detail in the following section) from the lower atmosphere deposit their energy in the lower thermospheric regions and contribute to a part of the heat budget. Moreover, during geomagnetic disturbance periods, precipitation of high energy charged particles of solar wind origin over high-latitude thermosphere, cause a sharp rise in temperature at those latitudes. The Joule heating by electrical currents at high-latitudes during geomagnetically disturbed periods, sets up horizontally propagating waves. These waves affect the thermospheric temperature over mid- and low-latitudes. In the upper part of thermosphere, the density is very small and the heat is conducted downwards efficiently. Hence, an isothermal condition is set up in the upper thermosphere. Thus, with increasing altitude from the thermospheric altitudes, the temperature rises sharply but an equilibrium is maintained due to high thermal conductivity at higher altitudes.

Above the thermosphere, the portion of the atmosphere is known as the **exosphere**. The density is so low at these altitudes that the mean free path of the constituents like H and O exceeds the scale height. Collisions between the neutrals are so infrequent that they follow ballistic orbit under the influence of gravity only. The base of the exosphere is called the *exobase* or the *baropause*.

Till now we have discussed about the neutral part of the atmosphere. Whereas, the Earth's atmosphere contains both neutrals and charged species. In the upper mesosphere and thermosphere, the high energetic solar radiations strip atmospheric atoms and molecules of their electrons, producing an electrically conductive region known as the **ionosphere**. The ionosphere broadly ranges from about 60 km to around 1000 km. However, the ionosphere has no sharp upper boundary. It merges into the protonosphere which is primarily populated with hydrogen ions.

The ionosphere extends through the upper part of the mesosphere, thermosphere and exosphere. The ionosphere plays an important role in the Earth's atmosphere, as it influences the radio wave propagation over large distances. The ionosphere contains free electrons, ions, and neutrals. Within a certain volume, the number of ions and electrons are equal and hence, quasi-neutrality condition is valid. Thus, the ionosphere is considered to contain the plasma. Although the density of charged particles is smaller by nearly 3-4 orders of magnitudes as compared to the neutrals, they have substantial influence on the electrical properties of the medium.

The production and loss processes of the charged particles depend upon the available energy, ambient constituents, and transport processes. So the net electron densities have temporal and altitudinal variations. Depending on the electron density distribution, the ionosphere is divided into different regions, namely; D region (about 60-90 km), E region (about 90-160 km), and F region (>160 km) (see Figure 1.2). During the daytime all these regions can be distinguishable, but during night the D and F_1 region vanish and the E region becomes much weaker.

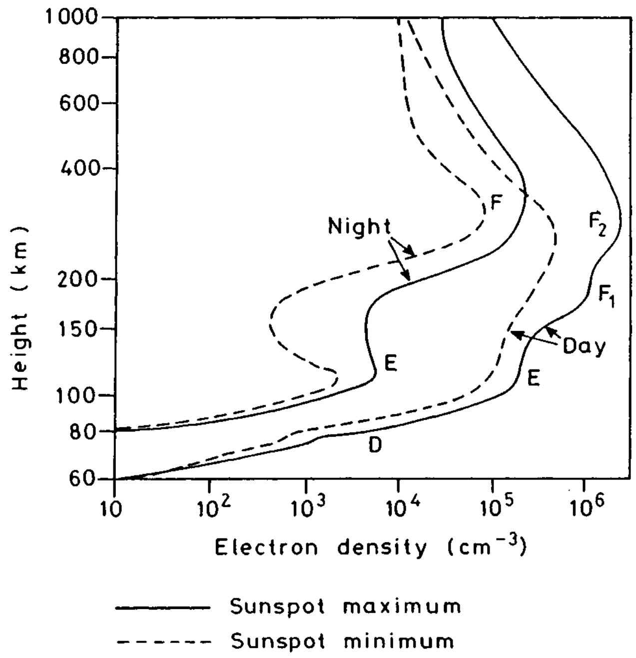

Figure 1.2: Typical electron density profiles during the day and nighttime in solar maximum and minimum periods. After *Hargreaves* [1992].

The Lyman-α line, EUV, hard X-rays, energetic particles from sun, and galactic cosmic rays are responsible for the production of ionization in the D region. Solar X-rays (1-10 nm) and EUV radiations (80-102 nm) cause ionization in the E region. Ionization of the neutral species processes in the 15-80 nm wavelength range produces the F region of the ionosphere. Sometimes during the daytime, the F region splits into two sub-layers, F_1 and F_2. Mostly molecular ions (e.g. NO^+ and $O_2{}^+$) are present in the E and lower F region and atomic ions (e.g. O^+) in the upper F region. The loss rate for molecular ions obey square law but for atomic ions it is linear law and are operative at lower and upper part of the ionosphere, respectively. Therefore, a differentiation occurs in the region of separation between the molecular and atomic ions. This occurs at about 160-200 km altitude. When this transition region matches with the altitude where the ion production is the highest, then F layer splits into F_1 and F_2 layers. Transport processes dominate the F region and the life time of atomic ions are of the order of a few hours. Hence, even after the sunset also the F layer exists. On the other hand, due to faster recombination processes of the molecular ions, the E layer almost vanishes during the nighttime.

It is to be noted that the charged particles (both ions and electrons) show different type of movements in the D, E, and F regions of the ionosphere. In the D region, due to larger neutral atmospheric density, movement of both ions and electrons are dominated by their collisions with the neutrals than by the effect of the Earth's geomagnetic field (i.e. collision frequencies, $\nu_{in}, \nu_{en} \gg$ gyro frequencies, ω_i, ω_e). The gyro frequency, $\omega = qB/m_{i,e}$, where q is charge, B is magnetic field and m is mass. At 80 km, $\left(\frac{\nu_{in}}{\omega_i}\right) \gg 1$, $\left(\frac{\nu_{en}}{\omega_e}\right) \approx 2$. In the E region the situation is different. Due to larger mass and larger collision cross section of ions, they move along with the neutral winds. But in case of electrons, the gyro frequencies are greater than their collision frequencies. Thus, in the E region, the movement of electrons are controlled by the magnetic filed lines, whereas, ions are still dominated by their collision frequencies (i.e. $\nu_{in} > \omega_i$ but $\nu_{en} < \omega_e$). At 120 km, $\left(\frac{\nu_{in}}{\omega_i}\right) \approx 2$, $\left(\frac{\nu_{en}}{\omega_e}\right) \ll 1$. In the F region, movement of both ions and electrons are dominated by the magnetic field lines (i.e. $\nu_{in} \ll \omega_i$ and $\nu_{en} \ll \omega_e$). At 300 km, $\left(\frac{\nu_{in}}{\omega_i}\right) \approx \frac{1}{300}$, $\left(\frac{\nu_{en}}{\omega_e}\right) \ll 1$. More detailed explanation on this can be found out in *Rishbeth and Garriott* [1969]; *Rishbeth* [1997].

The ionospheric plasma can exist in very small densities within the plasmasphere upto 4-5 R_E (where R_E is the radius of Earth), beyond which, there is another region called the **magnetosphere**. The magnetic field lines in the plasmasphere are bousnd to the Earth and therefore, the plasma co-rotates with the Earth. In the magnetosphere, however, the magnetic field lines are governed by the convective fields of solar wind origin. The magnetosphere ends at the magnetopause, where the influence of geomagnetic field ceases to exist. On the dayside, the magnetopause lies at a distance of $\sim$10 R_E , whereas, on the nightside it can extend to $\sim$100 R_E.

From the above discussion, it is clear that the thermosphere and ionosphere basically refer to the neutral and ionized part of the upper atmosphere. The behavior of the thermospheric dynamics is governed by the gravity, neutral winds, and atmospheric waves. On the other hand, the ionospheric behavior is regulated by the electric and magnetic fields. Both the thermosphere and ionosphere share the same portion of the upper atmosphere and therefore, are coupled with each other. This, as a whole is called the ionosphere-thermosphere system (ITS). Thus, to have a complete understanding of the upper atmospheric state, information of both thermosphere and ionosphere is needed.

1.3 Ionospheric and Thermospheric Dynamics

The upper atmospheric behavior is controlled by neutral winds, waves and electric fields in conjunction with the Earth's magnetic field. The magnitudes and directions of these parameters have latitude, longitude, altitude, local time, seasonal, and solar activity dependence.

1.3.1 Thermospheric Neutral Winds

The thermospheric neutral wind is an important driver of the ITS. Winds influence the composition, neutral dynamics and electrodynamics of the upper atmosphere. Moreover, winds play a crucial role in the generation of electric fields and setting up of the current systems. Discussions on the source and propagation of thermospheric winds started preceding the space age [*Greenhow*, 1954]. There are reports on the wind measurements from satellites [e.g., *Forbes et al.*, 1987; *Hedin et al.*, 1988; *Shepherd et al.*, 2012], ground-based 630.0 nm Fabry-Perot Interferometric measurements [e.g., *Hernandez and Roble*, 1976; *Meriwether et al.*, 1984, 1986, 2011; *Burnside and Tepley*, 1989; *Shiokawa et al.*, 2003], as well as Incoherent Scatter Radar (ISR) derived thermospheric winds [e.g., *Salah and Holt*, 1974] during different geomagnetic conditions. Empirical characterizations and modeling simulations of the thermospheric neutral wind have been carried out both for geomagnetically quiet [*Geisler*, 1967; *Kohl and King*, 1967; *Hedin et al.*, 1996; *Drob et al.*, 2008, 2015] and disturbed conditions [*Roble et al.*, 1987; *Emmert et al.*, 2008].

The thermospheric neutral wind has meridional, zonal, and vertical components. Thermospheric winds are influenced by the coriolis force due to Earth's rotation. Apart from this, the winds are also affected by the frictional forces due to the viscosity of the air and by the collisions of neutrals with the ambient ions.

Ions move along the magnetic field lines and inhibit the motion of the air by posing a drag force, which is called the 'ion-drag'. The ion-drag force is a major factor that limits the wind speeds in the thermosphere. Frictional forces due to the ion drag (and viscosity) dominate over the coriolis force in the thermosphere.

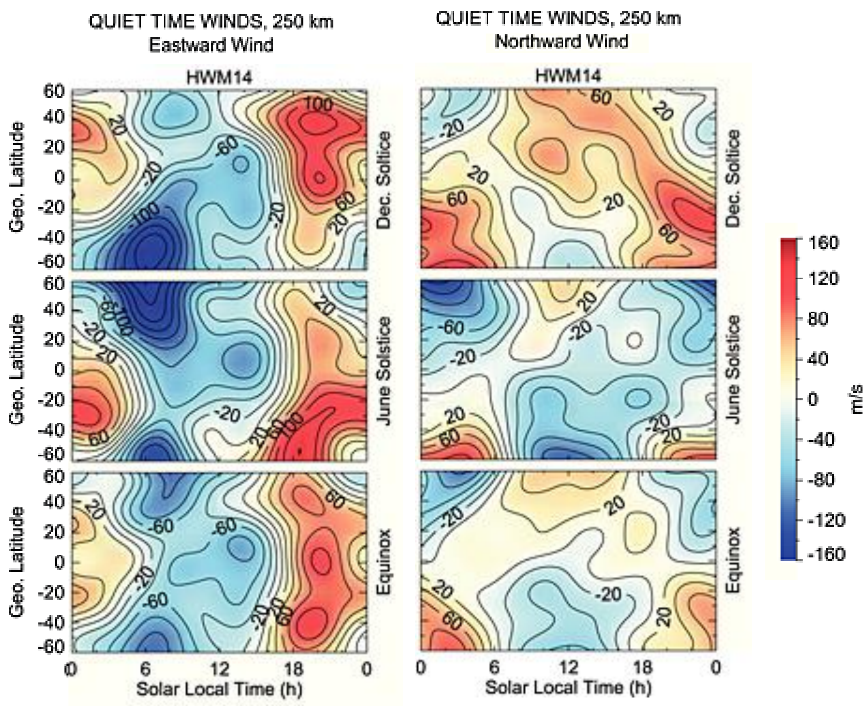

Figure 1.3: Latitudinal variations of the geomagnetically quiet time zonal (left) and meridional (right) winds as a function of the solar local time at 250 km altitude derived using HWM14. The model winds are evaluated for December solstice (upper), June solstice (middle), and equinox (bottom). After *Drob et al.* [2015].

During the daytime in equinoxes, the solar radiations fall more on the equatorial region than on the polar regions. This results in a net temperature gradient between the two regions. Therefore, meridional winds flow from the equator to poles (Figure 1.3). In the nightside, due to Joule heating over polar regions, winds blow from the polar to equatorial region and can be very strong especially during geomagnetic storms. The winds move the F region ions and electrons along the geomagnetic field lines due to ion-neutral collisions. As the ions in the F region are strongly coupled to the magnetic field lines, as a reaction force they also exert a drag force on the neutral winds, which is given by $\nu_{ni}(u - v_i)$, where, ν_{ni} is the ion neutral collision frequency, u is the neutral wind velocity, and v_i is the ion drift velocity. Due to this reason, the F region wind speed during daytime is generally less than that in the night. If the geomagnetic field lines are inclined (not horizontal), then the vertical component of the geomagnetic field will guide the motion of ions and electrons to different altitudes. As the loss-coefficient of ions are altitude dependent, the net concentration of ions and electrons will change. Since the meridional winds are poleward mainly during the daytime, they move the ions and electrons down to lower altitudes. During the nighttime as the meridional winds are equatorward, they lift the ions and electrons in the F region to higher altitudes. Such effects, being dependent on the geometry of geomagnetic field lines, have latitudinal variations (Figure 1.3). As the magnetic field lines are horizontal above the geomagnetic equator, meridional winds have no effect on the plasma over this region [*Rishbeth*, 1972]. During different seasons, the thermosphere in the summer hemisphere suffers greater solar EUV heating and trans-equatorial (meridional) winds are set up.

The zonal winds in the thermosphere flow along the east-west direction. During the daytime zonal winds are generally westward and during the nighttime these are eastward due to the pressure gradient forces set up due to differential heating between the day and night. The zonal winds give rise to the electric fields and currents through the dynamo action in the E region over the geomagnetic equatorial region[*Gouin and Mayaud*, 1967; *Onwumechilli*, 1967; *Anandarao and Raghavarao*, 1987; *Rishbeth*, 1997]. Observation of the vertical component of the thermospheric winds is very sparse [e.g., *Biondi and Sipler*, 1985; *Raghavarao et al.*, 1987, 1993]. Vertical winds can play an important role in the thermospheric wave dynamics and also in the growth of plasma instabilities associated with Equatorial Spread F [e.g., *Sekar and Raghavarao*, 1987; *Raghavarao et al.*, 1993].

1.3.2 Waves

Waves play a crucial role in the dynamics of the Earth's upper atmosphere just like the thermospheric neutral winds. The upper atmosphere is affected by the waves which propagate from the lower atmosphere and high-latitude regions (during geomagnetic storms) in addition to those that are locally generated. Depending on the ambient atmospheric conditions, the effect of wave dynamics on the upper atmosphere show a seasonal dependence.

The waves are produced basically due to the perturbations originating from inside the medium or from outside. A simple example of the atmospheric wave motion is that of a displaced air parcel, which is governed by two forces. One is the thermal forcing which takes the air parcel up and the other is the restoring force due to the gravity. As a resultant of these two oppositely directed forces, the air parcel starts oscillating in the medium and generates waves. The waves can propagate in any directions through the medium. The fundamental properties of the wave propagation are (i) the transfer of energy and momentum from one point to other, (ii) the disturbance travels through the medium without changing the mean positions of the species in the medium.

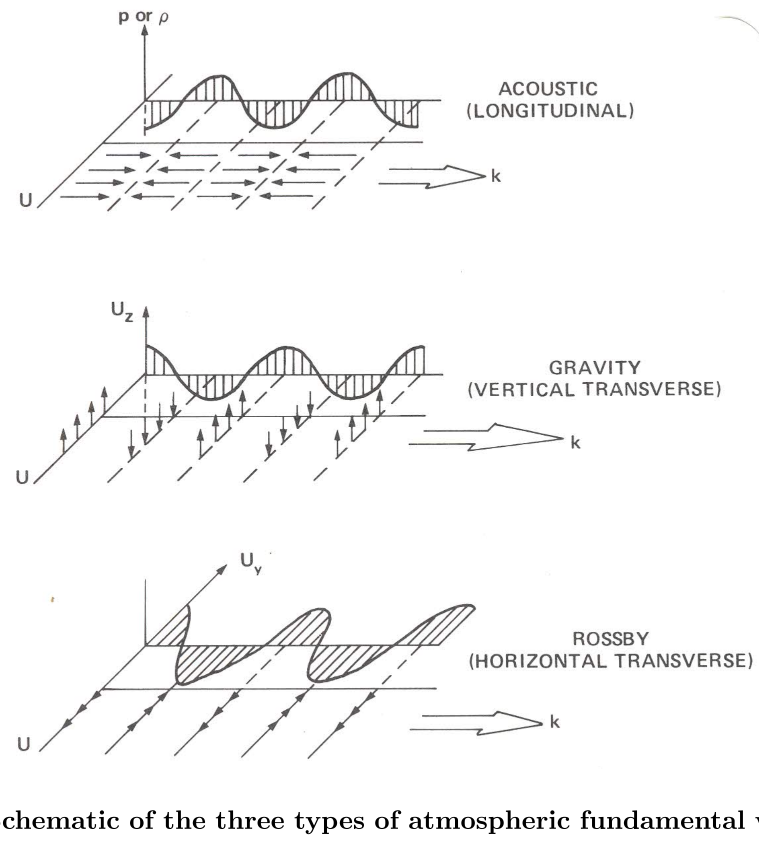

Figure 1.4: Schematic of the three types of atmospheric fundamental waves. After *Beer* [1974].

Depending on the direction of propagation and displacement of the medium, the atmospheric waves are classified into three classes. (1) The waves that propagate along the direction of displacements (longitudinal), (2) The waves that propagate horizontally and are composed of vertical displacements (vertical transverse waves), and (3) The waves that propagate horizontally with horizontal displacements perpendicular to the propagation direction (horizontal transverse waves). Figure 1.4 show the schematic of the three types of atmospheric fundamental waves.

It is to be noted that in the atmosphere, the wave motions are generally a superposition of all these three types of waves. However, two waves with different amplitudes and wavelengths can propagate in the same medium but in different directions without interacting with each other. When the waves propagate in the medium, their amplitudes can grow or attenuate. In such cases the waves can interact to produce a non-linear resultant effect.

Based on the nature of sources for perturbation, time-scales (periodicities), spatial lengths (scale sizes), and amplitudes of oscillation the atmospheric waves are categorized into different types, which are given in table 1.1.

Waves	Period	Horizontal Scale Size	Importance
Acoustic	< 270 sec	$\sim$ 0.01s-10s m	Ionosphere
Gravity	BV to 3 Hrs.	$\sim$10s-100s km	Ionosphere, UA
Atmospheric tides	24/m, m=1,2,	$\sim$1000s km	Ionosphere, UA
Planetary	$\sim$ days	$\sim$1000s km	Meteorology, UA

UA=Upper Atmosphere

Table 1.1: Categorization of atmospheric waves according to time periods and scale sizes. Where BV stands for Brunt-Väisälä period (the natural period of oscillation of an air-parcel in the atmosphere). After *Beer* [1974].

The general treatment of the atmospheric waves is very complicated. The detailed descriptions on the waves can be found out in the books [e.g., *Beer*, 1974; *Hines*, 1974; *Andrews*, 2010]. In the present thesis work, investigations of the thermospheric wave dynamics have been carried out in the Gravity Wave (GW) domain. Hence, we have discussed the GWs in detail. For the sake of completeness and for broader appreciation of the physics of waves, we have also briefly discussed other types of waves.

Gravity Waves

Sound waves (acoustic wave) are the most well-known waves in the atmosphere. Sound waves are longitudinal waves which propagate through the medium by a balance between the compressibility of the medium (resistance of the fluid to change in its volume) and inertia of the wave (resistance to change in the wave velocity). In the absence of external forces (like gravitational and magnetic, etc.), sound waves are the only waves that can exist in the medium.

As the Earth's atmosphere is a fluid and is acted upon by gravity, the density is well stratified. The density gradient provides a static stability which is absent in a homogeneous medium. When the downward force due to the Earth's gravity and the magnitude of the stabilizing restoring force (upward buoyancy force) due to the atmospheric density gradient becomes comparable, the resulting waves are called the atmospheric gravity waves (AGWs). These waves are no longer purely longitudinal because gravity has produced a transverse component to the propagation direction [*Beer*, 1974]. The waves in which gravity acts as the restoring force are called the GWs.

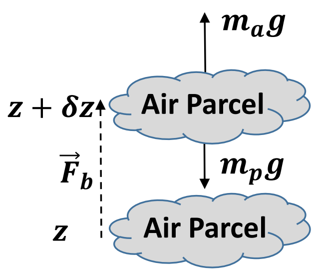

Figure 1.5: Air parcel displaced vertically upward with a displacement of δz from its equilibrium position.

Let us consider the atmosphere to be at rest. An air parcel of mass m_p has been displaced adiabatically (no net heat transfer with the surroundings) vertically upward with a displacement of δz from its equilibrium position, as shown in Figure 1.5. The buoyancy force (vertically upward), $\vec{F_b}$ acting on the air parcel is given as,

$$\vec{F_b} = -g(m_p - m_a)\hat{z} \tag{1.1}$$

where, g is the acceleration due to gravity and m_a is the mass of the air fluid displaced by the air parcel at its new position. Because of the density gradient between the air parcel and ambient atmosphere, m_a and m_p will be different. Applying Newton's second law of motion, we can rewrite equation 1.1 as

$$m_p \frac{d^2(\delta z)}{dt^2} = -g(m_p - m_a) \tag{1.2}$$

Assuming volume of the air parcel and the displaced air fluid to be equal and using ideal gas law in equation 1.2, we can get

$$\frac{d^2(\delta z)}{dt^2} = -g\frac{T_a - T_p}{T_a} \tag{1.3}$$

where, T_a and T_p are the temperatures of ambient environment and the air parcel.

Expanding T_a and T_p to the first order and considering the temperature gradient to be very small as compared with the ambient temperature, equation 1.3 can be written as,

$$\frac{d^2(\delta z)}{dt^2} = -\frac{g}{T_a}\left(\frac{\partial T_a}{\partial z} - \frac{\partial T_p}{\partial z}\right)\delta z = -\frac{g}{T_a}(\Gamma - \varUpsilon_a)\delta z \tag{1.4}$$

where, $\Gamma = -\frac{\partial T_p}{\partial z} = \frac{g}{c_p}$ is the adiabatic lapse rate of the air parcel, c_p is the specific heat capacity at constant pressure (For dry air c_p=1005 J kg^{-1} K^{-1}) and $\varUpsilon_a = -\frac{\partial T_a}{\partial z}$ is the atmospheric temperature gradient.

Equation 1.4 can be written as,

$$\frac{d^2(\delta z)}{dt^2} = -N^2\delta z \tag{1.5}$$

where, $N = \left[\frac{g}{T_a}(\Gamma - \varUpsilon_a)\right]^{1/2}$ is the Brunt-Väisälä (BV) frequency of the oscillation of the wave parcel.

Let us define the potential temperature, β, as that temperature of an air parcel which would be if it is brought adiabatically from an altitude at pressure P to that having a pressure of 1000 mbar or 100 hPa (i.e. sea surface of the Earth).

The potential temperature of the air parcel is given by,

$$\beta = T_a\left(\frac{1000}{P}\right)^{R/c_p} \tag{1.6}$$

where, R is the specific gas constant (for dry air R=287 J kg^{-1} K^{-1}) and R/c_p=0.286.

Taking the logarithmic derivative of β and applying the hydrostatic equilibrium $\left(\frac{\partial P}{\partial z} = -\rho g\right)$, we can get

$$\frac{1}{\beta}\frac{\partial \beta}{\partial z} = \frac{\Gamma - \Upsilon_a}{T_a} \tag{1.7}$$

Thus, the BV frequency can also be written as, $N = \left[\frac{g}{\beta}\frac{\partial \beta}{\partial z}\right]^{1/2}$

Equation 1.5 represents a simple harmonic motion in the vertical direction, whose solution is,

$$\delta z(t) = Ae^{iNt} + Be^{-iNt} \tag{1.8}$$

where, A and B are constants.

If N is real (i.e. $\Gamma > \Upsilon_a$), then the air parcel will oscillate with its natural frequency N. On the other hand, if N is imaginary (i.e. $\Gamma < \Upsilon_a$), then the air parcel will have an unbounded vertical displacement, which is an unstable condition. Such type of instability arises due to the thermal properties of the medium and is known as convective instability. Thus, BV frequency is the maximum permissible frequency in a medium and its values are different at different altitudes.

Till now we have discussed about the motion of the air parcel in a vertical upward direction. This is possible only when the wave motion is horizontal (e.g. waves on the surface of water). But, this is not the case in the atmosphere, where GWs propagate along an inclined plane with respect to the horizontal due to the density, temperature, and pressure gradients. Thus, GWs have both horizontal and vertical components. It is to be mentioned here that the vertically propagating AGWs have no horizontal component. So these are longitudinal in nature and are a special type of gravity waves, called acoustic gravity waves.

Let us consider the motion of the air parcel in an inclined plane as shown in Figure 1.6. The air parcel is displaced by a displacement of δs from its equilibrium position along a plane inclined at angle θ with the horizontal.

The equation of motion of the air parcel can be written as,

$$\vec{F}_s = m_p\frac{d^2(\delta s)}{dt^2} = -g\sin\theta(m_p - m_a) \tag{1.9}$$

Following the same method as done before for vertical displacement of air parcel,

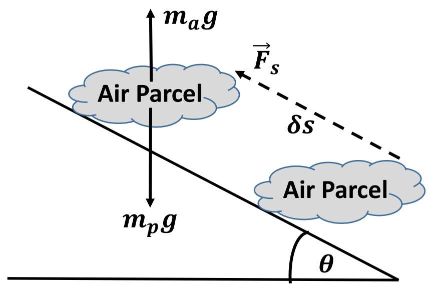

Figure 1.6: Air parcel displaced along an inclined plane with a displacement of δs from its equilibrium position.

we can get

$$\frac{d^2(\delta s)}{dt^2} = -\left[\frac{g}{\beta}\frac{\partial \beta}{\partial z}\sin^2\theta\right]\delta s = -N'^2\delta s \tag{1.10}$$

Here, buoyancy frequency, $N' = \left[\frac{g}{\beta}\frac{\partial \beta}{\partial z}\sin^2\theta\right]^{1/2} = N\sin\theta$

It is to be noted that if $\theta = 0^0$ then N' becomes zero, i.e. the wave motion is completely horizontal with no oscillation. If $\theta = 90^0$ then $N' = N$. Thus, it is clear that depending on the angle of inclination, the frequency of the oscillation varies from 0 to N (BV frequency). Frequencies of tides and planetary waves are smaller than the GWs. Thus, to differentiate GWs from other waves, the minimum angular frequency of the GWs is considered to be $f = 2\Omega\sin\phi$. Here, Ω and ϕ are the rotation rate of the Earth (=$7.29\times10^{-5} rad.s^{-1}$) and geographic latitude. Waves with frequencies below this, will be affected by the coriolis force of the Earth. The example of such waves are tides and planetary waves, which are discussed in the following sections.

Let us consider the propagation of the GW in a two-dimensional (h,z) plane whose wave solution is of the form $\exp[i(\omega t - k_h - k_z)]$ as shown in Figure 1.7. The dashed straight lines are called the wavefronts. The wave numbers $k_h(= 2\pi/\lambda_h)$ and $k_z(= 2\pi/\lambda_z)$ are parallel to the h- and z- axis, respectively, and have the components of wave vector k. The phase propagation angle is given as,

$$\theta = \tan^{-1}\left(\frac{k_z}{k_h}\right) = \tan^{-1}\left(\frac{\lambda_h}{\lambda_z}\right) \tag{1.11}$$

The wave vector k can be written as,

$$k^2 = k_h^2 + k_z^2 \tag{1.12}$$

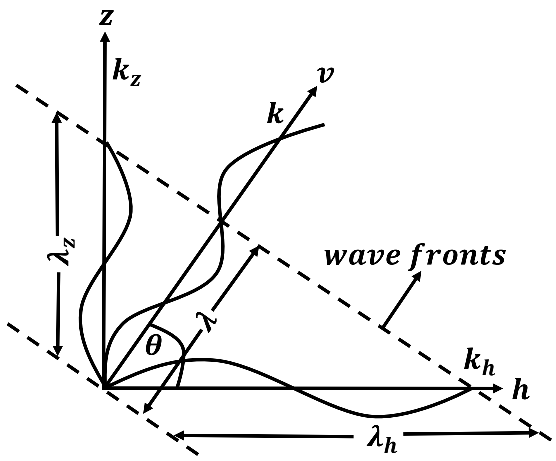

Figure 1.7: An illustration of wavefronts, wave vectors, phase velocity and phase propagation angle of a wave.

Therefore,

$$\frac{1}{\lambda^2} = \frac{1}{\lambda_h^2} + \frac{1}{\lambda_z^2} \tag{1.13}$$

The phase velocity along the direction of θ is,

$$c = \frac{\omega}{k} = \frac{\lambda}{\tau} \tag{1.14}$$

where, τ is the time period of the wave.

The relation between the phase speed and the wave number is called the dispersion relation. The permissible vertical wavelength of the GW can be derived from the GW dispersion relation [*Hines*, 1960], which is given as,

$$k_z^2 = \frac{N^2}{(u - c_h)^2} - \frac{u''}{(u - c_h)} + \frac{1}{H}\frac{u'}{(u - c_h)} - k_h^2 - \frac{1}{4H^2} \tag{1.15}$$

The first term in equation 1.15 is the buoyancy term, where N is the BV frequency, u is the component of the ambient wind and c_h is the horizontal phase speed. The second and third terms are contributions due to the curvature and wind shear terms. The last terms represent the background information (ambient condition), and H is the scale height, $\left(H = \frac{KT}{mg}\right)$.

Let us assume the background mean wind flow to be constant (system is dynamically stable i.e. no wind shearing). Also, the AGWs are not global in nature, and therefore, the curvature and rotation of the Earth are not relevant. Thus, we can neglect the second and third terms from the dispersion relation.

Therefore, equation 1.15 is now reduced to:

$$k_z^2 = \frac{N^2}{(u - c_h)^2} - k_h^2 - \frac{1}{4H^2} \tag{1.16}$$

From equation 1.16 it is clear that, increase of background wind speed (u) in the direction opposite to that of wave propagation will increase the vertical wavelength of the GW. At higher altitudes, as the scale height increases, this results in an increase in the vertical wavelength of the GW.

For a stable atmosphere (i.e. $u = 0$) assuming $\lambda z \ll H$, the GW dispersion equation 1.16 becomes

$$k_z^2 = \frac{N^2}{c_h^2} - k_h^2 = \frac{N^2 k_h^2}{\omega^2} - k_h^2 \tag{1.17}$$

$$\Rightarrow \omega^2 = \frac{N^2 k_h^2}{k_z^2 + k_h^2} \tag{1.18}$$

The vertical phase velocity, $c_{pz} = \dfrac{\omega}{k_z} = \pm \dfrac{N k_h}{k_z \left(k_z^2 + k_h^2\right)^{1/2}}$

The vertical group velocity, $c_{gz} = \dfrac{\partial \omega}{\partial k_z} = \mp \dfrac{N k_z k_h}{\left(k_z^2 + k_h^2\right)^{3/2}}$

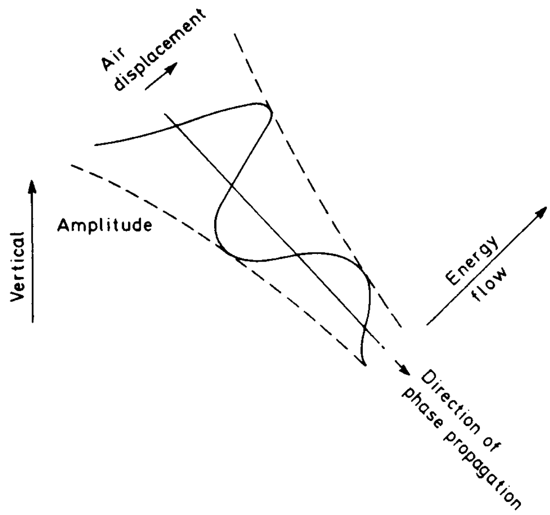

Figure 1.8: Schematic of a vertical propagating GW depicting direction of phase propagation and energy flow. After *Hargreaves* [1992].

It is to be noted that the direction of vertical phase velocity and group velocity are opposite to each other. This shows that for GWs, the downward phase propagation is associated with vertical wave propagation [*Lindzen*, 1990]. Figure 1.8

shows the schematic of a GW propagating upward and the phase is propagating in downward direction. The energy of the wave is flowing along the displacement direction i.e. perpendicular to the direction of phase and wave propagation.

The energy density associated with a wave is given by,

$$< E_t > \propto \rho A^2 \tag{1.19}$$

where, ρ is the atmospheric density and A is the amplitude of the wave. In order to maintain the energy flux constant, the amplitude of the vertical propagating wave increases, since the density decreases.

GWs have typically a localized source and propagate with a limited range of spatial lengths. In the Earth, the GWs can be generated in the lower atmosphere and mesosphere, which then propagate to the thermospheric altitudes. They can be generated *in situ* in the thermosphere as well.

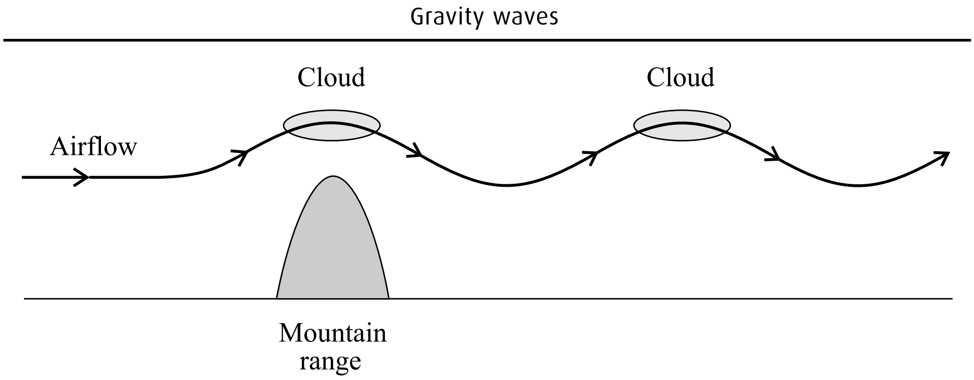

Figure 1.9: Schematic of mountain wave (Lee wave), an internal GW that blow over a mountain range. After *Andrews* [2010].

In the lower thermosphere, AGWs can be generated by perturbations of temperature fluctuations which could be due to orography (Figure 1.9). When an air parcel moves to higher altitudes from its equilibrium position due to mountains, gravity acts as the restoring force. Due to force imbalance, it will move down from its equilibrium position and again due to buoyancy and decrease in temperature, it will move up. In this way the mountain waves act as the source for the GWs. Moreover, from the lower atmosphere, GWs also propagate upward during thunderstorms, volcanic eruptions, wind shears [*Pramitha et al.*, 2015], and tsunamis [*Makela et al.*, 2011a; *Tsugawa et al.*, 2011; *Huba et al.*, 2015; *Smith et al.*, 2015;

Singh and Pallamraju, 2016]. In the upper atmosphere, GWs are generated by temporal and spatial fluctuations in the heating generation due to particle precipitation at high-latitudes, equatorial electrojet over equator, the crests of EIA over tropical regions, etc. Breaking of the upward propagating tides from the lower atmosphere cause GWs in the upper atmosphere. Some other sources for the GWs are the locations of rapid movement of the solar terminator [*Forbes et al.*, 2008] and the supersonic movement of the lunar shadow during solar eclipses [*Chimonas and Hines*, 1971].

Depending on the time period and scale sizes, typically GWs are divided into large-scale and medium-scale waves. The large-scale GWs have horizontal scale sizes of around 1000 km, time periods of more than an hour, and horizontal velocities of 500-1000 ms^{-1}. The medium-scale GWs have horizontal scale sizes of several hundred kilometers, time periods of around 5-60 minutes, and horizontal velocities of 100-300 ms^{-1}. The smallest spatial scales pertain to acoustic waves.

Tides

Tides are generated in the Earth's atmosphere mainly due to the differential heating from the sun and differential effects of lunar gravitational pull. Hence, the time periods of tides are of the order of a solar (24 h) or lunar (24.8) day. These waves are generally treated as the rotationally modified GWs and are global in nature [*Beer*, 1974]. The horizontal wavelengths (scale sizes) of these waves are around several thousand km and the vertical wavelengths are of the order of few tens km. Depending on the source, tides are divided into two categories; namely the thermal tide (e.g. solar tide) and the gravitational tide (e.g. lunar tide). The gravitational tides due to the sun and the thermal tides due to the moon are negligible.

Due to the rotation of the Earth, the atmosphere is heated periodically. As mentioned in the previous section, the thermosphere is heated due to the absorption of solar EUV and X-ray radiations. In the stratosphere and the mesosphere, the heat is generated due to the absorption of solar radiation by water vapor, ozone, atomic and molecular oxygen, etc. Apart from these, the radiations from

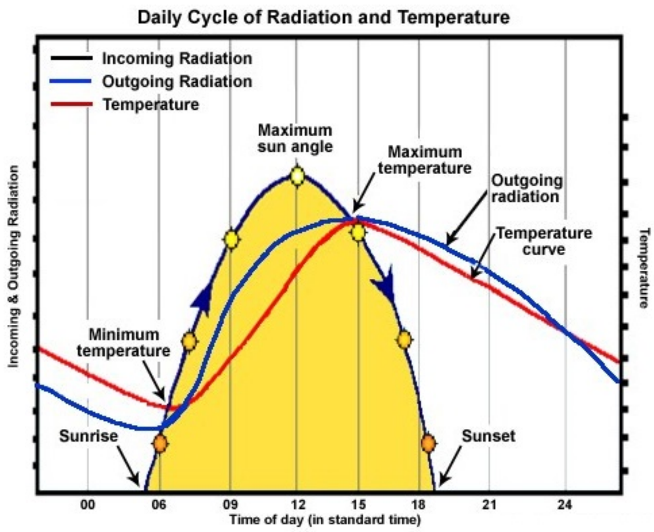

Figure 1.10: Schematic of the diurnal temperature profile of the Earth's atmosphere. (Figure is obtained from Introduction to tropical meteorology, 2nd edition, produced by the COMET program).

Earth's surface heat the lower atmosphere. The schematic of the diurnal temperature pattern of the atmosphere is shown in Figure 1.10. As lifetimes of the atmospheric constituents are different at different altitudes, their contributions to the net temperature vary with local time. It can be seen that the diurnal temperature profile shows an asymmetric behavior and the peak is attained in the afternoon. So, along with the strong diurnal (T=24h) periodicity, semi diurnal (T=12h) and terdiurnal tides (T=8h) are also observed in the Earth's atmosphere. However, the diurnal tides are dominant in the thermosphere. Semidiurnal tides are mostly dominant in the mesosphere and stratosphere regions.

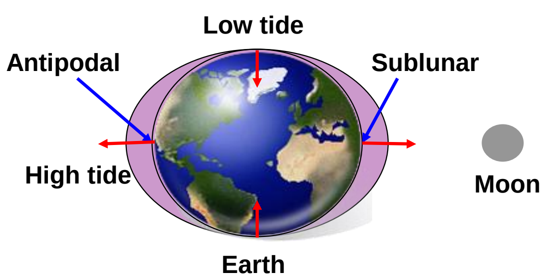

Figure 1.11: Schematic of the lunar gravitational tides. There are two bulges of the atmosphere, one at sublunar point and the other at antipodal point.

The lunar tides are generated due to the differential gravitational attraction of the moon. As the revolution period of the moon around the Earth is 28 day, hence, there occur two maxima and two minima for each revolution of the moon around the Earth, as shown in Figure 1.11. One maxima occur at the time when the moon lies overhead (sublunar) and the other is when the moon lies at the opposite side (antipodal) of the observer. Thus, the lunar tide has a strong time period of $\sim$14 days.

Depending on the propagation directions, tides are again classified into two types, namely migrating tides and non-migrating tides. The migrating tides are synchronized with the solar position and hence, they propagate westward. While, the non-migrating tides do not follow the position of the sun and can move in any direction.

Planetary Waves

The planetary waves (PWs) are larger scale size waves and are global in nature. The horizontal scale sizes are of the order of thousands of km, whereas, the vertical scale sizes are around tens of km. In the atmosphere, the PWs have periods about 2-20 days. For these large scale waves, the Earth's rotation, curvature and coriolis effect cannot be neglected.

The PWs are classified into two types as Rossby waves and Kelvin waves. Rossby waves are generated due to the strong contrast in heating over land and sea. The restoring force is the latitudinal variation of coriolis frequency and hence, get diverted away from the equator and can propagate along both eastward and westward directions. Rossby waves are stronger over the equatorial region and weaker at the pole. The kelvin wave is a special type of gravity waves that are affected by the Earth's rotation and are trapped at the equator or along the lateral vertical boundaries such as coastlines or mountain ranges. These are large-scale wave motion which depend on the gravity and stable stratification for sustaining a gravitational oscillation, coriolis acceleration, and the presence of vertical boundaries or the equator. These waves are trapped to the equatorial region and propagate unidirectionally. They propagate equatorward/poleward along a western/eastern boundary, and counter clock-wise/clock-wise in the northern/southern hemisphere. At the equator, these waves propagate always eastward. The PWs consist of both migrating and non-migrating/stationary modes. The migrating modes are fixed in local time and are driven by the heating at the sub-solar point. Whereas, the non-migrating tides are fixed with respect to a rotating planet.

From the discussions about the atmospheric waves so far, it is clear that the waves are mostly generated in the lower atmosphere and propagate to the upper atmosphere. Propagation of the waves to the upper atmosphere is regulated by different atmospheric dissipation mechanisms, such as, nonlinear wave-induced diffusion, eddy diffusion, radiative damping, molecular diffusion and thermal conduction, and ion-drag [*Pitteway and Hines*, 1963; *Vadas and Fritts*, 2005; *Yigit et al.*, 2008]. Among these dissipation mechanisms, the first three are dominant below the turbopause, whereas, the last two are prevalent above the turbopause. As the waves propagate from low- to high-altitudes, the amplitudes increase and at some altitude the waves become unstable and break down. The breaking of waves occurs mostly in the altitude range of the mesosphere lower thermosphere (MLT) region and secondary waves with smaller scale sizes that are generated, propagate to the upper atmosphere under favorable wind conditions.

1.3.3 Solar Forcing

As discussed above, the upper atmospheric behavior is influenced by the winds and waves which are of atmospheric origin and are influenced by the solar forcing.

With the advent of both ground and space based measurement techniques, continuous observations could yield significant information on the variations of the solar activities. The internal magnetic field of the sun flips its polarity every 11 years. Apart from this 22 year cycle, another strong 27-day variation is also observed in the solar activity due to the rotation of sun about its own axis. The magnitudes of solar EUV, UV, and X-ray radiations vary with the solar activity. The spectral irradiance at these wavelength ranges can increase by a factor of two in the high solar activity as compared to the low solar activity level [*Lean*, 1997]. Thus, an EUV or, X-ray index is one of the best suited index to observe the

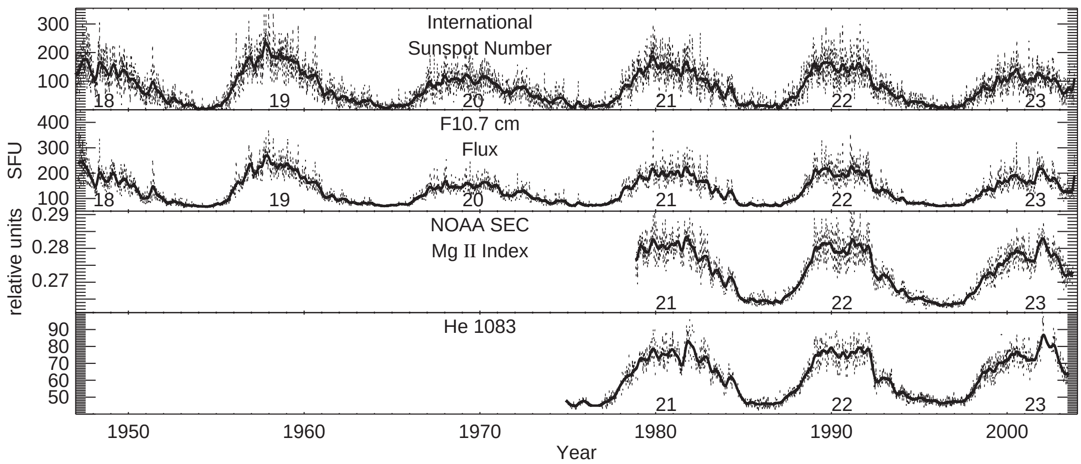

Figure 1.12: Solar cycle variation of sunspot number, F10.7 cm index, Mg II index and He 1083 equivalent width index. The solid line represents the 81-day Gaussian FWHM filtered values for each data set. After *Floyd et al.* [2005].

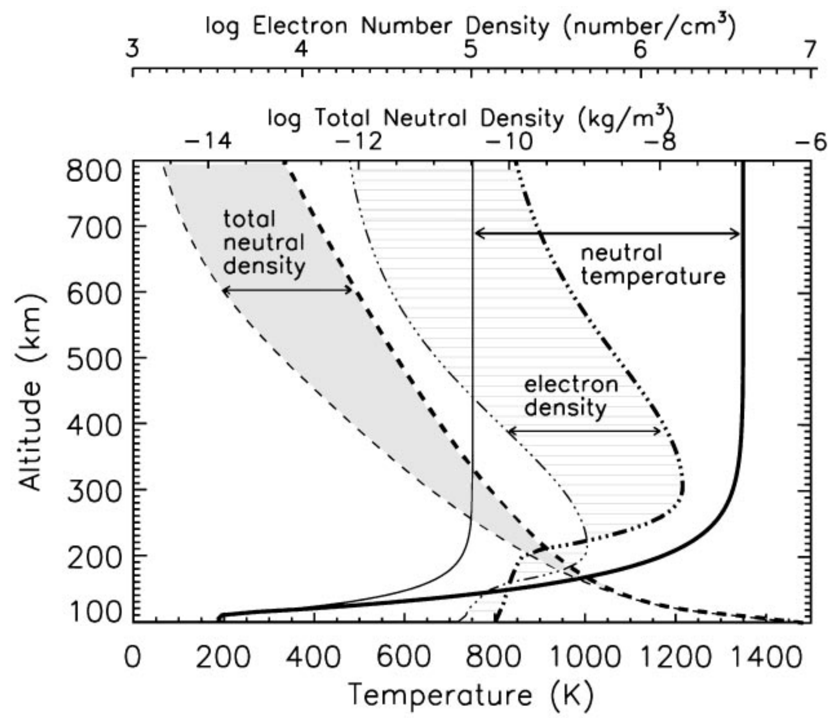

Figure 1.13: Altitudinal variations of thermospheric neutral density and temperature and ionospheric electron density during high and low solar activity periods. Parameters shown in thin/thick lines correspond to low ($F_{10.7}$=70)/high ($F_{10.7}$=230) solar activity periods. These profiles are obtained by the Mass Spectrometer and Incoherent Scatter (MSIS) and International Reference Ionosphere (IRI) models. After *Lean* [1997].

solar activity. However, this radiation gets absorbed in the upper atmosphere as discussed above and hence, cannot be measured from the ground. In the absence of direct measurements, there are many indices developed to characterize the variations of the solar activity. The most common index is the sunspot number (SSN). It has been shown that the solar radiation at 10.7 cm wavelength, to which the Earth's atmosphere is transparent, varies similarly with the sunspot number (Figure 1.12) [e.g., *Floyd et al.*, 2005]. Hence, F10.7 cm flux index is also used as a proxy to measure the solar activity. The F10.7 cm flux index is measured in solar flux units (sfu, 1 sfu=$10^{-22} W m^{-2} Hz^{-1}$). Figure 1.12 depicts the variation of international sunspot number, F10.7 cm index, Mg II index, and He 1083 equivalent width during four solar cycles (1947-2004). It can clearly be seen that F10.7 cm index vary with international sunspot number.

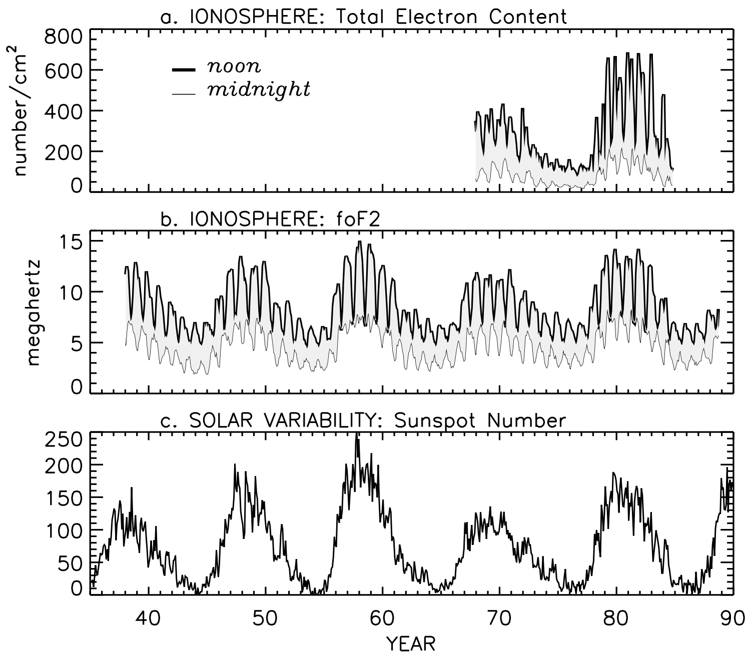

Figure 1.14: Solar cycle variations of Total Electron Content (TEC), F-region critical frequency (f_0F_2) and sunspot number. The three parameters are showing a similar type of variations. After *Lean* [1997]

During high solar activity periods, the incoming EUV, UV, and X-ray radiations increase and this brings significant changes in the thermodynamic, chemical, and radiative state of the thermosphere and the ionosphere. During a complete solar cycle, the upper atmospheric temperature varies by factors of two, whereas, the neutral and electron densities fluctuate by a factor of ten (Figure 1.13). Moreover, from Figure 1.14, it can be seen that the ionospheric total electron content (TEC) and the F layer critical frequency, f_oF_2 (explained in detail in section 2.4.2) show similar variations with sunspot number. This signifies the solar activity dependence of the ionosphere electron densities as a whole. Further, this has been discussed in Chapter-3 of the thesis. Such variations in the background conditions alter the dissipation characteristics of the waves. During low solar activity periods, effect of the lower atmospheric GWs and PWS on the thermospheric variations are found to be significant [*Laskar et al.*, 2013, 2014]. Whereas, during high solar activity periods, the thermospheric behavior is controlled by the solar activity [*Pallamraju et al.*, 2010; *Laskar et al.*, 2013, 2015].

1.4 Daytime Equatorial-Low Latitude Upper Atmospheric Phenomena

Due to the horizontal nature of the Earth's magnetic field lines above the magnetic equator (dip equator) several interesting geophysical phenomena occur which extend to low-latitudes of the upper atmosphere. During the daytime in the E region of the ionosphere both ions and electrons are present and their response to the neutral tidal winds are different. This is because of the difference in their masses and their ratios of collision to gyro-frequencies as discussed in section 1.2. At these altitudes the collision frequencies of ions with neutrals are greater than their gyro frequencies. Therefore, the ions follow the neutral winds. Whereas, for electrons the gyro frequencies are greater than their collision frequencies with neutrals and so they are tied to the magnetic field lines. The tidal wind system in the E region is such that an ambient eastward electric field exists in the daytime ionosphere. These are called the solar quiet (S_q) time eastward electric fields (E_{sq}). The phenomena of the generation of the electric fields by mechanical forces is called dynamo action and the E region is called the dynamo region [*Heelis et al.*, 1974]. However, in the F region of the ionosphere such type of electric fields are not formed, since the gyro frequencies of both the ions and electrons are greater than their collision frequencies and hence, they move together along the magnetic field lines.

The tidal E region wind field is global in nature. This drives a global current system which is counter clockwise in the northern hemisphere and clockwise in the southern hemisphere. This primary zonal eastward electric field ($\vec{E}_x$) crosses with the northward magnetic field ($\vec{B}$) giving rise to a ($\vec{E}_x \times \vec{B}$) vertically upward drift. Even though this drift is independent of charge and mass, as the ions are tied up with the tidal wind, and hence, only the electrons respond to this upward drift. As the perpendicular Hall conductivity falls sharply above 110 km altitude, the up drifting of electrons decrease above this altitude and a layer of electrons gets formed at the upper end of this slab. This result in a vertical polarization electric field ($\vec{E}_z$) which is directed upward. Again this polarization electric field ($\vec{E}_z$) crosses with the northward magnetic field which results in the drift of electrons in westward direction.

The polarization electric field ($\vec{E}_z$) maximizes at an altitude of about 105 km and its value is about 30 times greater ($\sim$ 15 mV/m) than the primary electric field ($\vec{E}_x$) ($\sim$ 0.5 mV/m) [*Anandarao*, 1976; *Pandey et al.*, 2016]. Thus, the zonal westward drift of electrons is very strong, as a result, an intense jet of current flows along the eastward direction in a narrow latitudinal band of $\pm 3^0$ region centered around 105 km over the dip equator. This flow of jet current is called

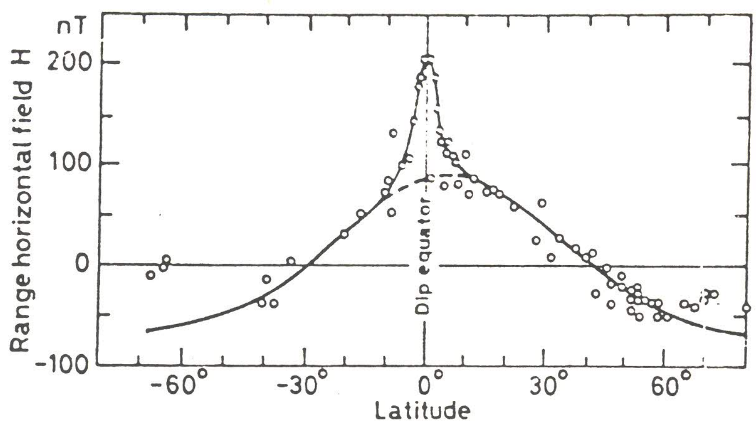

Figure 1.15: Latitudinal distribution of the horizontal magnetic field strength measured by ground-based magnetometers during noon at various latitudes. After *Onwumechilli* [1967]

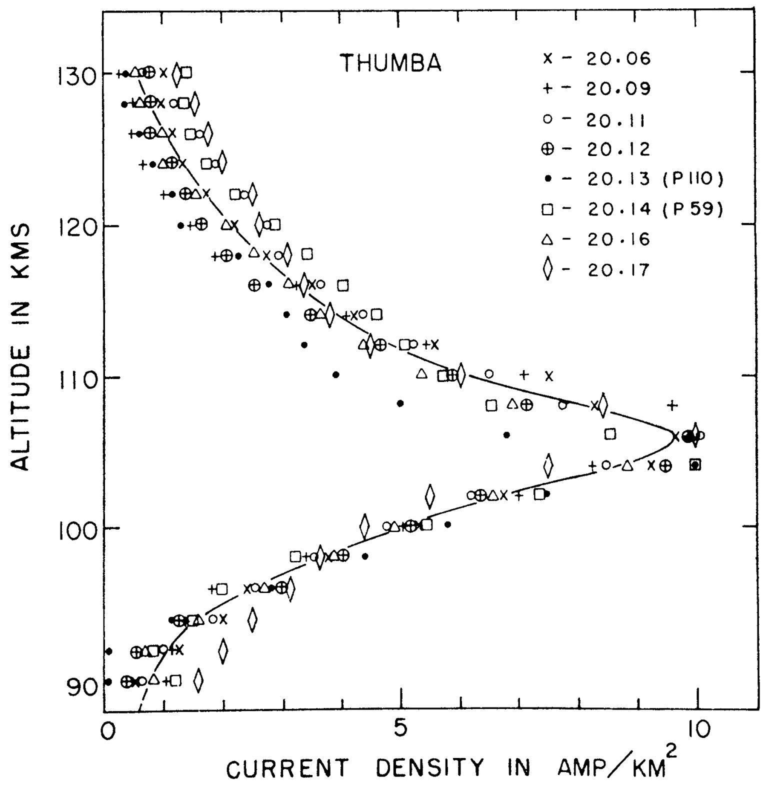

Figure 1.16: Altitudinal distribution of the current density measured during mid-day by rocket magnetometer from Thumba, India. After *Sampath and Sastry* [1979]

the Equatorial Electrojet (EEJ), which is directed eastward during the daytime [*Forbes*, 1981; *Anandarao and Raghavarao*, 1987; *Raghavarao et al.*, 1988].

Figure 1.15 show the variation of horizontal component (H) of magnetic field strength over different latitudes as recorded by ground-based magnetometer. At the dip equator the sharp rise in the value of H seen is due to the equatorial electrojet currents in the ionosphere [*Onwumechilli*, 1967]. Figure 1.16 show the altitudinal distribution of the East-West current density as measured during the mid-day by rocket-borne magnetometer from an equatorial station, Thumba over Indian longitude regions [*Sampath and Sastry*, 1979]. The current density has a sharp peak at ~105 km altitude. From Figures 1.15 and 1.16 it can clearly be seen that the EEJ is confined to a narrow range of latitude and altitude. Since E region electron density is smaller in nighttime, EEJ is less evident.

There are occasions when the horizontal component of the magnetic field (H) measured by the magnetometer goes below the nighttime mean base value. This is called the counter electrojet (CEJ) which occurs mostly during the low solar activity periods. During CEJ the zonal electric field becomes westward and the reasons for the change of electric field direction are still being debated [*Raghavarao and Anandarao*, 1980; *Somayajulu et al.*, 1993; *Stening et al.*, 1996; *Gurubaran*, 2002].

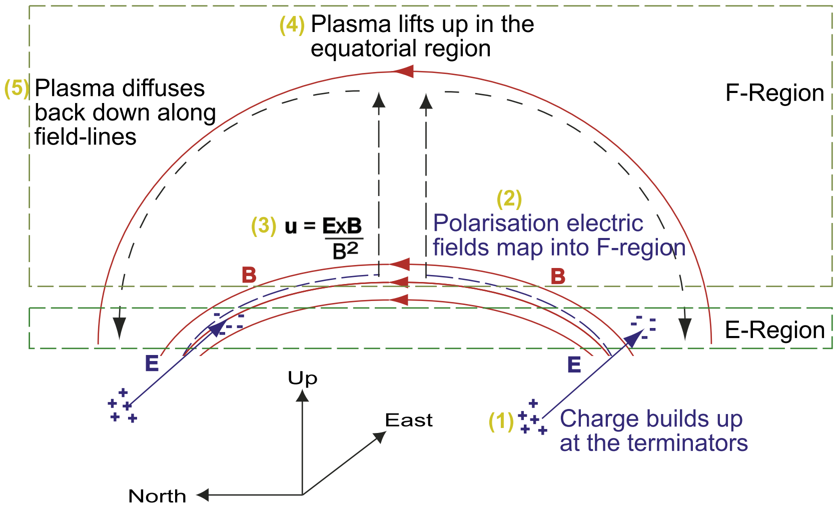

Figure 1.17: Schematic presentation of the development of EIA. (1) Development of zonal eastward electric field in the E region due to the charge separation. (2) Mapping of eastward zonal electric field from off-equatorial E to equatorial- F region along the magnetic field lines. (3,4) $\vec{E} \times \vec{B}$ up drifting of F region plasma. (5) Diffusion of plasma from equatorial- to off-equatorial regions through magnetic field lines. After *Immel et al.* [2006]

From the geometry of the Earth's magnetic field lines above the equatorial- and low-latitude regions, as shown in Figure 1.17, it can be seen that the E region magnetic field lines over the off-equatorial regions are connected to the equatorial F region. Because of the high conductivity along the magnetic field lines, the eastward electric fields (E_{sq}) generated in the off-equatorial E region map to the equatorial F region. This mapped eastward electric fields cross the northward magnetic field and creates a vertical upward ($\vec{E} \times \vec{B}$) drift of plasma in the F region. In the F region, both electrons and ions are influenced by this ($\vec{E} \times \vec{B}$) drift. Thus, the plasma moves up and descends down along the magnetic field lines in both the hemispheres under the influence of gravity and the pressure gradient forces. This is called the fountain effect. The diffused plasma

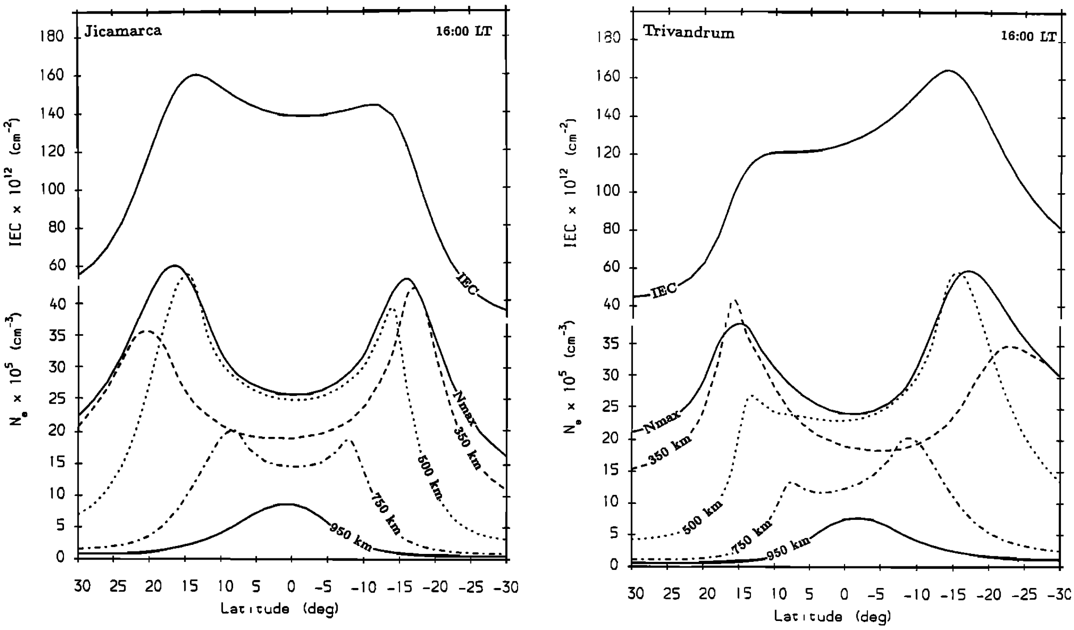

Figure 1.18: Latitudinal variations of the model values of IEC, N_{max} and N_e at different altitudes over Jicamarca and Trivandrum for a fixed time. It is to be noted that with increasing altitude, the strength of the EIA gradually decreases. After *Balan et al.* [1997].

accumulates at around $\pm 15^0$ to $\pm 20^0$ latitudes. These processes are depicted schematically in Figure 1.17. Thus, the plasma density shows a minimum at the equator and two maxima around 15^0-20^0 north and south of it. This creates a double humped structure in the latitudinal distribution of the F region ionization during the daytime with two crests on both side and a trough over the dip equator (Figure 1.18). Typically during an equinoctial period due to photo ionization greater ionization is expected over the equatorial region as compared to that over low-latitudes. Whereas, the observations show an opposite behavior and looks like an anomalous. Hence, this is has traditionally been referred to as Equatorial Ionization Anomaly (EIA) or the Appleton anomaly [*Appleton*, 1946]. This shows the dominance of electrodynamic processes over the photochemical processes and is a good example of E and F region coupling. The product of the latitudinal extent of the crest to trough and the ratio of the electron density at the crest to trough is the measure of the strength of the EIA [*Rush and Richmond*, 1973]. The crest to trough ratio shows altitudinal variations. It maximizes around the peak F_2 altitude and gradually decreases both upward and downward [*Balan et al.*, 1997]. The EIA pattern is also asymmetric about the geomagnetic equator due to the north south (summer to winter) seasonal meridional wind [*Anderson*, 1973; *Raghavarao et al.*, 1988; *Balan et al.*, 1995]. The local time integrated EEJ strength till noontime shows a good correlation with the EIA strength [*Raghavarao et al.*, 1978]. Moreover, the EIA strength shows local time, day-to-day, seasonal and solar activity dependence [*Rajaram*, 1977; *Raghavarao et al.*, 1988; *Sastri*, 1990; *Walker et al.*, 1994; *Pallam Raju et al.*, 1996]. The role of the EIA process in affecting the low-latitude upper atmospheric behavior will be discussed in Chapters-3 and 4.

As a consequence of the EIA, the ion density is more at the crest than the trough region of the EIA. Thus, the neutrals at the crest region of the EIA experience more ion-drag force. Moreover, higher ion densities at the EIA crests as compared to the troughs offer larger resistance to the zonal wind motion that

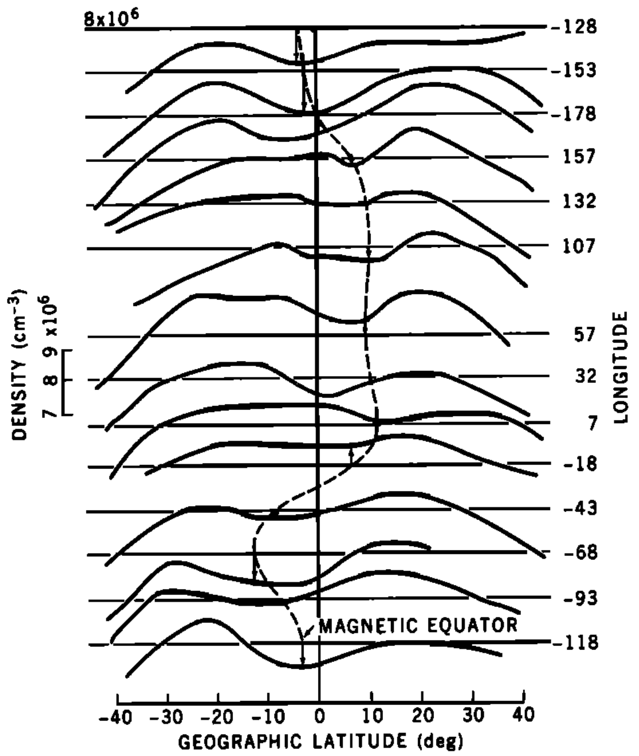

Figure 1.19: Latitudinal distribution of N_2 density at different longitudes around 17 LT as obtained by OGO-6 neutral mass spectrometer. It is to be noted that the N_2 density enhances at the crest region of the EIA (i.e. $\pm 17^0$ dip latitude). After *Hedin and Mayr* [1973].

transports neutrals from the day to the nightside. As a result, accumulation of more neutrals occur at the EIA crest as compared to the trough region. This anomalous behavior in neutral with respect to latitude is called the Neutral Anomaly (NA). By observing the latitudinal distribution of N_2 obtained from the OGO-6 neutral mass spectrometer, *Hedin and Mayr* [1973] showed an enhancement of N_2 density at the crest region of the EIA by 20% than the EIA trough region at around 17 LT (Figure 1.19). Whereas, in morning time around 6 LT, the N_2 density is observed to peak over the dip equator. This is due to the very weak strength of the EIA during the morning hours. The neutral anomaly has a strong local time and solar cycle variation [*Lei et al.*, 2012; *Hsu et al.*, 2014].

As discussed above, due to larger plasma densities over the EIA crests, the zonal-wind magnitude reduces in this region. Due to large ion-neutral collision and chemical heating by molecular dissociative recombination, the temperature increases in this region. Whereas, at the trough region of the EIA due to less plasma densities, magnitudes of the zonal wind are greater which carry the heat from day to nightside. Thus, the neutral temperature is smaller over the trough as compared to the crest. This phenomena of higher temperature and lower zonal wind at the crest as compared to those at the trough of the EIA is called the Equatorial Temperature and Wind Anomaly (ETWA) [*Raghavarao et al.*, 1991]. From satellite observations of latitudinal distribution in temperature and zonal winds through Wind and Temperature Spectrometer (WATS) instrument, *Raghavarao et al.* [1991] first reported this phenomena. The temperature gradient between the crest and trough produces a secondary meridional circulation cell with neutral winds from the crests towards the magnetic equator resulting in a vertical upward/downward winds at the crest/trough regions of the EIA [*Raghavarao et al.*, 1993]. This vertically downward wind over the magnetic equator is considered to play an important role in the generation of plasma irregularities [*Sekar and Raghavarao*, 1987].

Thus, all the daytime phenomenon described above are considered to play an important role in making the ionosphere thermosphere conditions conducive for the formation of the equatorial plasma irregularities in the nighttime [*Sridharan* *et al.*, 1994; *Pallam Raju et al.*, 1996; *Pallamraju et al.*, 2001]. Hence, in order to gain greater insights in these coupling processes, it is required that the daytime wave dynamical characteristics be understood.

1.5 Disturbed Time Low Latitude Upper Atmospheric Behavior

All the processes discussed above depend on the ambient ionospheric thermospheric conditions, such as electric fields, neutral temperature, winds, densities, and wave dynamics, all of which are affected during geomagnetic disturbance periods. As a result, behavior of these processes change during the disturbance periods. In this section we will discuss the effect of geomagnetic disturbances on the equatorial- and low-latitude processes.

The sun constantly emits energy in the form of electromagnetic radiation and charged particles. The electromagnetic radiation range from high energy gamma rays (∼1.24 MeV) to very low energetic radio wave (∼12.4 feV). The solar flare is a process of violent explosion on the sun's surface that releases huge amount of energy in the form of electromagnetic radiation. Solar flares occur mostly around sunspots, which are intense magnetic hotspots on the surface of the sun. Generally, the solar flare lasts for a short duration. The sudden increase of solar radiations in EUV and X-rays during solar flares sharply enhance the dayside ionization which result in enhancement of plasma densities, photoelectron concentrations, and the dayglow emission intensities [*Thome and Wagner*, 1971; *Das et al.*, 2010]. Studies have shown the immediate response of the ionosphere to the solar flare [*Immel et al.*, 2003; *Tsurutani et al.*, 2005], whereas the thermosphere is known to show a delay response [*Sutton et al.*, 2006]. However, there are reports on the immediate response of thermosphere to solar flare [*Liu et al.*, 2007; *Das et al.*, 2010; *Sumod et al.*, 2014].

Due to the huge pressure difference between the outer corona of the sun and the interstellar space, supersonic outflow of electrically charged particles, such as protons, electrons, and alpha particles occur which is called the solar wind and it carries with it the remnant solar magnetic field. The solar wind is extremely tenuous and is a collision-less plasma. Therefore, the electrical conductivity is very high. As a consequence, the magnetic field is frozen in the solar wind, which is called the Interplanetary Magnetic Field (IMF), also known as the Heliospheric Magnetic Field (HMF) [*Owens*, 2013]. Sometimes, because of the sudden explosions in the solar corona due to sun's internal magnetic field, an enormous mass and energy gets released from the sun with speed ranging from ∼500-2000 km.s^{-1}, which is known as Coronal Mass Ejection (CME). The solar wind physically brings the enhanced densities of the charged particles emitted during the CME events. This can take 3-5 days of time depending on the solar wind speed.

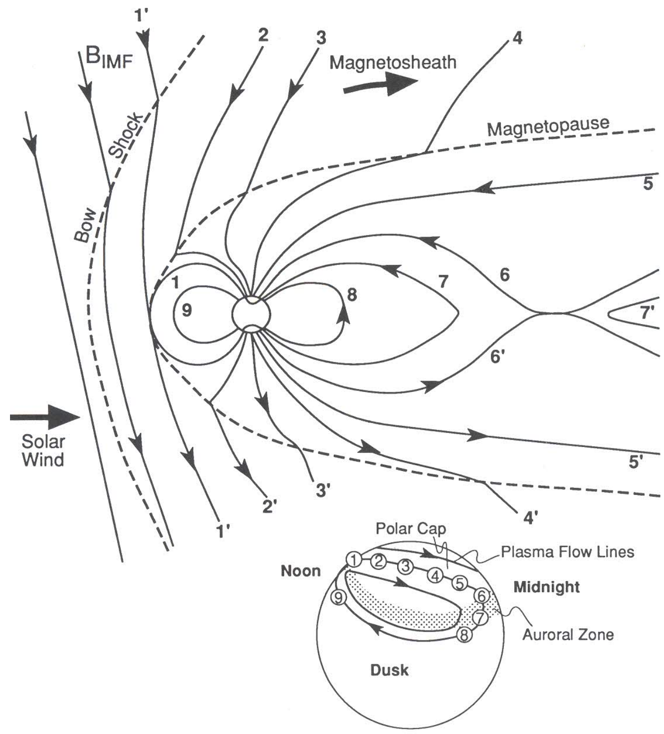

Figure 1.20: Schematic illustrates the reconnection of IMF B$_z$ field lines with Earth's magnetic field lines both in day and nightside. Numbers in succession represent the steps during the whole reconnection process. The inset depicts positions of the origin of the numbered magnetic field lines in the northern polar region along with the high-latitude plasma flows. After *Kivelson and Russell* [1995].

The solar wind follows a spiral path in the interstellar medium due to the rotation of the sun [*Parker*, 1958; *Owens*, 2013]. When solar wind plasma reaches the Earth's magnetosphere and the Z-component of the interplanetary magnetic field (IMF B_z) is southward, then it gets reconnected with the Earth's dayside magnetic field lines (which are directed northward). Due to the reconnection of magnetic field lines (Figure 1.20), the high energy charged particles of solar wind origin move along the Earth's magnetic filed lines towards the polar regions. The open field lines are dragged by the solar wind to the nightside which reconnect in the magnetotail region. As a result, the plasma from magnetotail region gets accelerated towards the Earth. When these accelerated charged particles encounter the closed field lines of the Earth, they experience Lorentz force. The electrons and ions turn towards east and west direction of Earth's dipole field, which result in a westward ring current that is formed at a distance of ~4-6 R_E. The ring current is constituted by three types of motions of the charged particles, namely, (i) gyration about the magnetic field lines, (ii) bounce motion along the magnetic field lines, and (iii) drift motion perpendicular to B. Because of the first two motions, the charged particles gyrate and bounce along the magnetic field lines between the two mirror points. The gradient and curvature drifts move the ions and electrons along westward and eastward directions. The ring current produces an induced magnetic field on the Earth, which is negative to the Earth's magnetic fields as, the current is enhanced in the westward direction. This indicates the onset of a geomagnetic storm which is reflected in the ground-based magnetometers on the Earth and is characterized by the D_{st} index. Details about the variation of D_{st} index during the storm is explained in section 2.4.3.

1.5.1 Electrodynamic Perspective

During geomagnetic disturbances (southward IMF B_z), the dawn-dusk component of the convective electric fields map to the high-latitude ionosphere through the highly conducting geomagnetic field lines and forms a two-cell convection pattern, which are known as DP2 (Disturbance Polar current type 2) cells [*Nishida*, 1968a; *Troshichev*, 1982]. This is an good example of the magnetosphere-ionosphere coupling. The mapped electric field promptly penetrates to the equatorial- and low-latitude ionosphere. This is known as prompt penetration electric field (PPEF) [*Nishida*, 1968b; *Kelley and Makela*, 2002; *Sastri et al.*, 2002; *Chakrabarty et al.*, 2015]. The PPEF is also associated with the under-shielding electric fields which are active mostly during the main and recovery phase of the storm [*Fejer et al.*, 1979; *Kikuchi et al.*, 2008]. When the plasma in the outer magnetosphere, driven by the convective electric field, reaches the closed field lines of the Earth, the differential drift motion of the charged particles take place. Therefore, a polarization electric field is set up in the inner edge of the ring current which will shield the penetration of convection electric field. To satisfy the divergence of the current density, two types of field-aligned currents (Region-1 and Region-2) are generated which connect the high- and mid-latitude ionosphere to the magnetosphere. Figure 1.21 shows a schematic of the field-aligned currents. Again this is an example of the magnetosphere-ionosphere coupling. The electric field from mid- and high-latitude ionosphere get mapped to the equatorial ionosphere [*Fejer et al.*, 1979; *Gonzales et al.*, 1979; *Fejer and Scherliess*, 1997].

The PPEF modulates the geomagnetically quiet time behavior of the equatorial- and low-altitude ionospheric electric fields and currents. Such change of electric fields also alters the distribution of ionospheric plasma by creating a positive

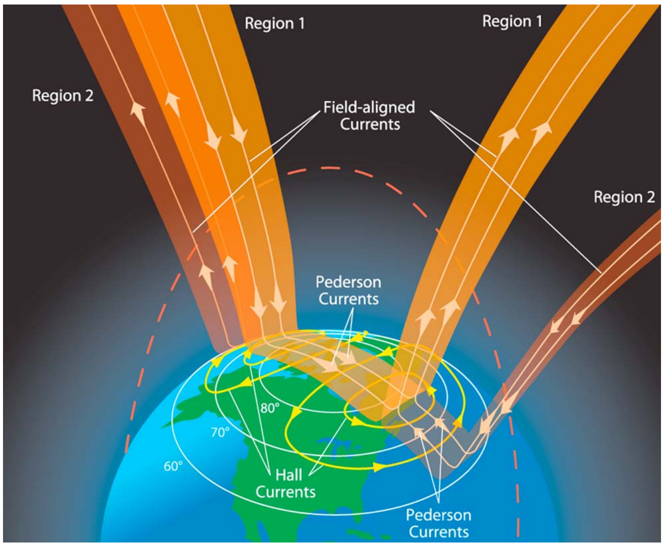

Figure 1.21: Schematic of the combined field-aligned currents (FACs) and ionospheric current system. It is to be noted that Region 1 FACs are confined to latitudes around ~67-75^0, whereas, Region 2 FACs are confined to latitudes around ~63-68^0. The FACs connect the ionosphere and the magnetosphere. After *Le et al.* [2010].

storm (electron density increases) and /or negative storm (electron density decreases), which can cause the formation of plasma density irregularities mainly over middle- and low-latitudes [*Abdu et al.*, 1991; *Basu et al.*, 2001a]. The penetration of intense convective electric fields to the equator during storm time also enhances the DP2 currents on the dayside as compared to its normal diurnal value [*Kikuchi et al.*, 2008]. During geomagnetic storms, if the IMF B_z turns northward, then the convective electric field reverses, as a result the electric fields over the low- and mid-latitudes are observed to be reversed [*Fejer et al.*, 1979; *Gonzales et al.*, 1979]. Moreover, as the PPEF is eastward during the daytime, it enhances the daytime ionospheric zonal eastward dynamo electric field and vertical drifts over equatorial- and low-latitude regions [*Nishida*, 1968b; *Kelley and Makela*, 2002; *Sastri et al.*, 2002; *Chakrabarty et al.*, 2015]. As an effect of the PPEF, the strength of the EIA (product of the distance between crest and trough and the ratio of ion densities at the crest and trough) increases [*Zhao et al.*, 2005; *Bagiya et al.*, 2011] and TEC shows an enhancement/decrement in the day/nightsides of the ionosphere [*Maruyama et al.*, 2004; *Abdu et al.*, 2007].

The precipitation of high energy charged particles enhances the E-region dynamo over polar regions and thereby, strength of the conductivities and the electric fields over polar regions increase. The higher conductivity and electric fields drive currents that dissipate energy through Ohmic heating, i.e. Joule heating. This heating of atmosphere modifies the quiet time pattern of the global quiet time wind circulation resulting in the generation of the Disturbance Dynamo Electric Field (DDEF). As a result of the DDEF, net polarization electric fields are set up from dusk to dawn sector (i.e. westward) in the dayside and from dawn to dusk sector (i.e. eastward) in the nightside. This is called ionospheric disturbance dynamo [*Blanc and Richmond*, 1980; *Fejer and Scherliess*, 1997]. The DDEF can prevail for a longer time (around one day) and affect the low-latitude ionosphere. Direction of the polarization electric field is opposite to the ionospheric dynamo electric field. Thus, it can suppress the EIA and deplete the TEC on the dayside (negative ionospheric storm) [*Tsurutani et al.*, 2004]. Since, the effects due to both PPEF and DDEF are observed over the equatorial- and low-latitudes, it is a challenge to isolate their individual contributions [*Maruyama et al.*, 2005].

1.5.2 Neutral Dynamics Perspective

Till now we have discussed about the effect of geomagnetic disturbances on the equatorial- and low-latitude upper atmosphere from an electrodynamic perspective. In this section we will discuss about the effect of geomagnetic disturbances through neutral dynamics point of view.

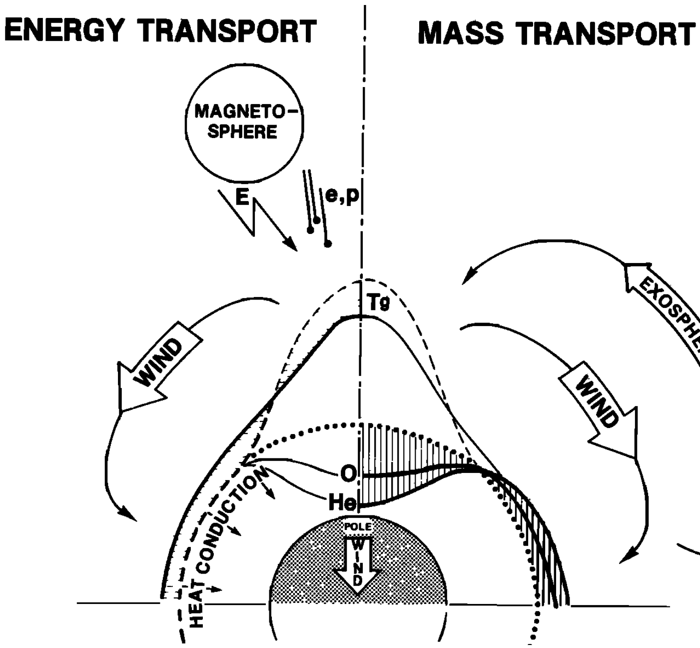

Figure 1.22: Schematic presentation of the energy and mass transport during geomagnetic storm period. After *Mayr et al.* [1978].

Figure 1.22 schematically depicts the processes of energy and mass transport that occur in the atmosphere during geomagnetic disturbance periods. *Mayr and Volland* [1973] computed the storm response of kinetic gas temperature (T_g) and compared it with a short fictitious 'diffusive equilibrium temperature (T)'. The values of T were deduced under the assumption of diffusive equilibrium from the variations in the mass density at 450 km obtained from satellite drag data. It was observed that T increased by about 40 K from the equator to the pole, whereas, for T_g it was 250 K. This can be understood from Figure 1.22 that at high-latitudes, effects of temperature can increase the total mass density (at a given altitude due to increase of scale sizes with an increase in the gas temperature T_g).

In this context, it is obvious that change of thermospheric winds and compositions are coupled to each other.

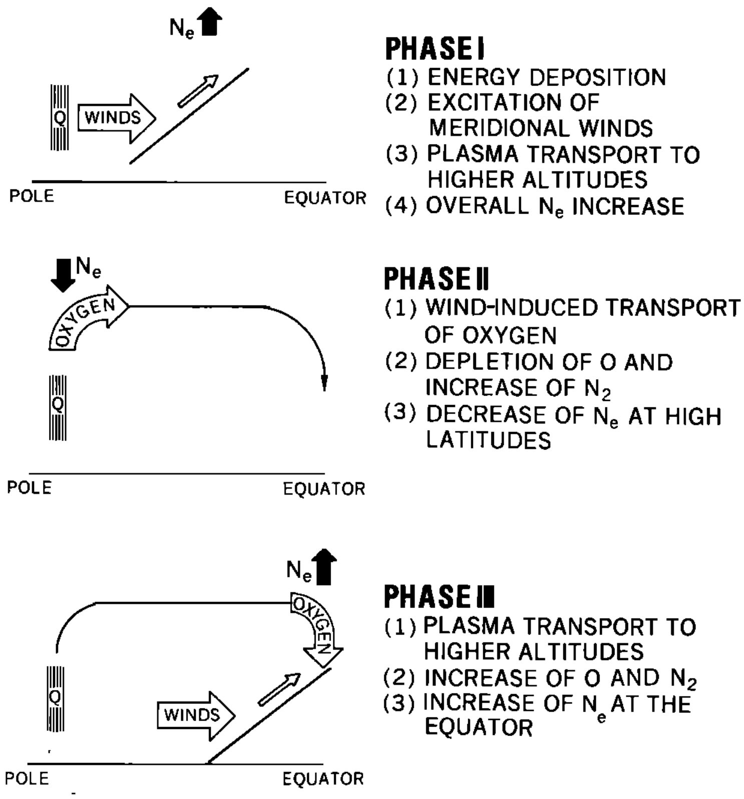

Figure 1.23: Schematic presentation of composition and the wind effects during geomagnetic storm period. After *Mayr et al.* [1978].

During the process of geomagnetic disturbances as explained in the previous section, the high energy solar wind particles directly precipitate in the auroral regions and enhance the polar E-region dynamo. Auroral conductivities and electric fields strengthens up in both the hemispheres. Thus, during storm time, electric currents due to auroral electrojet and precipitation of the charged particles at high-latitudes account for significant energy in the thermosphere. Due to Joule heating, atmospheric pressure increases at high-latitudes. Immediately equatorward meridional wind circulation is set up due to the pressure gradient forces. Due to ion-neutral collisions, the neutral winds drag the ionization to higher altitudes where the loss rates are very small. This increases the ion density at the peak F_2 layer (Phase I; Figure 1.23). With time, the wind induced diffusion gradually depletes the O density at higher latitudes, while densities of heavier species like O_2 and N_2 continue to increase. As a result ionization at high-latitudes is reduced (Phase II; Figure 1.23). Due to the transport of O towards the equator, the ionization and O/N_2 values over equatorial- and low-latitudes increase (Phase III; Figure 1.23) [*Mayr et al.*, 1978; *Prolss*, 1980]. In addition, a large-scale wave motion is engendered at high-latitudes during this process which results in the generation of AGWs, traveling atmospheric disturbances (TADs) and related traveling ionospheric disturbances (TIDs). TAD and TID are named depending on whether the effects are seen in the thermospheric or in the ionospheric parameters. After the propagation of TADs from both the hemispheres, there is an increase in temperature and densities over low-latitudes. The related effects can be seen even after 20-30 hours after the storm. The TADs and TIDs also bring about changes in the thermospheric composition, dynamics, and chemical state over low-latitude regions [e.g., *Richmond and Matsushita*, 1975; *Hunsucker*, 1982; *Hocke*, 1996; *Pallamraju et al.*, 2004b].

Appleton and Ingram [1935] first noted the decrease of maximum frequency of F_2 region during geomagnetic storm periods and *Seaton* [1956] explained this to be associated to thermospheric neutral composition. Since then many modeling studies have been proposed and observations have been carried out to understand the effect of the geomagnetic storm on the thermospheric behavior over low- and mid-latitudes. The fundamental understanding of the relation between AGWs and TIDs was developed by *Hines* [1960]. From satellite observations of thermospheric O/N_2 density, storm time behavior of thermospheric neutral densities have been characterized over low- and mid-latitude regions [e.g., *Hedin et al.*, 1977; *Mayr et al.*, 1978; *Prolss et al.*, 1988; *Strickland et al.*, 1999; *Zhang and Shepherd*, 2000; *Zhang et al.*, 2004, 2014]. Global-scale simulations show that the storm time increased equatorward meridional neutral winds cause an increase of zonal winds at mid-latitudes via the coriolis effect [*Fuller-Rowell et al.*, 1994].

From the discussions in the above section, it can be understood that the geomagnetic disturbances affect the upper atmospheric dynamics over equatorial- and low-latitudes through neutral and electrodynamic variations. A greater discussion on the effect of geomagnetic storms on the low-latitude thermosphere will be presented in Chapter-5.

1.6 Methods To Investigate The Upper Atmospheric Dynamics

The upper atmospheric dynamics of the Earth can be investigated by both direct and indirect methods. In direct methods, observations are carried out by placing the instruments in the medium itself, whereas, in indirect methods of observations, measurements are carried out remotely. Some examples of direct method of observations are, probing of sounding rockets and *in situ* measurements from satellites. The ground-based balloon-borne measurements of the upper atmosphere can be categorized as indirect methods of observations. Even though the satellite observations give a good spatial coverage, these are limited with temporal resolution. Ground-based observations are best suited for investigations of upper atmospheric parameters at high temporal resolutions. Both active and passive remote sensing techniques are used to carry out the observations of the atmosphere. In active remote sensing techniques electromagnetic radiations are transmitted into the atmosphere and observations are carried out from the reflected/backscattered echoes. Whereas, in case of passive remote sensing techniques, observations are carried out of the naturally occurring radiations in the atmosphere.

The upper atmospheric dynamics can be investigated by optical, radio, and magnetic methods of measurement.

1.6.1 Optical Method of Measurement

Observations through optical method of remote sensing of the atmospheric emissions (emissions originating in the atmosphere due to various photo chemical reactions, discussed in detail in Chapter-2) by photometry, interferometry, spectrometry, and imaging yield information about the neutral dynamics of the upper atmosphere. From the airglow emission measurements information on the variations of the density of emitting species, temperature (doppler/rotational), and line of sight winds etc., can be obtained. Larger field-of-view (FOV) optical emission measurements can yield information on neutral wave characteristics. Moreover, vertical coupling of atmospheres can be studied through measurements of optical emissions at multiple wavelengths that emanate from different altitudes.

Since the time of beginning of upper atmospheric observations, ground-based optical airglow measurements have been carried out during nighttime [*Jones and Harrison*, 1955; *Chamberlain*, 1961]. These initial measurements have been followed up by advancements in technology to obtain nightglow emission intensities at higher spectral and temporal resolutions [e.g., *Hernandez and Roble*, 1976; *Hays et al.*, 1973; *Kulkarni*, 1976; *Hays et al.*, 1978; *Mendillo and Baumgardner*, 1982; *Meriwether et al.*, 1986; *Sridharan et al.*, 1991a; *Mendillo et al.*, 1997; *Shiokawa et al.*, 1999; *Chakrabarty et al.*, 2005; *Meriwether*, 2006; *Makela et al.*, 2011b; *Makela and Otsuka*, 2011; *Marshall et al.*, 2011; *Makela et al.*, 2013; *Phadke et al.*, 2014; *Chakrabarty et al.*, 2015; *Singh and Pallamraju*, 2017].

However, it is a challenge to obtain dayglow emission intensities as these are buried in a large solar background continuum. *Wallace* [1961] attempted for the first time to measure the dayglow emissions by using a low resolution spectrograph from a balloon-borne platform but was unsuccessful. Later by using high resolution spectrograph the dayglow was measured [*Wallace*, 1963; *Wallace and McElroy*, 1966]. But in those observations, the measured dayglow was contaminated by Fraunhofer absorption features. As the solar scattered light is polarized and atmospheric dayglow emissions are unpolarized, *Noxon and Goody* [1962]; *Noxon* [1968] measured the dayglow through a scanning polarimetry technique. Due to the difficulty in canceling the background intensity which is solar zenith angle dependent, continuous and systematic observations could not be carried out by this technique. By using combinations of high and low resolution Fabry-Perot (FP) etalons, OI 630.0 nm dayglow feature has been obtained [*Jarrett and Hoey*, 1963; *Bens et al.*, 1965; *Barmore*, 1977; *Cocks et al.*, 1980; *Gerrard and Meriwether*, 2011]. However, due to the difficulty of optical alignment and temperature stability of FP etalons, observations using such technique have been limited to mainly establishing the proof of concept. By using a pressure-tuned low-resolution

FP etalon as a high spectral resolution filter along with a unique optical mask system, dayglow photometry (DGP) technique was developed [*Narayanan et al.*, 1989; *Sridharan et al.*, 1992a], which was successful in making systematic and continuous dayglow measurements [*Pallam Raju et al.*, 1996]. By modifying the mask to a spiral shape [*Sridharan et al.*, 1993a] multiwavelength dayglow photometer (MWDPM) was evolved [*Sridharan et al.*, 1998]. By using DGP and MWDPM many new and insightful results on the daytime upper atmospheric behavior were reported from equatorial- and low-latitudes [e.g., *Sridharan et al.*, 1991a,b, 1992b, 1993b, 1994; *Pallam Raju et al.*, 1996; *Pallamraju and Sridharan*, 1998a; *Sridharan et al.*, 1999] as well as from from high-latitudes [e.g., *Pallam Raju et al.*, 1995; *Sridharan et al.*, 1995; *Pallamraju and Sridharan*, 1998b]. This is the period when the field of daytime optical aeronomy was rejuvenated through ground-based instrumentation.

Michelson interferometer technique is used to measure nightglow emissions from satellite based platforms [*Shepherd et al.*, 1985, 1993a]. Visible Airglow Experiment (VAE) on-board Atmospheric Explorer-C satellite ([*Hays et al.*, 1978; *Solomon and Abreu*, 1989]) was used to study airglow emissions. The Upper Atmosphere Research Satellite (UARS) satellite carried the High Resolution Doppler Imager (HRDI) [*Hays et al.*, 1993] and WIND Imaging Interferometer (WINDII) [*Shepherd et al.*, 1993a, 2012] to study the aurora and airglow which gave a global perspective of visible airglow emissions in the daytime.

By using echelle grating, small band-width interference filter and Charge Coupled Device (CCD) detector, *Chakrabarti et al.* [2001] developed a High Throughput Imaging Echelle Spectrograph (HITISE) to obtain spectral image of the night sky. A daytime variant of HITISE called HIgh Resolution Imaging Spectrograph using Echelle grating (HIRISE) was developed to obtain the high resolution daytime spectra [*Pallamraju et al.*, 2002]. Many new and exciting results in terms of upper atmospheric behavior over several latitudes during various geophysical conditions were reported from the dayglow measurements using HIRISE [e.g., *Pallamraju et al.*, 2000, 2004a,b, 2010, 2011; *Pallamraju and Chakrabarti*, 2005, 2006; *Das et al.*, 2010]. Even though HIRISE was capable of obtaining multiwavelength dayglow emissions, it was limited in spatial information. A new instrument called Multiwavelength Imaging Spectrograph using Echelle grating (MISE) was developed which is capable of obtaining dayglow emission intensities at multiple wavelengths over a large FOV of $\sim 140^0$ [*Pallamraju et al.*, 2013]. Several results pertaining to vertical coupling of atmospheres during different solar activity conditions and due to coupling from high-latitudes during sudden stratospheric warming events were obtained by this technique [e.g., *Laskar et al.*, 2013, 2014, 2015; *Laskar and Pallamraju*, 2014; *Laskar*, 2015]. Investigations of the MLT wave dynamics have been carried out by obtaining the UV dayglow emission intensities using an Ultraviolet imaging spectrograph (UVIS) from a balloon-borne experiment [*Pallamraju et al.*, 2014]. Simultaneous optical dayglow measurements using HITISE and MISE are also used for this investigation. The primary data set used in the thesis work is the optical dayglow emission intensities at multiple wavelengths (OI 557.7, 630.0, and 777.4 nm) obtained by MISE. Many new and first of the kind results have been obtained and will be described in the subsequent chapters. Details about MISE are discussed in section 2.3.

1.6.2 Radio Measurements

As discussed in sections 1.2, 1.4, and 1.5 along with the neutral behavior, study of the electrodynamic behavior of the upper atmosphere is essential. Radio techniques such as ionosonde, digisonde, RADAR (RAdio Detection And Ranging) and GPS (Global Positioning System) have been used for this purpose.

Digisonde refers to digital ionosonde. Ionosonde is based on radio wave propagation in which radio waves of sweep frequency are transmitted from the ground and from the time delay of reflected waves from the ionosphere plasma characteristics, such as, plasma densities, drifts, layer height variations, etc. are obtained conventionally. More information on this technique is discussed in section 2.4.2. We have used digisonde data from two different stations in the present thesis work which is discussed in Chapter-3.

Radar is another powerful technique to measure the ionospheric parameters [*Dougherty and Farley*, 1963; *Farley*, 1969]. From the measurements of incoherent scatter radars many small and large scale variations of ionospheric behavior under different geophysical conditions have been reported.

GPS (Global Positioning System) is generally used to determine the position and velocity of an object on Earth. But it has a great potential to provide useful ionospheric information about the density of charged particles along a path between the satellites to receiver i.e. TEC (Total Electron Content). Mathematically, $TEC = \int_{receiver}^{satellite} N.ds$, where N is the electron density. From a GPS satellite two carrier waves in L band are transmitted with frequencies 1575.42 MHz (L1 band) and 1227.60 MHz (L2 band). Four parameters such as; the approximate distances between satellite and receiver, called pseudoranges and the carrier phases are calculated from the received data. These parameters are used to calculate the TEC.

1.6.3 Magnetic Measurements

Various types of electric currents develop in Earth's ionosphere and magnetosphere during different geophysical conditions and their induced magnetic fields modify the Earth's magnetic field on the surface of Earth. Magnetometers on the Earth measure the net magnetic field from which the quiet time values are subtracted to obtain the induced magnetic fields due to ionospheric currents. In the thesis work, we have used magnetometer data to measure the EEJ strength (section 2.4.2) and D_{st} index (section 2.4.3).

1.7 Objective of The Thesis

The daytime upper atmospheric processes over equatorial- and low-latitudes (as discussed in section 1.4) are affected by the solar forcing from above, wave activities from lower atmosphere as well as from high-latitudes during geomagnetically disturbed periods. As a result, these processes have short/long temporal and spatial scale variations. Systematic investigations of the wave characteristics for daytime conditions are essential in order to gain a comprehensive understanding of the ionospheric and thermospheric system as a whole. Thus, the objective of this thesis is to study the daytime thermospheric wave dynamics over low-latitudes and their response to neutral and electrodynamic effects under various geophysical conditions.

1.8 Overview of The Thesis

Neutral oxygen dayglow emission intensities at three wavelengths (OI 557.7 nm, OI 630.0 nm, and OI 777.4 nm) over a large field-of-view (FOV) have been obtained using high spectral resolution optical technique. Many new and insightful results have been obtained in terms of the variations in the diurnal pattern of the dayglow emission intensities, existence of longitudinal differences in equatorial processes in close separations (3^0-8^0), response of GWs over low-latitudes due to geomagnetic storms, and GW characteristics in three dimensions, etc. These results are described in detail in this work.

In *Chapter-1* we have discussed the necessary background of the upper atmosphere that is aimed to build the essential platform for the reader to appreciate the scientific results that have emerged out of this thesis work.

Chapter-2 includes detailed information on various data sets used, the measurement techniques, and the different methods of analyses carried out to address the science objectives of the thesis.

Chapter-3 discusses the predominant effect of equatorial electrodynamics on the off-equatorial dayglow emission intensities.

Chapter-4 presents the results which reveal the existence of longitudinal differences in the EEJ and thermospheric wave dynamics at even as small as 3^0-8^0 spatial extent.

Chapter-5 presents the seasonal response of low-latitude thermospheric wave dynamics due to the effect of geomagnetic disturbances.

Chapter-6 presents the first three dimensional GW characteristics over the low-latitude regions.

Chapter-7 provides the summary of the thesis work along with future projection of this research.

1.9 Summary

In this chapter we have discussed the structure of different layers of the Earth's atmosphere in terms of their composition, energetics and dynamics. Upper atmospheric structure is explained in more detail. Different aspects of dynamics such as, neutral winds, waves and solar forcing which affect the upper atmospheric behavior are discussed. Due to these dynamics, several phenomena which occur in the equatorial- and low-latitude upper atmosphere are also explained in detail. Effect of the geomagnetic disturbances on the low-latitude processes are discussed from both electrodynamic and neutral dynamic perspectives. Various methods used to study the different mechanisms which occur in the upper atmosphere, are also discussed in detail. In conclusion the objective and overview of the thesis are given.

Chapter 2

Experimental Technique and Data Analysis

2.1 Introduction

As discussed in the previous chapter the scientific objective of this thesis work is to investigate the nature of coupling in the ionospheric and thermospheric system during daytime over the equatorial- and low-latitudes. The objective is also to study the daytime thermospheric wave dynamics over low-latitudes and investigate their response to the neutral and electrodynamic effects under varying geophysical conditions. In order to address the scientific objectives, various data sets such as optical, radio, and magnetic, as well as model outputs have been used. Optical data are used as the primary data set throughout the investigations. All the other data are used for supporting and substantiating our findings and for placing the results in a broader context. Investigations of the data sets have been carried out by using various methods of analysis. In this chapter we will discuss in detail about all the data sets, measurement techniques used and the analysis methods carried out in the thesis work.

2.2 Optical Dayglow Emissions

Depending on the available solar energy flux, nature of the ambient constituents (either molecular or atomic species from where the emissions originate) and their densities, reaction rates, etc., different photochemical reactions occur in the Earth's atmosphere at different altitudes. These photochemical reactions emit characteristic emissions depending on the energies associated with the excited states of the species that produce it. Such emissions that originate in the daytime are called the dayglow emissions. The upper atmospheric dynamic processes and phenomena (explained in sections 1.3, 1.4, and 1.5) bring changes in the densities of the reactants at the dayglow emission altitudes. Hence, the dayglow emissions are imprinted with the signatures of the dynamic processes that occur at their respective emanating altitudes. Thus, the temporal variations in the dayglow emission intensities can be used as tracers of the atmospheric dynamics that exist at their respective emission altitudes. In this thesis work, we have used the neutral optical oxygen dayglow emission intensities at three wavelengths i.e. OI 557.7 nm, OI 630.0 nm, and OI 777.4 nm. The details about these three dayglow emissions are described below.

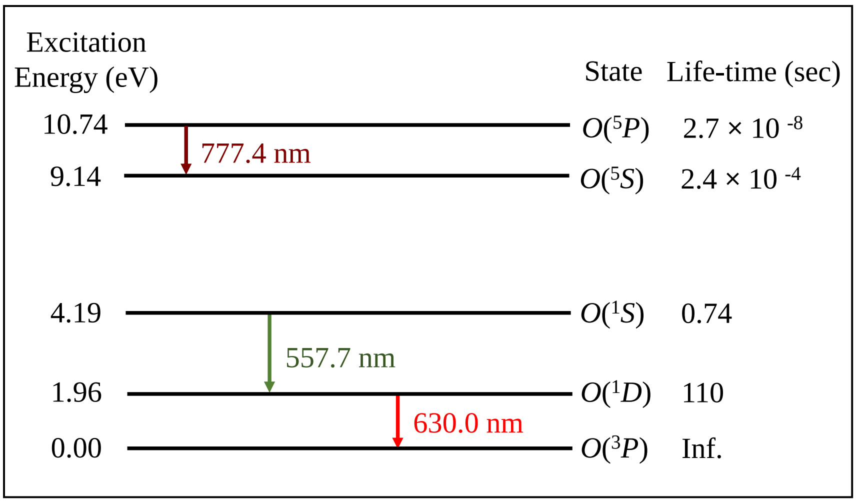

Figure 2.1: The energy level diagram of the excited states of atomic oxygen responsible for 557.7 nm, 630.0 nm, and 777.4 nm emissions.

Dayglow emissions at OI 557.7 nm, 630.0 nm, and 777.4 nm wavelengths are produced due to the de-excitation of $O(^1S)$ to $O(^1D)$, $O(^1D)$ to $O(^3P)$, and

$O(^5P)$ to $O(^5S)$ state, respectively [*Torr and Torr*, 1982]. Figure 2.1 shows the energy level and average lifetime of each state. The $O(^5P) \rightarrow O(^5S)$ is an allowed transition, while the other two are forbidden. The lifetimes of $O(^1S)$, $O(^1D)$, and $O(^5P)$ states are 0.74, 110, and 2.7 $\times$ 10^{-8} sec, respectively. Details of each of the dayglow emissions is discussed below.

2.2.1 OI 557.7 nm (Oxygen Green Line)

The OI 557.7 nm dayglow emission occurs when a transition takes place from the atomic oxygen $O(^1S)$ to $O(^1D)$ state. The $O(^1S)$ state can de-excite either by yielding 557.7 nm emission (equation 2.1) or through quenching (equation 2.2) with ambient constituents.

$$O(^1S) \rightarrow O(^1D) + h\nu(\lambda = 557.7nm), \tag{2.1}$$

$$O(^1S) + (O_2, N_2) \rightarrow O(^3P) + (O_2, N_2) \tag{2.2}$$

The $O(^1S)$ state is produced due to various sources, e.g. photoelectron impact excitation of atomic oxygen O, photodissociation of O_2, dissociative recombination of O_2^+ and e^-, collisional deactivation of N_2 and a three-body recombination (Barth mechanism) [e.g., *Frederick et al.*, 1976; *Rees*, 1989; *Tyagi and Singh*, 1998; *Witasse et al.*, 1999; *Zhang and Shepherd*, 2005].

i. Photoelectron impact excitation of O:

When a photoelectron (e_{ph}) with energy >4.19 eV collides with an atomic oxygen O, the e_{ph} transfers its energy to O to produce $O(^1S)$ state and in this process the e_{ph} is left with the remaining energy.

$$O + e_{ph} \rightarrow O(^1S) + e_{ph} \tag{2.3}$$

ii. Photodissociation of O_2:

Solar photons in the wavelength range of 100-120 nm dissociate the O_2 to produce $O(^1S)$ state.

$$O_2 + h\nu \rightarrow O + O(^1S) \tag{2.4}$$

iii. Dissociative recombination of O_2^+ and e_{th}:

The O_2^+ and the ambient thermal electron (e_{th}) dissociatively recombine to produce $O(^1S)$ state.

$$O_2^+ + e_{th} \rightarrow O(^1S) + O \tag{2.5}$$

iv. Collisional deactivation of N_2:

N_2 gets excited to $N_2(A^3\Sigma_u^+)$ state after colliding with e_{ph}. Again the excited N_2 ($N_2(A^3\Sigma_u^+)$) de-excites to N_2 by colliding with O, and thereby the $O(^1S)$ state is produced.

$$N_2 + e_{ph} \rightarrow N_2(A^3\Sigma_u^+), \tag{2.6}$$

$$N_2(A^3\Sigma_u^+) + O \rightarrow N_2 + O(^1S) \tag{2.7}$$

v. Three-body recombination mechanism:

In 1931, Chapman proposed a chemical excitation mechanism to understand the OI 557.7 nm airglow emission [*Chapman*, 1931]. In this mechanism an O atom gets excited to the $O(^1S)$ state by recombination with two other oxygen atoms.

$$O + O + O \rightarrow O_2 + O(^1S) \tag{2.8}$$

By using paramagnetic resonance spectrometry and optical spectrometry, Barth in 1961 calculated the rate co-efficient for the 557.7 nm emission resulting from the three-body recombination of oxygen atoms. In his experiment, he observed that the nighttime emission intensity by Chapman's three-body recombination mechanism is 0.2 Rayleigh but the typical nightglow intensity is 250 Rayleigh. So Chapman's three-body recombination mechanism as a source of 557.7 nm airglow emission is discarded.

Barth in 1964, proposed a modified mechanism called the "Barth mechanism". He suggested that O is a nascent element. It is stable in its molecular state. The two atomic oxygen combined with each other to form excited O_2^* state. The formation of this O_2^* state is not possible in the three-body recombination mechanism as proposed by Chapman. For enhancing the collision cross-section a molecule M is required. This excited O_2^* again collides with O to form a nascent

O_2 molecule and $O(^1S)$ state [*Barth and Hildebrandt*, 1961; *Barth*, 1964].

$$O + O + M \rightarrow O_2^* + M, \tag{2.9}$$

$$O_2^* + O \rightarrow O_2 + O(^1S) \tag{2.10}$$

Figure 2.2 show the model green line volume emission rate profiles along with the contributions from various production mechanisms on two days. The model profiles are compared with the WINDII observations. The photoelectron impact excitation of O has a major contribution to the total volume emission rate at altitudes above 110 km and peak around 150-200 km. Some studies found that its production rate is larger than the dissociative recombination [*Witasse et al.*, 1999; *Culot et al.*, 2004]. However, it was shown that both have almost the same F region contribution (Figure 2.2) [*Tyagi and Singh*, 1998; *Upadhayaya and Singh*, 2002]. The photodissociation of O_2 has lower thermospheric contributions which peak around 105 km. The dissociative recombination process is reported to have contributions mostly at altitudes above 150 km and is not considered as one of the main production process *Witasse et al.* [1999]; *Culot et al.* [2004]. However, this reaction is also reported to have a major contribution to the production of $O(^1S)$ states with two peaks, one around 150-180 km and other at 100-110 km (Figure 2.2) *Tyagi and Singh* [1998]; *Upadhayaya and Singh* [2002]. The collisional

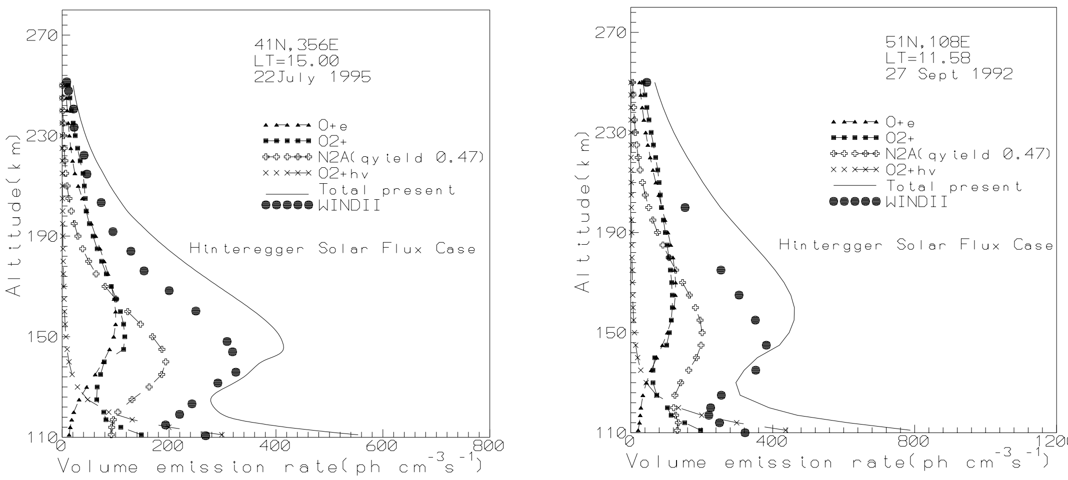

Figure 2.2: Green line (OI 557.7 nm) volume emission rate profiles along with the contributions from various production mechanisms on two sample days are shown. After *Upadhayaya and Singh* [2002].

deactivation of N_2 has two peaks, one above 130 km and other below 120 km. The three-body recombination mechanism contributes to the lower thermospheric (E region) contribution which peaks at around 100 km. Contributions from all the production mechanisms result in two peak emission altitudes of the 557.7 nm dayglow, one at around 160 km and other at 100 km. In this thesis work, as we are measuring the column integrated emissions, an average altitude of around 130 km is considered to be the peak emission altitude of 557.7 nm dayglow emission [*Pallamraju et al.*, 2014].

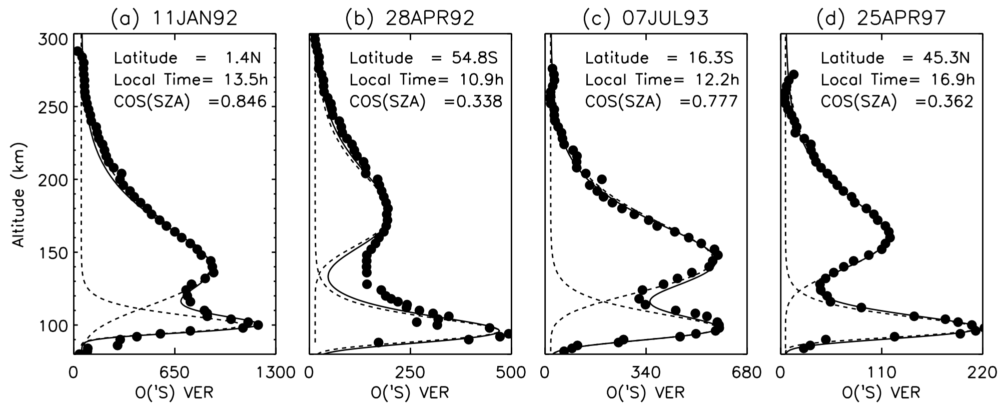

Figure 2.3: Green line (OI 557.7 nm) volume emission rate profiles obtained from WINDII measurements are shown with fitted curves on four sample days. After *Zhang and Shepherd* [2005].

Figure 2.3 shows the daytime green line volume emission rate profiles obtained from WINDII measurements on four sample days. The profiles are taken during different local times at various locations. The two emission peaks are distinctly noticeable. The peak emission altitude in the F region occurs anywhere between 130-180 km, whereas, the peak in the E region is comparatively stable at around 100 km.

The dissociative recombination of O_2^+ depends on the electron densities and contributes significantly to the production of 557.7 nm dayglow emissions at higher altitudes, especially in equatorial- and low-latitudes [e.g., *Tyagi and Singh*, 1998; *Upadhayaya and Singh*, 2002; *Taori et al.*, 2003]. Rocket-borne $O(^1S)$ 557.7 nm measurements [*Wallace and McElroy*, 1966; *Kulkarni*, 1976], nightglow measurements from Wind Imaging Interferometer [*Shepherd et al.*, 1997], and ground-based optical dayglow measurements [*Taori et al.*, 2003] reported a dominant F

region contribution as compared to that of the lower altitudes.

2.2.2 OI 630.0 nm (Oxygen Red Line)

Due to the transition of atomic oxygen $O(^1D)$ to $O(^3P)$ state the OI 630.0 nm dayglow emission occurs. Like $O(^1S)$ state, the $O(^1D)$ state can de-excite either by yielding 630.0 nm emission or through quenching with ambient constituents.

$$O(^1D) \rightarrow O(^3P) + h\nu(\lambda = 630.0nm), \tag{2.11}$$

$$O(^1D) + (O_2, N_2) \rightarrow O(^3P) + (O_2, N_2) \tag{2.12}$$

The $O(^1D)$ state is produced due to various mechanisms, e.g. photoelectron impact excitation of atomic oxygen O, photodissociation of O_2, dissociative recombination of O_2^+ and cascading from loss of $O(^1S)$ [e.g., *Solomon and Abreu*, 1989; *Witasse et al.*, 1999].

i. Photoelectron impact excitation of O:

When a photoelectron with energy >1.96 eV collides with an atomic oxygen O, the e_{ph} transfers its energy to O to produce $O(^1D)$ state and in this process the e_{ph} is left with the remaining energy.

$$O + e_{ph} \rightarrow O(^1D) + e_{ph} \tag{2.13}$$

ii. Photodissociation of O_2:

Solar photons in the Schumann-Runge continuum (135-175 nm) dissociate the O_2 to produce $O(^1D)$ state.

$$O_2 + h\nu \rightarrow O + O(^1D) \tag{2.14}$$

iii. Dissociative recombination of O_2^+ and e_{th}:

The O_2^+ and e_{th} dissociatively recombine to produce $O(^1D)$ state.

$$O_2^+ + e_{th} \rightarrow O(^1D) + O \tag{2.15}$$

iv. Cascading from loss of $O(^1S)$:

The $O(^1S)$ state de-excites to $O(^1D)$ state to emit 557.7 nm dayglow emission.

$$O(^1S) \rightarrow O(^1D) + h\nu(557.7nm) \tag{2.16}$$

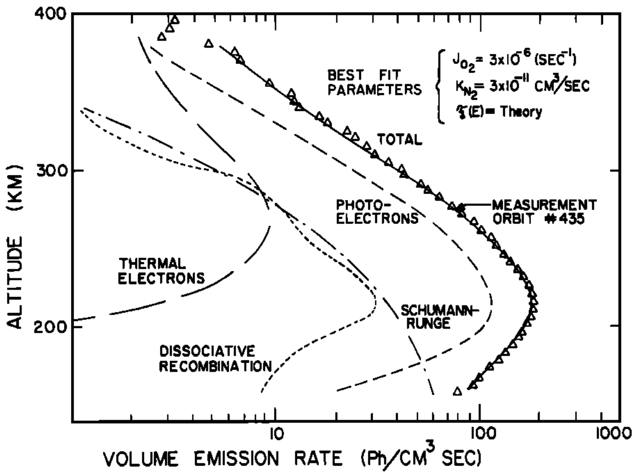

Figure 2.4: Vertical profile of 630.0 nm dayglow emission intensity obtained by limb scanning method by the visible airglow experiment on-board the AE-C satellite. After *Hays et al.* [1978].

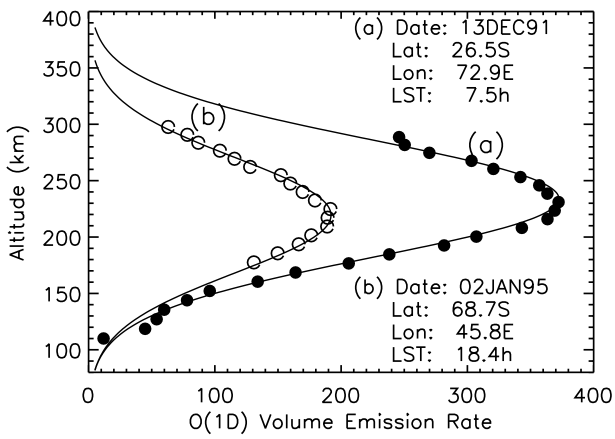

Figure 2.5: Red line (OI 630.0 nm) volume emission rate profiles obtained from the WINDII measurements are shown with Gaussian fitted curves on two days. After *Zhang and Shepherd* [2004].

The photoelectron impact excitation of O contributes most to the 630.0 nm dayglow emissions followed by the photodissociation mechanism. The contribution of dissociative recombination to the 630.0 nm dayglow emission is around 20-30% (Figure 2.4) [*Hays et al.*, 1978; *Singh et al.*, 1996]. However, the dissociative recombination contributes significantly to the temporal variability observed in the emissions [*Sridharan et al.*, 1992b, 1994; *Pallam Raju et al.*, 1996]. Over equatorial- and low-latitudes contribution of the dissociative recombination at the peak emission height could be larger by a factor of 1.5 to 2 [*Solomon and Abreu*, 1989]. Whereas, over the high-latitudes these are nearly comparable. Cascading from the loss of $O(^1S)$ has a minor contribution to the total production of 630.0 nm dayglow emissions [*Solomon and Abreu*, 1989; *Witasse et al.*, 1999]. Figure 2.5 shows red line volume emission rate profiles on two days obtained from the WINDII measurements. The solid line shows the Gaussian fitting curves. It can clearly be seen that the 630.0 nm dayglow emission peaks at around 230 km altitude and has a emission layer width of around 100 km. More information on this emission can be obtained from *Pallamraju* [1996].

2.2.3 OI 777.4 nm

The OI 777.4 nm dayglow emission results from the transition of $O(^5P)$ to $O(^5S)$ state. The $O(^5P)$ state is produced due to the radiative recombination of O^+ and e_{th} [*Tinsley et al.*, 1973].

$$O^+ + e_{th} \rightarrow O(^5P), \tag{2.17}$$

$$O(^5P) \rightarrow O(^5S) + h\nu(777.4nm) \tag{2.18}$$

OI 777.4 nm dayglow emission maximizes at the peak altitude of F region, where densities of both the reactants, O^+ and e^- are greatest. For the daytime conditions, the peak emission altitude for this emission is considered to be 300 km during the investigation of the thesis work. The daytime OI 777.4 nm emission measurement started since the advent of a high spectral resolution technique [*Pallamraju et al.*, 2013], described in the following section.

2.3 Observational Technique

It is a challenge to obtain the dayglow emission intensities as these are buried in the huge solar scattered background continuum. Different types of techniques have been used to obtain the dayglow emission intensities since a long time, which have been discussed in section 1.6.1. In the thesis work, we have used a ground-based high spectral resolution multiwavelength optical spectrograph called MISE (Multiwavelength Imaging Spectrograph using Echelle grating) to obtain the three dayglow emission intensities of our interest (OI 557.7, 630.0, and 777.4 nm) [*Pallamraju et al.*, 2013].

2.3.1 Optical Design of MISE

The schematic diagram and detailed information of the components of MISE are shown in the Figure 2.6 and table 2.1, respectively. MISE is a large field-of-view (FOV=140^0) slit spectrograph. Light falls on the all sky objective lens that is

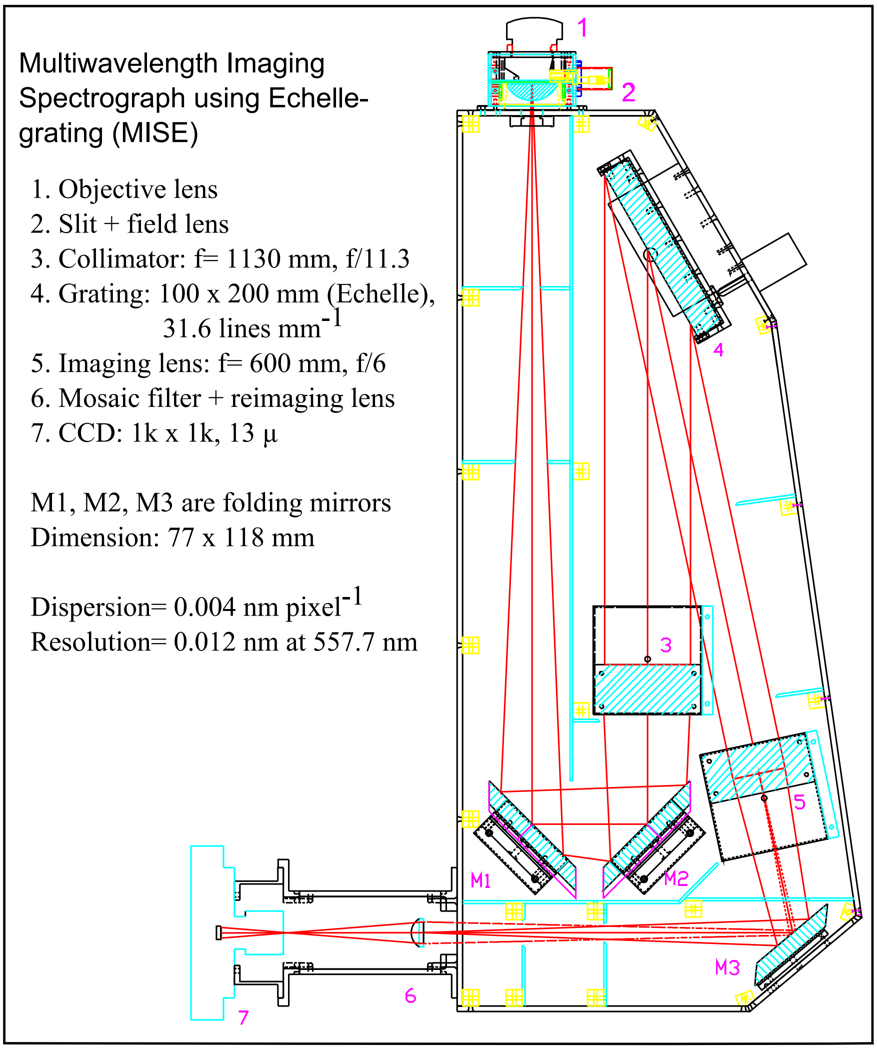

Figure 2.6: Schematic of Multiwavelength Imaging Spectrograph using Echelle grating (MISE). MISE is used to obtain the dayglow emission intensities simultaneously at OI 557.7, 630.0, and 777.4 nm wavelengths without any need of changing the grating angle. The red lines show the optical ray diagram. After *Pallamraju et al.* [2013].

Slit length	3.9 cm
Slit width	0.012 cm
Throughput (AΩ)	2.8785×10^{-4} cm^2 sr
Collimator	f=113 cm (f/11 Apochromat)
Grating	31.6 lines mm^{-1}, blaze angle 63.5^o
	(Size: 110×220×30 mm)
Camera lens	f=60 cm ($f/6$ Apochromat)
Total optical trans., τ	0.010197 (557.7 nm); 0.030775 (630.0 nm);
	0.066338 (777.4 nm)
CCD (e^- ph^{-1})	quantum eff., q(λ): q (557.7 nm)=0.95,
	q(630.0 nm)=0.93, q (777.4 nm)=0.8,
	Gain, g=1.5259 e$^-$ DN^{-1}
Total efficiency, Q(λ)	Q (557.7 nm)=0.62259, Q (630.0 nm)=0.6095,
	Q(777.4 nm)=0.5243 DN ph^{-1},
	13μ, 1k×1k, E2V Chip
No. of rows (n_{rows})	110 for 8 pixel binning along the slit
Dispersion, d (nm pixel^{-1})	d(557.7 nm)=0.004, d(630.0 nm)=0.0049,
	d(777.4 nm)=0.0059

Table 2.1: Characteristics of MISE. Specifications of each optical components are given. After *Pallamraju et al.* [2013].

focused to infinity. The focal length of this objective lens is 12 mm. Behind the objective lens a slit is placed. The length and width of the slit are 39 mm and 0.12 mm, respectively. Light from the slit fall onto the field lens which has a focal length of 75 mm. The field lens reduces the divergence of the transmitting beam from the slit and makes it to fall onto the collimating lens with the help of two identical plane mirrors M1 and M2 placed orthogonal to one another (see Figure 2.6). Dimension of the mirrors are 77 × 118 mm. The collimating lens is kept at such a position to have the slit on its focus. The collimating lens used in MISE is an apochromat with a focal length of 113 cm ($f/11$). An apochromatic lens uses three elements in its preparation and is chosen here to optically correct the chromatic aberrations for all the visible wavelengths. The chromatic aberration of light and its correction by apochromat is shown in Figure 2.7.

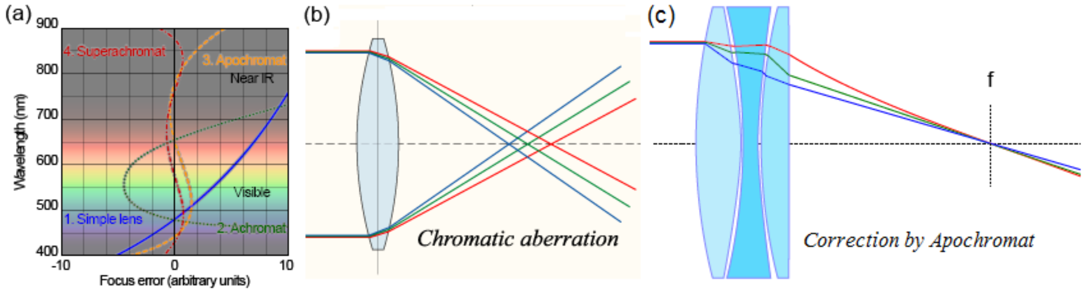

Figure 2.7: (a) Shows error in focus for four types of lens in visible and near infrared spectrum. (b) Shows the chromatic aberration of a lens for different wavelengths of light. (c) Shows configuration of apochromat lens to correct the chromatic aberration for different wavelengths of light. These figures are borrowed from (https://en.wikipedia.org/wiki/Apochromat) dated 25 July 2017.

The transmitted parallel beam from the collimating lens fall on a special type of grating called echelle grating. It's size is 110 $\times$ 220 mm with groove density of 31.6 lines per mm and blaze angle of 63.5^0. Simulations have been carried out using the grating equation and for the $f/11$ input optics to obtain the right combination of the groove density and blaze angle of the grating such that all the three wavelengths simultaneously fall on the 24 mm$\times$ 24 mm area at the image plane where the filters are placed.

Echelle grating is a special type of grating which is designed to operate at larger values of angle of incidence and diffraction for obtaining high spectral resolution spectra. In order to understand the advantage of echelle grating over a normal grating, let us look at the grating equation which is defined as,

$$n\lambda = d(\sin\alpha + \sin\beta)\cos\gamma \tag{2.19}$$

where, n is the order of diffraction, λ is the wavelength of the light, α, β and γ are incidence, diffraction, and lateral angle, respectively, and d is the groove spacing.

The lateral angle from off-axis makes the diffracted beam to be shifted so that the diffraction pattern gets curved. The geometry of the grooves, optical ray diagram at the edge of a groove and the lateral angle are shown in Figure 2.8.

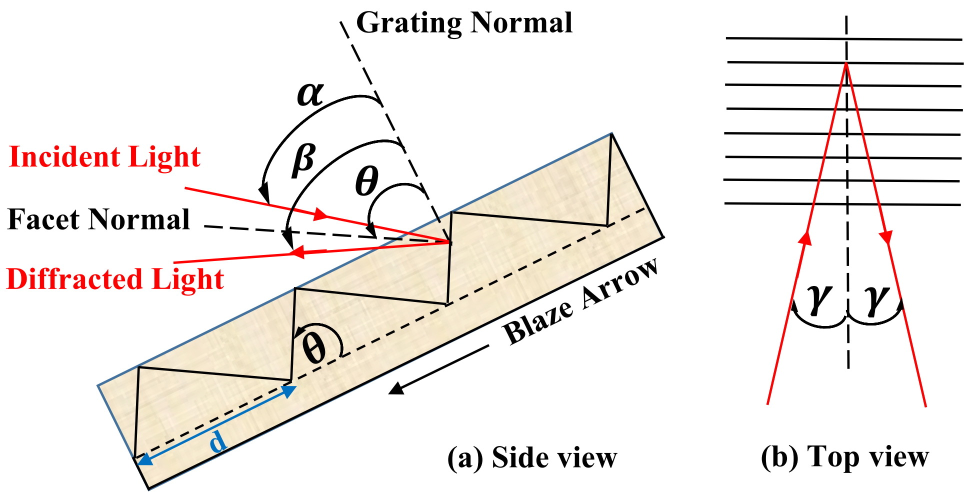

Figure 2.8: Geometry of the echelle grating depicting the groove spacing, grating normal, facet normal, angle of incidence and diffraction, blaze angle and lateral angle.

Considering a normal incidence of light (γ=0) on the echelle grating and differentiating equation 2.19 w.r.t. β, we can get

$$d\beta/d\lambda = n/(d\cos\beta) \tag{2.20}$$

Substituting n/d from equation 2.19 in equation 2.20 we can get

$$d\beta/d\lambda = (\sin\alpha + \sin\beta)/(\lambda\cos\beta) \tag{2.21}$$

From equation 2.21 it can be seen that, for a fixed wavelength of light, the angular dispersion $d\beta/d\lambda$ depends only on α and β and therefore the angular dispersion is higher for larger values of α and β. For a higher grating efficiency (ratio of incident intensity to diffracted intensity) the blaze angle [θ=(α+β)/2] should be close to α and β. At larger blaze angles, the facet length of the grating (=$d\cos\theta$) needs to be large. For this, the groove spacing d needs to be larger as the value of $\cos\theta$ is small at higher values of θ. This, therefore results in a small groove density for the grating. From equation 2.19, it can be seen that for a given wavelength of light, larger values of d, α and β are supported at high values of n. Thus, echelle gratings operate at high orders of diffraction. In MISE order number for 557.7, 630.0, and 777.4 nm emission wavelengths are 102, 90, and 73, respectively. At higher diffraction orders, there would be overlapping of several wavelengths at different orders at a same location according to the relation,

$$n_1\lambda_1 = n_2\lambda_2 = n_3\lambda_3 = ... \tag{2.22}$$

This problem of order overlap is overcome by using narrow-bandwidth interference filters which allows light from a small spectral region around the required wavelength.

The diffracted beam from the echelle grating is imaged at the detector by using another imaging lens with focal length of 60 cm ($f/6$). Transmitted beam from the imaging lens is made to fall on the detector using another plane mirror M3 identical to M1 and M2. To get light of the required wavelengths, three strips of interference filters (full-width at half maximum vary from 10-20 nm) at the three required wavelengths are glued together and placed in front of the detector at the image plane. The filtered light at these three wavelengths are imaged by a macro-lens in the ratio of 1.8:1. The macro-lens re-image the light onto a 1 k$\times$1 k pixel format charge coupled device (CCD) detector of 13μ pixel size (image plane around 13 mm$\times$13 mm).

The light from the slit falls on the echelle grating. If the light does not fall normally on the grating, an angle γ (lateral angle) will be created between the incident beam and the diffracted beam as mentioned above. This angle will result in a curvature effect on the image [*Chakrabarti et al.*, 2001; *Pallamraju et al.*, 2002, 2013]. An on-chip binning of the image on spatial direction is carried out to increase the signal to noise ratio, and this curvature of the image will decrease the spectral resolution during the processes of binning. Thus, the curvature effect of the image needs to be minimized. Hence, the slit is made curved in the opposite direction to offset the curvature effect. Because of the curved slit, light from a curved portion of the sky falls on MISE. As the spatial structures at the emission altitudes are larger than the spatial distance between the regions of the sky that are covered by the curved slits, the curved slit is acceptable [*Pallamraju et al.*, 2013].

The $f/11$ and $f/6$ lenses reduce the size of the image by a factor of 2. The macro-lens also reduces the image size by a factor of 1.8. As a combined effect of all the three lenses, the image size has been reduced without compromising the spatial information along the slit at the front-end, and is imaged onto the 13 mm $\times$ 13 mm sized CCD chip. This feature of MISE enables us to obtain simultaneous information of the dayglow emission intensities that emanate at three different altitudes over a large FOV ($\sim$140^0). The dispersion of MISE is 0.004, 0.0049, and 0.0059 nm pixel^{-1} at 557.7, 630.0, and 777.4 nm spectral regions, respectively. The signal to noise ratio (SNR) for 557.7, 630.0, and 777.4 nm dayglow emission lines vary from 2-18, 5-28, and 3-8, respectively, throughout the day. These high spectral resolution dayglow data sets are used as the primary data set in this thesis work.

The operation of MISE is fully automated through scripts developed using Microsoft visual basic language and interfaced with MaximDL software. Depending on the solar zenith angle, the exposure times are scheduled in the software. The software and the operations of MISE can be accessed and controlled from anywhere through internet. Any modification on data acquisition can be made through these programmable software.

2.3.2 Sample Spectral Image Obtained From MISE

The dayglow emission intensities at all the three wavelengths are imaged onto a 1k $\times$ 1k CCD detector to form a high resolution spectral image. A sample image obtained from MISE is shown in Figure 2.9. Pixels along the horizontal axis give information of the wavelength. The two thick vertical dark lines are the edges of

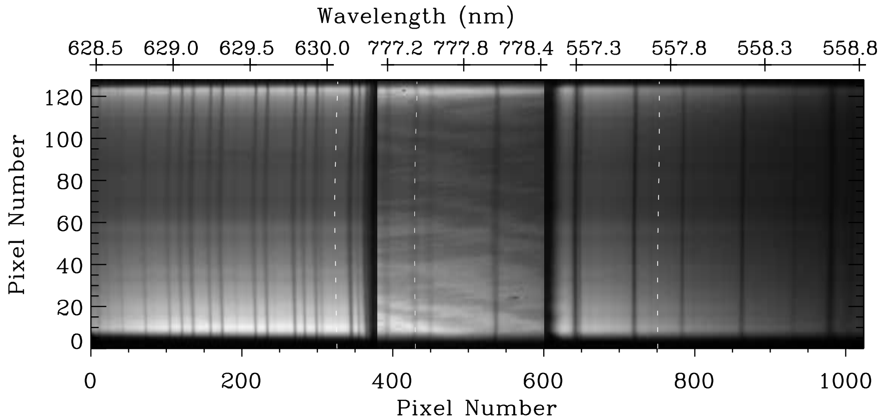

Figure 2.9: Sample image obtained from MISE. After *Pallamraju et al.* [2013].

the filters that are glued to one another. The left, middle, and right panels of the image correspond to the emission intensities in the spectral region of 630.0, 777.4, and 557.7 nm, respectively. The bottom X-axis show the pixel number whereas, the top X-axis show the wavelengths corresponding to different spectra. The small vertical dark lines are the Fraunhofer absorption lines. The three vertical white dashed lines are drawn to mark the position of the three emission lines of our interest. Pixels along the vertical axis retains the spatial information along the slit direction. On-chip binning of 8 pixels along the spatial direction is carried out to increase the signal-to-noise ratio. This makes the resultant pixel number along the spatial direction to be 128.

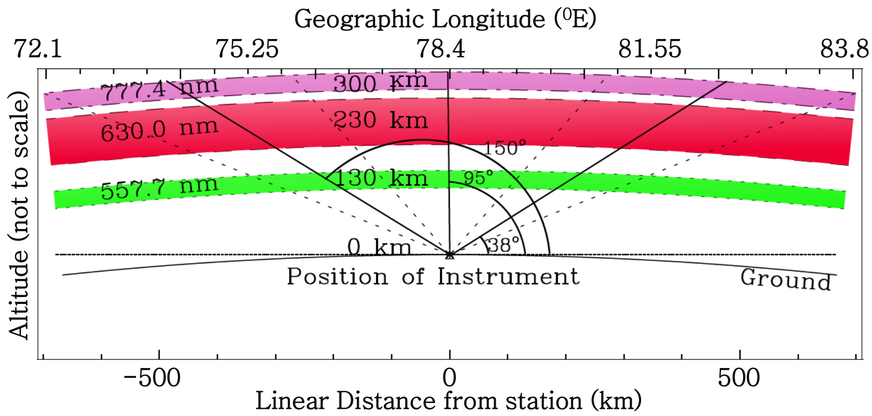

Figure 2.10: Schematic of viewing geometry of MISE.

As the dayglow emission intensities considered in this thesis work emanate from varying altitudes, the spatial coverage at their corresponding emission altitudes are different which is depicted in Figure 2.10. It is to be noted that the altitude on the Y-axis is not to the scale. The spatial coverages at the emission altitudes of 557.7, 630.0, and 777.4 nm dayglow corresponding to 140^0 FOV are approximately 5^0, 9^0, and 11^0 longitudes, respectively.

2.3.3 Extraction of Dayglow Emission Intensities

Dayglow emission intensities at the three wavelengths are extracted from the images obtained by MISE. Figure 2.11 explains one sample method of extraction for 630.0 nm dayglow emission intensities.

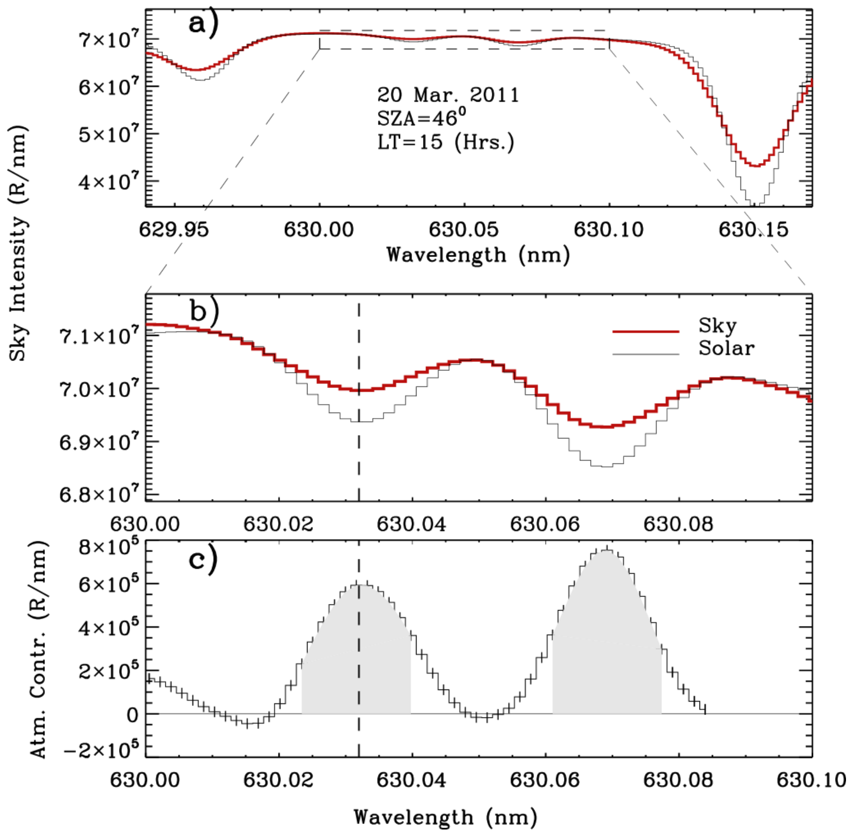

Figure 2.11: Method of extraction of dayglow emission intensities at 630.0 nm wavelength. After *Pallamraju et al.* [2013].

The daysky spectra (shown in red line in Figure 2.11a) obtained from MISE are compared with the normalized standard/reference solar spectrum (dark line) in order to calibrate them in the wavelength domain. The calibrated day sky spectra are scaled at the continuum regions with the solar spectra. The resolution of the solar spectra used in the present study is 0.0002 nm. It is obtained from BASS2000 Solar Survey Archive site (http://bass2000.obspm.fr/solar_spect.php). The region of interest in the spectra is zoomed in and shown in Figure 2.11b. The two Fraunhofer absorption lines (non-telluric lines) of our interest in this region are 630.03 and 630.06 nm. The vertical dashed line is drawn at the 630.03 nm wavelength. The increase in brightness at both these spectral regions are clearly notable, which can be either due to (i) atmospheric emissions, or (ii) scattering in the atmosphere, or, both. The filling-in of intensities due to atmospheric scattering (mainly Rotational Raman scattering) at the Fraunhofer lines is called the Ring effect [*Grainger and Ring*, 1962; *Pallamraju et al.*, 2000]. Filling-in of intensities at 630.03 nm wavelengths are contributed by both atomic oxygen emission mechanisms (described in section 2.2.2) and atmospheric scattering effect (Ring effect), whereas the filling-in at 630.06 nm emission wavelength are contributed only by scattering effect. The solar spectra is subtracted from the sky spectra to obtain only the atmospheric contribution, which has been shown in Figure 2.11c. From an earlier work by *Pallamraju et al.* [2000], it is known that the Ring effect contribution at two nearly adjacent (around 0.03 nm) spectral regions of identical equivalent widths (normalized depth × half width) can be considered to be the same. It is important to estimate this contribution since many atmospheric dayglow emissions occur near the Fraunhofer absorption lines. If the data analysis procedure does not properly account for the Ring effect contributions, then the dayglow emissions will be overestimated. Thus, taking the Ring effect contribution at 630.06 nm into account and subtracting it from the total intensities at 630.03 nm, the atmospheric emission is calculated.

If I_{c1} is the normalized intensity at the continuum level, I_{d1} is the depth of the Fraunhofer line where emission is present, and $\lambda_{\omega 1}$ is the half width of the Fraunhofer absorption line centered at 630.03 nm, and I_{c2}, I_{d2} and $\lambda_{\omega 2}$ are the corresponding values at 630.06 nm (Figure 2.11b), then the scattering (Ring effect) contribution present at the Fraunhofer absorption line, where (630.03 nm) emission exists as compared to the neighboring 630.06 nm region is the ratios of the equivalent widths (normalized depth × half width) at each of the Fraunhofer absorption region.

Mathematically, this ratio is a factor, f, which is given as

$$f = \frac{(I_{c1} - I_{d1}) \times \lambda_{\omega 1}}{(I_{c2} - I_{d2}) \times \lambda_{\omega 2}} \tag{2.23}$$

The value of f scales the amount of scattering contribution from 630.06 nm region to be taken into account in the 630.03 nm region.

Now, the contribution of the dayglow emission at 630.03 nm is given by,

$$Dayglow = [(Area)_{Curve_1}] - [(Area)_{Curve_2}] \times f \tag{2.24}$$

where, $(Area)_{Curve_1}$ is the area under the curve of the Fraunhofer line which has both atmospheric emission and scattering contribution (centered at 630.03

nm); $(Area)_{Curve_2}$ is the area under the curve of the Fraunhofer line which has only scattering contribution (centered at 630.06 nm).

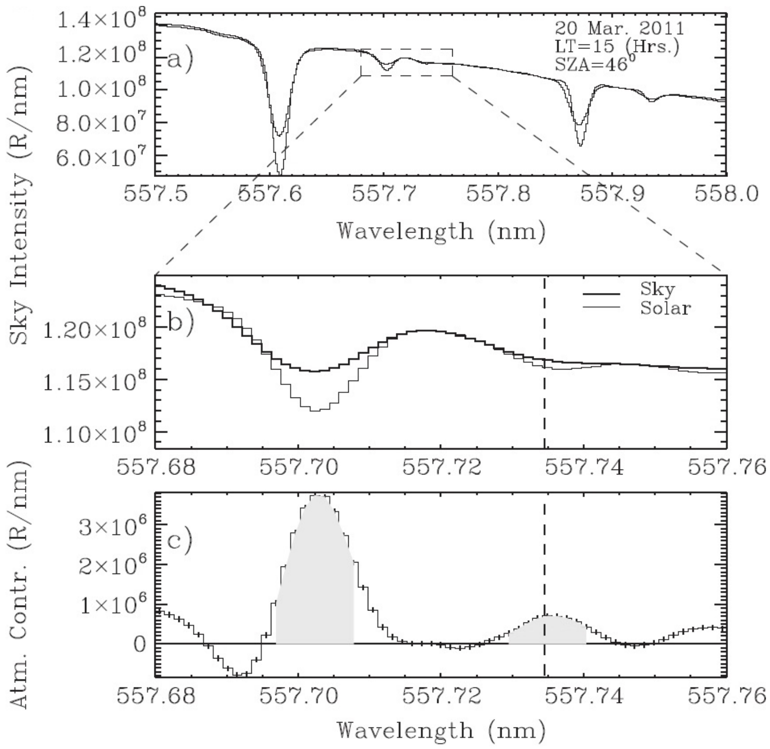

Figure 2.12: Method of extracting dayglow emission intensities at 557.7 nm wavelength. After *Pallamraju et al.* [2013].

The same method as explained above for 630.0 nm dayglow is followed to extract the dayglow at 557.7 and 777.4 nm emission wavelengths and are shown in Figures 2.12 and 2.13, respectively. In order to extract the dayglow emissions at 557.73 and 777.53 nm wavelengths, scattering contributions at 557.70 and 778.05 nm are considered.

This method of retrieval of dayglow is well-established and is described in detail in the literature [*Pallamraju et al.*, 2002, 2013]. By using this method, the dayglow emission intensity can be obtained as count numbers registered on the CCD detector. The absolute value of the dayglow emission intensity can be estimated in Rayleigh unit (1 Rayleigh = 10^6 photons cm^{-2} s^{-1}) as follows.

If $B(\lambda)$ is the dayglow emission intensity (in Rayleigh unit) that enters into MISE and $N(\lambda)$ is the registered count number on the detector for an integration

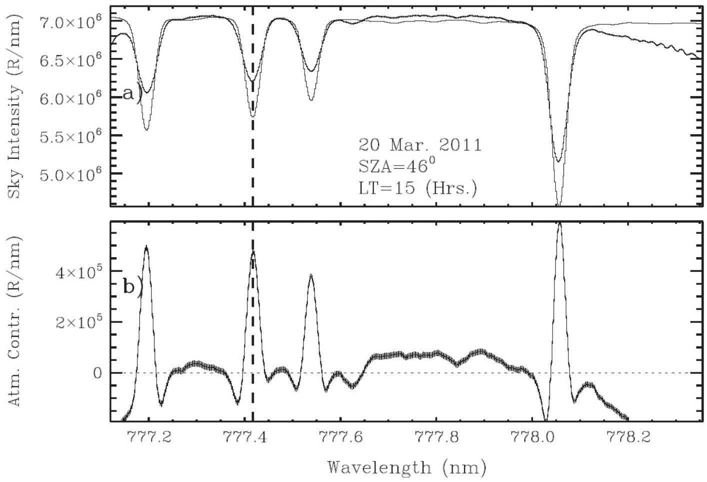

Figure 2.13: Method of extracting dayglow emission intensities at 777.4 nm wavelength. After *Pallamraju et al.* [2013].

time of t seconds then,

$$N(\lambda) = B(\lambda)S(\lambda)t \tag{2.25}$$

and $S(\lambda)$=$(10^6/4\pi)\times Q(\lambda)\times A\times\Omega\times\tau(\lambda)\times d(\lambda)/n_{rows}$ [*Pallamraju et al.*, 2002] is the sensitivity per nm of MISE. where, $Q(\lambda)$ is the overall efficiency of the CCD detector (quantum efficiency $q(\lambda)$/gain, g); A is the area of the slit; Ω is the solid angle of the sky that the slit sees; $\tau(\lambda)$ is the optical efficiency of the instrument; $d(\lambda)$ is the dispersion in nm pixel^{-1}, and n_{rows} are the number of rows that have been obtained after on-chip binning in the spatial direction. Considering specifications of all the optical components as given in table 2.1, the sensitivity was calculated to be [*Pallamraju et al.*, 2013]:

$$S_{pix}(\text{OI } 557.7\,\text{nm}) = 0.5205 \times 10^{-5}(\text{DN}\,\text{nm}\,\text{R}^{-1}\,\text{s}^{-1}) \tag{2.26}$$

$$S_{pix}(\text{OI } 630.0\,\text{nm}) = 1.8837 \times 10^{-5}(\text{DN}\,\text{nm}\,\text{R}^{-1}\,\text{s}^{-1}) \tag{2.27}$$

$$S_{pix}(\text{OI } 777.4\,\text{nm}) = 4.2057 \times 10^{-5}(\text{DN}\,\text{nm}\,\text{R}^{-1}\,\text{s}^{-1}) \tag{2.28}$$

Taking the sensitivity into account, the count numbers can be converted to Rayleighs by using equation 2.25.

Extraction of the dayglow emission intensities as explained above is an involved processes for which programmable codes have been developed using Interactive Data Language (IDL). As nature of the spectra for the three emission wavelengths are different (Figures 2.11, 2.12, 2.13), separate codes are developed for the extraction of emission intensities at each of the wavelengths.

2.3.4 Commissioning of MISE

MISE is commissioned at a low-latitude location, Hyderabad, India (Geographic 17.5^0 N, 78.4^0 E; 8.9^0 N Mag. Lat). It is installed at Jawaharlal Nehru Technological University, Hyderabad (JNTUH), under PRL-JNTUH collaboration since 2010 and is running in an automated schedule. This location is selected due to its geomagnetic importance. Hyderabad is located in the midway between the EIA trough and crest regions. Hence, by using the large FOV optical measurements, spatio-temporal variations in the low-latitude thermospheric dynamics can be studied.

Initially MISE was installed with its slit oriented along the North-South (Meridional) direction. Many interesting results in terms of the vertical coupling of the thermosphere [*Laskar et al.*, 2013; *Pallamraju et al.*, 2014], effect of solar forcing and gravity waves (GWs) on the thermosphere [*Laskar et al.*, 2013, 2015], set up of new meridional circulations during the SSW events and daytime wave characteristics in the MLT regions [*Laskar et al.*, 2014; *Laskar and Pallamraju*, 2014] came out from these data sets.

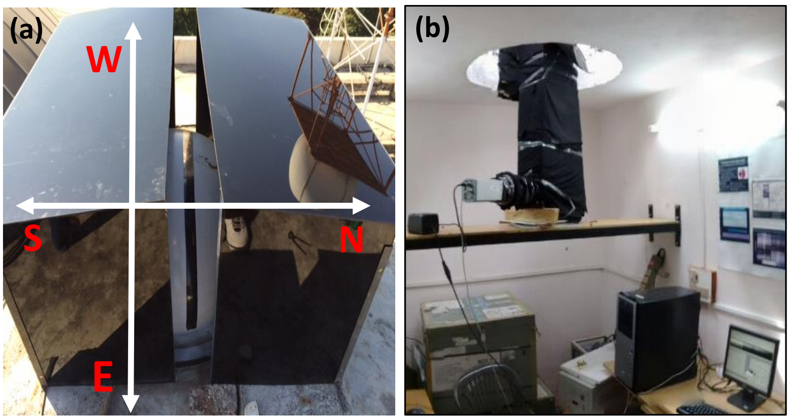

Figure 2.14: (a) Installation of the hood to reduce the duration of effect of solar glare, and (b) MISE supported to the roof while it's operation.

During the present work to investigate the variations of the thermospheric wave dynamics along the zonal direction, the position of MISE is oriented such that the slit is aligned along the East-West (zonal) direction. As the slit of MISE is aligned along the zonal direction, for low solar zenith angle, effect of solar glare is maximum and the images get saturated. To reduce the effect of solar glare, a hood with narrow opening is set up above the dome, as shown in Figure 2.14a. Further, special field campaigns are conducted to obtain the dayglow emission intensities along both the directions (zonal and meridional) in order to study the wave features in both these directions. The results obtained from such data sets are explained in the subsequent chapters of this thesis. Figure 2.14 shows the hood installed from outside and view of MISE from inside the laboratory.

2.4 Other Data Sets Used

Since both the neutral and ionized species are present in the upper atmosphere, information of both the species are required for a complete understanding of the upper atmospheric behavior. Neutral optical oxygen dayglow emission intensities give information of the thermosphere. In the previous section we have discussed in detail about the dayglow emissions. However, in this thesis work, in order to carry out the scientific investigations, we have also used other data sets, which are explained below.

2.4.1 EEJ data

Equatorial Electrojet (EEJ) refers to the intense narrow jet of current in the eastward direction that flows in the daytime over the dip equator at an altitude of around 105 km. The detail of EEJ has been discussed in the section 1.4. EEJ strength can be obtained by measuring the induced magnetic field using magnetometers placed on the surface of the Earth. Over Indian longitudes the horizontal component (H) of the Earth's magnetic field is obtained from two stations. One station is at Tirunelveli (TIR) (Geographic 8.7^0 N, 77.8^0 E; 0.15^0 N Mag. lat.), in a magnetic equatorial region which records the influence of currents induced due to the EEJ, and the other is at Alibag (ABG) (Geographic 18.6^0 N, 72.9^0 E; 10.5^0 N Mag. Lat.), magnetically an off-equatorial station, that is much less influenced by the EEJ currents. From each station, variations of H relative to their nighttime base values (i.e. ΔH_{TIR} and ΔH_{ABG}) are calculated. In this process contributions from the magnetospheric current system, if any, are removed. Difference of the measured ΔH at the equatorial- and off-equatorial stations (ΔH_{TIR}-ΔH_{ABG}) will give the EEJ strength. The variation in the EEJ strength can be used to infer the behavior of equatorial electrodynamics and can be related to the low-latitude processes, such as the EIA, ETWA, etc, [*Raghavarao et al.*, 1978, 1991; *Pallamraju et al.*, 2010, 2014; *Karan et al.*, 2016]. The EEJ data used in this thesis work were obtained from the Indian Institute of Geomagnetism, India.

2.4.2 Ionospheric data

In order to investigate the coupled nature of the thermosphere and ionosphere, ionospheric information is needed. We have used digisonde (digital ionosonde) to get the ionospheric information required for our investigation.

Digisonde is an active remote sensing device which works on the principle of basic radar technique and has been used for over seven decades. Digisonde transmits radio wave signals in a scanning mode in the range of 1-20 MHz.

The plasma has a characteristic frequency called plasma frequency (f_p), which is a function of electron density of plasma (N_e), given by,

$$f_p^2 = N_e e^2/4\pi\varepsilon_0 m = 80.5 N_e \tag{2.29}$$

where, f_p is the plasma frequency in Hz, N_e is the electron density in m^{-3}, e and m are the charge and mass of an electron, ε_0 is the permittivity of free space.

As the transmitted radio signal with frequency (f) enters into the ionosphere, it will encounter plasma with gradually increasing density i.e., increasing f_p (equation 2.29). The refractive index (n) of the medium is given as,

$$n^2 = 1 - \frac{f_p^2}{f^2} \tag{2.30}$$

At the altitude of $f_p > f$, the refractive index (n) becomes imaginary and the signal cannot propagate further. Hence, at the altitude where, $f_p = f$, the signal is reflected back [*Hargreaves*, 1992] and the reflected echo is received by the receiving antenna of digisonde. From the time delay of the echo, the height of the reflecting layer is calculated. This process of calculating the height is continued by scanning the transmitted signal for different frequencies. The height information is recorded as a function of frequency, which is called an "Ionogram". The ionogram gives information of the electron density and height of different layers of the ionosphere. By integrating the electron densities over the ionospheric altitudes, the ionospheric electron content (IEC) can be obtained. In general frequencies corresponding to the peak density in E, F_1, and F_2 layer of the ionosphere are called as critical frequencies of the layers and are written as f_0E, f_0F_1, and f_0F_2, respectively. Similarly, base altitude corresponding to f_0E, f_0F_1, and f_0F_2 are defined as h_mE, h_mF_1, and h_mF_2, respectively.

For the thesis work, we have used digisonde data from two stations. One station is at Trivandrum (Geographic 8.5^0 N, 76.9^0 E; 0.07^0 N Mag. Lat.), a geomagnetically equatorial location, and the other is at Ahmedabad (Geographic 23.0^0 N, 72.5^0 E; 14.9^0 N Mag. Lat.), typically a northern EIA crest location in Indian longitudes.

2.4.3 D$_{st}$ index

The D$_{st}$ (Disturbance storm time) index denotes the change in the horizontal component, H, of the Earth's geomagnetic field (approximately represented by a uniform magnetic field parallel to the Earth's magnetic dipole axis and directed southward) at mid-latitude regions, and, in essence, indicates the magnetic field induced at ionosphere due to the strength of the ring current in the inner magnetosphere. It is estimated in units of nT (nano Tesla) by using the H measurements from four well separated mid-latitude stations which are sufficiently far away from both the overhead auroral and the equatorial electric currents.

Figure 2.15 represents a classical example of the variation of D$_{st}$ index during weak, moderate, and severe geomagnetic disturbances. A geomagnetic disturbance consists of three phases, namely (i) Initial phase, (ii) Main phase, and (iii) Recovery phase. When the solar wind reaches the Earth's magnetosphere, due to the increase of solar wind ram pressure ($P_{dyn} = \frac{1}{2}\rho v^2$; where ρ and v are the

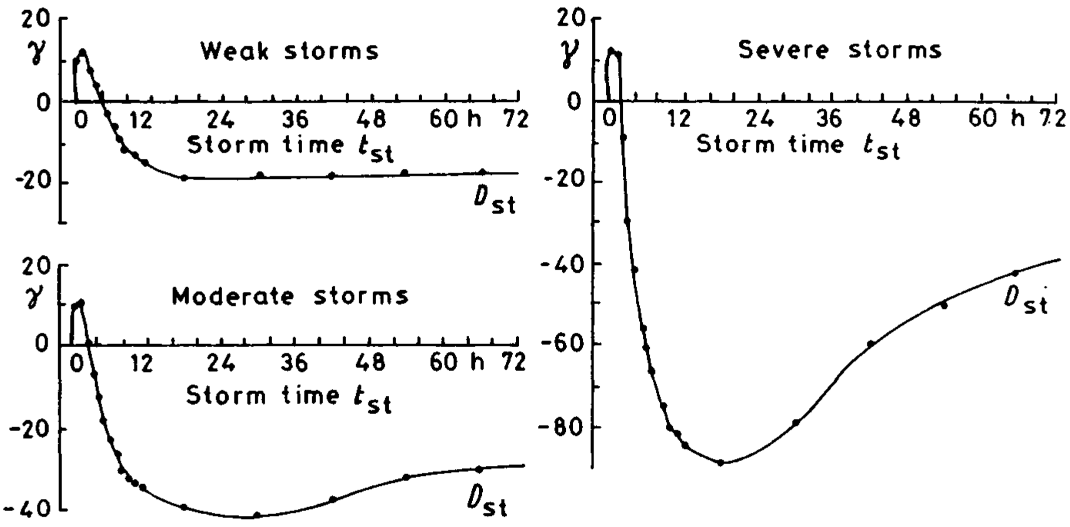

Figure 2.15: Variation of D$_{st}$ index during different types of geomagnetic storms are shown. After *Hargreaves* [1992].

solar wind mass density and velocity), the magnetic field lines get compressed and move closer to the Earth. This causes an increase in the induced magnetic field on the surface of the Earth as measured by the magnetometers and results in a sudden rise in D$_{st}$. This is referred as the storm sudden commencement (SSC) and lasts for few hours only, which is followed by the initial phase of the storm. During the initial phase of the storm, the D$_{st}$ values remain elevated. During geomagnetic storms, due to the enhancement of the ring current (westward), the induced magnetic field (southward) on the Earth increases and the D$_{st}$ values decrease, which forms the main phase of the storm. This phase generally continues for about several hours to a day. During the recovery phase of the storm, D$_{st}$ values increase to its normal level and this phase can vary from a couple of days to tens of days depending on the interplanetary magnetic field configuration. The D$_{st}$ data used in the thesis work have been obtained from ISGI website (isgi.unistra.fr).

2.4.4 Thermospheric O/N_2 data

The thermospheric $\Sigma O/N_2$ data is obtained from the Global Ultraviolet Imager (GUVI) on-board the NASA TIMED (Thermosphere Ionosphere Mesosphere Energy and Dynamics) satellite. GUVI is a spatial imaging spectrograph which scans back and forth across the limb and disc of the Earth in every 15 sec. During each scan, it covers an area 2500×100 km at 150 km altitude. The spatial resolution at nadir is 7×7 km [*Christensen et al.*, 2003; *Zhang et al.*, 2004]. GUVI obtains airglow images of the Earth's atmosphere in five selected spectral bands in the range of far ultraviolet (FUV) emissions (115.0-180.0 nm) to investigate the composition, temperature of thermosphere, variables related to auroral particle precipitation and solar EUV irradiance. The five spectral bands include the Hydrogen Ly-α line (121.6 nm), OI (130.4 and 135.6 nm), and N_2 Lyman-Birge-Hopfield (LBHS, 140-150 nm and LBHL, 165-180 nm) bands [*Christensen et al.*, 2003; *Zhang et al.*, 2004]. As the airglow emission intensities are proportional to the densities of the reactants, variation in the emission rates is expected to show a good correlation with the variation of densities. Following this procedure, $\Sigma O/N_2$ is calculated by taking the ratio of the vertical column density of atomic oxygen (OI 135.6 nm) to that of the molecular nitrogen (N_2 LBHS emissions). The base or reference of the column is the altitude where N_2 column density is 10^{17} cm^{-2} [*Strickland et al.*, 1999; *Zhang et al.*, 2004]. The column extends from around 140 to 250 km. *Strickland et al.* [1995] has explicitly reported the relationship between the ratio of the column densities and the airglow emission rates at 135.6 and LBHS wavelengths. In the thesis work, we have used the thermospheric $\Sigma O/N_2$ (Level 3) data corresponding to spatial location over Hyderabad, India (from where the optical data has been obtained). A spatial extent of $20^0 \times 20^0$ in latitudes×longitudes centered on Hyderabad has been considered to obtain information of the neutral composition. Throughout the text of the thesis O/N_2 is used in place of $\Sigma O/N_2$.

2.5 Data Analysis

In the previous section of this chapter we have discussed different types of data sets and their measurement techniques that are used for this thesis work. Spectral analysis of such data sets are carried out to obtain the spectral information at different stages of these investigations. There are different effective spectral analysis methods such as, fourier series, fourier transform, least-square fitting of sine and cosine waves of different time periods to the data, lomb scargle fourier transform, wavelet transform, Hilbert transform, Wigner distributions, etc. to carry out this analysis depending on the scientific requirements. To avoid repetition of the explanation of the spectral analyses methods used in the thesis work, the result of which are described in various chapters, these methods are explained in this chapter and are appropriately referred in subsequent chapters later.

2.5.1 Fourier Series

J. Fourier, a French mathematician first showed that any periodic function can be expressed as an infinite sum of periodic complex exponential functions. Many years after his discovery, this idea was generalized for non-periodic continuous and discrete functions.

Before discussing the fourier transform, let us first look at fourier series. Consider a periodic continuous function $f(x)$ with time period T $\big($i.e. angular frequency, $\omega_0 = \frac{2\pi}{T}\big)$. The fourier series expansion of $f(x)$ within the interval of $-L \le x \le L$ with the corresponding time period $T = 2L$ can be represented as,

$$f(x) = a_0 + \sum_{n=1}^{\infty} \Big(a_n \cos\frac{n\pi x}{L} + b_n \sin\frac{n\pi x}{L}\Big) \tag{2.31}$$

$$\Rightarrow f(x) = a_0 + \sum_{n=1}^{\infty} \Big(a_n \cos n\omega_0 x + b_n \sin n\omega_0 x\Big) \tag{2.32}$$

where, $a_0 = \frac{1}{2L}\int_{-L}^{L} f(x)dx$,

$a_n = \frac{1}{2L}\int_{-L}^{L} f(x)\cos n\omega_0 x dx$; for n=1,2,3,...

$b_n = \frac{1}{2L}\int_{-L}^{L} f(x)\sin n\omega_0 x dx$; for n=1,2,3,...

Substituting the values of a_n and b_n in equation 2.32, we can get

$$f(x) = a_0 + \sum_{n=1}^{\infty} \left(a_n^2 + b_n^2\right)^{1/2} \left[\frac{a_n}{(a_n^2 + b_n^2)^{1/2}} \cos n\omega_0 x + \frac{a_n}{(a_n^2 + b_n^2)^{1/2}} \sin n\omega_0 x)\right] \tag{2.33}$$

Assuming A_n(**Amplitude**)$=\left(a_n^2+b_n^2\right)^{1/2}$, δ_n(**Phase angle**)=arctan $\left(-b_n/a_n\right)$, and $\cos\delta_n = \dfrac{a_n}{(a_n^2+b_n^2)^{1/2}}$, equation 2.33 can be written in the **Amplitude-Phase angle form** as,

$$f(x) = a_0 + \sum_{n=1}^{\infty} A_n \cos\left(n\omega_0 x + \delta_n\right) \tag{2.34}$$

When $f(x)$ is expressed in the form of equation 2.34, then ω_0, $2\omega_0$, $3\omega_0$... and A_0,A_1, A_2... are called the frequency and amplitude spectrum of $f(x)$. The amplitude or the power (square of amplitude) spectrum can be represented as a function of the harmonic frequencies of $f(x)$. This is called a **discrete spectrum** as the powers are calculated for the discrete frequencies in the frequency spectrum. Fourier series analysis is applied to a continuous and periodic function but cannot be applied for an aperiodic function. To carry out spectral analysis of such aperiodic function fourier transform is used.

2.5.2 Fourier Transform (FT)

To convert a continuous data set (either periodic or aperiodic) from time domain $f(t)$ to frequency domain $f(\omega)$, fourier transform (FT) is used. The FT can be written as,

$$f(\omega) = \int_{-\infty}^{\infty} f(t)\exp^{-i\omega t}\, dt \tag{2.35}$$

An exponential term $\exp^{-i\omega t}$ at a fixed t is multiplied with $f(t)$ and integrated over all times to calculate the power of the frequency corresponding to the fixed t. If $f(t)$ has a high amplitude component of time period t, then that component will be multiplied with the sinusoidal component of $\exp^{-i\omega t}$ to give a larger value of the power. On the other hand if time period t is not a major component of $f(t)$, then the power will be smaller. And if $f(t)$ has no component with time period t, then the power will be zero. It is to be noted that as the product of $f(t)$ and $\exp^{-i\omega t}$ is integrated over times from $-\infty$ to ∞, so information of the occurrence time of the frequencies is lost.

In order to convert a data set from frequency domain $f(\omega)$ to time domain $f(t)$, inverse fourier transform (IFT) is applied, which can be written as,

$$f(t) = \int_{-\infty}^{\infty} f(\omega)\exp^{i\omega t}\, d\omega \tag{2.36}$$

The experimental observations or the natural data sets are discrete in nature. The FT of such data sets are called discrete fourier transform (DFT). Suppose $f(t_k)$ is an one dimensional continuous function with k=0, 1, 2, ..., N-1.

The DFT of $f(t_k)$ can be defined as,

$$f(\omega_k) = \frac{1}{N}\sum_{k=0}^{N-1} f(t_k)\exp^{-i\omega_k t_k}\,dt \tag{2.37}$$

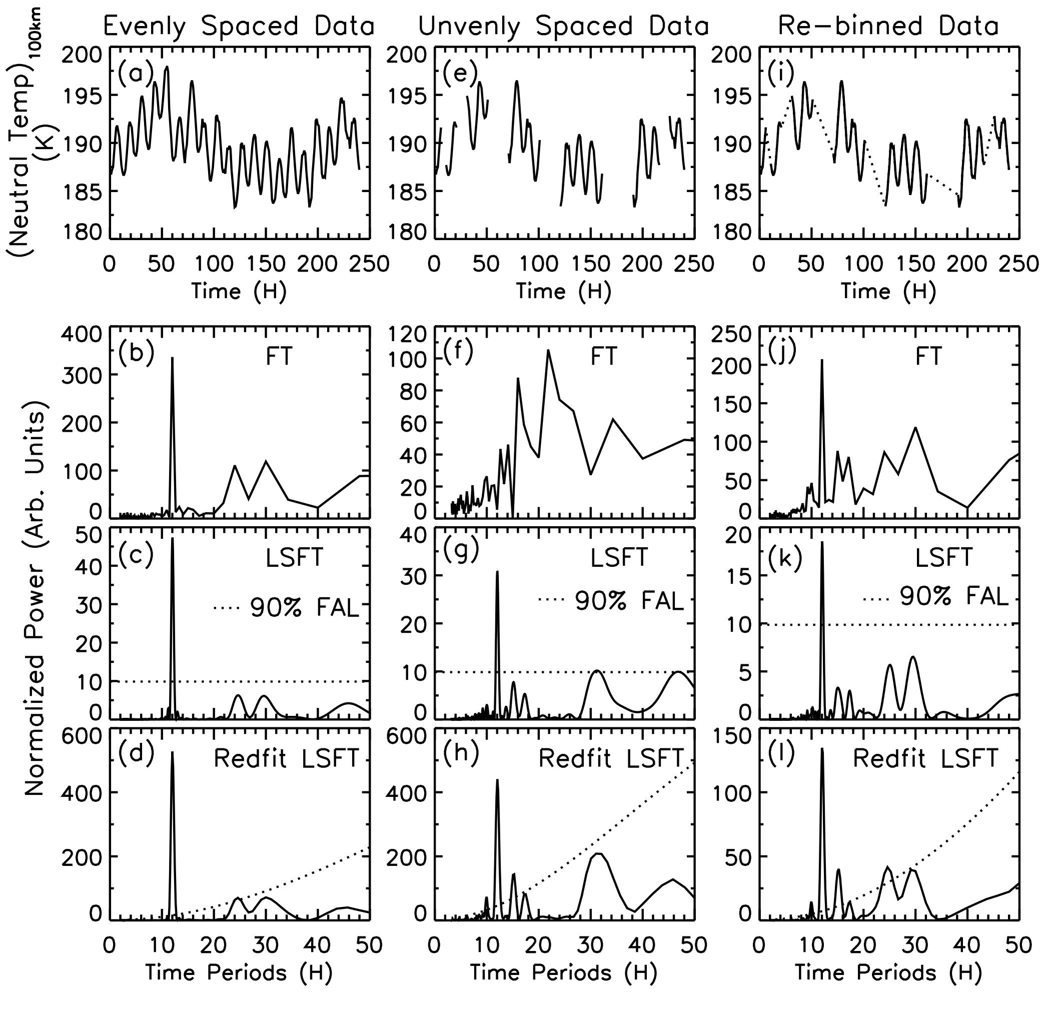

Figure 2.16: (a) Variation of the evenly spaced thermospheric neutral temperature at an altitude of 100 km obtained from the NRLMSISE-00 model during 1 to 10 January 2017 (e,i) Same as Figure a but for unevenly spaced and re-binned temperature data. Fourier transform, Lomb scargle fourier transform and Redfit Lomb scargle fourier transfrom of data shown in Figures (a,e,i) are presented in Figures (b,f,j), (c,g,k), and (d,h,l), respectively.

And the inverse discrete fourier transform can be defined as,

$$f(t_k) = \frac{1}{N}\sum_{k=0}^{N-1} f(\omega_k)\exp^{i\omega_k t_k}\, d\omega \tag{2.38}$$

The DFT computes N^2 complex multiplications and small number of additional operations to generate $f(\omega_k)$. The DFT can be computed faster using $N\log_2 N$ number of operations using another transform called fast fourier transform (FFT).

Figure 2.16a shows the thermospheric neutral temperature at 100 km altitude obtained from the NRLMSISE-00 model (https://ccmc.gsfc.nasa.gov /modelweb/models/nrlmsise00.php) during 1 to 10 January 2017. Here the data are continuous and evenly spaced at every hour. Figure 2.16b shows the FT of the data shown in Figure 2.16a. The X- and Y- axes show the time periods and power, respectively. It is to be noted that FT can clearly extract the dominant 12 h periodicity (semidiurnal component) in the temperature data. Now let us consider an unevenly spaced data set. Figure 2.16e shows the same type of data as shown in Figure 2.16a but is unevenly spaced. Figure 2.16f shows the FT of the data shown in Figure 2.16e. On comparison with Figure 2.16b it can be noted that FT does not yield accurate information on the periodicities that are existing as FT treats the data to be continuous data set. Hence, FT cannot be used to find out the dominant periodicity in an unevenly spaced data set. This is the limitation with this method. The unevenly spaced data shown in Figure 2.16e is re-binned linearly to make the data set evenly spaced, which is now shown in 2.16i and its FT is shown in Figure 2.16j. The dominant time period in the data is obtained accurately from the Figure 2.16j, but this may not be true always. Moreover, by the process of re-binning, the interpolated data may not carry the true picture of the variations as can be seen by the presence of periods from ∼12-18 h in Figure 2.16j as compared with Figure 2.16b. Therefore, use of interpolated data in FT will increase the uncertainty in the calculation of the time period. From above discussions it is clear that FT can be useful only for evenly spaced data sets. This limitation is overcome by the Lomb Scargle Fourier Transform (LSFT).

2.5.3 Lomb Scargle Fourier Transfrom (LSFT)

The fourier series, fourier transforms explained in the previous section are applied only to an evenly spaced data sets. But in practical scenario, mostly we come across unevenly distributed data sets. This is because of unfavorable sky conditions, issues with electric power during remote operation, technical issues with the instrument, etc. Scargle in 1982, derived a modified normalized periodogram to carry out the spectral analysis of the unevenly spaced data sets [*Lomb*, 1976; *Scargle*, 1982]. Before discussing Scargle's modified normalized periodogram, let us first look at the standard classical periodogram analysis.

The DFT for an arbitrary sampled data set, $X(t_i); i = 1, 2, ..., N_0$ is defined as,

$$FT_x(\omega) = \sum_{j=1}^{N_0} X(t_j)\exp(-i\omega t_j) \tag{2.39}$$

The periodogram is then conventionally defined as [*Deeming*, 1975],

$$\begin{aligned} P_x(\omega) = \frac{1}{N_0}\left|FT_x(\omega)\right|^2 &= \frac{1}{N_0}\left|\sum_{j=1}^{N_0} X(t_j)\exp(-i\omega t_j)\right|^2 \\ &= \frac{1}{N_0}\left[\Big(\sum_j X_j \cos\omega t_j\Big)^2 + \Big(\sum_j X_j \sin\omega t_j\Big)^2\right] \end{aligned} \tag{2.40}$$

This classical periodogram can be evaluated for any values of ω. It is to be noted that if X is pure Gaussian noise then $P_x(\omega)$ is distributed exponentially. If X contains a signal with frequency ω_0, then at or, near $\omega = \omega_0$, X and $\exp(-i\omega t_j)$ are in phase and $P_x(\omega)$ becomes large. Whereas, for other values of ω, $P_x(\omega)$ turns out to be small. For an evenly spaced data set at a cadence of Δt and assuming Δt=1, $t_j = j$, and $X_j = X(t_j)$, $P_x(\omega)$ can be written as,

$$P_x(\omega) = \frac{1}{N_0}\left|\sum_{j=1}^{N_0} X_j \exp(-ij\omega)\right|^2 \tag{2.41}$$

The FFT process has two major problems. First one is a statistical problem. $P_x(\omega)$ is very noisy inspite of increasing the number of data points or decreasing ΔT [*Richards*, 1967]. The power spectra of a signal will be error-free as long as the mean sampling rate exceeds or equals the Nyquist rate (i.e. the mean sampling rate is greater than or equal to twice the highest frequency of the signal). But in unevenly spaced data sets due to the data gaps the mean sampling frequency becomes smaller than the Nyquist rate and thereby the noise in the power spectra increases. The second problem is the spectral leakage of power to nearby frequencies of ω_0. These problems can be solved by convolving the spectrum with a spectral window function [*Harris*, 1978]. All the convolution procedures can be applied to the periodogram with arbitrary sampling. These are basically equivalent to smoothing in the spectral domain. The problem with such smoothing procedures is that the values of the power at various frequencies are not independent. Hence, the periodogram in equation 2.40 is not best suited for spectral analysis particularly in case of unevenly sampled data sets.

Scargle derived a modified periodogram analogous to the periodogram in equation 2.40 which is defined as,

$$P_x(\omega) = \frac{1}{2}\left\{ \frac{\left[\sum_j X_j \cos\omega(t_j - \tau)\right]^2}{\sum_j \cos^2\omega(t_j - \tau)} + \frac{\left[\sum_j X_j \sin\omega(t_j - \tau)\right]^2}{\sum_j \sin^2\omega(t_j - \tau)} \right\} \tag{2.42}$$

where, $\tan 2\omega\tau = \dfrac{\sum_j \sin 2\omega\tau_j}{\sum_j \cos 2\omega\tau_j}$

This modified periodogram (2.42) is suggested over the classical periodogram (2.40) because it has a simple statistical behavior and is equivalent to the minimization of the sum of squares using least-squares fitting of sine waves to the data. The use of τ makes the periodogram time translation invariance. Most importantly for the modified periodogram, $P_x(\omega)$ follows exponential probability distribution. The modified periodogram is normalized by σ^2 (total variance of the data set) [*Scargle*, 1982] because it is the only normalization which yields correct statistical behavior of the periodogram and also it produces the desired exponential probability distribution [*Horne and Baliunas*, 1986].

The False Alarm Probability And Significant Power Level

$P_x(\omega)$ shows an exponential probability distribution. For any ω_i the probability of $P_x(\omega_i)$ for a power level of z or greater is e^{-z}.

Let us assume that N is the total number of independent frequencies and z is the maximum power of the periodogram. Probability of each independent frequency smaller than z is $1 - e^{-z}$ and therefore probability of all frequencies smaller than z is $[1 - e^{-z}]^N$. Hence, probability (False Alarm Probability, FAL, p_0) of some frequencies with height z or greater is defined as,

$$p_0 = 1 - [1 - e^{-z}]^N \tag{2.43}$$

And hence, the power level can be written as,

$$z = -\ln[1 - (1 - p_0)^{1/N}] \tag{2.44}$$

The maximas in $P_x(\omega)$ can either be due to the frequency of the signal or due to the random noise present in the data. The values of $P_x(\omega)$ above this power level (z) are considered to be statistically significant. For p_0=0.01, the power level z is calculated with 99% confidence [*Scargle*, 1982; *Horne and Baliunas*, 1986].

The common practice to evaluate the significance of the power spectrum statistically is to measure the background noise level. The background noise level can be white noise or red noise. The white noise is a flat spectrum having zero mean, constant variance and uncorrelated with time. It spreads uniformly for all frequency range. In spectral analysis of many observational data sets, the spectral powers of higher frequencies are smaller than than the lower frequencies. Thus, the background noise level should be accounted carefully with varying frequencies. The red noise has zero mean, constant variance and is correlated with time. A simple model to estimate the red noise is the univariate lag-1 autoregressive (AR1) or Markov process, which is defined as,

$$x_n = \alpha x_{n-1} + z_n \tag{2.45}$$

where, α is the characteristic time scale of the AR1 process and z_n indicates the Gaussian white noise.

The normalized discrete fourier power spectrum of x_n can be defined as,

$$P_k = \frac{1 - \alpha^2}{1 + \alpha^2 - 2\alpha\cos(r\pi k/N)} \tag{2.46}$$

where, k=0,...,$N/2$ is the frequency index.

Hence, by selecting an appropriate lag-1 autocorrelation, the red noise spectrum can be estimated using equation 2.46 [*Gilman et al.*, 1963; *Torrence and Compo*, 1998].

The Number of Independent Frequencies

One important factor to decide the FAL is the number of independent frequencies N. By carrying out simulations for a large number of data sets with various time spacing, powers were estimated for all reliable frequencies. The highest peaks from each periodograms were selected and then combined. A false alarm function was then fitted to the peak distribution of the powers keeping N as variable. After fitting a parabola to the empirically generated values of N_i as a function of N_0, the folowing function was derived.

$$N_i = -6.362 + 1.193N_0 + 0.00098N_0^2 \tag{2.47}$$

For unevenly spaced data sets, number of independent frequencies reduce. In case of three data points clumped per time point, N_i is estimated to be $N_0/2.9$ [*Horne and Baliunas*, 1986].

Spectral Leakage

Sometimes we come across situations when more than one statistically significant frequencies are obtained. In those cases one needs to be careful in deciding the frequencies of the signal in the data. Because of the irregular spacing and finite length of the data set, the desired frequency of the signal may not appear at the correct position. These type of problems are known as spectral leakage and can be taken care of as follows.

A sine curve with the frequency ω_1 obtained from periodogram-1 is to be removed from the data and then periodogram-2 is to be calculated. Now the remaining frequencies in periodogram-2 are considered to be the frequencies of the signal. The periodogram-2 needs to be normalized to the variance of the data after subtracting the sine curve with frequency ω from the periodogram-1 [*Horne and Baliunas*, 1986].

Uncertainty in the Frequency

The standard deviation ($\delta\omega$) of the frequency (ω) can be defined as [*Kovács*, 1981; *Horne and Baliunas*, 1986],

$$\delta\omega = \frac{3\pi\sigma_N}{2\sqrt{N_o}TA}, \tag{2.48}$$

where, A is the amplitude of the signal, σ_N is the standard deviation of the noise after the signal has been subtracted, and T is the total length of the data set.

This was derived for evenly spaced data. However, the uncertainty does not degrade much for unevenly spaced data set. So this can also be used for unevenly spaced data sets.

The lomb scargle fourier transform of the evenly, unevenly spaced and rebinned data as shown in Figures 2.16a,e,i have been carried out and the results are depicted in Figures 2.16(c,d),(g,h),(k,l), respectively. The dotted lines in Figures 2.16c,g,k and d,h,l correspond to background white and red noise at 90% confidence level. It can be seen that the red noise level is small for smaller time periods. By using the lomb scargle fourier transform the 12 h semidiurnal variation in all the three types of data sets is found out to be significant. The dominant time periods and uncertainties in Figures 2.16b,c,d,g,h,j,k and l are 12.00 ± 0.14, 11.99 ± 0.17, 12.00 ± 0.13, 12.01 ± 0.24, 12.02 ± 0.17, 12.0 ± 0.14, 12.02 ± 0.19, and 12.0 ± 0.14 h, respectively.

2.5.4 Wavelet Analysis

In the previous section we have discussed about the different types of fourier transforms which can give information about the time period/frequency in a given time series data. But, these methods cannot give information about the time of occurrence of the frequencies as explained in section 2.5.2. For example in Figure 2.16 we do not have any information about the occurrence of 12 h periodicity during the 10 days (240 h) observation. For more clarity let us consider another example.

Figures 2.17a,b show two periodic continuous signals with 25, 50 and 100 h periodicities. In Figure 2.17a all the three time periods are present during the

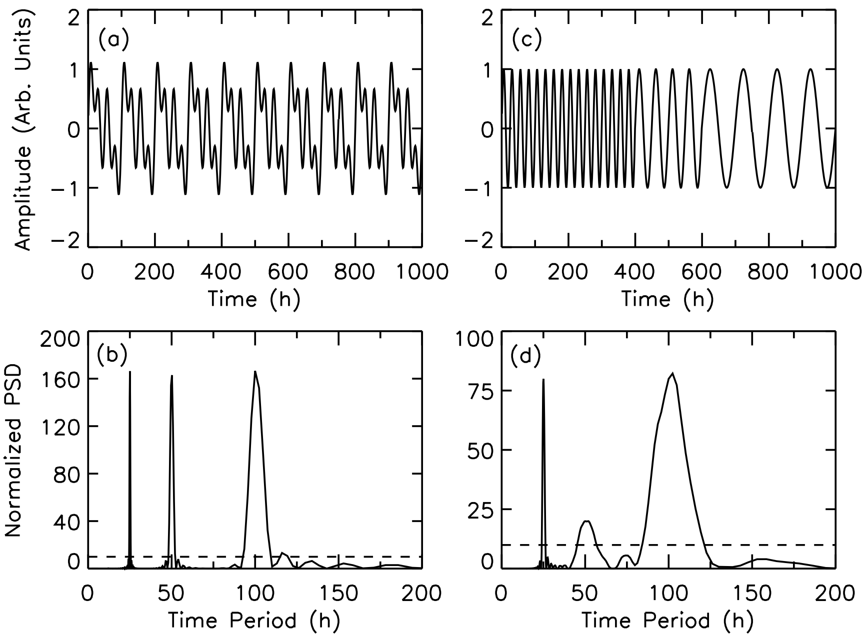

Figure 2.17: Signals depicting (a) uniform and (c) discrete distribution of periodicities in time. Fourier transform of the data (a,c) are shown in (b,d).

whole 1000 h time duration i.e. the signal is stationary. But in Figure 2.17c 25, 50 and 100 h time periods exist during 0-250, 250-600, and 600-1000 h, respectively, which means the signal is non-stationary. Figures 2.17b,d show the LSFT of the signals shown in Figures 2.17a,c. The horizontal dashed line corresponds to the 90% significance level. In both the LSFT spectra the only information that can be obtained is that 25, 50 and 100 h time periods are significant in both data sets. The only difference is that in Figure 2.17d the power values are different for different time periods. It is because of the existence of 25, 50, and 100 h time periods for 250, 350, and 400 h, respectively.

LSFT treats the periodic variations to be stationary through out the observation in both the cases (Figures 2.17a,c) which is not true for Figure 2.17c. Thus, another transform is needed which can give information of both frequency components of a signal and the duration of their existence in the signal. Short Time Fourier Transform (STFT), Multi Resolution Analysis (MRA), Wigner distribution, Wavelet Transform (WT) are some of the transforms which can yield such informations. In the thesis work we have used wavelet transform. Before discussing about wavelet transform, to have background information STFT is discussed below.

Short Time Fourier Transform (STFT)

Short time fourier transform divides the signal into small segments within which the signal is assumed to be stationary. For this a window function, $W(t-d)$ (width equal to the small segment) is selected and multiplied with the signal, $f(t)$ and an exponential term, $\exp^{-i\omega t}$ and then FT is carried out. d is the translation parameter.

The STFT of a time series data set, $f(t)$, is given by

$$STFT(d,\omega) = \int_{-\infty}^{\infty} f(t)W(t-d)\exp^{-i\omega t}\,dt \tag{2.49}$$

The window function (W) can be any one of the rectangular, Gaussian, Hanning, or Hamming type depending on the application. The STFT coefficients are calculated for each value of d and ω. Thus, a 2-dimensional plot of the coefficients in time and frequency domain can be generated.

The problem with the STFT is the time and frequency resolution. As the selected window is of finite length, it covers a small portion of the signal data and we will get information about the frequency band instead of exact frequencies within that window. This will make the frequency resolution poor. Thus, the width of the window function which is not well defined, limits the time and frequency resolution. If the width of the window is increased for better frequency resolution, the time resolution will be poorer. This limitation is like Heisenberg's uncertainty principle which states that "The momentum and position of a moving

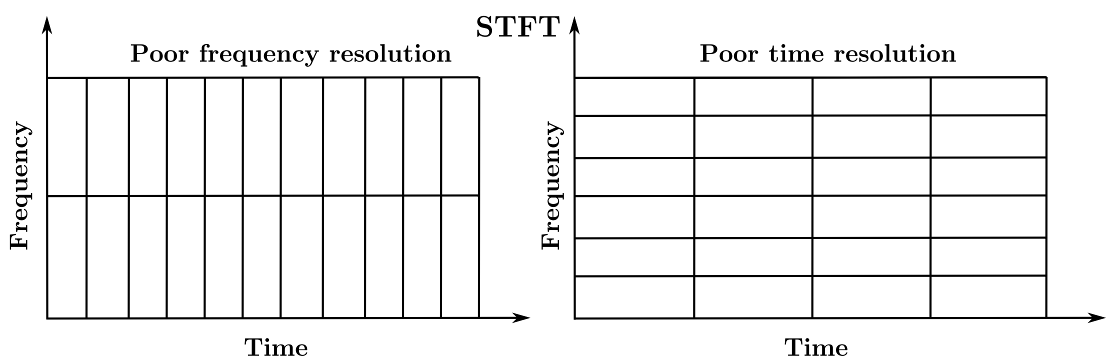

Figure 2.18: Box presentation of uncertainty in time-frequency resolution in STFT.

particle can't be measured simultaneously with 100% accuracy". Here the same principle is applied for time and frequency.

This is illustrated in Figure 2.18, where, the length and width of each box decides the time and frequency resolution. Each point inside a box corresponds to a fixed STFT coefficient and the coefficient changes for different boxes. On the left panel of Figure 2.18, the length of the boxes are smaller than their widths. This implies a better time resolution but poor frequency resolution. On the right panel of the Figure 2.18, the length is greater than the width of the boxes. This makes the time resolution poorer but the frequency resolution better. Thus, prior information on periodic components in the signal will help the user to select the window function and width while using STFT. The wavelet transform solves this difficulty to a certain extent, which is discussed in the next section.

Wavelet Transform (WT)

Wavelet analysis is a popular technique for data and image analysis particularly for non-stationary signals. It decomposes the periodic components of a signal by passing the signal through different frequency band filters and construct a picture of the same in spatial, temporal or wavelet scale (frequency) domain. Detailed information about the WT method can be found out in various literatures e.g. [*Daubechies*, 1988; *Goupillaud et al.*, 1984; *Grossmann and Morlet*, 1984; *Lau and Weng*, 1995; *Mallat*, 1989; *Morlet et al.*, 1982].

The continuous wavelet transform (CWT) of a square integrable function or data set $f(t)$ is defined as,

$$CWT(d,s) = \frac{1}{\sqrt{|s|}} \int_{-\infty}^{+\infty} f(t)\psi^{*}\left(\frac{t-d}{s}\right) dt \tag{2.50}$$

Here, d and s are the shift or translation (dilation) and scale parameters. Low and high value of s correspond to high and low frequencies, respectively. $\psi(t)$ is the transforming function called the Mother wavelet. Depending on $f(t)$, mother wavelets are selected. Some examples of the mother wavelets are Coiflet, Daubechies, derivatives of Gaussian, Haar, Morlet, Paul, Symlet function. $\psi\left(\frac{t-d}{s}\right)$ is called the daughter wavelet as it is derived from the mother wavelet by translation and scaling and the superscript (*) on it represents its complex conjugate. $1/\sqrt{|s|}$ is a energy normalizing factor to equalize the energy level of the transferred signals at every scale. By shifting the values of d and s, all the coefficients of the CWT are calculated. We have used Morlet wavelet fuction to calculate the wavelet coefficients which gives a complex output array. From these coefficients the amplitude, phase and power spectrum of the wavelet can be obtained.

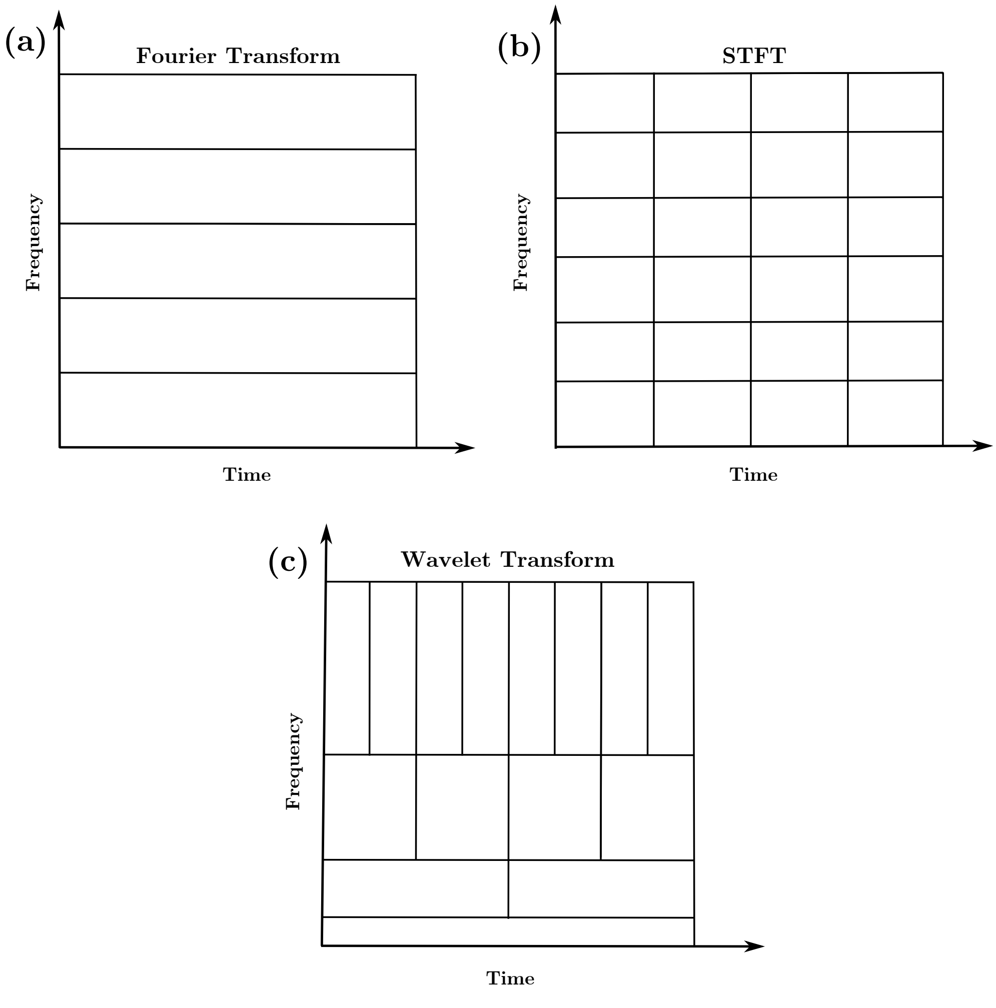

Figure 2.19: Box presentation of the uncertainty in time-frequency resolution in FT, STFT and WT.

As discussed in the previous section, STFT results a wavelet spectrum with constant time and frequency resolution. But CWT has a better time resolution and poor frequency resolution at high frequencies but at low frequencies it has a poor time resolution and better frequency resolution. For a better comparison of the time-frequency resolution of the FT, STFT and WT, box presentation of the time-frequency resolution in each transform is shown in Figure 2.19. From Figure 2.19a it is clear that FT does not give any information of time. Figure 2.19b shows that both time and frequency information can be obtained using STFT. At the same time the constant dimension of each box depicts the limitation in the simultaneous measurements of time and frequency. Different dimension of the boxes in Figure 2.19c clearly represent the advantage of WT over STFT.

Cone of Influence (COI)

In practical cases, mostly we deal with finite length of data series. FT assumes the data series to be cyclic while calculating the power spectra. Hence, errors will occur at the edges of the wavelet power spectrum. One solution for this is zero padding at the edges of the time series. But zero padding at the edges of the data series will again introduce discontinuities at the endpoints and at larger scales the amplitude will decrease because of the zeros. The cone of influence (COI) is the region of the wavelet spectrum in which the edge effects become important. The COI is defined as the e-folding time for the autocorrelation of wavelet power at each scale. The e-folding time will drop the wavelet power by a factor of e^{-2} at the discontinuities and ensures that the edge effects are negligible beyond this point [*Torrence and Compo*, 1998]. As zero padding is not required for cyclic data sets, COI is not needed. For Morlet wavelet the e-folding time is $\sqrt{2}s$.

Wavelet transform of the data shown in Figures 2.17a,c are shown in Figures 2.20a,b. The X- and Y-axes show the time duration and time period. Normalized power is shown in the Z-axis in different colors. The color bar on the right side of the figure show the values of the normalized power. The white lines show the cone of influence.

From 2.20a it can clearly be seen that the 25, 50, and 100 h time periods are significant through out the 1000 h time duration. In Figure 2.20b, the WT distinguishably separates the occurrence time of these three periodicities.

WT of the evenly and re-binned spaced thermospheric model neutral temperature data (as shown in Figures 2.16a,i) is shown in Figures 2.21a,b. The 12 h

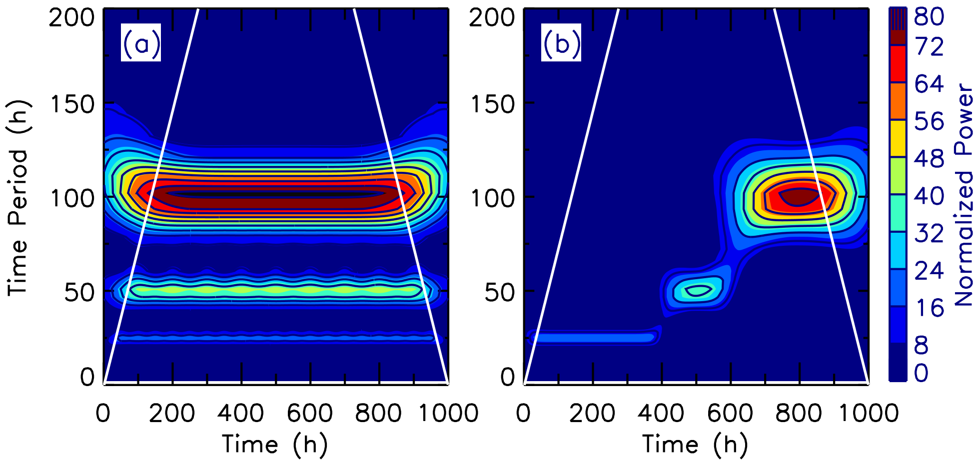

Figure 2.20: Wavelet transform of the signals with uniform and discrete distribution of periodicities as shown in Figures 2.17a,c. The white lines correspond to the Cone of Influence (COI).

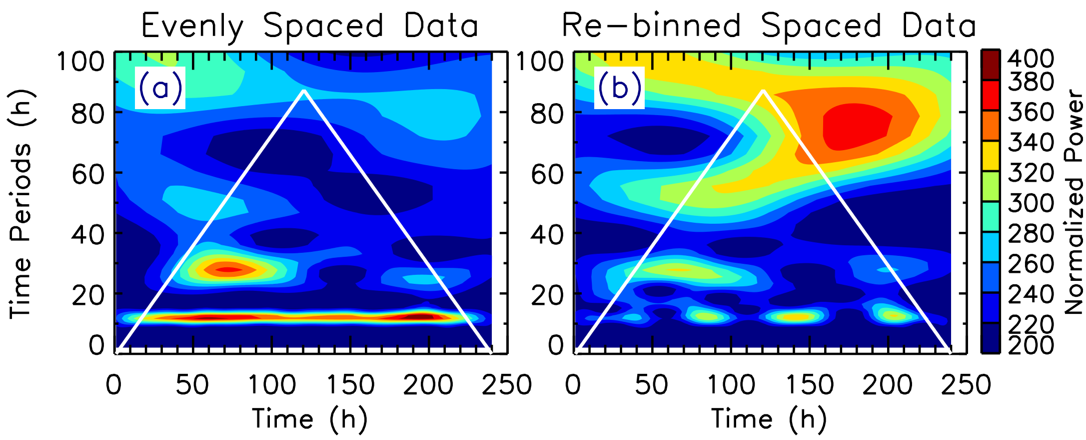

Figure 2.21: Wavelet transform of both evenly and unevenly spaced thermospheric neutral temperature data as shown in Figures 2.16a,e.

periodicity as obtained in the LSFT spectra (Figures 2.16b,c,d) is found to be present through out the 250 h in the evenly spaced data. The discontinuity of this time period in the re-binned data is also clearly notable.

The WT technique is widely used in various fields such as geophysics, medical science, astronomy, computer science, and engineering, etc. The wavelet transform is applied for time-scale power spectrum analysis, noise filtering, detection of coherent structures, edge detection, image compression and enhancement, etc.

All the transform methods explained till now are used to carry out the spectral analysis of different types of data sets in the thesis work. Samples of the spectral analyses carried out for dayglow data using these methods are discussed in the next section.

2.5.5 Spectral Analysis of Dayglow Data

MISE is operated through out the day to obtain the dayglow emission intensity data over a large FOV. So we have dayglow emission intensity data both in temporal and spatial domain. Thus, through periodogram and wavelet analyses we can get information about the frequency and its time of occurrence. Also, we can get information of the scale sizes (scale size is a different terminology used for the wavelength of the atmospheric waves) from the spatial varying dayglow data by wave number spectral analysis as the information along the spatial direction is obtained simultaneously. All these processes are explained below.

Periodgram and Wavelet Analysis

Figure 2.22a shows a sample diurnal behavior of OI 630.0 nm dayglow emission intensity obtained from zenith on 06 February 2014 as a function of local time (LT). Figures 2.22a and b depict the steps involved in obtaining the spectral information. The diurnal pattern of the 630.0 nm dayglow emission intensity (solid red) (Figure 2.22a) shows a broad solar zenith angle dependent variation along with other small period fluctuations, which are attributed to Gravity Waves (GWs). Since, in the thesis work, our focus is on the fluctuations in the GW regime, time periods in this range are obtained from the dayglow emission intensities by subtracting a 3 h smoothed line (solid dark) from the dayglow intensities. As the large-time scale variations are subtracted, the residuals (red dotted line) now correspond to time periods that are smaller than 3 h. Periodgram analysis has been carried out using the Lomb-Scargle technique (described in section 2.5.3) to obtain the GW time periods, the result of which is shown in Figure 2.22b. Here, the X- and Y-axes represent the time periods in hours and normalized power spectral density (PSD), respectively. The frequency (in h^{-1}) of the PSD is noted in the X-axis on the top. The horizontal dotted line shows the 90% false alarm limit (FAL) value. On this day, time periods of 2.28, 1.57, 0.8, and 0.5 h are

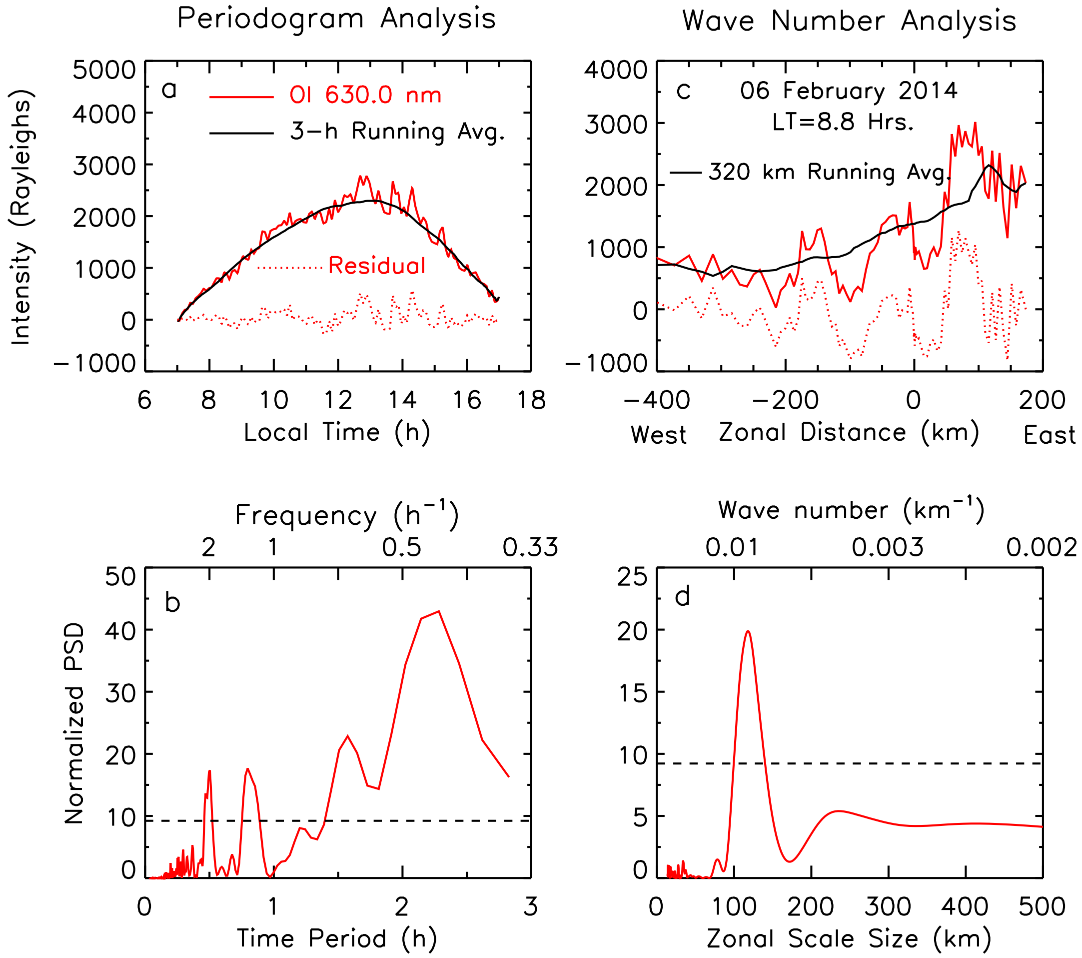

Figure 2.22: (a) The diurnal pattern of the OI 630.0 nm dayglow emission intensity over the zenith is shown (red). The 3-h running average (dark line) is subtracted from the dayglow to obtain the residuals (dotted red line). (b) Periodogram analysis of the residuals in Figure 2.22a is shown. (c) The OI 630.0 nm dayglow emission intensity along the zonal direction at 8.8 LT on the same day is shown. The 320 km running average (dark line) is subtracted from the dayglow to obtain the residuals (dotted red line). (d) Wave number spectral analysis of the residual in Figure 2.22c is shown.

found to be significant (>90% FAL) in the 630.0 nm dayglow emissions in zenith.

To know the time of occurrence of these time periods, we have carried out the wavelet analysis which is shown in Figure 2.23. The X- and Y-axes show the local time and time periods in hours. The normalized power is shown in colors along the Z-axis. The color bar on the right side of the figure show the normalized power values for different colors. The white line show the COI. It can be seen that the larger time periods (i.e. 2.28 and 1.57 h) were present during 10 to 12 LT

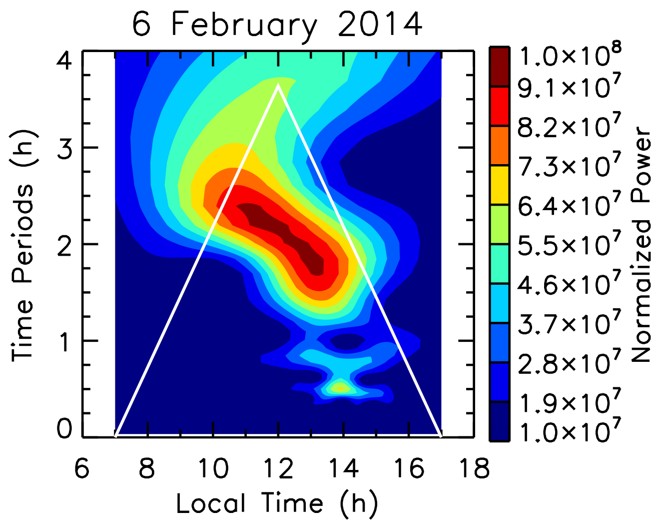

Figure 2.23: Wavelet transform of the 630.0 nm dayglow emission intensities as shown in Figure 2.22a.

whereas the smaller ones (i.e. 0.8 and 0.5 h) occurred during 12 to 14 LT. Also it is to be noted that all the time periods are within the COI and are significant.

Wave number spectral Analysis

The spatial coverage of MISE at the emission altitudes of 557.7, 630.0, and 777.4 nm dayglow emission wavelengths are around 340, 600, and 800 km (3^0, 5.5^0, and 7.3^0 in longitude), respectively. An 8-pixel binning of the image along the spatial direction results in the image with 128 pixels along the spatial direction. Out of the 128 pixels, data from pixel numbers 10 to 109 onto which the light from sky falls are used for the analysis. The rest of the pixels on either side of the image correspond to regions of the sky at low elevation angles which are susceptible to large scattering in the lower atmosphere and so are not used for analysis. An 11-pixel running average of the image from pixel number 10 to 109 is carried out along the spatial direction to get 90 useful segments. In this process the smaller scale fluctuations are averaged out so that random fluctuations which do not have any physical significance are eliminated. The non-linear nature of the relation between the FOV and the distance covered in space results in pixel-to-pixel variation in the spatial extent as imaged on the detector. Spatial resolutions over the zenith correspond to 0.4, 0.7, and 0.9 km.pixel^{-1} for the emission heights of 130, 230, and 300 km, respectively, whereas, it is 11, 20, and 25 km.pixel^{-1}, at higher view angles for the 557.7, 630.0, and 777.4 nm emission wavelengths. Considering a 2-pixel resolution to ascertain the position, the maximum spatial uncertainty for each of these emissions is 22, 40, and 50 km, respectively. The maximum spatial extent covered for the given FOV at the emission altitudes of 557.7, 630.0 and 777.4 nm dayglow emission intensities are ~340, ~600 and ~800 km, respectively. Lomb-Scargle wave number spectral analyses [*Lomb*, 1976; *Scargle*, 1982] of the residuals have been carried out to obtain the significant scale sizes.

Figures 2.22c and d illustrates a sample of the method for wave number spectral analysis for 630.0 nm dayglow emission intensity at 8.8 LT on 06 February 2014. The X- and Y-axes in Figure 2.22c show the zonal distance from zenith (positive eastwards) and dayglow emission intensity, respectively. The spatial variation of 630.0 nm dayglow emission intensity is shown as the solid red line. One can clearly notice the small and large wave like structures. To ensure that at least two repeatable cycles of the wave of a given scale size exist in the observed spatial extent, we have obtained residuals after taking running average of the zonally distributed dayglow emission intensity data at 777.4, 630.0, and 557.7 nm wavelengths by 425, 320, and 181 km, respectively. The dark solid line corresponds to the running averaged of the zonally distributed dayglow emission data. Thus, the residual (dotted lines) contains the contribution of scale sizes which are statistically significant. Lomb-Scargle wave number spectral analyses of the residuals have been carried out to obtain the significant scale sizes, which is shown in Figure 2.22d. The X- and Y-axes show the values of scale sizes (in km) and their normalized PSD. The upper X-axis shows the wave number (in km^{-1}). The 90% FAL is shown as the horizontal dashed line. A significant zonal scale size of 118 km is found to be present at the altitude of origin of the OI 630.0 nm emissions at 8.8 LT.

Methods of the spectral analysis for OI 630.0 nm dayglow data that have been carried out both in temporal and spatial domain and explained above are followed during various stages of the investigations of different works. Such analysis will be carried out for the dayglow data at all the three emission wavelengths. The results obtained by the use of such analysis methods will be presented in subsequent chapters.

2.6 Conclusion

In this chapter the production and loss mechanisms of the three neutral optical oxygen dayglow emission intensities (OI 557.7, 630.0, and 777.4 nm) are explained. These dayglow emission intensities are obtained by using a large FOV high spectral resolution optical spectrograph called MISE. Details about the optical design, viewing geometry, output images and commissioning of MISE are discussed. Extraction of dayglow emission intensities from the images obtained by MISE is very challenging and involved task, which is carried out through programmable codings using IDL. The method of extraction of dayglow emission intensities is explained in detail. In order to carry out the scientific investigations and to substantiate our findings, we have made use of other supporting data sets, such as EEJ strength, ionospheric data, D_{st} index, and thermospheric O/N_2 data. We have also discussed about all these data sets and the methods to obtain these data. During various stages of the investigation, we require the knowledge of periodicity information in the data sets. For this different spectral analyses such as FT, LSFT and WT have been performed, which are discussed in detail. Through these transforms, we have carried out the periodogram and wavenumber spectral analyses of the temporal and spatial dayglow emission intensity data to obtain the periodicity and scale sizes information which have also been discussed in detail with examples. Many new and exciting results have been obtained by the scientific investigations carried out on the data sets, wherein different analysis methods discussed in this chapter have been used. The results will be presented in the subsequent chapters.

Chapter 3

Influence of Equatorial Electrodynamics on Daytime Low-Latitude Thermospheric Optical Emissions

3.1 Introduction

It is well-known that the optical airglow emission intensities act as tracers of the atmospheric behavior that exists at the altitudes of their origin. In the Earth's upper atmosphere optical emissions originate when atomic or molecular constituents or their ions de-excite from their higher energy states to the lower ones. The emissions emanate at different altitudes depending on the reactants and the type of chemical/photochemical reactions that produce them at those altitudes as described in Chapter-2. We have also seen from Chapter-1 that there are several large scale phenomena that exists, especially over low-latitudes. With the knowledge that the dissociative recombination is responsible for the 630.0 nm nightglow, all-sky images of this emission yielded unique signatures on the reversal of the EIA in the nighttime [*Sridharan et al.*, 1993b]. The nighttime all-sky images provide information on the dynamics of the large scale plasma bubbles [e.g., *Taylor et al.*, 1995; *Makela et al.*, 2013]. The mesospheric (OH, O_2 band)

and the lower thermospheric (OI 557.7 nm) nightglow emission variability has been used to derive information on the mesospheric temperatures [e.g., *Taylor et al.*, 1995; *Singh and Pallamraju*, 2015], AGWs [*Shiokawa et al.*, 2009; *Singh and Pallamraju*, 2016], tides, and PWs [*Nakamura et al.*, 1998].

With regard to the dayglow, similar variations between the daily averaged 630.0 nm dayglow emission intensity and the daily sunspot number indicated the influence of solar flux on the optical dayglow emissions [*Pallamraju et al.*, 2010]. With the addition of OI 557.7 nm dayglow measurements, investigations have been extended to study various aspects such as, GW dynamics in the lower thermosphere [*Laskar et al.*, 2013, 2015], effect of the tidal and solar flux variations on the MLT dynamics from on-board UARS satellite [e.g., *Maharaj-Sharma and Shepherd*, 2004; *Zhang and Shepherd*, 2004, 2005], and the three dimensional daytime wave characteristics [*Pallamraju et al.*, 2016]. In all these measurements, it was seen that the diurnal behavior of the daytime emission intensity broadly varied as a function of the solar zenith angle. In fact, the empirical models for OI 557.7 nm and OI 630.0 nm dayglow emissions that were developed [*Zhang and Shepherd*, 2004, 2005] do have solar zenith angle as one of the inputs. This is not unexpected, as the solar photons through the processes of photodissociation, photoelectron production, and ionization at a given location do affect the volume emission rates of the dayglow emissions as explained in section 2.2. This gives rise to a broad solar zenith angle dependent behavior for the diurnal emission intensity distribution [*Solomon and Abreu*, 1989]. Thus, to the first order considering purely photochemical production processes one would expect that with decreasing/increasing solar zenith angle, the dayglow emission intensities will increase/decrease giving rise to maximum dayglow emission intensities around local noon resulting in a symmetric behavior in the diurnal variation of the dayglow emission intensities with respect to local noon.

The transport of plasma from the equatorial- to off-equatorial region by the process of the EIA (described in detail in section 1.4) can affect the thermospheric contribution of the dayglow emission intensities. Thus, it is interesting to investigate how the F layer plasma transport affects the diurnal behavior of the dayglow emission intensities. For this, we have investigated the diurnal behavior of the dayglow emission intensities at three wavelengths (OI 557.7, 630.0, and 777.4 nm). The high temporal resolution ground-based measurements that we have carried out by using MISE (discussed in detail in section 2.3) do show that the diurnal behavior of the dayglow emission intensities do not follow a symmetric pattern with respect to local noon on several days. On some days the dayglow emission intensity peaks during before noon or afternoon. Such non-symmetric or asymmetric diurnal behavior in the dayglow emission intensity pattern with respect to local noon is not expected considering purely the photochemical nature of the production of dayglow emission intensities. The peak of dayglow emission intensities in afternoon could be due to the increase of densities of reactants which produce the dayglow emissions. Hence, we have investigated this asymmetric diurnal emission intensity behavior in greater depths to characterize and to find the source of such behavior.

Following the procedure of extraction of the dayglow emission intensities as described in detail in section 2.3, we have obtained the dayglow emission intensities at the three wavelengths from Hyderabad, a low-latitude location in India. The low-latitude thermospheric behavior is affected by the thermospheric neutral winds as well as by the equatorial electrodynamics. This has been discussed in detail in sections 1.3 and 1.4. Thus, the influence of the neutral winds versus that of the equatorial electrodynamics on the production mechanisms of the dayglow emission intensities and, thereby, their diurnal behavior have been assessed.

3.2 Data Set

To carry out the investigation for this work, we have used the optical (dayglow emission intensity), magnetic (EEJ strength), radio (IEC, f_0F_2, h_mF_2), and model driven thermospheric neutral wind data sets. Details about these data sets and their measurement techniques are described in Chapter-2.

Figure 3.1 shows the geophysical locations of all the stations from where the data are obtained for the present work. The X- and Y-axes show the geographical

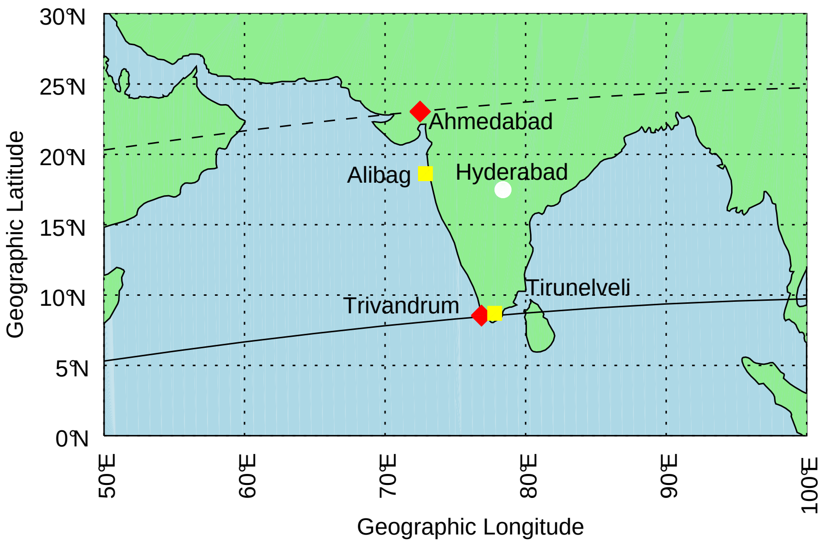

Figure 3.1: The geographic locations of the stations from where data have been obtained are shown. The neutral optical dayglow emission intensity data have been obtained by MISE commissioned at Hyderabad (white dot). The ionospheric data obtained from digisondes located at Trivandrum and Ahmedabad are shown as red diamonds. Stations from where the magnetic data are obtained to calculate the EEJ strengths are marked as yellow squares. The solid and the dashed dark lines represent the geomagnetic equator (obtained from IGRF-12) and the EIA crest location in the northern hemisphere (+15^0), respectively, for a given set of geophysical locations corresponding to the year 2014.

longitudes and latitudes, respectively. The neutral optical dayglow emission intensity data are obtained from the location, Hyderabad, marked as a white solid circle on the map. The red diamonds and yellow squares show the stations from where the ionospheric information and the EEJ strength data are obtained. The dark solid line represents the geomagnetic equator (obtained from International Geomagnetic Reference Field (IGRF)-12 model for 2014.0), whereas, the dashed line shows the typical northern crest region (15^0 N Mag. Lat.) of the EIA in Indian longitudes.

In this investigation the optical dayglow emission data obtained during December 2013 to March 2014 have been used. Independent ionospheric and the EEJ strength data obtained during this period have also been used to substantiate the findings.

3.3 Results and Discussion

Figure 3.2 depicts examples of typical diurnal variability on two days for OI 630.0 nm dayglow emission intensities, with the X- and Y-axes showing the local time (LT) in hours and the emission intensity in Rayleighs. The black solid line shows the 11-point running average. A dotted vertical line is drawn at local noon to aid the eye in bringing out the contrast between the pre- and post-noon behavior in the emission intensity variability patterns. It can be readily noted that on 05 January 2014 (Figure 3.2a), the diurnal emission intensity behavior is symmetric with peak intensity around noontime, which seems almost like an inflexion point. This behavior is opposed to that obtained on 19 December 2013 (Figure 3.2b), wherein the peak emission intensity was reached in afternoon and the diurnal pattern is asymmetric. As discussed above, the photochemical production is ex-

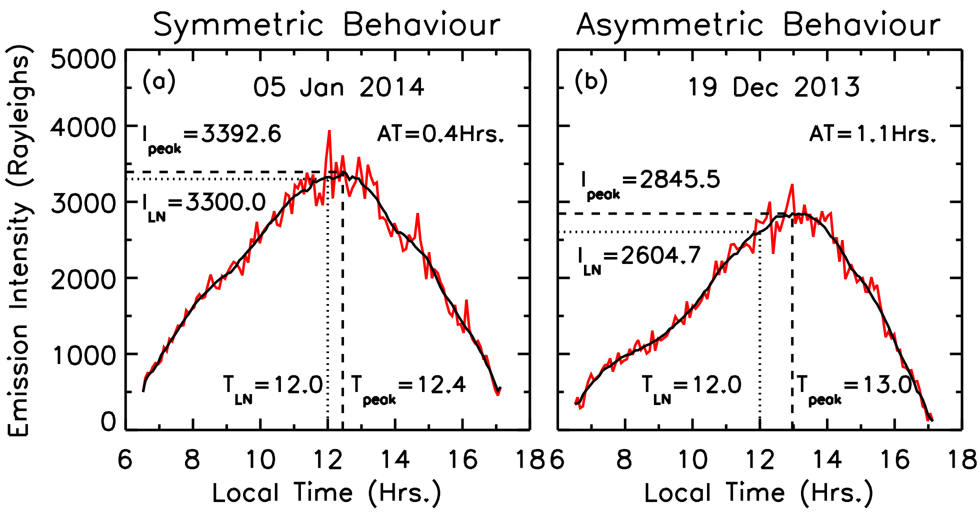

Figure 3.2: Samples of the diurnal behavior of OI 630.0 nm dayglow emission intensities. (a) Symmetric diurnal behavior in the emission intensities with respect to local noon. The behavior shows solar zenith angle dependent variation. Notice that with respect to noon the rise and fall in the emission intensities seem symmetric. (b) Asymmetric diurnal behavior in the emission intensities with respect to local noon. The peak in emission intensity is achieved after about an hour from noon. Notice the rise in the emission intensities to be more gradual than the decrease. The product of ratio of the emission intensities at the peak to those at noon and the difference in times between the peak reached and local noon yield the value of asymmetricity in time (AT), which are also shown in both the panels.

pected to peak around noontime and therefore, this asymmetric diurnal behavior in the dayglow emission intensities seems anomalous. It may also be noted that the rate of rise in emission intensities is different on these two days. The extent of asymmetry can be quantified as the product of difference in times between those of peak intensity and local noon and the ratios of the intensities at those times. Mathematically, the asymmetricity in time (AT) can therefore, be defined as follows.

$$AT = \frac{I_{peak}}{I_{noon}} \times (T_{peak} - T_{noon}) \tag{3.1}$$

where, T_{peak} and T_{noon} are the times of peak emission intensity and local noon. I_{peak} and I_{noon} are the emission intensity values corresponding to T_{peak} and T_{noon}, respectively. If the peak emission intensity occurs in before noon, it can be seen from equation 3.1 that the AT value becomes negative. To characterize the diurnal pattern of the dayglow emission intensity as symmetric and asymmetric, area under the curve in before noon and afternoon are calculated. If both the areas are comparable to each other, the diurnal behavior is characterized as the symmetric behavior day. Following this characterization method, the diurnal emission intensity behavior is considered to be symmetric or, asymmetric for AT $\leq$ 0.4 h and AT $>$ 0.4 h, respectively. The AT values for 05 January 2014 and 19 December 2013 are calculated to be 0.4 h (symmetric diurnal behavior) and 1.1 h (asymmetric diurnal behavior), respectively.

Such unexpected asymmetric diurnal behavior is seen not only in the OI 630.0 nm dayglow emission intensities, but also in the OI 777.4 nm and OI 557.7 nm dayglow emission wavelengths that emanate from altitudes above and below that of the OI 630.0 nm dayglow. Figure 3.3 shows the diurnal emission intensity behavior, wherein the X-axes represent the local time and the Y-axes show the intensity of the optical emissions. The vertical dotted line represents local noon. All the data included here correspond to magnetically quiet days (Ap $<$ 23). The total number of days plotted in each panel may be noted on the top right corner of each figure. The upper (Figures 3.3a,d), middle (Figures 3.3b,e), and lower (Figures 3.3c,f) panels show the diurnal behavior of the dayglow emission intensities at 777.4 nm, 630.0 nm, and 557.7 nm wavelengths, respectively. Figures

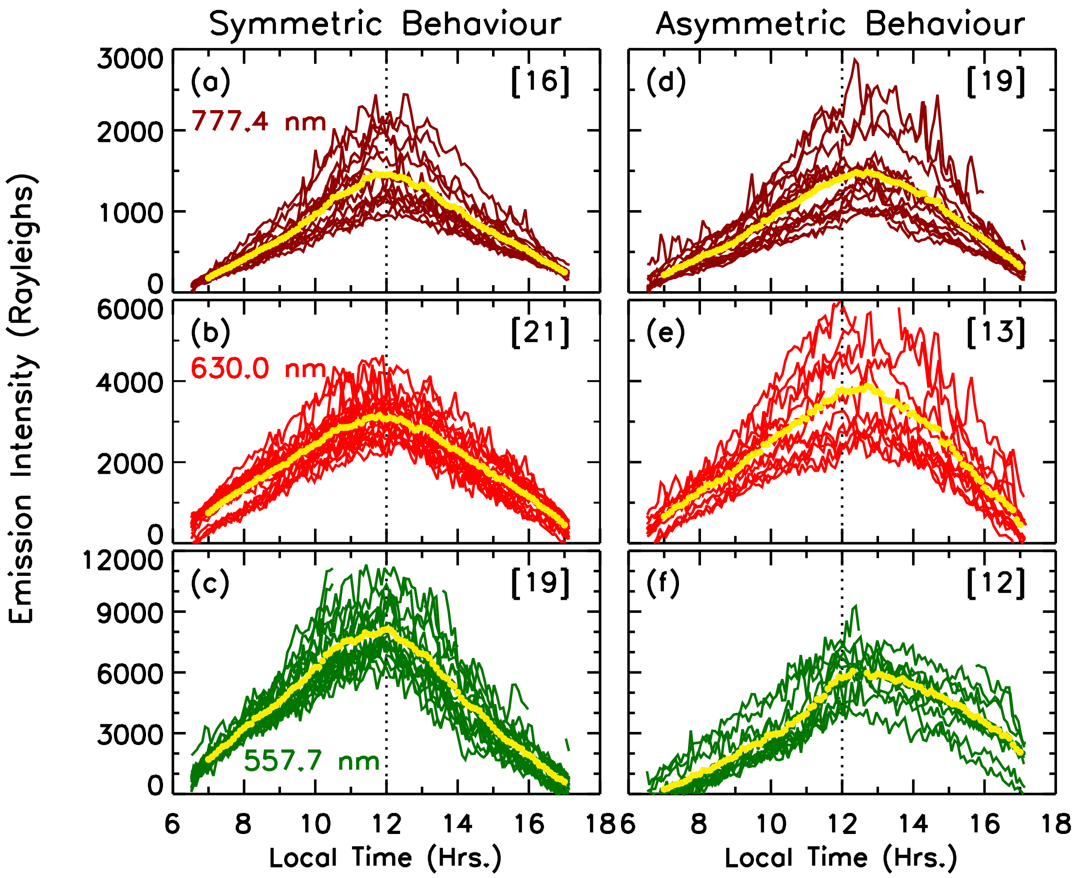

Figure 3.3: The diurnal behavior of the optical dayglow emission intensities at (a,d) OI 777.4 nm; (b,e) OI 630.0 nm; and (c,f) OI 557.7 nm wavelengths. The plots on the left column (a,b,c) show the symmetric diurnal behavior in the emission intensities with respect to local noon. Plots on the right (d,e,f) show asymmetric diurnal behavior in the emission intensities with respect to local noon. The line in yellow color shows the average of all the days of the data. The number of days of data that exist for a given diurnal behavior is shown in square brackets.

3.3a-c and Figures 3.3d-f, show the emission intensity behavior on several days wherein the diurnal emission intensity behavior was symmetric (AT $\leq$ 0.4 h) and asymmetric (AT $>$ 0.4 h), respectively. Note the difference in the timings of the occurrence of peak intensities with respect to local noon, which are different for different days. The yellow line shows the average of all the days of data, which is drawn to essentially show the contrasting diurnal behavior in each emission intensity. The difference in behavior of the emission intensities on the days with symmetric/asymmetric diurnal pattern is clearly contrasting in many ways. (1)

It may be noted that the emission intensity variability on the days with symmetric diurnal behavior is not as much as that seen on the days with asymmetric diurnal behavior particularly in 630.0 nm and 777.4 nm emissions. (2) The afternoon spread in the emission intensities on the days with asymmetric diurnal pattern is much greater as compared with that in the forenoon. (3) The pattern of rise in emission intensity is different between these two types, with a slow rate of rise on the days with asymmetric diurnal behavior, while it is relatively faster on the days that show symmetric diurnal behavior. (4) While the emission intensity pattern is skewed towards post-noon on the days with asymmetric diurnal behavior; it is slightly skewed before noon, especially in the 630.0 nm and OI 557.7 nm emissions, on the days with symmetric diurnal behavior. In Figure 3.3 we collated the days with symmetric/asymmetric diurnal behavior in emission intensities at each of the wavelengths, obtained during December 2013 - March 2014. There are days when intensities only at one or two emission wavelengths show symmetric diurnal behavior but the others show asymmetric. There are also common days when emission intensities at all the three wavelengths show symmetric/asymmetric diurnal behavior. All these features make this very interesting and intriguing at the same time, as there seems to be a combination of atmospheric processes, the constituents/reactants available at a given time, neutral dynamics (winds), and electrodynamic forces operative at different altitudes on these days.

To begin with, let us look at the production mechanisms of all these emissions which originate in the lower-thermosphere/thermosphere as discussed in the section 2.2. It is clear that the 557.7 nm and 630.0 nm dayglow emissions depend on both neutral and electron densities, whereas, the 777.4 nm dayglow emissions depend only on the ion and electron densities. Thus, the production of all the three dayglow emission intensities depend on the available solar flux, temperature dependent reaction rates, and the densities of neutrals and ions. It can be readily seen that the photoelectrons, EUV flux for photodissociation, and ionization at any location vary with respect to the solar zenith angle. So the diurnal behavior of the three dayglow emission intensities are expected to be symmetric with respect to local noontime as mentioned in section 3.1. Thus, the asymmetric diurnal behavior observed in the three optical dayglow emission intensities (Figure 3.3) can mainly be due to the variation of either the neutral densities, or the electron densities, or both, which can be engendered by neutral dynamics or electrodynamics, or both.

Firstly, we consider the changes in the electron densities due to neutral winds, especially the meridional wind, as it is known that the wind-assisted movement of electrons along the magnetic field lines alter the electron densities at a given location [*Rishbeth and Garriott*, 1969]. An increase/decrease of the electron number densities result in corresponding increase/decrease in the optical emission intensities. A poleward wind moves the ionospheric layer to lower altitudes where the dissociative recombination mechanism can be significant, thereby increasing the yield of OI 630.0 nm and OI 557.7 nm dayglow emissions. Similarly, the yield of OI 777.4 nm dayglow emission is also expected to show an enhancement through radiative recombination mechanism. An equatorward wind will move the ionospheric layer to higher altitudes thereby reducing the potential yield of the dayglow emissions. In a similar manner, poleward winds, especially from the summer hemisphere, bring in additional plasma into the winter hemisphere and so give rise to greater yield in the dayglow emission intensities.

Other than the meridional winds, the equatorial electrodynamical forcing is another potential cause which is capable of bringing plasma from equatorial- to low-latitude regions. In the equatorial region, due to the horizontal nature of the geomagnetic field lines, several interesting phenomena such as the EEJ, EIA, ETWA take place. The formation of these phenomena along with their effects on the equatorial- and low-latitude ionospheric-thermospheric system has been discussed in detail in section 1.4. EEJ strength can be used to infer the effectiveness of the electrodynamical processes operative on a day over the low-latitudes. The excess ionization that is brought in to a given off-equatorial region from the equatorial region by the process of the EIA, results in greater emission intensities through the dissociative recombination and radiative recombination mechanisms. Moreover, E region electric field in the off-equatorial low-latitude regions are mapped to equatorial F region through the geomagnetic field lines and can contribute to the ($\vec{E} \times \vec{B}$) plasma drifts, thereby increasing the EIA strength. Thus, effect of the zonal winds on the optical dayglow emission intensities can also be brought about through the equatorial electrodynamics. The relative importance between these two sources, namely, the neutral winds and the equatorial electrodynamics, in making the diurnal emission behavior to be asymmetric in the dayglow emission intensities is evaluated below.

Figure 3.4 shows two days (columns) of dayglow emission intensity data for all the three wavelengths, the thermospheric neutral winds, and the EEJ strengths (rows). The left column shows the day with symmetric diurnal behavior (26 December 2013) and the one on right shows the day with asymmetric diurnal behavior (07 February 2014) in all the three dayglow emission intensities. The X-axes show the local time, while the Y-axes (in the top three rows) show the dayglow emission intensities and (fourth row) the thermospheric zonal wind, U_x (dotted line, positive eastward) and meridional wind, U_y (solid line, positive northward) at all the three emission altitudes on both the days as obtained by the Horizontal Wind Model, (HWM14) [*Drob et al.*, 2015]. The bottom-most row shows the EEJ strength in nT and the horizontal dashed line drawn corresponds to 0 nT value. The solid lines in the dayglow emission intensities represent an 11-point running average of the data. The vertical dotted lines are drawn at local noon. The dates of the data and the AT values for each of the diurnal behavior of the emission intensities are shown in the plots. For these days, panels 3.4d,i show the zonal and meridional winds at 130, 230, and 300 km altitudes that are representative of those of the OI 557.7, 630.0, and 777.4 nm emissions, respectively.

It is expected that larger meridional winds bring the ionospheric layer to lower altitudes, which gives rise to larger dayglow emission intensities, as discussed above. The meridional wind magnitudes were large on 26 December 2013 at all the altitudes, which as per the discussion above are favorable for giving rise to asymmetric diurnal behavior in emission intensities, however, the observations do not show such a behavior. Conversely, on the day (07 February 2014) with lower

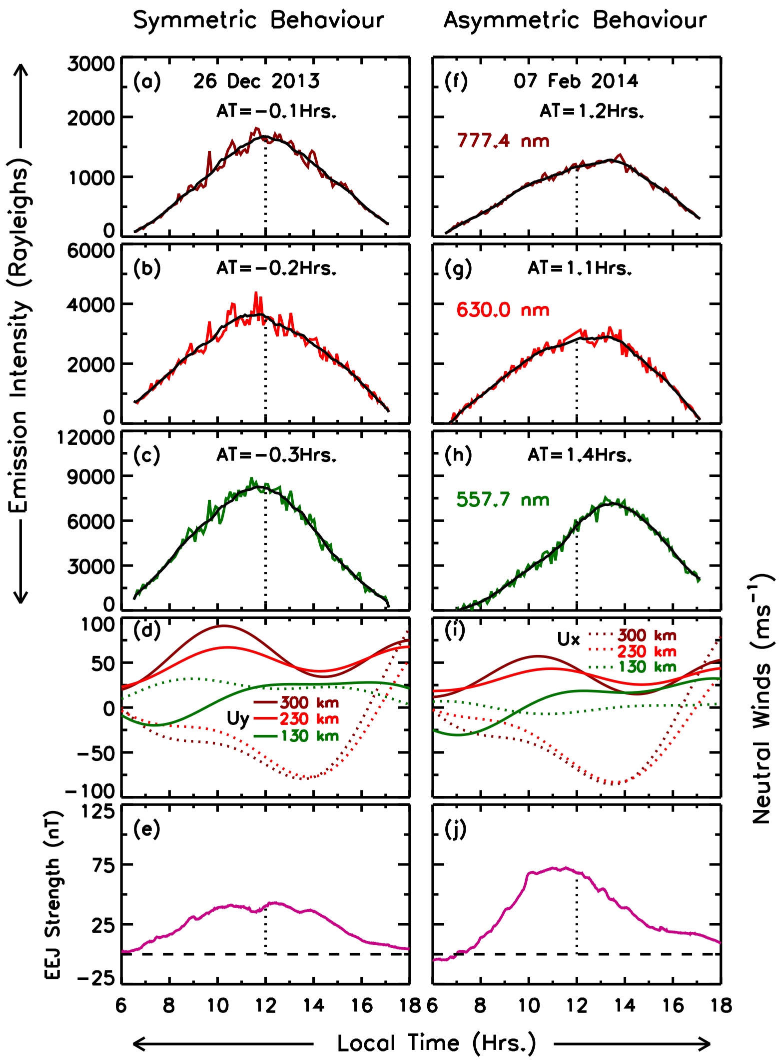

Figure 3.4: Top row (a,f) show the diurnal variability of the dayglow emission intensity in OI 777.4 nm wavelength on two selected days. Plots (b,g) and (c,h) show the diurnal behavior of OI 630.0 nm and OI 557.7 nm emission intensities on the same days as of OI 777.4 nm emissions. Plots (d,i) show the HWM14 neutral wind magnitudes. Plots (e,j) show the electrojet strengths. The plots in the left column correspond to the day with symmetric diurnal behavior in all the three oxygen dayglow emission intensities, while those on the right correspond to the day with asymmetric diurnal behavior in all the dayglow emission intensities.

meridional wind magnitudes, asymmetric diurnal behavior was observed in all the dayglow emission intensities. Therefore, the meridional wind hypothesis as the cause for the asymmetric diurnal behavior is not supported by the observations.

In this context, the possibility of equatorial electrodynamical influence in bringing about the asymmetric diurnal behavior in the emission intensities is examined using the EEJ strength as the reference. It is known that the EEJ dynamics have a significant role in influencing the distribution of electron densities over the low-latitude regions [*Moffett*, 1979]. Further, as a consequence of the EIA, ETWA is formed (as discussed in section 1.4) and the zonal winds and temperatures are affected [*Raghavarao et al.*, 1993]. It should be noted that the peak EEJ strengths on these two days were different (40 and 75 nT), however the peak emission intensities on these days were similar, and therefore it is apparent that the peak EEJ strengths have no direct relationship with the magnitudes of the peak dayglow emission intensities. However, it had been shown in earlier works [*Raghavarao et al.*, 1978] that the integrated EEJ strength until noon has a direct one to one correlation with the strength of the EIA. Although ionization is not being measured through optical measurements, it has been shown by earlier studies that the ionization brought in from the equatorial-latitudes contribute to the OI 630.0 nm dayglow emissions through dissociative recombination mechanism [*Sridharan et al.*, 1992b; *Pallam Raju et al.*, 1996; *Pallamraju et al.*, 2002]. Thus, the asymmetricity in time (AT) observed in the optical dayglow emission intensity measurements at all the three wavelengths is compared with the values of the EEJ strengths, (A_{EEJ}), integrated over 07 to 12 LT. On these days with symmetric and asymmetric diurnal pattern in the dayglow emission intensities, the values of A_{EEJ} were 147 and 214 nTh (shown in Figure 3.4). As discussed above in this section, the larger value of A_{EEJ} on the day with asymmetric diurnal behavior contributes to the strength of the EIA to a greater extent, which results in higher values of AT. The values of AT on the day with asymmetric diurnal behavior were calculated to be 1.2, 1.1, and 1.4 h for 777.4, 630.0, and 557.7 nm emissions, respectively, whereas on the day with symmetric diurnal behavior, these values were -0.1, -0.2, and -0.3 h for these emissions. The negative AT value indicate that the peak in the emission intensity has occurred before noon, which could most probably be due to the weaker equatorial electrodynamics on that day. The zonal wind magnitudes show nearly similar behavior on both these days. In any case, as the zonal winds affect the equatorial electrodynamics, their effect are implicit in the integrated EEJ strength.

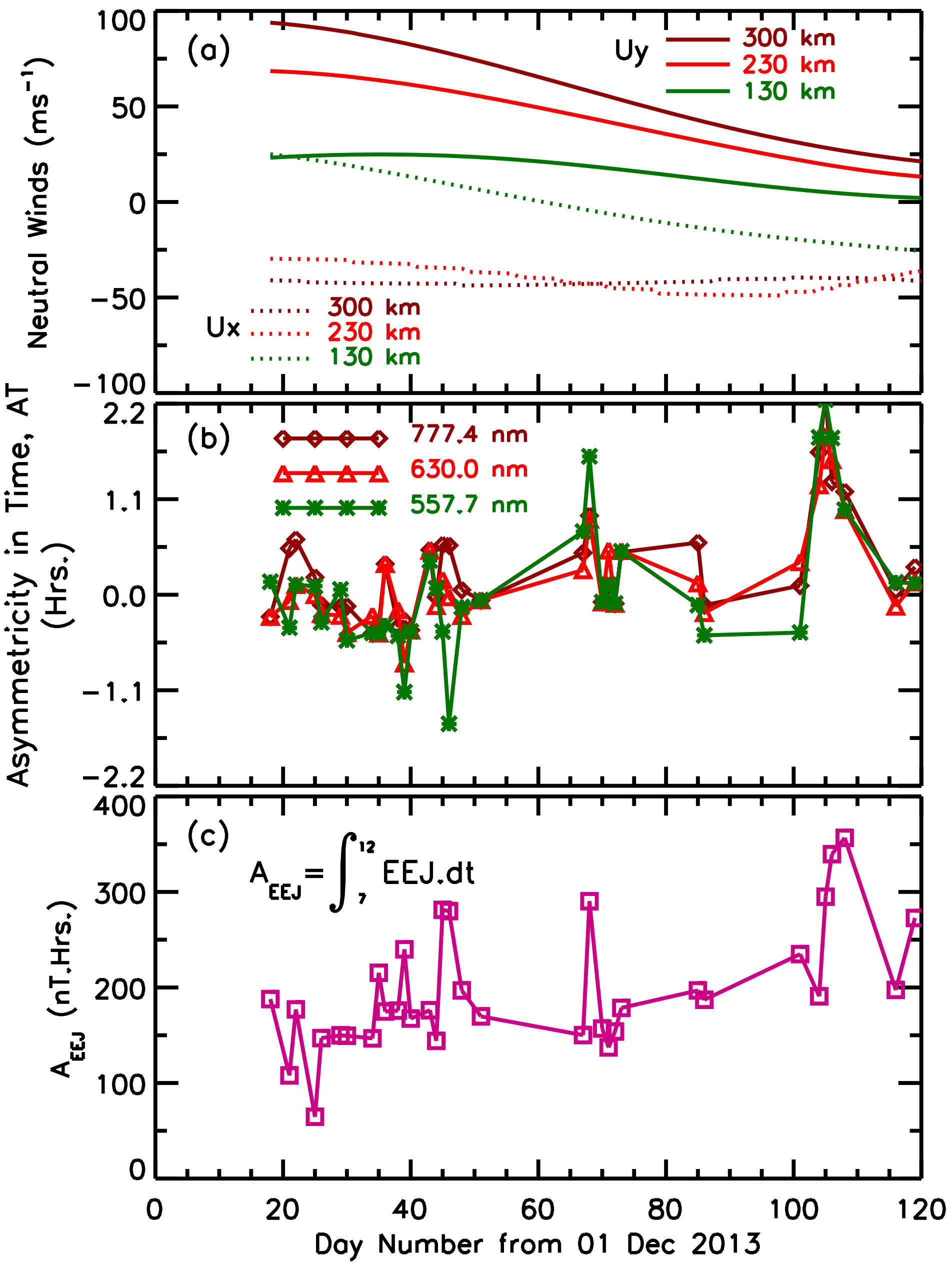

Figure 3.5: The variations in (a) the neutral winds at the three different emission altitudes, (b) the asymmetricity in time (AT) at the three dayglow emission intensities on different days, and (c) EEJ strength integrated over 07-12 LT (A$_{EEJ}$) on the days corresponding to optical data are shown. The X-axis shows the day number starting from 01 December 2013.

Figure 3.5 comprehensively summarizes the results of the present investigation. The X-axis shows the day number beginning on 01 December 2013. Figure 3.5a shows the peak meridional wind, Uy (solid line) and the corresponding zonal wind, Ux (dotted line) magnitudes obtained from the HWM14 model at the three emission altitudes. It can be seen that the magnitudes of the meridional wind reduces, expectedly, from December to March, which is consistent with the seasonal wind behavior as one moves from solstice to equinox, whereas, the variation in zonal winds is not significant. Figure 3.5b shows the AT values for all these three emissions, which over this period varied from -1.5 to +1.5 h. From the uncorrelated behavior between the values of AT and the meridional winds, it is clear that the meridional winds are not the cause for the observed asymmetric diurnal behavior in the optical emission intensities. Figure 3.5c shows the EEJ strengths, A_{EEJ}, integrated in forenoon (07-12 LT), which display a similar behavior as that in the AT values in the optical dayglow emission intensities at all the three wavelengths. The optical dayglow emission intensities are affected by both the neutral dynamics and the electrodynamics. Both of these show seasonal dependence. So their contributions in the observed fluctuations in the dayglow emission intensities are different in various seasons. The strength of equatorial electrodynamics decides the latitudinal extent of the EIA. Also, the effect of the EIA can first be seen at lower altitudes in off-equatorial latitudes and then at higher altitudes. Thus, on a given day this can result in a better agreement between A_{EEJ} and values of AT in 557.7 nm emission intensity but not in 630.0 nm/777.4 nm emissions. In Figure 3.5, AT values are calculated for all the clear-sky days irrespective of the symmetric or asymmetric diurnal behavior at all the three emission wavelengths, which shows a broad similarity with the values of A_{EEJ} at different wavelengths of emissions. This clearly indicates that the electrodynamical variations primarily govern the diurnal behavior of the neutral dayglow emission intensities.

For the sake of completeness, it should however be mentioned that the thermospheric winds used in this study are a climatological model driven, whereas, the EEJ values were obtained from measurements. Model values of the winds have been used because, measurements of the winds during the daytime are not available for comparison. Nevertheless, being driven primarily by the solar heating, it is not expected that the measured winds (had they been available) would yield any different result, as they are not expected to show significant variations from one day to another during geomagnetically quiet times, to which the data in this study corresponds.

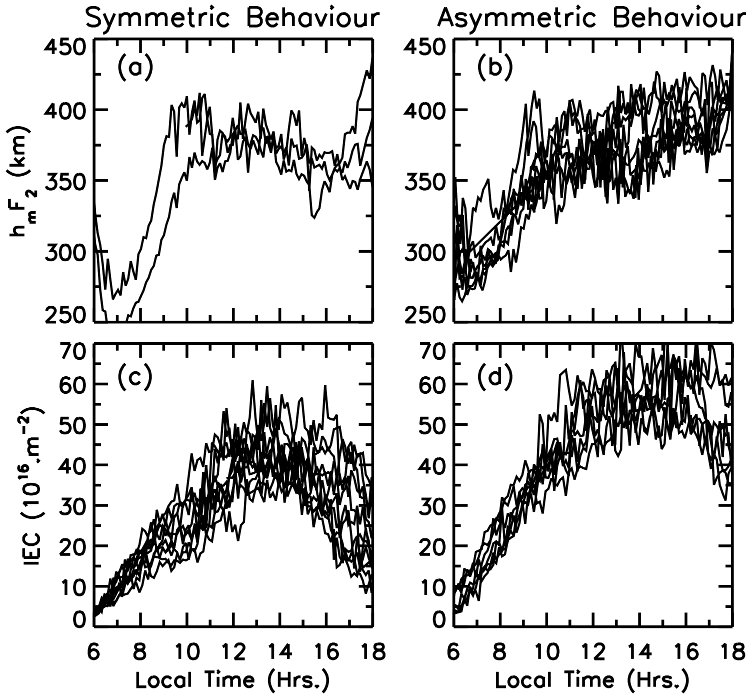

Figure 3.6: Variation of peak height of F$_2$ layer (i.e. h_mF_2) over Trivandrum (equatorial station) and ionospheric electron content (IEC) over Ahmedabad (station typically under the northern crest of the EIA) on the days with (a,c) symmetric, and (b,d) asymmetric diurnal dayglow emission intensity behavior, respectively, are depicted.

To further confirm the role of electrodynamic influence on the dayglow emission intensities, we have investigated the ionospheric behavior at two different locations, Trivandrum (magnetic equatorial location) and Ahmedabad (typically the northern crest location of the EIA). These independent ionospheric measurements were segregated into two categories: those corresponding to the days when the dayglow emission intensities at all the three wavelengths showed symmetric diurnal behavior (AT $\leq$ 0.4 h), and those that showed asymmetric diurnal behavior (AT $>$ 0.4 h). Figures 3.6a and b show the variation in the peak F region height (h_mF_2) over Trivandrum on the days with symmetric and asymmetric diurnal behavior of the dayglow emission intensities, respectively. Ionosonde data corresponding to the days with symmetric diurnal behavior in optical emission intensities are not available from Trivandrum during December 2013. The variations of F region electric field over the equator will alter the height of the F layer due to $(\vec{E} \times \vec{B})$ drifts. Hence, the variation in the values of h_mF_2 is considered to be the representative of the F region electric field over the dip equator which is largely modulated by zonal winds. It can be seen in Figure 3.6a that the peak h_mF_2 decreases in afternoon on the days with symmetric diurnal behavior. However, on the days with asymmetric diurnal behavior (Figure 3.6b), h_mF_2 shows an increasing trend, indicating that the equatorial electrodynamics are active in afternoon. Figures 3.6c and 3.6d show the ionospheric electron content (IEC) obtained from the digisonde measurements over Ahmedabad on these days. As the $(\vec{E} \times \vec{B})$ drifts of plasma over the equatorial region increases the ionospheric electron content (IEC) over the crest of the EIA, increases the IEC over Ahmedabad will be seen concurrently. It is very clear from these figures that the IEC over Ahmedabad peaked around 14:00 LT on the days with symmetric diurnal behavior, whereas, on the days with asymmetric diurnal behavior the electron density keeps increasing and its peak occurs later than 15:00 LT. It also indicates that the electrodynamics had been active in the late afternoon on the days with asymmetric diurnal behavior observed in the dayglow emission intensities. Further, the IEC values are of greater magnitudes on the days with asymmetric diurnal behavior (Figure 3.6d) as compared to the days with symmetric diurnal behavior (Figure 3.6c). It is striking to note that the optical dayglow measurements obtained over Hyderabad (a location between Trivandrum and Ahmedabad, Figure 3.1), show the peak emission intensities at around 13:00 LT on the days with asymmetric diurnal behavior in comparison to 15:00 LT in IEC over Ahmedabad, which can be attributed to the movement of the crest of the EIA. These independent measurements add credence to our interpretation that the temporal behavior seen in the optical neutral dayglow emission intensities are governed by the electrodynamic forces that originate at the geomagnetic equator, thus, strongly implying a like temporal behavior in the neutral winds.

The nightglow emission intensities vary purely as a function of the densities of the reactants, and their behavior does not show any set pattern, whereas, the dayglow show a broad solar zenith angle dependent variation primarily due to the solar control of several of the production mechanisms. The emission intensities at all times do respond to the geomagnetic storm time induced electric field variations or the neutrals that are brought in from higher-latitudes. All of these vary from one storm to another and do not show any specific type of diurnal/nocturnal pattern. However, it is quite interesting to note the clear changes that are brought-in in the diurnal variation of the neutral dayglow emission intensities.

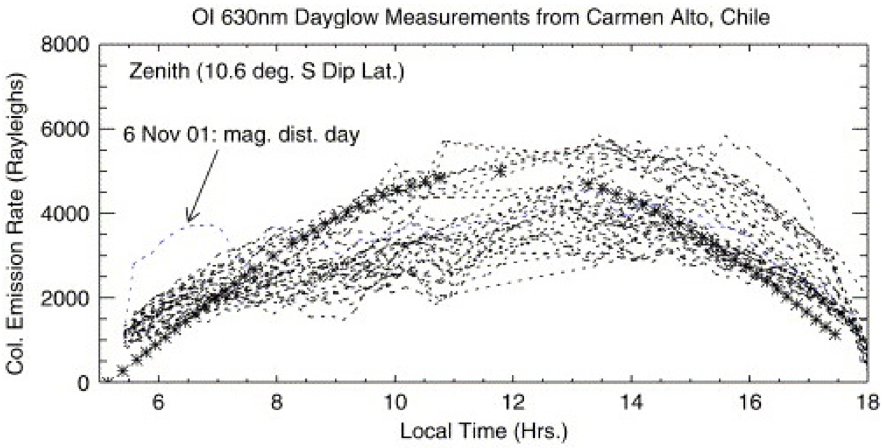

Figure 3.7: Zenith measurements of the OI 630.0 nm dayglow emission intensities from Carmen Alto (10.6^{0}S Mag. Lat.), Chile for 30 days during November-December 2001 are shown. The thick plot shows the variation of cosine of the solar zenith angle (on November 29) scaled to 5000 R for comparison. Notice the afternoon peaks in the zenith emission intensities. These deviations in the times of the peaks towards afternoon are due to the electrodynamical effects, which differ day-to-day. This feature shows a clear evidence of the ionosphere-thermosphere coupling in equatorial- and low-latitudes. Reproduced from Figure No 2 of *Pallamraju and Chakrabarti* [2006].

To see if such symmetric and asymmetric diurnal behavior in the dayglow emission intensities have been seen in earlier studies, we have investigated all the existing data sets in the literature to assimilate this information. For OI 630.0 nm dayglow emission, the data obtained during 2001 from a low-latitude location, Carmen Alto, in Chile, [*Pallamraju and Chakrabarti*, 2006] showed such asymmetric diurnal behavior (Figure 3.7) as seen in the present study. However, later

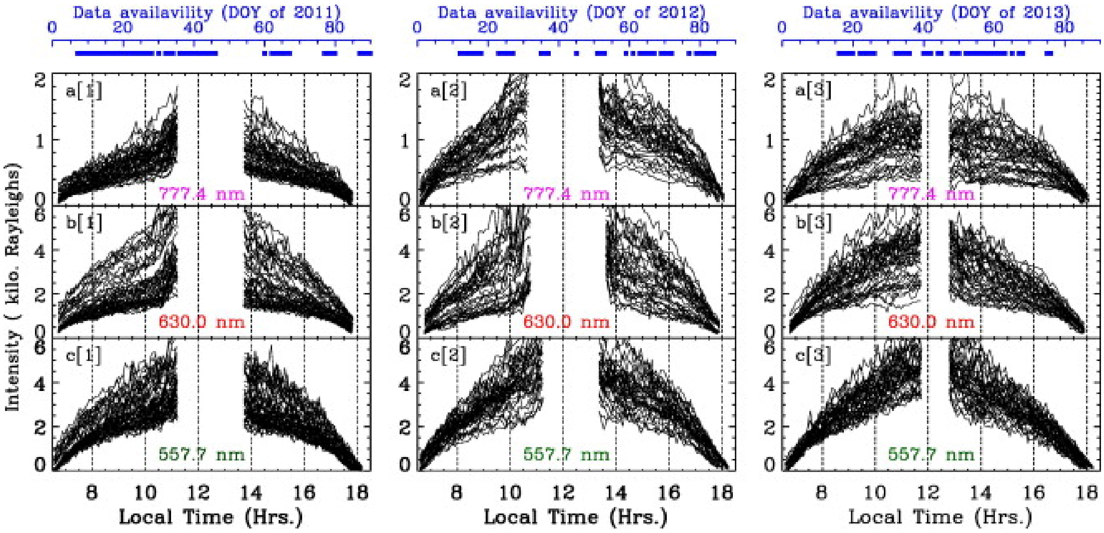

Figure 3.8: The diurnal variations of the dayglow emission intensities for the three years 2011-2013 (left to right) and for the three wavelengths (top to bottom) are shown. The additional axes at the top represent the day of the year (DOY) on which dayglow data are available. It can be noted that the diurnal behavior of the dayglow emission intensities in all the three wavelengths are symmetric, broad solar zenith angle dependence in these years unlike the ones reported in the present data from the year 2014, wherein deviations from the solar zenith angle dependence seem to exist (Figures 3.3d,e,f). Reproduced from Figure No 1 of *Laskar et al.* [2015].

in low solar activity epoch, such an asymmetric diurnal pattern in the dayglow emission intensities was not noted. In Figure 3.8 the Figure No 1 from *Laskar et al.* [2015] is reproduced, wherein the data that were obtained from Hyderabad, India over the years of 2011-2013 are shown. The diurnal behavior in the emission intensities in all these years showed a broadly symmetric pattern as seen in Figures 3.3a, b, and c of the present study. The optical data obtained from that epoch did not show any asymmetric diurnal behavior in the emission intensities. Since the slit of MISE was oriented in the meridional direction, the data around noon were not obtainable, as the images obtained by MISE got saturated due to the presence of the sun overhead. Even though the zenith data do not exist to see when the peak emission intensity has occurred, we can say that these data showed symmetric behavior by looking at the diurnal emission intensity pattern. It was noted earlier that on the days with symmetric diurnal behavior, the slopes of rise/fall during before/after noon showed similarity. If one looks at the plots in Figure 3.8, they seem to be closely matching with the behavior as seen in the left column of Figure 3.3.

It is important to note that for the days of optical data that exist in the years 2001, 2011, 2012, 2013, and 2014, the average sunspots numbers were 160, 35, 52, 53, and 144, respectively. Therefore, not only asymmetric diurnal behavior exists (along with symmetric diurnal behavior) in the past data but also there seem to be a solar activity dependence in the observed AT values in optical dayglow emission intensities.

In order to characterize the solar activity effect, we have looked at the OI 630.0 nm optical dayglow emission intensity pattern as presented in the literature at different times obtained from different locations. The 630.0 nm dayglow emission intensity is chosen due to the availability of large set of observations at this wavelength of emission (for over 25 years, although not continuous) in the published literature. Figures 3.9 and 3.10 show sample diurnal behaviors of the 630.0 nm dayglow emission intensities obtained from published literatures.

The images were digitized to obtain the dayglow emission intensities and the corresponding AT values were calculated for each day, and their mean values in different years are shown in Figure 3.11. The X-axis shows the year and the Y-axis (on the left) shows the mean AT values (red dots) (the relevant literature which have been considered for these data are shown in the figure). It can be noted that the mean values of AT vary from one year to the other. Observations by *Laskar et al.* [2015] during 2011-2013 show a symmetric diurnal behavior at all the three emission wavelengths and in the absence of any possibility to calculate the AT values for these days (as the emission peak occurs around noon, however, as the solar glare enters directly over the slit of the spectrograph, no data were obtainable), the values of AT are approximated to zero during these years. It should be mentioned here that in the present experimental setup the slit of MISE is oriented in the zonal direction (for the study of longitudinal variations of the thermospheric behavior) due to which the direct entry of the solar glare during noon is avoided, enabling us to obtain continuous dayglow data through the day without any gap.

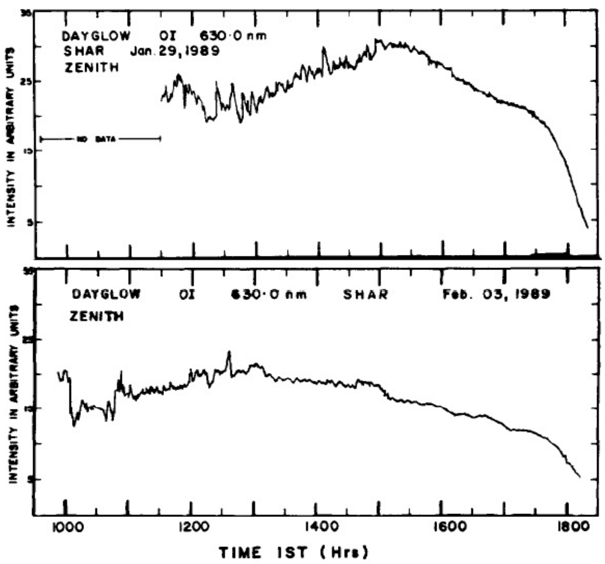

(a)

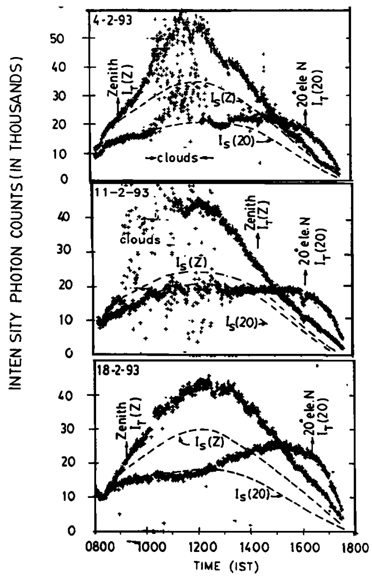

(b)

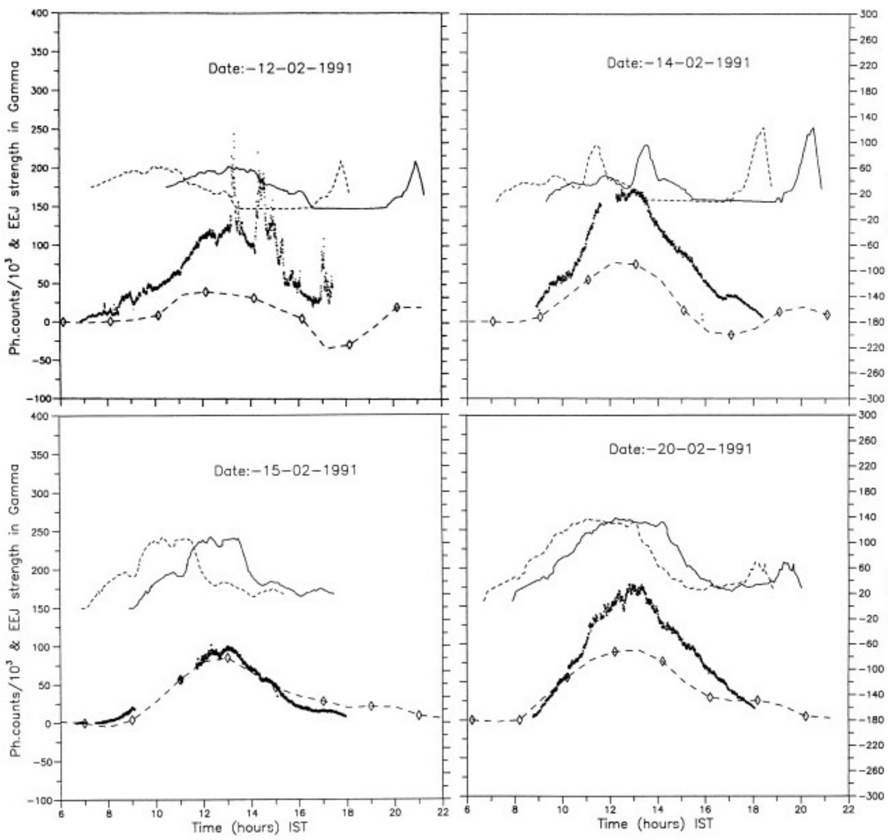

(c)

Figure 3.9: Sample figures obtained from (a) *Sridharan et al.* [1991b] (b) *Sridharan et al.* [1994] and (c) *Sridharan et al.* [1999] show the diurnal behavior of the 630.0 nm dayglow emission intensity of which the AT values are based/calculated.

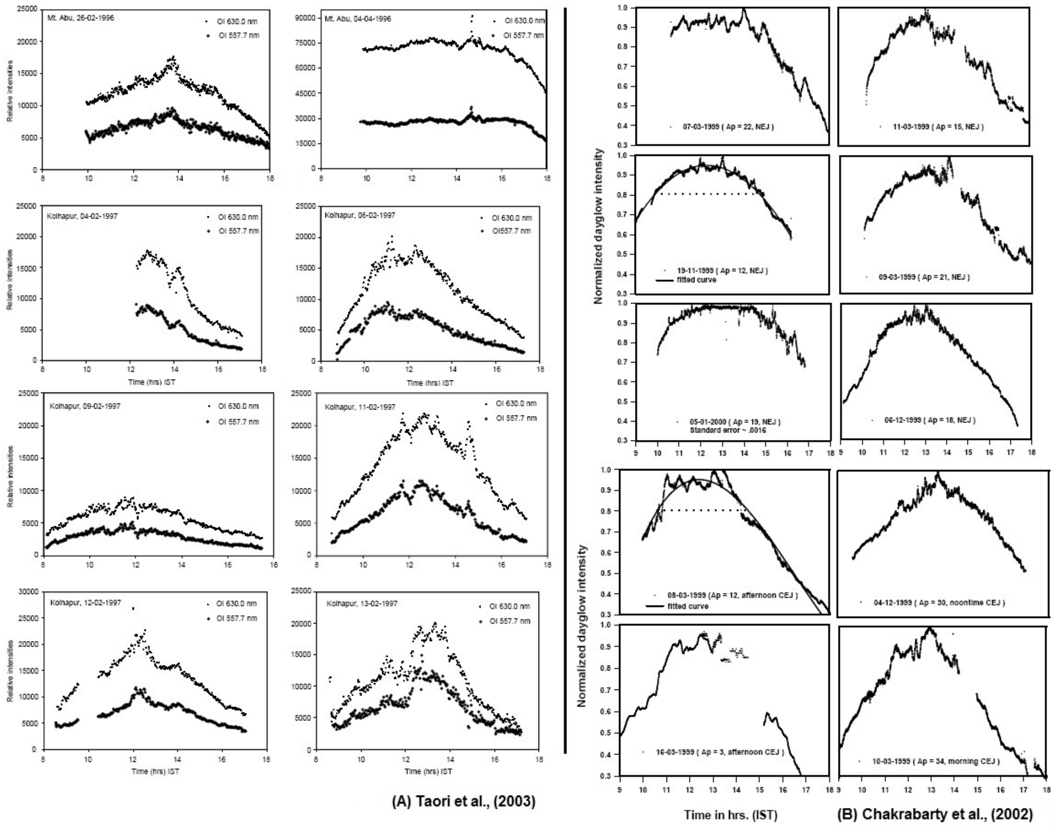

(a)

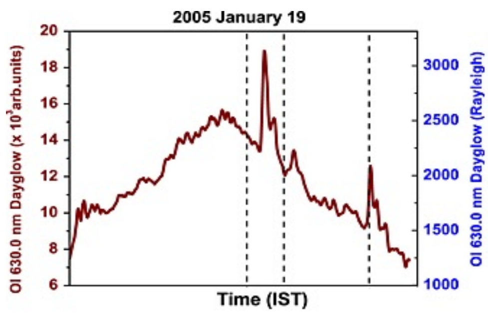

(b)

Figure 3.10: Sample figures obtained from (a) *Taori et al.* [2003] and *Chakrabarty et al.* [2002] and (b) *Sumod et al.* [2014] show the diurnal behavior of the 630.0 nm dayglow emission intensity of which the AT values are based/calculated.

Also, some of the earlier results published in the literature that are used in this study to estimate the AT values plotted in Figure 3.11, had a smaller FOV, of $\sim 4^0$ [*Sridharan et al.*, 1999] because of which direct entry of the solar glare was not an issue. The mean AT values calculated from the present observations at all the three emission wavelengths are shown in different colors. We have also

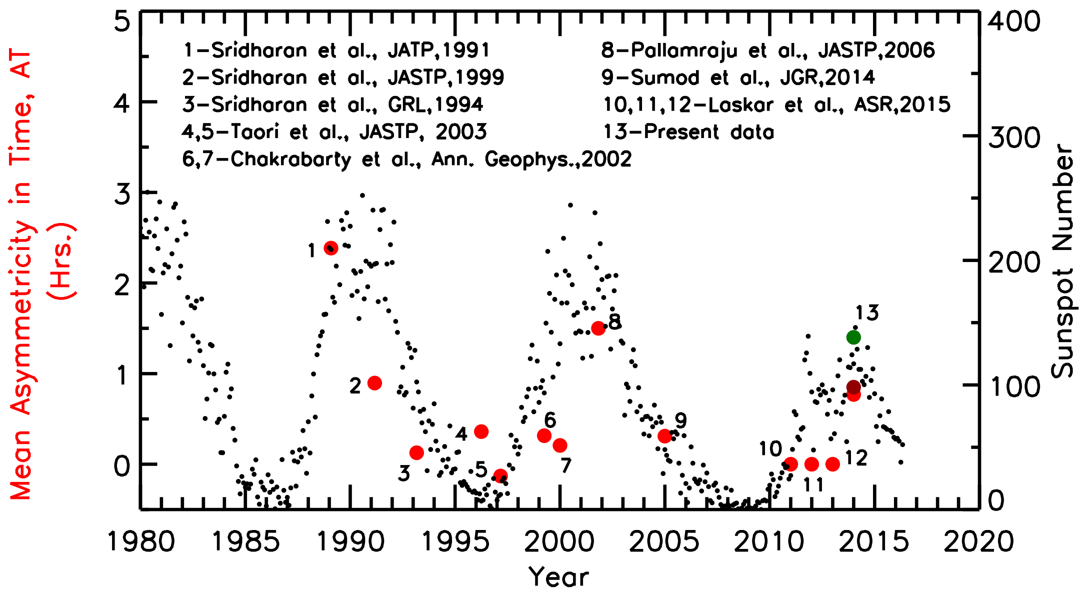

Figure 3.11: Variation of the mean asymmetricity in time (AT) at OI 630.0 nm dayglow emission intensities in different years as obtained from the published literature is shown. The monthly averaged sunspot number is also plotted. A striking similarity between them indicates the influence of solar activity on the dayglow emission processes over the low-latitudes through changes in the ionospheric electric field over the dip equator.

plotted the monthly average sunspot numbers (dark dots) on the Y-axis (on the right side) of Figure 3.11. The sunspot number data are obtained from the daily solar data set maintained by NOAA (ftp://ftp.swpc.noaa.gov/pub/indices). It is striking to note that the variations of AT values go almost hand-in-hand with those in sunspot numbers. This clearly shows that the asymmetricity in time observed in the optical neutral dayglow emission intensities has a solar activity dependence. The extreme ultraviolet (EUV) and X-ray radiation which is mainly responsible for the ionization in the thermosphere vary with the solar activity (discussed in section 1.3). Hence, for the same value of electric fields, more plasma is transported to the off-equatorial thermosphere in the high solar activity period than the low solar activity period. Thereby, the dayglow emission intensities can increase in the high solar activity period. At this point, the similar variations between the sunspot number and the AT values clearly indicate the dominance of the equatorial electrodynamics over the neutral dynamics on the optical dayglow emission intensities.

It thus shows the dominance of electrodynamic processes over the photochemical processes in bringing about the temporal variations in the neutral dayglow emissions and is also a good example of E and F region coupling in the equatorial- and low-latitude ionosphere-thermosphere system. A consequence of this effect is shown in Figure 3.6, where a movement of F region height in afternoon to higher altitudes on some days over Trivandrum (equatorial station) (Figure 3.6b) and a corresponding increase in the IEC over Ahmedabad (station near the northern crest of the EIA) is seen (Figure 3.6d). Depending on the strength of the equatorial electrodynamics, its effect on the off-equatorial thermospheric dayglow emissions will have a latitudinal variation. Thus, on a given day, the AT values will be different for observations at different latitudes. Hence, the characterization of AT value as has been done in the present work (AT $\leq$ 0.4 h and AT $>$ 0.4 h for days with symmetric and asymmetric diurnal behavior of the dayglow emission intensities), is valid for observations at this latitude. Similar type of dayglow observations from different latitudes are required to investigate the latitudinal variation of the effect of equatorial electrodynamics more comprehensively. However, the strength of this coupled phenomenon varies with respect to the local time, season, and solar activity. In the low-solar activity period (2011-2013), the electric field strengths are smaller [*Fejer and Scherliess*, 1995] and apparently not sufficient to move the ionization to regions far away from the magnetic equator. Hence, the dayglow emission intensities measured from Hyderabad (8.9^0 N Mag. Lat) showed a symmetric diurnal behavior in their respective emission intensities. This can also be seen in the present study wherein the negative AT values on some days correlate with smaller integrated electrojet strengths (Figures 3.5b and c) and hence, weaker electrodynamics (Figures 3.6a and c). Further, the results from mid-latitudes, Boston (48.3^0 N Mag. Lat), where equatorial electrodynamical effects do not exist, do show symmetric type of behavior in OI 630.0 nm diurnal emission intensities [*Pallamraju and Chakrabarti*, 2006] as seen in the study with weaker electrodynamics during 2011-13. These issues add credence to the inference on the influence of electrodynamical effect on the neutral dayglow emission intensities.

To appreciate this issue further, attention is drawn to another study wherein the dayglow OI 630.0 nm emissions were measured from the magnetic equatorial station, Thumba, in India. It was seen that the shape of the diurnal pattern of the 630.0 nm dayglow was similar to that of the EEJ with a time shift as can be seen in Figure 3.9c [*Sridharan et al.*, 1999]. This time gap had been interpreted to be the time taken for the plasma to move from the E to F region under the influence of $(\vec{E} \times \vec{B})$ drifts. The fact that it was indeed so was also confirmed by simultaneously operating the VHF Doppler radar, wherein the time taken for the ionospheric layer movement due to the $(\vec{E} \times \vec{B})$ drifts obtained by the measured eastward electric fields were consistent with the observed time shifts between the EEJ and 630.0 nm dayglow variation. This result indicated the imprint of electrodynamical effect on the 630.0 nm dayglow emission intensities, both of which were obtained from the same location. Observations from an EIA crest region, Mt. Abu, (Geographic 24.6^0 N, 72.8^0 E) in India, during high solar activity showed different diurnal behavior (Figure 3.10a) in the OI 630.0 nm emission intensities on the equatorial electrojet and counter electrojet days [*Chakrabarty et al.*, 2002].

All these results corroborate our conclusion that the asymmetric diurnal behavior of the optical dayglow emission intensities (at OI 630.0 nm) seen in the low-latitudes are mainly due to the equatorial electrodynamic variations. However, the effect of the neutral winds on the dayglow emission intensities can not be ruled out completely. Ultimately, a comprehensive model is needed to fully understand the complex coupled behavior of the thermosphere and ionosphere and the underlying processes at the equatorial- and off-equatorial low-latitude regions. It should be remembered that the peak dayglow emission intensities at any of the wavelengths are correlated not with the EEJ strengths, but with the asymmetricity in time, indicating that not the total emission intensities, but their temporal variability is governed by the EEJ strength. Day to day variation in AT values can be compared with the electric field models and an empirical relation between the AT and electric field can be obtained. Such an exercise is being planned for the future.

3.4 Conclusion

In this study oxygen dayglow measurements at three emission wavelengths were obtained during 2013-2014. It is shown that the diurnal behavior of the dayglow emission intensities not only at the OI 630.0 nm emission but also those at OI 777.4 nm and OI 557.7 nm emissions were both symmetric and asymmetric with respect to local noon. While the symmetric diurnal behavior can be understood in terms of the solar zenith angle variation of the production mechanisms, the cause of asymmetric behavior in the diurnal emission intensities is not apparent. Against this background, its possible causes have been investigated in terms of the effect of neutral winds and the equatorial electrodynamics. Using the EEJ strength data and ionospheric parameters on all these days, it has been conclusively shown that the equatorial electrodynamics that is operative on a given day gives rise to the observed asymmetric diurnal behavior in the neutral oxygen dayglow emission variability. This aspect has been discussed in larger context. It has been noted that during the low solar activity period the diurnal variability in the oxygen dayglow emission intensities were predominantly symmetric with respect to local noon, while they were asymmetric during the high solar activity period. This again gives a broader picture to the ionosphere-thermosphere systemic behavior as the neutral dayglow emission intensities are sensitive to the electrodynamical changes that happen over a solar cycle.

These findings have great potential and implication in terms of understanding the thermospheric wave dynamics and the spatio-temporal variations associated with them both during geomagnetically quiet and disturbed times. The results from these aspects are presented in the subsequent chapters.

Chapter 4

Longitudinal Variations in Daytime Thermospheric Wave Dynamics Over Low-Latitudes

4.1 Introduction

The Earth's upper atmosphere consists of both neutrals as well as plasma, and hence, it is affected by both the neutral and electrodynamic processes. Many interesting coupled processes occur over the equatorial- and low-latitudes, which are explained in detail in section 1.4. These coupled processes vary along the meridional directions and hence, bring in changes in both the neutral and plasma densities across the latitudes. The details on the formation mechanism of these phenomena and their effects in bringing about changes across latitudes is now well understood [e.g., *Moffett*, 1979; *Raghavarao et al.*, 1978, 1991, 1993]. The strength of the EEJ has been shown to be directly proportional to the strength of the EIA [*Raghavarao et al.*, 1978] and therefore, it plays an important role in bringing about changes in the meridional variations in the development of equatorial upper atmospheric processes. Moreover, during geomagnetic disturbances due to the precipitation of highly energetic particles and the enhancement of auroral electrojet current, joule heating occurs over polar regions which sets in higher speed winds and larger amplitude atmospheric waves. These winds and waves move away from the high-latitudes and the large scale motion in neutrals and plasmas are set up, which are referred to as the TADs and TIDs, respectively. The formation of the TADs and TIDs along with their effect on the mid- and low-latitudes have been discussed in detail in section 1.5. The TADs and TIDs alter the densities of the upper atmospheric constituents bringing about latitudinal variations from high- to low-latitudes [e.g., *Richmond and Matsushita*, 1975; *Hajkowicz*, 1991; *Hocke*, 1996; *Pallamraju et al.*, 2004b]. Due to the above mentioned mechanisms, variations in the neutrals and the electrodynamic processes over equatorial- and low-latitudes can be brought in along the meridional direction.

In addition to the meridional variations, these neutral and electrodynamic processes also show zonal variations. Many studies have been carried out on the zonal variations of the ionosphere and thermosphere at different longitude sectors. Variation in the geomagnetic field strength at different longitudinal sectors can bring about changes in the strengths of the dynamo action and thereby cause the longitudinal variations in the equatorial electrodynamics. As can be seen from Figure 4.1, the magnetic field strengths over the Indian, African, and American longitudes are different. For example, the magnetic field strength at the dip

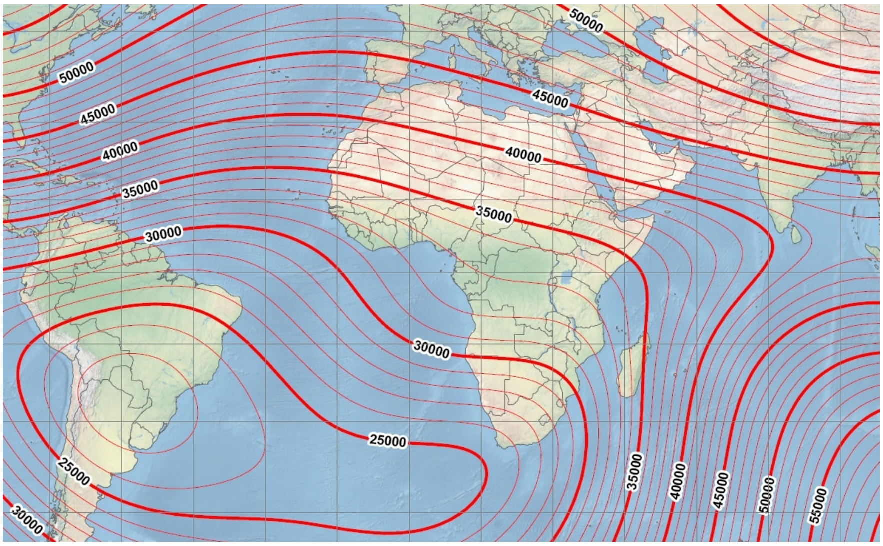

Figure 4.1: Magnetic field intensity (F) map obtained from world magnetic model for the year 2015. Map developed by NOAA/NGDC and CIRES.

equator over the Indian sector is ~40000 nT and is greater than that over the

American sector, which is ~25000 nT. Therefore, the vertical drifts (V_d), of the equatorial plasma over the Indian sector are smaller than those over the American sector for same value of $\vec{E}$ at both the sectors [*Kelley*, 2009] (as V_d=$(\vec{E} \times \vec{B})/|\mathrm{B}|^2$; where $\vec{E}$ is the zonal electric field and $\vec{B}$ is the geomagnetic field intensity). This difference in the vertical drifts has the potential to contribute to the differences in the extents of the EIA crests at these two longitude sectors [*Raghavarao et al.*, 1988].

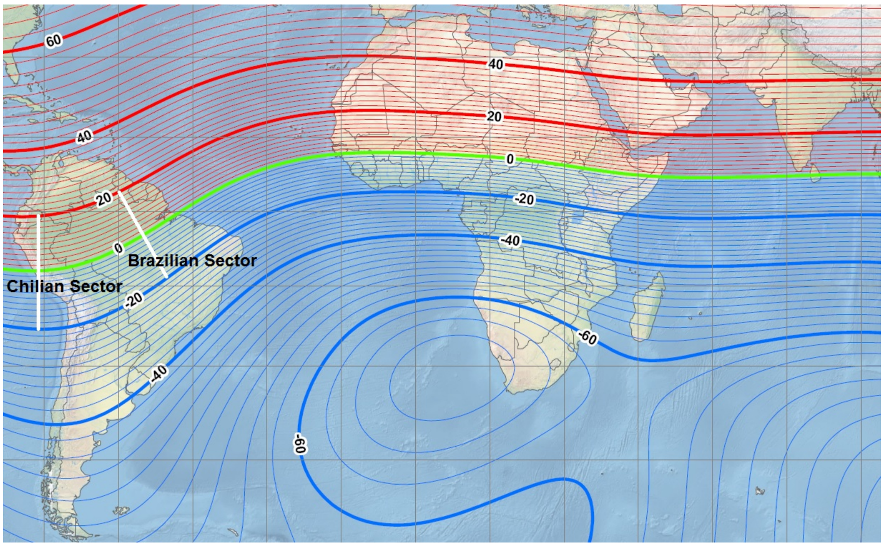

Figure 4.2: Magnetic main field inclination (I) map obtained from world magnetic model for the year 2015. Map develpoed by NOAA/NGDC and CIRES.

The changes in the magnetic declination angle with respect to the longitudes also contribute to the longitudinal variability in the equatorial electrodynamic processes, which is most prominent over the Brazilian sector (South Atlantic anomaly region) in comparison to that over the Chilian longitudes. As the Earth's axis of rotation is tilted with respect to the solar ecliptic plane, the relative angle between the magnetic declination and the solar terminator keeps on changing at a given location in a year. The preferential occurrence of the plasma irregularities across the longitudes was shown to be matching with the durations when the solar terminator was aligned with the north-south plane of the magnetic field lines [e.g., *Abdu et al.*, 1981; *Tsunoda*, 1985]. This is because, this configuration enables simultaneous sunset in both the hemispheres, thereby preventing the shorting of the F region electric currents by the highly conducting E region. It can clearly be seen from Figure 4.2 that the locations of the geomagnetic conjugate positions on either side of the geomagnetic equator are aligned differently with respect to the geographic longitude over Brazilian sector. This prevents the simultaneous sunset at the conjugate locations at one longitude but not at the other and hence, brings the longitudinal differences in the electrodynamic behavior.

In the recent past, analysis of the far ultraviolet (FUV) emissions (OI 135.6 nm) obtained on-board the IMAGE satellite showed the existence of a significant longitudinal structure in the emission intensities [e.g., *England et al.*, 2006; *Immel et al.*, 2006; *Sagawa et al.*, 2005]. The ionospheric densities as inferred in the nightglow emissions were found to be peaking at four fixed longitudes (shown in

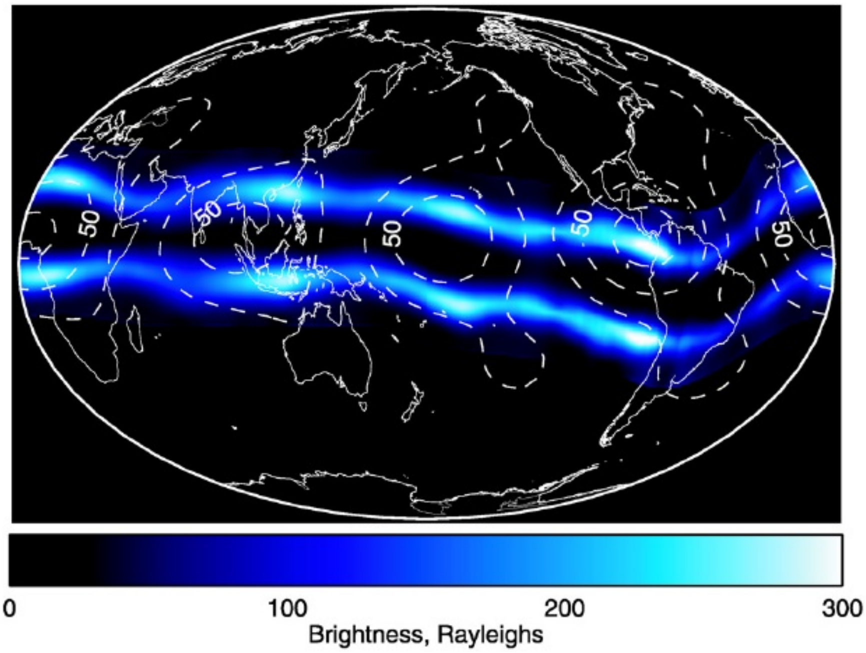

Figure 4.3: Reconstruction of the nightglow emissions from 30 days (2002 March 20 to April 20) of observations with the IMAGE-FUV imager. The average location and brightness of the equatorial ionospheric anomaly stand out in this representation. Due to the poor sampling of the emissions from the southern anomaly, it is represented here with a mirror image of the northern anomaly across the magnetic equator. This image is the representative of the local ionospheric behavior at 20:00 LT. Overlaid on this figure with white dashed contours are the amplitude of the diurnal temperature variation at 115 km due to the upward-propagating lower atmospheric tides, as reported by the GSWM. Reproduced from Figure 3 of *Immel et al.* [2006].

Figure 4.3) around the globe, viz. South America, West Africa, South-East Asia, and the Central Pacific Ocean. The contours in Figure 4.3 show the equinoctial amplitude of the diurnal temperature variations at 115 km altitude which was determined by the Global Scale Wave Model (GSWM) [*Hagan et al.*, 2001]. The peaks in the temperature represent the locations on the Earth where the major components of the diurnal tide combine most effectively to alter the winds and temperatures at the given altitudes. It is striking to note the matching between the locations of the peak temperature and that of the enhanced EIA crests. Such enhancement of the EIA crests at these four longitudes were attributed to be due to the modulation of E region electric field due to the diurnal non-migrating tides. The non-migrating tides are generated by the latent heat release from the lower atmosphere due to the prevalent convective processes [*Immel et al.*, 2006]. In an earlier work carried out using ISIS-2 satellite measurements of electron densities at two different longitudes (51^0 E and 80^0 E) separated by 30^0, the EIA strengths were reported to be behaving differently from one another [*Sharma and Raghavarao*, 1989]. Now we know that, the two longitudes happen to be in different regions of tidal forcing and the tidal peaks in zonal winds in the E region are near the regions of strong convection in the troposphere is a coincidence [*Immel et al.*, 2006]. Using GPS Aided Geo Augmented Navigation (GAGAN) network derived measurements differences in the values of TEC over Indian longitudes (70^0 E to 95^0 E) were reported which seem consistent with the global wave number 4 structure [*Sunda and Vyas*, 2013]. More recently, from the magnetic measurements at two different Indian longitude regions (separated by 15^0) the existence of the longitudinal variations in the equatorial electric fields and the current densities were reported [*Phani Chandrasekhar et al.*, 2014].

To summarize, all the measurements/results reported in the literature over the years show that the zonal differences are localized over fixed longitudinal sectors. These could be due to (i) the differing conditions in the geomagnetic anomalies, (ii) the geomagnetic field line geometry, or (iii) the tides that are setup in response to the forcing from the tropospheric convective zones. The longitudinal differences in the dynamical process thus obtained using satellite observations, ground-based measurements, and through simulations give information on the existence of variability in the electrodynamic processes over longitudinal separations greater than 1000 km. However, it is not known if any longitudinal difference exists over distances that are shorter than 1000 km. If they do, then what are the mechanisms responsible for such small-spatial scale changes in the zonal direction? To the best of our knowledge longitudinal differences of the daytime electrodynamic processes within separations smaller than 10^0 has not been reported in the literature. In other sectors where such drastic differences in the geomagnetic conditions as in South Atlantic anomaly region does not exist, the minimum separation in longitudinal differences has been of the order of 15^0 [*Phani Chandrasekhar et al.*, 2014].

Satellites with high inclination orbit can yield information on the small-scale meridional variations, but are not well-suited for the studies of the temporal variations of any phenomenon over a given longitudinal region which may possibly have zonal structures. Measurements from ground-based instruments in close separation (e.g. 1^0 latitude x 1^0 longitude) could be useful to study such small-scale zonal differences. However, in the absence of such instruments in grids of such fine spacing, optical measurements with high spatial resolution are best suited for such studies. It is known that the density fluctuations due to the winds and waves alter the reactants that produce nightglow/dayglow emissions and thus, contribute to the modulations in their intensities [*Teitelbaum et al.*, 1981; *Shepherd et al.*, 1993b; *Pallamraju et al.*, 2010]. Hence, optical emission intensity variations can be used as tracers of the dynamic processes that occur at their respective altitude of emissions.

In Chapter-3, we have discussed that the equatorial electrodynamics predominantly affect the thermospheric behavior over off-equatorial and low-latitude regions during geomagnetically quiet times. The diurnal behavior of the dayglow intensities at all the three emission wavelengths were observed to be asymmetric when the equatorial electrodynamics were stronger. This was studied by taking the zenith measurements of the dayglow emission intensities and this finding was supported by independent ionospheric measurements. Also, it was shown that the inter coupling between the equatorial electrodynamics and the off-equatorial thermospheric behavior showed a solar activity dependence. Over the Indian longitudes where the magnetic field lines over low-latitudes (where magnetic declination angle is close to zero) are nearly parallel to the geographic longitudes, similar type of behavior in the coupling processes over a range of longitudes are expected. In order to investigate whether the longitudinal behavior of the electrodynamic processes in this region is similar or different, we have made use of the optical dayglow emission intensities originating from the upper atmosphere over a large spatial extent along the zonal direction. Such investigations will also give us information about the intricacies of the longitudinal behavior in the equatorial electrodynamics.

4.2 Data Used

As described in the previous section, to carry out the present investigation we require optical dayglow emission intensity measurements over a large spatial extent along the zonal direction. We have obtained the dayglow emission intensities using MISE. The details about these three dayglow emission intensities (OI 557.7,

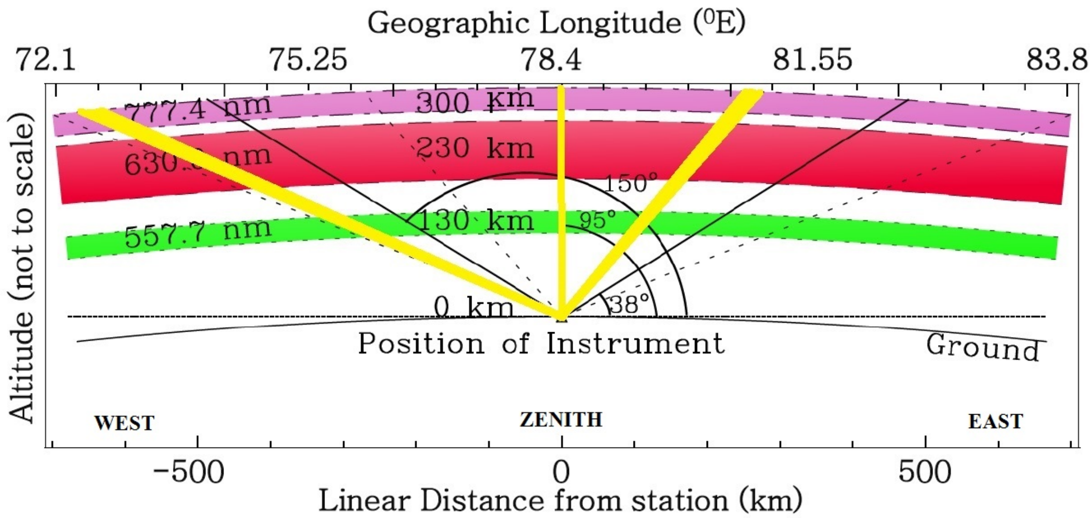

Figure 4.4: Schematic of viewing direction of MISE. The yellow lines show the three independent regions (not to scale) in west, zenith, and east from where the dayglow emission intensity data are obtained for the periodogram analysis.

630.0, and 777.4 nm), MISE and the method of extraction of dayglow emission intensities have been explained in sections 2.2 and 2.3. Dayglow emission intensity data obtained during December 2013 to March 2014 are used in the present investigation. During this period the slit of MISE was oriented along the zonal direction.

Figure 4.4 shows the schematic of the viewing direction of MISE along the zonal direction. The yellow lines correspond to the viewing directions of MISE along the west, zenith, and east directions. Due to technical constraints the spatial coverage of MISE along the east direction is smaller than the west direction. The dayglow emission intensities along the FOV are obtained simultaneously. The spectra from different spatial segments of an image are independently analyzed to obtain the dayglow emission intensities along the zonal direction.

4.3 Results

As mentioned above, the slit of MISE was oriented along the zonal (East-West) direction for the present investigation. Due to the imaging property of MISE, information on the spatial variations (across longitudes) in the dayglow emission intensities are obtained simultaneously. Diurnal variation in the three dayglow emission intensities are obtained along three independent segments towards the west, zenith, and east directions (shown in yellow lines in Figure 4.4) for each image as a function of time. As the altitudes of origin of the three optical emissions are different, the zonal distances to which the emission intensity data correspond are also different.

Behavior of the dayglow emission intensities at all the three wavelengths are linear superposition of the waves of different periodicities, such as GWs, tidal oscillations, diurnal, and semidiurnal modulations, which have been explained in section 1.3. In the present work, our focus is on the fluctuations in the GW regime. Hence, periodogram analyses (explained in section 2.5.5) have been carried out to obtain the GW time periods from the dayglow emission intensity variations along the three directions (west, zenith, and east) as shown in Figure 4.4 in all the three emission wavelengths. GWs in all the three directions whose values of time periods are similar are assessed with respect to the time period(s) obtained over the zenith within a range of ±0.25 h (which is equal to the maximum Brunt Väisälä period amongst the altitudes considered in the present study). Existence of a common time period in the emission intensity variability at all these three well-separated spatial regions cause to consider the same source driving the wave features in all these directions. Hence, it is inferred that on such days no longitudinal differences exist in the neutral wave dynamics over the given spatial extent. On the other hand, absence of waves whose values of time period(s) are similar in the emission intensity variations at all the three directions indicates that the sources of the waves prevalent in these three directions are different and hence, there exist longitudinal differences in the zonal wave features within this spatial extent.

Figure 4.5 shows the result of such periodogram analyses over west, zenith, and east for four sample days, with the X- and Y-axes showing the time period and the normalized PSD. Periodograms in the upper, middle, and lower panels represent those that were obtained for 777.4, 630.0, and 557.7 nm wavelength emission intensities, respectively. This type of depiction is maintained for all the figures that follow in this chapter. Periodgrams at west, zenith, and east are shown by different line styles. The blue shaded regions correspond to the time periods with similar values in all the three directions. The vertical arrows on the top of each panel points to the values of time periods which are similar in any of the two directions. On 30 December 2013, significant time periods of 0.9 h (Figure 4.5a), 1.6 h (Figure 4.5b), and 1.2, 0.9, 0.7, and 0.5 h (Figure 4.5c) are found to be similar in all the three directions at the emission altitudes of 777.4, 630.0, and 557.7 nm wavelengths, respectively. On 20 January 2014, although no time periods with similar values were found along the three directions at the 777.4 nm emission altitude, similarity in time periods in all the three directions were found at 630.0 and 557.7 nm dayglow emission altitudes for 0.4 h (Figure 4.5e) and 0.8 h (Figure 4.5f), respectively. As described above, the existence of time periods with similar values in all the three directions at a given altitude indicates the existence

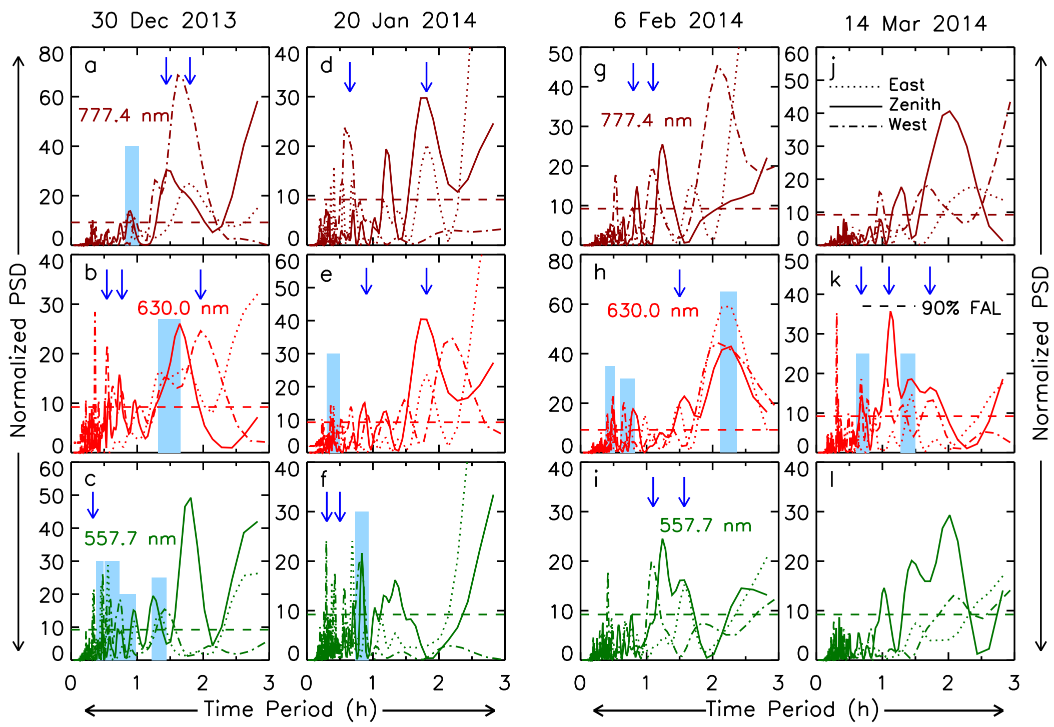

Figure 4.5: Results of the periodogram analyses carried out in the dayglow emission intensity data at all the three wavelengths obtained over west, zenith, and east directions on four sample days are shown. Periodograms in the upper (Figures 4.5a,d,g,j), middle (Figures 4.5b,e,h,k), and lower (Figures 4.5c,f,i,l) panels represent those that were obtained for 777.4, 630.0, and 557.7 nm wavelengths, respectively. The shaded portion in blue corresponds to the GW time periods with similar values in all the three directions. The blue arrows on the top indicate the values of GW time periods with similar values in any two directions. It may be noted that the similar GW periodicities at heights of all emission wavelengths and in two directions is seen more readily on the two days on the left as compared with the two on the right. The two days on the left/right correspond to symmetric/asymmetric diurnal behavior in the zenith dayglow emission intensities and are shown in Figure 4.8.

of a similar behavior in the thermosphere, and a common source driving the wave dynamics. This suggests that no significant longitudinal differences exist in the neutral wave dynamics within the longitudinal extent of 3^0-8^0 (spatial extents covered corresponding to the altitudes of the three dayglow emissions) on these two days. This, however, is not the case always. On 6 February 2014 and 14 March 2014, no time periods with similar values were found in all the three directions at the emission altitudes of 777.4 and 557.7 nm wavelengths (Figures 4.5g-l). The poor availability/non-availability of the similar time periods on these days points to a non-uniform or non-identical behavior of the sources in these three well-separated zonal locations that drive the thermospheric neutral wave mechanisms. Thus, these days indicate the existence of longitudinal differences in the neutral wave features within the spatial extent of 3^0-8^0 longitudes. An exception has been noticed for 630.0 nm dayglow emissions wherein similar time periods at 1.4 and 0.9 h were found on these two days.

Spatial extent of the sources which govern the behavior of the dayglow emission intensities over the west, zenith, and east regions may vary with time. The time periods with similar values in all the three regions is expected to occur at the same time for a large spatially extended source. Whereas, if the source has a small spatial extent and it moves from one region to other with time, then time varying occurrence of the similar time periods are expected.

In order to investigate the duration of occurrence of the time periods with similar values in the three spatially separated regions, wavelet analyses have been carried out following the method explained in section 2.5.5. Figures 4.6 and 4.7 show the results of wavelet analyses of the dayglow emission intensities as shown in Figures 4.5a,b,c for 30 December 2013 (day without longitudinal differences of the wave dynamics) and Figures 4.5g,h,i for 6 February 2014 (day with longitudinal differences of the wave dynamics), respectively.

In Figures 4.6 and 4.7 the X- and Y-axes show the local time and time periods, respectively. Normalized powers of the time periods at different local times are shown in various colors. Values of each color is shown on the bars on the right side of each panel. The white lines show the cone of influence (COI). During afternoon the dayglow emission intensity data from western directions are affected by the solar glare and are removed from the analyses, which limit the duration of dayglow emission intensity data in that direction. The left (a,d,g), middle (b,e,h), and right (c,f,i) panels show the wavelet analyses of the dayglow emission intensity data obtained from west, zenith, and east regions, respectively. The result of wavelet analysis of the dayglow emission intensity data at 777.4, 630.0,

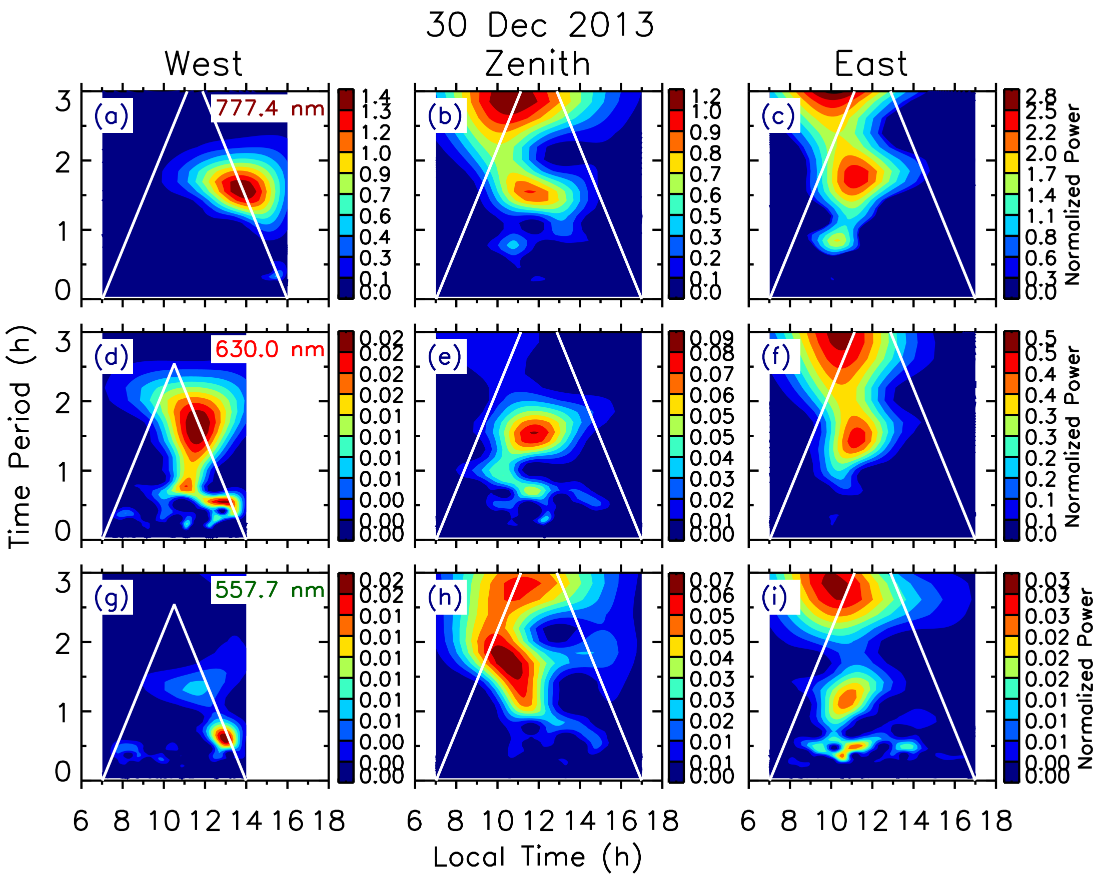

Figure 4.6: Wavelet analyses of the dayglow emission intensities at all the three wavelengths obtained along the west, zenith, and east directions on a sample day (30 December 2013) with the existence of similar time periods are shown. The duration of the occurrence of the time periods with similar values is seen to be nearly simultaneous in all the three directions.

and 557.7 nm wavelengths are shown in the top (a,b,c), middle (d,e,f) and bottom (g,h,i) panels, respectively.

From Figures 4.6d,e,f it can be seen that the similar time periods of around 1.6 h (see Figure 4.5b) occurred around 12 LT in all the three directions. This indicates that the source governing the dynamics at the emission altitude of 630.0 nm dayglow is spatially extended from the west to east direction as covered by MISE. But at the emission altitude of 557.7 nm dayglow, the time periods with similar values occurred at different local times. The 0.7 h time period occurred on the east, zenith, and west directions (Figures 4.6i,h,g) around 10, 11, and 13 LT. This points to the westward movement of the waves with time. Similar time variation of the time periods is also observed at 777.4 nm dayglow emission altitude. Both smaller 0.9 h (similar time periods) and a larger ∼1.5 h (not similar as the time periods in the three directions do not fall within ±0.25 h range) time periods are present around 10, 12 and 14 LT in east, zenith, and west regions, respectively. The time difference in the occurrence of the time periods with similar values between the zenith and west direction is more than that in between the east and zenith. This could be due to the larger/smaller distance of the sky (from where dayglow emissions are obtained) in west/east from the zenith (see Figure 4.4). Such observations on the movement of waves at different emission altitudes carried out in the time domain matches well with the movement of waves in the spatial domain (Figures 4.11a,b,c), as discussed later in this chapter.

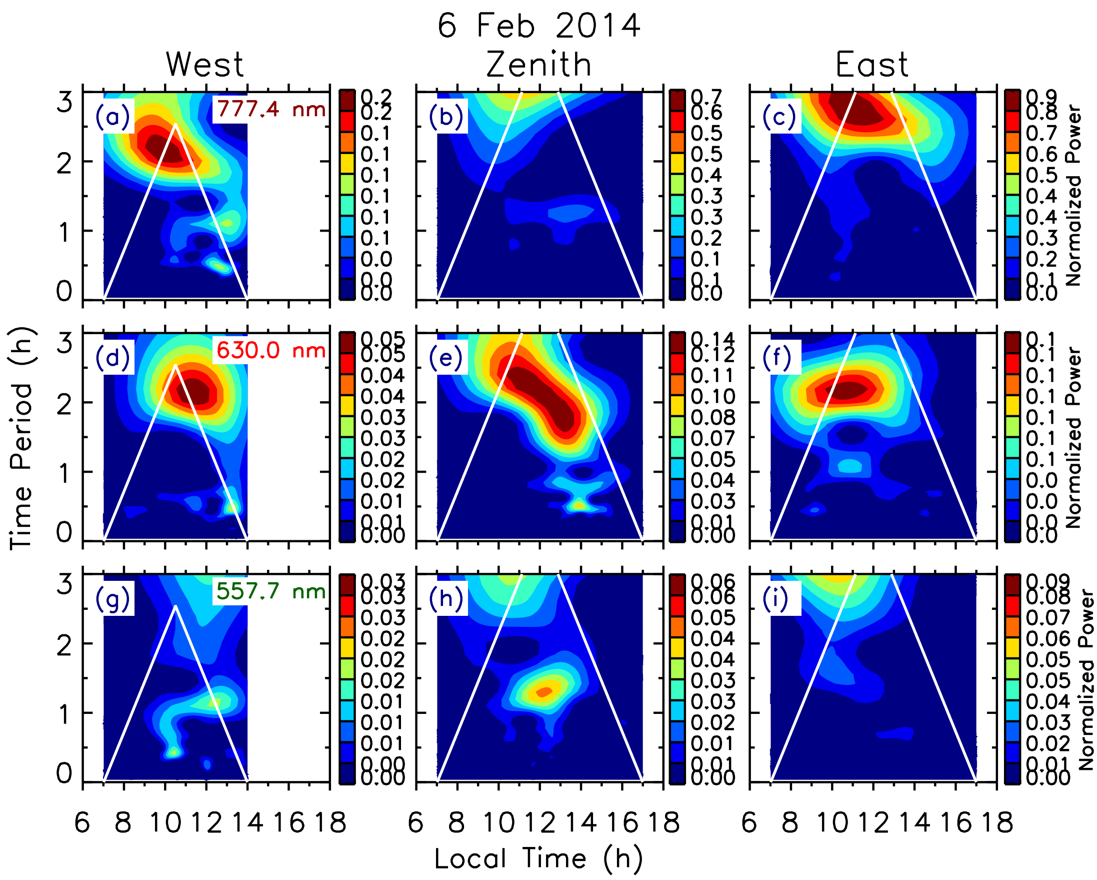

Figure 4.7: Same as in Figure 4.6 but for 6 February 2014.

Absence of the time periods with similar values at the emission altitude of 777.4 and 557.7 nm dayglow on 6 February 2014 (as shown from the periodogram analyses in Figures 4.5g,i) is clearly noted in Figures 4.7a,b,c and 4.7g,h,i, respectively. At the emission altitude of 630.0 nm dayglow, the larger similar time period i.e. 2.2 h is found to be present around 10.5, 12, and and 11 LT on the east, zenith, and west regions, respectively. Whereas the smaller time periods of 0.6 and 0.4 h occurred during 11, 14, and 13 LT on the east, zenith, and west regions, respectively.

To summarize the above discussions, it is to be noted that the duration of occurrence of the time periods with similar values do not vary much with time on the days with no longitudinal differences. This indicates to a uniform extended source on such days.

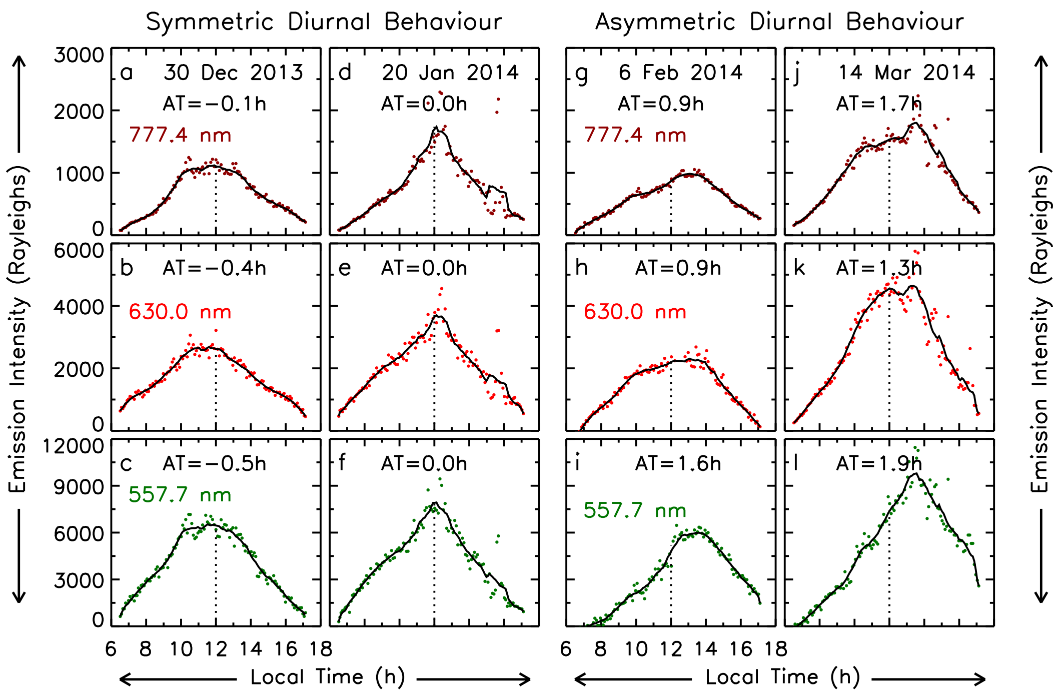

Figure 4.8: Zenith diurnal emission intensity variability along with the respective AT values for OI 777.4 nm (top row), OI 630.0 nm (middle row), and OI 557.7 nm (bottom row) are shown on the four days considered for the periodogram analyses in Figure 4.5. The dark solid line in each of the figures represents the 11-point running average of the dayglow emission intensities. A vertical dotted line is drawn at the local noon to aid the eye for appreciating the symmetric/asymmetric behavior in the diurnal dayglow emission intensities. Figures (4.8a-f)/(4.8g-l) correspond to two days on which the diurnal behavior of the dayglow emission intensities were symmetric/asymmetric in all the three emission wavelengths.

The diurnal behavior of the zenith dayglow emission intensities at all the three emission wavelengths on the four days considered for the periodogram analyses (depicted in Figure 4.5) are shown in Figure 4.8. The X-axis shows the LT in hours. The Y-axes for all these plots indicate the dayglow emission intensities in Rayleigh. An 11-point running average of the dayglow emission intensities is over plotted as a continuous line for a clear visualization of the diurnal behavior. A vertical dotted line is drawn at the local noon to aid the eye for comparing the diurnal emission intensity behavior between forenoon and afternoon. As discussed in detail in Chapter-3, the dayglow emission intensities at each of the wavelengths on the two left panels (Figures 4.8a-c and 4.8d-f) for 30 December 2013 and 20 January 2014 show symmetric diurnal behavior (with respect to local noon). Whereas, in the two panels on the right (Figures 4.8g-i and 4.8j-l) for 6 February 2014 and 14 Mar 2014, the dayglow emission intensities at all the three emission wavelengths show asymmetric diurnal behavior. The AT values for each diurnal behavior are noted in their corresponding panels in Figure 4.8. It is striking to note that waves with similar time periods (as shown in Figure 4.5) over west, zenith, and east were found to exist on the days when the diurnal behavior of the dayglow emission intensities over zenith were symmetric. On the other hand, no waves with similar time periods were found on the days when the diurnal behavior of the dayglow emission intensities were asymmetric.

As discussed in Chapter-3 the neutral optical dayglow emission intensities at low-latitudes are predominantly affected by the equatorial electrodynamics [*Karan et al.*, 2016]. This was based on systematic investigations of the EEJ strength and the diurnal variability of the three dayglow emissions. It was shown that on the day when the electrodynamic forcing is large/small (as seen in the EEJ strength), the diurnal behavior of the dayglow emission intensity is asymmetric/symmetric. Such imprint of the electric field effect in the neutral dayglow have been shown in earlier studies as well [e.g., *Sridharan et al.*, 1999; *Pallamraju et al.*, 2004b, 2010, 2014]. For the days being discussed in this study the integrated EEJ strengths (A) between 7 to 12 h (A=$\int_7^{12} EEJ.dt$) values are 149.5, 169.7, 290.3, and 190.8 nTh on 30 December 2013, 20 January 2014, 6 February 2014, and 14 March 2014, respectively. It may be noted that the values of A are larger on the days with asymmetric diurnal behavior than on the days with symmetric diurnal behavior. Figure 3.5 shows the effect of equatorial electrodynamics on the dayglow emission intensity behavior as characterized by A and AT values. It was shown in that Figure that, to a first order, the equatorial electrodynamics and not the meridional winds, to be the cause for the observed asymmetric diurnal behavior in the dayglow emission intensities. The broadly similar behavior of AT and A (Figures 3.5b and c) clearly indicates that the asymmetric diurnal behavior of the dayglow emission intensities are predominantly due to the effect of electrodynamics. Independent ionospheric observations confirmed the clear relation between the EEJ strength and AT not only during a few months but also from the reconstructed data for over two solar cycles [*Karan et al.*, 2016]. Thus, we use the dayglow behavior over this low-latitude location as a qualitative indicator of the variation of the equatorial electrodynamics.

Further, we have investigated the waves with time periods of similar values in all the three directions on all the days with symmetric (17 days) and asymmetric (8 days) diurnal behavior in the zenith emission intensities at the three wavelengths. Table 4.1 shows the percentage of similarity in the GW periodicities, range and mean values of the time periods with similar values. It may be noted that the waves with similar time periods in different directions are observed in more number of days with symmetric diurnal behavior in comparison to those on the days with asymmetric diurnal behavior. Correspondingly, the percentage of occurrence of days with similar time periods on "days with symmetric diurnal behavior", is greater than those on "days with asymmetric diurnal behavior", mainly at 777.4 and 557.7 nm emission wavelengths. The range of values of the similar time periods is from 0.4 to 2.1 h for all the three emission intensities for all the days. The values of integrated EEJ strengths (A) on the days (considered here) with symmetric diurnal emission intensity behavior range from 64 to 196 nTh, whereas on the days with asymmetric diurnal emission intensity behavior the values of A range from 124 to 295 nTh. This clearly indicates that the equatorial electrodynamics is, in general, stronger on the days with asymmetric diurnal emission intensity behavior in which longitudinal differences are found to exist.

Emission Wavelength (nm)	Diurnal behavior in all the three emissions	No. of days showed GW time period(s) with similar values	% of similarity in GW periodicities	Range and mean of similar Time periods (h)	Zonal Scale Sizes (km)
OI 777.4	Symmetric	11	64	0.4-2.1 1.2	Before 10LT:–;– After 10LT:–;227-638
	Asymmetric	2	25	2.0-2.1 2.0	Before 10LT:–;265-290 After 10LT:50-66;240-638
OI 630.0	Symmetric	7	41	0.4-1.9 1.1	Before 12LT:40-128;244-490 After 12LT:47-165;–
	Asymmetric	4	50	0.5-2.2 0.9	Before 12LT:116-135;– After 12LT:42-185;201-306
OI 557.7	Symmetric	14	82	0.5-2.0 0.9	Before 11LT:86-98;106-115 After 11LT:23-99;106-230
	Asymmetric	5	62	0.6-2.0 1.0	Before 11LT:25-98;274-276 After 11LT:23-81;115-197

Table 4.1: Summary of the GW characteristics (similarity in time periods and zonal scale sizes) on the days with a similar type of diurnal behavior (either symmetric or asymmetric) in all the three dayglow emission intensities.

At this point, it is to be appreciated that longitudinal differences in the GW time periods are observed in the optical dayglow emission intensity variations which is a neutral phenomena. We have seen above that when the diurnal behavior of the dayglow emission intensities over zenith is asymmetric, there is a strong equatorial electrodynamic forcing on that day. This is a good example of electrodynamic and neutral coupling in the equatorial- and low-latitude upper atmosphere. The contrast in symmetric and asymmetric diurnal behavior in 630.0 nm dayglow emission is poorer than in 557.7 and 777.4 nm dayglow emissions [*Karan et al.*, 2016]. This is most probably due to the combined effect of the equatorial electrodynamics and the neutral winds to the 630.0 nm dayglow emission, and thus, this seems to be resulting in the observed time periods with similar vlaues even on the days with an asymmetric diurnal behavior as seen in Figure 4.5.

As discussed above, the EEJ strengths have a strong influence on the diurnal behavior of the dayglow emission intensities. This suggests that the varying equatorial electrodynamic processes at different longitudes would have their imprint on the neutral dayglow emission intensities at different longitudes, just as reflected in our optical observations over the zenith. If that be the case, the zonal GW characteristics would be different on all these days. In order to understand the different nature of the thermospheric wave characteristics in greater detail, we have carried out the wave number spectral analyses (method is explained in detail in section 2.5.5) on these days.

In section 2.5.5, the sample wave number spectral analysis carried out in 630.0 nm dayglow emission intensities is shown. For the sake of completeness, Figure 4.9 illustrates one sample wave number spectral analysis of the dayglow emission intensities at all the three wavelengths (OI 557.7, 630.0, and 777.4 nm) carried out for 7.8 LT on 10 May 2015. Similar method of wave number spectral analysis, as discussed in section 2.5.5 is followed here. The left panels (Figures 4.9a,b,c) show the dayglow emission intensity distribution along the zonal direction, with the upper, middle, and lower panels for 777.4, 630.0, and 557.7 nm emission wavelengths, respectively. In the left panels of Figure 4.9, the X- and Y-axes

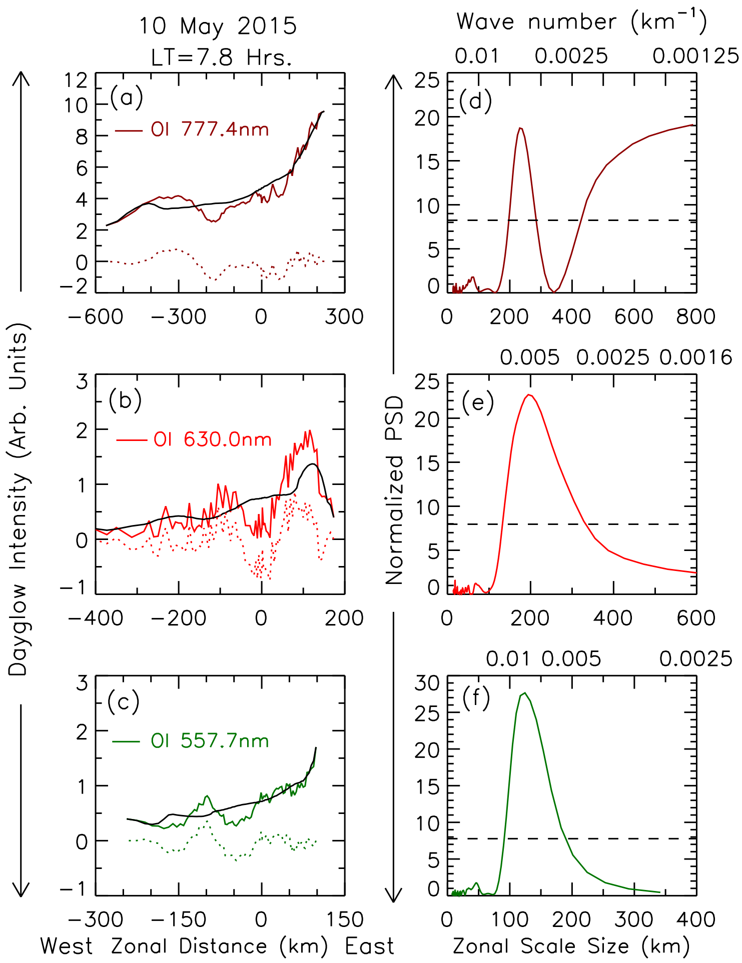

Figure 4.9: Sample of the wave number spectral analyses of the dayglow emission intensity data at all the three wavelengths obtained along the zonal direction at 7.8 LT on 10 May 2015 are shown. The left column shows the dayglow emission intensity distribution along the zonal direction for 777.4 nm (Figure 4.9a), 630.0 nm (Figure 4.9b), and 557.7 nm (Figure 4.9c), respectively. Wave number spectral analyses of the residuals (after subtracting the smoothed zonal intensities) are shown on the right column (Figures 4.9d,e,f). The horizontal dashed line corresponds to 90% FAL limit.

show the zonal distance from zenith (positive eastward) and dayglow emission intensity. On the right panels of Figure 4.9, the X- and Y-axes show the zonal scale sizes (scale size is a different terminology used for the wavelength of the atmospheric waves) in km and normalized power spectral density (PSD). The upper X-axis in the right panels shows the wave number in km^{-1}. The horizontal dashed lines in these panels show the 90% significant value. Here, the significant scale sizes in 777.4, 630.0, and 557.7 nm dayglow emission intensities are 232, 195, and 124 km, respectively.

This method has been followed to obtain the diurnal behavior of the statistically significant scale sizes for all the days at all the three emission wavelengths at a cadence of 15 minutes. In one of our recent studies [*Pallamraju et al.*, 2016], this method has been demonstrated to yield the neutral GW characteristics (both in space and time) and the first three-dimensional wave structure in the daytime upper atmosphere had been obtained (which will be discussed in detail in Chapter-6).

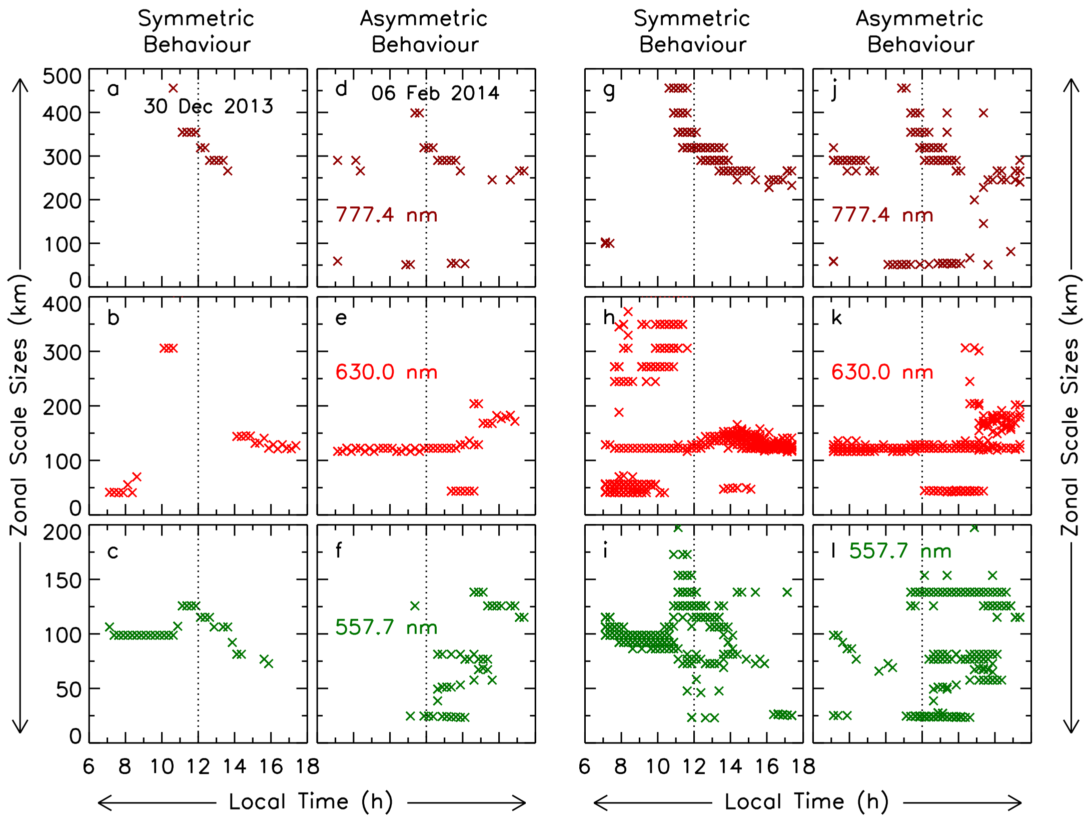

Figure 4.10: Diurnal distribution of the significant zonal scale sizes on two sample days (Figures 4.10a,b,c) with symmetric, and (Figures 4.10d,e,f) with asymmetric zenith diurnal emission intensity behavior are shown. Diurnal distribution of the significant zonal scale sizes are collated for all the days with (Figures 4.10g,h,i) symmetric, and (Figures 4.10j,k,l) asymmetric diurnal emission intensity behavior in all the three wavelengths. Significant differences may be noted in the scale sizes between the days with symmetric and asymmetric diurnal behavior in the emission intensities.

Diurnal distribution of the zonal scale sizes obtained for two sample days, with symmetric and asymmetric zenith diurnal emission intensity behavior for all the three wavelengths are shown on the two left columns of Figure 4.10. Figures 4.10a-c/Figures 4.10d-f show the diurnal distributions of the zonal scale sizes on 30 December 2013/6 February 2014, which were the days with symmetric/asymmetric behavior in the diurnal emission intensity at all the three wavelengths. The X- and Y-axes show the LT in hours and the scale sizes in km. Notable contrast exists for the values of the zonal scale sizes and their diurnal behavior obtained between the days with symmetric/asymmetric diurnal behavior in the dayglow emission intensities at all the three wavelengths. The diurnal behavior of the zonal scale sizes has been shown for only one sample day each for symmetric/asymmetric diurnal behavior in Figures 4.10a-f. However, it was noted that all the other days showed almost similar behavior as characterized by the symmetric/asymmetric diurnal behavior. Therefore, we have overlaid the diurnal distribution of the significant GW scale sizes obtained for all the days with respect to symmetric/asymmetric diurnal behavior in Figures 4.10g-i and Figures 4.10j-l, respectively. It is striking that the pattern of the diurnal distribution of the zonal scale sizes is: (i) remarkably similar within the days with symmetric or asymmetric diurnal behavior, and (ii) distinctly different when compared with one type to another in zenith emission intensity behavior.

Table 4.1 includes the summary of the diurnal distribution of the GW zonal scale sizes on both the type of days (either with symmetric/asymmetric diurnal emission intensity behavior in all the three wavelengths). The contrast is apparent in terms of the magnitudes of the zonal scale sizes and the times at which they exist at a given emission wavelength between the two types of diurnal emission intensity behaviors. The dashed line corresponds to the non-availability of the significant scale sizes within the observational window of this experiment. As mentioned above, the ranges of the integrated EEJ strengths (A) on the days (considered for Figures 4.10g-l) with symmetric/asymmetric diurnal emission intensity behavior are 64-196/124-295 nTh. This points to the important role of the EEJ strength in all these days.

At the emission altitude of 777.4 nm dayglow, on all the days (either with symmetric or asymmetric diurnal emission intensity behavior), GWs with zonal scale sizes greater than 200 km are present, mostly during noon which seem to be decreasing gradually towards afternoon (Figures 4.10a,d,g,j). However, on the days with asymmetric diurnal emission intensity behavior, larger- and smaller-scale sizes of around 300 and 50 km are also seen in forenoon and noon (Figures 4.10d,j), which are absent on the days with symmetric diurnal emission intensity behavior (Figures 4.10a,g). From Figure 4.10b and h, it is clear that at 230 km altitude, on the day with symmetric diurnal emission intensity behavior, larger-scale sizes (>200 km) are present only during forenoon and seem to be increasing towards noon. Waves of scale sizes >200 km and ∼50 km are present during forenoon on the days with symmetric diurnal emission intensity behavior (Figures 4.10b,h), whereas, these are absent on the days with asymmetric diurnal emission intensity behavior (Figures 4.10e,k). Presence of the waves with smaller-scale sizes of around 120 km is clearly noticeable on the days of both types of diurnal emission intensity behavior (Figures 4.10h,k). At 130 km altitude GW zonal scale sizes of around 100 km are seen in forenoon which increase during noon and then gradually decrease with time on the days with symmetric diurnal behavior (Figure 4.10i). Contrary to this, on the days with asymmetric diurnal behavior, the spread in the values of the significant scale sizes are clearly seen during afternoon (Figure 4.10l). The 557.7 nm dayglow emission has contributions from both lower thermosphere and higher above (F region). The lower altitude contribution is mostly affected by the wave activities from the mesosphere/lower thermosphere regions while the higher one gets affected by the equatorial electrodynamics as well. Hence, on the days with asymmetric diurnal behavior, as the equatorial electrodynamics is stronger, the F region contribution to the OI 577.7 nm dayglow could be significant and time varying, which could give rise to the observed values of multiple zonal scale sizes during afternoon.

Even though the three dayglow emissions considered in the present work originate from different altitudes and have different production mechanisms, the broad pattern of the presence of waves with larger-scale sizes in forenoon/noon of a day with symmetric diurnal behavior (Figures 4.10g,h,i) and of relatively smaller-scale sizes in afternoon on days with asymmetric diurnal behavior (Figures 4.10j,k,l) is clearly noticeable, especially for 630.0 nm dayglow emission intensities. It is to be emphasized here that the days with symmetric and asymmetric diurnal behavior in the zenith intensities are irregularly spaced in the duration of December 2013 to March 2014. Thus, it is striking to note that in spite of these belonging to different months, the diurnal distribution in the zonal scale sizes on all the days with symmetric diurnal behavior of the dayglow follow a similar configuration. Similar is the case for the days with asymmetric diurnal behavior of dayglow as well. This indicates that the neutral wave dynamics is mainly influenced by the strength of the equatorial electrodynamics and follows a broad order in the upper atmosphere.

As has been shown above, optical dayglow emissions over low-latitude regions are sensitive to the equatorial electrodynamics and display zonal variations. On the days with symmetric diurnal behavior of the dayglow emission intensities over zenith, the time periods of waves in a separation of 3^0-8^0 in longitudes are found to be similar. Contrary to this, on the days with asymmetric diurnal behavior in the zenith emission intensities, the similarity in time periods over these longitudinal separation is poor. Moreover, the diurnal distribution of the zonal scale sizes of GWs also shows differences with respect to these two types of diurnal emission intensity behaviors. Such contrasting behavior of time periods and scale sizes implies a clearly different behavior in the neutral wave dynamics on these two types of days.

To further investigate the behavior of the wave dynamics, information on the propagation characteristics of the waves at each altitude has been obtained. In order to do that, power of the statistically significant scale sizes of GWs at a given time is selected by centering a band-pass filter at the peak of the dominant scale size with widths of 22, 40, and 50 km for 557.7, 630.0, and 777.4 nm, respectively. Inverse Fourier transform is carried out on the selected scale sizes to obtain the corresponding emission intensity modulations. The positions of crests/troughs as seen in the emission intensities are laid one-next to the other as a function of time, in order to be able to track the movement of the wave. This procedure to obtain the keogram by tracking the modulations in emission intensities with time are explained in detail in chapter-6 [*Pallamraju et al.*, 2016]. The keogram analyses have been carried out on the days in which all the three dayglow emission intensities over zenith show a common type of diurnal behavior (i.e. either symmetric or asymmetric). Figure 4.11 shows the keograms on four sample days that were considered for periodogram analyses shown in Figures 4.5, 4.8, and 4.10. The X- and Y-axes show the zonal distance from the zenith in km and the local time, in hours, respectively. The differing extents in zonal distances covered at each emission wavelengths may be noted. Positive/negative values of the distance corresponds to the eastern/western directions with respect to the zenith. The normalized relative intensity is shown as contours and their values are represented by the color bars on the right hand side of the figure. The gaps in the figures at some times are due to the absence of statistically significant scale sizes in the GWs at those times as seen from the wave number spectral analysis. To follow the propagation of waves, black/violet lines have been drawn (to aid the eye) that join the crests/troughs with respect to time. Dotted lines are drawn to show the most probable movement of the GWs with time when the power of the scale sizes are found to be below the FAL.

On days with symmetric diurnal behavior of the zenith dayglow, westward movement of the zonal component of GWs are seen at the emission altitude of 777.4 nm dayglow emission (Figures 4.11a,d). At 230 km (emission height of 630.0 nm dayglow) and 130 km (altitude of 557.7 nm dayglow emissions), no significant movements of the crests and troughs are noticed. They seem to follow a standing wave type of pattern throughout the day (Figures 4.11b,c). On the second day as well, such standing wave type of pattern in the waves is clearly noticed (Figures 4.11e,f). A uniform pattern of waves without any significant zonal movement of wave-fronts on the days with symmetric diurnal behavior indicate to a systematic and uniform behavior in the dynamic processes over large spatial extent and the absence of zonal differences within the spatial coverage possible in this experiment. On the days with asymmetric diurnal behavior,

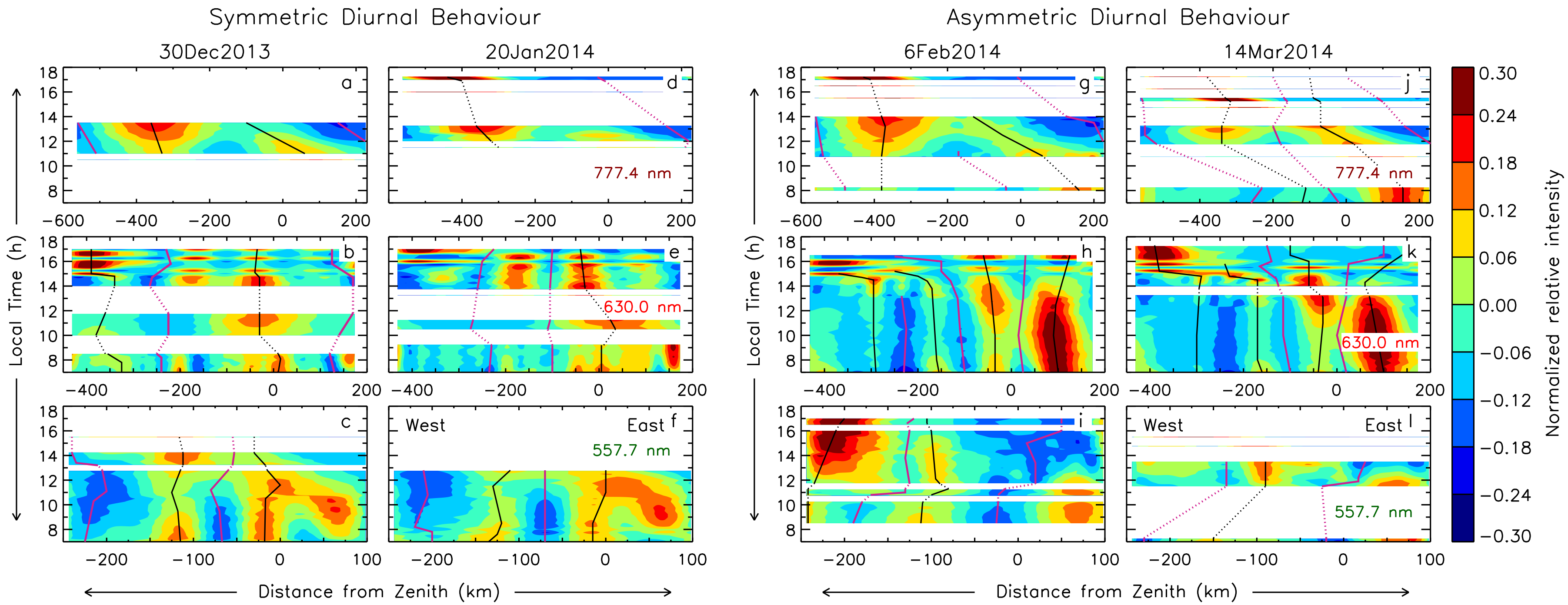

Figure 4.11: Contours of the normalized relative dayglow emission intensity variations obtained using band-pass filter centered at the dominant scale sizes on four sample days that are considered for periodogram analyses (in Figure 4.5) are shown. The values of the normalized relative intensity are shown in the bar on the right hand side. Figures (4.11a-f)/Figures (4.11g-l) show the days with symmetric/asymmetric diurnal dayglow emission intensity behavior in all the three emission wavelengths over zenith. Contrasting characteristics in the zonal propagation of the waves can be seen on the days with symmetric/asymmetric diurnal behavior.

the thermospheric neutral waves at 777.4 nm emission altitude show a westward propagation (Figures 4.11g,j) similar to the days with symmetric diurnal behavior. The behavior of the GW propagation at the top most layer of the F region as measured by OI 777.4 nm dayglow emission seems to be mainly westward on all the days, most probably due to the existence of strong daytime westward winds at this altitude. At 230 km altitude, the crest/troughs towards east of zenith move eastwards and those towards the west move westwards (Figures 4.11h,k). This kind of movement of waves in 630.0 nm emission was seen on other days as well, as reported in one of our earlier works [*Pallamraju et al.*, 2016]. The cause for such behavior is under investigation. On the days with asymmetric diurnal behavior, the waves at 130 km altitude show an eastward propagation (Figures 4.11i,l). It is interesting to note that the movement of the crests and troughs are significantly different after 13 LT at both the altitudes of 630.0 and 557.7 nm dayglow emissions. Moreover, at different longitudinal regions there seems to be changes in the gradients of propagation direction of the waves. This type of spatially varying direction of propagation of the waves in forenoon and afternoon clearly indicates to the different nature of the processes and dynamics that are prevalent at the respective longitudes.

4.4 Discussion

The neutral wave dynamics in the thermosphere show different pattern on the days with symmetric/asymmetric diurnal behavior in the optical dayglow emission intensities obtained over zenith. Analyses of the data obtained over large spatial distances show significant differences in terms of (i) the existence/non-existence of GWs with similar time periods, (ii) dissimilar diurnal distribution of the zonal scale sizes, and (iii) varying propagation characteristics of the zonal wave fronts on the days with symmetric/asymmetric diurnal behavior. All these distinct features suggest the existence of longitudinal variations in the thermospheric wave dynamics in smaller (3^0-8^0) longitude spatial extents. The magnetic declination angles and magnitudes of the geomagnetic field strengths do not vary within the zonal separations considered in this study. Hence, the differences in the zonal component of the neutral thermospheric waves as seen in the optical dayglow emission intensities at multiple wavelengths are most likely due to the differences in the equatorial electrodynamic processes along the respective longitude sectors. Changes in the magnitudes and directions of the thermospheric neutral wind, if any, can also bring about such small-scale zonal variations of the wave dynamics ([*Fritts and Alexander*, 2003]). Moreover, the effect of the localized wind shears in bringing about changes in the wind structure and thereby affecting the waves cannot be neglected, especially for the lower altitude emissions at 557.7 nm. During December/January when the equatorial electrodynamics are weaker [*Karan et al.*, 2016], the similarity in GW time periods was found to be greater, indicating the absence of longitudinal variations in the 3^0-8^0 longitudes. On the other hand, during March, the equatorial electrodynamics are stronger and the GW time periods of similar values along these longitudinal separations are observed less frequently suggesting a possible existence of longitudinal differences in the neutral wave dynamics. This could be due to stronger wave activities during equinoxes. In this background it is striking to note that the diurnal behavior in the zenith OI optical dayglow emission intensities, which are a part of the overall upper atmospheric system indicates as to whether longitudinal differences exist or, not.

These new results presented here hold a lot of promise on various aspects of the coupling of the atmospheres that vary as a function of time. In this work, we have considered only the days when all the three emission intensities showed a common type (i.e. either symmetric or, asymmetric) of diurnal behavior. However, there are days in which a couple of emission wavelengths show symmetric/asymmetric diurnal behavior while the remaining one shows an opposite behavior. Characterization of the dayglow emission intensity data on these days will provide information on the nature of inter-coupling among the thermosphere at different altitudes. Further, small-scale variations in the wave features could also be due to structures in the density distribution over space, which can vary with time. Also, there are cases when the distribution of the scale sizes on the days with symmetric/asymmetric diurnal behavior showed features similar to that on the days with asymmetric/symmetric diurnal behavior. These days are found to be relatively geomagnetically active among all the days considered and hence, are not included here. This indicates a positive response of the low-latitude thermospheric neutral GWs to the geomagnetic activity and is explained in detail in Chapter-5. Further, it is to be kept in mind that in this study the focus had been on the zonal component of the GWs. However, GWs are three dimensional in nature with different projections in zonal, meridional and vertical directions [*Pallamraju et al.*, 2016]. In this case, for zonal propagation, when the zonal scale sizes are seem to be varying with time, it is also possible that the direction of propagation is changing. For that investigation, near-simultaneous information of the dayglow emission intensity variations along both the zonal and meridional directions are required. Such data were acquired in campaign mode and the results of which will be presented separately.

For the sake of completeness, we have looked at results, if any, of smaller-scale size zonal variation in the published literature. Many of the all-sky measurements reported in the literature [e.g., *Shiokawa et al.*, 2009; *Taylor et al.*, 1995; *Nakamura et al.*, 1998; *Makela et al.*, 2013; *Hickey et al.*, 2015; *Martinis et al.*, 2015], do not highlight the existence of longitudinal differences. This is probably because the all-sky images of the nighttime ionosphere over equatorial- and low-latitudes are dominated by the significant feature of the movement of plasma bubbles (with greater occurrence during the high solar activity, and during equinoxes), and the smaller scale feature, if any, are masked. During the geomagnetic disturbances, the zonal variations could be due to shears in the zonal plasma flow in the equatorial- and low-latitude regions [e.g., *Sekar et al.*, 2012] or due to the prompt penetration electric field [*Basu et al.*, 2001b; *Chakrabarty et al.*, 2015]. However, in this work we present the results on the existence of longitudinal differences in the equatorial electrodynamic processes during geomagnetically quiet periods. The lower thermospheric emissions of OI 557.7 nm in the nighttime is governed mainly by the lower atmospheric forcing with waves of different scale sizes moving in different directions [e.g., *Taylor et al.*, 1995]. To the best of our knowledge, no result exists in the literature that describes a longitudinal differences in such small zonal separations as presented in this work.

In the present study, the longitudinal differences within 3^0-8^0 separations present in the daytime seems to be mainly due to the zonal differences in the EEJ strengths. As the equatorial electric field is electrostatic in nature (i.e. $\vec{\bigtriangledown}\times\vec{E}$=0), any changes in the values of $\vec{E}$ at certain longitude gives rise to changes of $\vec{E}$ at other longitudes around the globe so as to maintain the $\int \vec{E}.dl$=0 condition. Thus, possibility of the existence of changes in the EEJ strengths in such small separations seems to be the cause of longitudinal variations observed in this study. The fact that the integrated EEJ strengths play a distinct role in influencing the diurnal emission intensity behavior in the dayglow as shown in Figure 3.5, add credence to this conclusion arrived at. To the best of our knowledge, these experimental results that suggest to the possible existence of dissimilarities in the equatorial electric fields in the daytime in such short separations of 3^0-8^0 longitudes are first of their kind. Information as revealed in the present experiment has great potential in forming inputs to the regional and the global scale dynamical models.

4.5 Conclusion

Optical OI dayglow emission intensities were obtained over a large FOV along the zonal direction from a geomagnetic low-latitude station. Periodogram analyses were carried out on the dayglow emission intensity variability obtained in the west, zenith, and east directions to investigate the periodicities in them. Presence/absence of the time periods with similar values in these three directions suggests to a common/different source driving the wave features indicating the non-existence/ existence of longitudinal differences in the wave features within this spatial extent. Examples shown in Figures 4.6 and 4.7 of wavelet analysis indicate to no variation in the time duration or systematic variation in the occurrence time of the similar time periods. From the zenith emission intensity measurements it was found that the waves with similar time periods are present/absent on the days with symmetric/asymmetric diurnal dayglow emission intensity behavior. The non-existence of the waves with similar time periods on the days with asymmetric diurnal behavior was attributed to the stronger equatorial electrodynamics, which seems to show variations even within a $\sim 3^0$ longitudinal separation. This gives a clear and broader picture of the coupling processes between the equatorial electrodynamics and the off-equatorial neutral wave dynamics. Moreover, the GW features in terms of the zonal scale sizes and the propagation directions also show different behavior on the days with symmetric and asymmetric diurnal dayglow emission intensity behavior. The high spatio-temporal resolution measurements at the three optical dayglow emissions emanating from different altitudes revealed, for the first time, that there exist longitudinal differences of the equatorial electrodynamic processes in as small a separation as 3^0 in longitude. Such longitudinal differences observed over such short separations in the neutral wave features and the electrodynamic processes over the low-latitude thermosphere provide new insights into the understanding of the intricacies of the upper atmospheric dynamical processes regionally as well as globally.

We have discussed in detail about the effect of the equatorial electrodynamics on the off-equatorial neutral wave dynamics. Now we know that this coupling process have small scale zonal variations along with the large scale variations. All the aspects discussed till now are valid during geomagnetically quiet conditions. However, it is well-known that the equatorial- and low-latitude upper atmosphere get affected by the perturbations brought in due to the geomagnetic disturbances. Effect of the geomagnetic disturbances on our understanding of the equatorial- and low-latitude thermospheric wave dynamics will be discussed in detail in the next chapter.

Chapter 5

Response of Low-Latitude Thermospheric Wave Dynamics Due to Geomagnetic Storms

5.1 Introduction

The behavior of the thermosphere over the equatorial- and low-latitude regions are affected by various dynamical processes originating from different sources. As discussed in detail in section 1.4, the daytime coupling processes between equatorial- and off-equatorial regions like the EEJ, EIA, and ETWA alter the composition and dynamics in the thermosphere over the low-latitudes. Additionally, propagation of GWs that originate at both lower- and higher-latitudes bring substantial thermospheric compositional changes (discussed in section 1.3). These upward propagating waves also modify the prevalent wave structure in the thermosphere [*Hocke*, 1996; *Pallamraju et al.*, 2014; *Laskar et al.*, 2015]. The solar forcing from above also plays an important role in bringing changes in the upper atmospheric dynamics. These processes and their effects on the equatorial- and low-latitude thermosphere show seasonal and solar cycle variation. The seasonal variability is brought about mainly due to the changes in the background wind pattern, ambient densities, and variation of relative position of the Earth with respect to the sun. Moreover, during sudden stratospheric warming (SSW) periods, mesosphere-thermosphere meridional circulation is set up which not only affects the low-latitude thermospheric neutral densities but also brings about global scale circulation in the MLT region [*Laskar and Pallamraju*, 2014]. Further, independent parameters, such as the high-latitude TEC variations and the ring current (as measured through D_{st}) showed striking similarity [*Yadav and Pallamraju*, 2015] indicating a common source responsible for the observed magnetospheric-thermospheric-ionospheric coupled effects. It is likely that such coupled effects will have a corresponding signature in the neutral wave dynamical behavior as well.

As explained in detail in section 1.5, during geomagnetic disturbances, due to the strong electric currents and precipitation of high energy particles into the high-latitude upper atmosphere, significant amount of energy is deposited in the atmosphere. Because of these inputs, equatorward meridional wind circulation is set up. The TADs and TIDs that propagate from high- to low-latitudes also bring about changes in the thermospheric composition, dynamics, and chemical state over the low-latitudes. Moreover, during geomagnetic disturbances the equatorial zonal electric fields and plasma drifts show complex behavior due to the solar wind-magnetosphere dynamo and the ionospheric disturbance dynamo. Complex behaviour of the equatorial zonal electric fields during storm time can change the ($\vec{E} \times \vec{B}$) plasma drifts abruptly and hence, the equatorial thermospheric dynamics is affected [*Basu et al.*, 2001b; *Sastri et al.*, 2002; *Pallamraju et al.*, 2004b; *Chakrabarty et al.*, 2010].

The adverse effects/changes that a geomagnetic disturbance can create/bring to the low-latitude thermospheric dynamics, depend on the season and time (day/night) of its occurrence, speed and direction of the ambient winds and waves as discussed above. Many researchers have studied the effect of the geomagnetic disturbances at different latitudes/longitudes by using different observational techniques and also through simulations [e.g., *Mayr et al.*, 1978; *Prolss*, 1980; *Fujiwara et al.*, 1996; *Pant and Sridharan*, 1998; *Pallamraju and Chakrabarti*, 2005]. Atmospheric optical airglow emissions can be used to study the dynamical process occurring at the altitudes of their origin. During geomagnetic storms, the morning time dayglow emission intensities at low-latitudes have been reported to have enhanced by a factor of 2-3 when compared to the quiet day, which was attributed to the increase of neutral densities brought in from the high-latitude regions [*Pallamraju et al.*, 2004b]. From the measurements of WINDII (Wind Imaging Interferometer) on board UARS (Upper Atmospheric Research Satellite) winds of around 650 ms^{-1} have been reported at 200 km altitude during a geomagnetic storm with Kp value 7.7 [*Zhang and Shepherd*, 2000]. Moreover, by using ionosonde, RADAR, GPS measurements, effect of the geomagnetic disturbances are studied over equatorial- and low-latitude regions through nighttime scintillations [*Dabas et al.*, 1989]. Photochemical models have been used to estimate the volume emission rate of 557.7 nm and 630.0 nm dayglow emission intensity to study the geomagnetic disturbances over low-latitude regions [e.g., *Culot et al.*, 2005].

In Chapter-4, we have discussed the local time distribution of the thermospheric GW zonal scale sizes over low-latitude regions. The diurnal distribution of the zonal scale sizes were found to exhibit different patterns on the days with symmetric/asymmetric diurnal emission intensity behavior. Detailed discussion on symmetric or asymmetric diurnal behavior of the dayglow emission intensities can be found out in Chapter-3. Such investigation was carried out on the geomagnetically quiet days. As discussed above in this section, the geomagnetic disturbances are expected to bring variations in the observed thermospheric wave dynamics over the low-latitude regions. Event based investigations on the study of the effect of the geomagnetic storms on the low-latitude thermosphere have yielded many results as reported in the literature. However, a broad understanding of the response of the low-latitude thermosphere to the effect of the geomagnetic disturbances require a long term systematic observation. Thus, in the present work, we have carried out investigations to study the behavior of the thermospheric wave dynamics in the GW regime over low-latitudes during geomagnetically disturbed periods in a broader context.

For this investigation, we have used measurements of the thermospheric optical neutral oxygen dayglow emission intensities that emanate from three different altitudes. We have investigated their variations during different geomagnetic disturbance events which occurred during different months. In order to understand the seasonal variations observed in the dayglow emission intensities, we have compared them with the EEJ strength, IEC and thermospheric O/N_2. These are the first results of the kind on the investigations of daytime thermospheric wave dynamics and zonal wave scales during periods of geomagnetic disturbances.

5.2 Experimental Technique and Data Set

To address the objectives of this work as mentioned above, we have used the disturbance storm time index (D_{st}), thermospheric O/N_2, equatorial electrojet strength (EEJ), and ionospheric electron content (IEC) data.

We have obtained the optical oxygen dayglow emission intensities at 557.7, 630.0, and 777.4 nm wavelengths using MISE from a low-latitude station, Hyderabad, India (Geographic 17.5^0 N, 78.4^0 E; 8.9^0 N Mag. Lat) during the months of January and February of 2014, May 2015 and March of 2016 wherein geomagnetic disturbances of varying levels and durations occurred. The optical dayglow emission intensities imprint the signature of the dynamic processes that occur at their altitudes of emission. Hence, the temporal variations in the emission intensities act as tracers of the atmospheric dynamics that exist at the respective emission altitudes. In order to know the occurrence time of different stages of the geomagnetic storms during these periods, we have used the D_{st} index data.

To obtain the information about the thermospheric behavior during different geomagnetic periods, we have investigated the thermospheric O/N_2 data. The thermospheric O/N_2 data is obtained from the Global Ultraviolet Imager (GUVI) onboard the NASA TIMED (Thermosphere Ionosphere Mesosphere Energy and Dynamics) satellite. Details about the O/N_2 data have been discussed in section 2.4.4. We have used the O/N_2 data corresponding to spatial location over Hyderabad, India (from where the optical data has been obtained). A spatial extent of $20^0 \times 20^0$ in latitudes $\times$ longitudes centered at Hyderabad has been considered to obtain the information of the neutral composition.

To investigate the equatorial electric field effects on the off-equatorial plasma dynamics during geomagnetic storms, we have analyzed the EEJ strength and IEC data. The IEC data are obtained from Ahmedabad (typically the northern crest location of the EIA) in Indian longitudes. Details about these data sets are explained in sections 2.4.1 and 2.4.2.

5.3 Results

In the present study we have considered three events (February 2014, March 2016, and May 2015) to study the effect of the geomagnetic disturbances on the low-latitude thermospheric GW dynamics. Another event on January 2014 (Event-1) is additionally considered as a geomagnetically quiet event to serve as a reference. These three geomagnetic disturbed events occurred during different months and are used to study the seasonal variation in the low-latitude wave dynamics.

The Y-axes in Figure 5.1 depict the variation of the D_{st} (left Y-axes) and Ap indices (right Y-axes) for all the events. The horizontal dotted lines correspond to the zero D_{st} value. During January 2014 (Event-1), variations in the D_{st} values showed a typical geomagnetically quiet type pattern (Figure 5.1a). The maximum value of Ap index was 30 during this period. The main phase of the storm during the Event-2 (Figure 5.1b) started on 18 February 2014. During the recovery phase of this storm, the D_{st} values showed an oscillatory type of behavior that continued to 19-23 February 2014. The Ap value reached a maximum of 94. Event-3 describes the geomagnetic disturbance that occurred during 6-12 March 2016 (Figure 5.1c). Variation of D_{st} during this event showed a typical storm type pattern with a peak Ap value of 94. The disturbance reached its maximum on 7 March, then it recovered gradually. In the Event-4, we have considered the storm during 9-18 May 2015 (Figure 5.1d). In comparison to the Events-2 and 3, the Event-4 is a moderate geomagnetic disturbance (peak Ap=67). The main phase started on 11 May 2015 and continued for 3 days. It is to be noted that in the geomagnetic disturbance Events-2, 3, and 4, after the recovery phase of the first storm, another small storm occurred. The vertical downward arrows in blue color

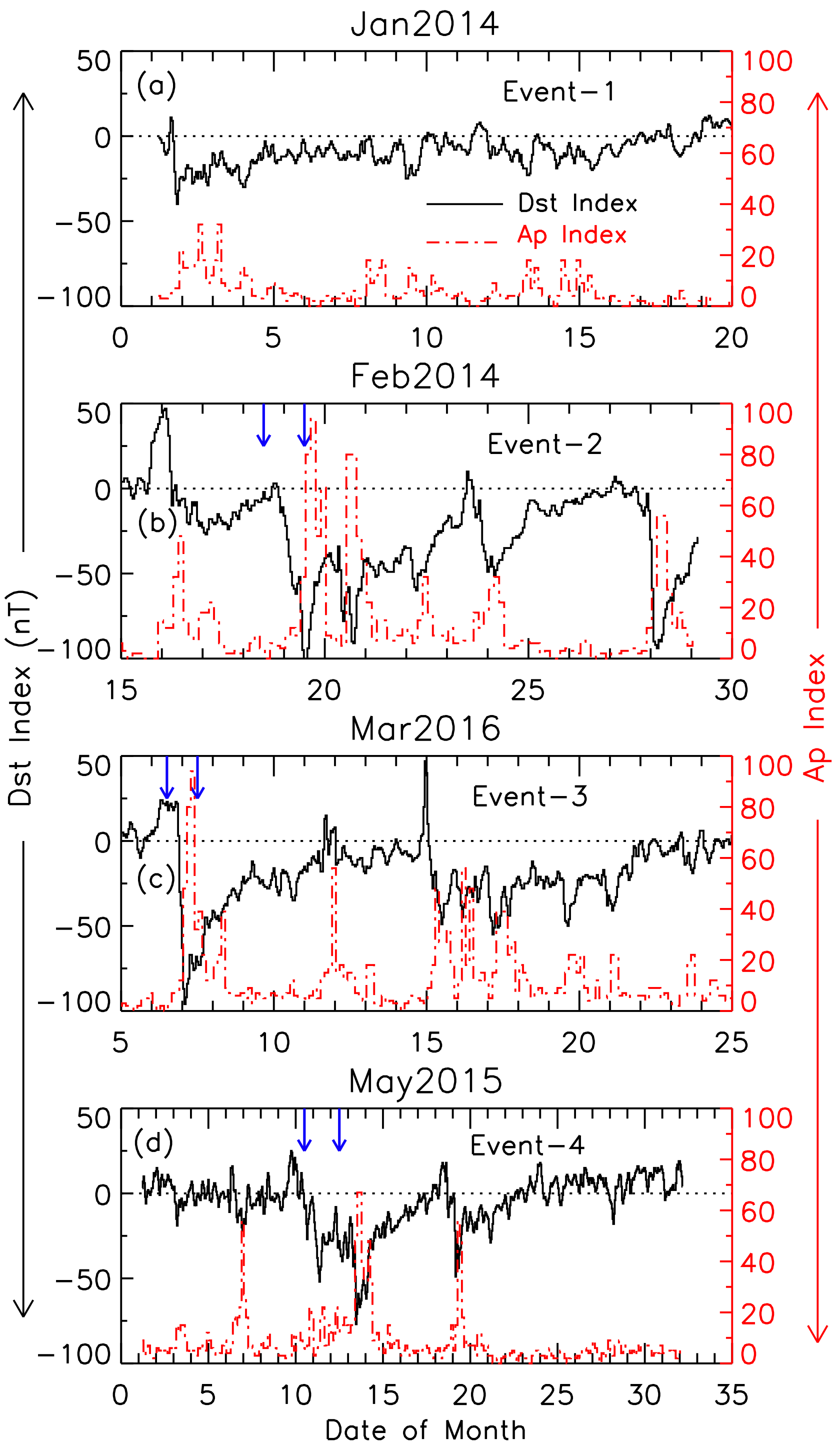

Figure 5.1: Variations of the D_{st} and Ap indices during the four events considered in the present study are shown.

on the top side of Figures 5.1b,c,d correspond to a pair of geomagnetically quiet and a disturbed day chosen for more detailed analyses of zonal wave dynamics on these days and are shown later in Figures 5.3-5.5.

5.3.1 Geomagnetic storm effect on the OI dayglow emission intensities over Hyderabad

Firstly, we present the variations of the D_{st} index, the dayglow emission intensities at all the three wavelengths (OI 777.4, 630.0, and 555.7 nm), thermospheric O/N_2, EEJ strength, and the IEC data for all the events in Figure 5.2. The X-axis represents the dates of the month. The upper panel of Figure 5.2 shows the variation of the daily mean of the D_{st} index on all the days of the month. For all the four events the daily mean dayglow intensities at each emission wavelengths are individually normalized with respect to their maximum values in that month. Variation of the normalized daily mean dayglow emission intensity with one sigma standard deviation at all the three wavelengths are joined by a solid line and are shown in the second row of Figure 5.2. By doing this, inter comparison of variations in all the dayglow emission intensities can be made for each of these events. However, in order to inter compare the behavior of the dayglow emission intensities in all the four events, the daily mean dayglow data are normalized with respect to their maximum values during the four events and has been shown in the third row of Figure 5.2. Data gaps (due to unfavorable sky conditions) of more than a day have been joined by dotted lines. The daily averaged thermospheric O/N_2 data (obtained over a spatial extent of $20^0 \times 20^0$ in latitudes $\times$ longitudes centered at Hyderabad) are shown in the fourth row of Figure 5.2. The peak EEJ strength and IEC values are plotted in the fifth row of Figure 5.2 for all the events and their values are shown on the left and right Y-axes.

From the D_{st} variation as shown in Figure 5.2a, it is clear that Event-1 is a geomagnetically quiet period. The optical dayglow emission intensities at all the three emission wavelengths (Figure 5.2b) show similar type of variations with an average correlation coefficient (R) value of 0.9 during this period except for the 557.7 nm emission on 12 January 2014. It can also be seen that on these days not only the correlation is good amongst all the three dayglow emission intensities but also these dayglow emission intensities show a broadly similar variations with the peak EEJ. Correlation analyses of the normalized daily mean dayglow at each of the emission wavelengths has been performed separately with the peak

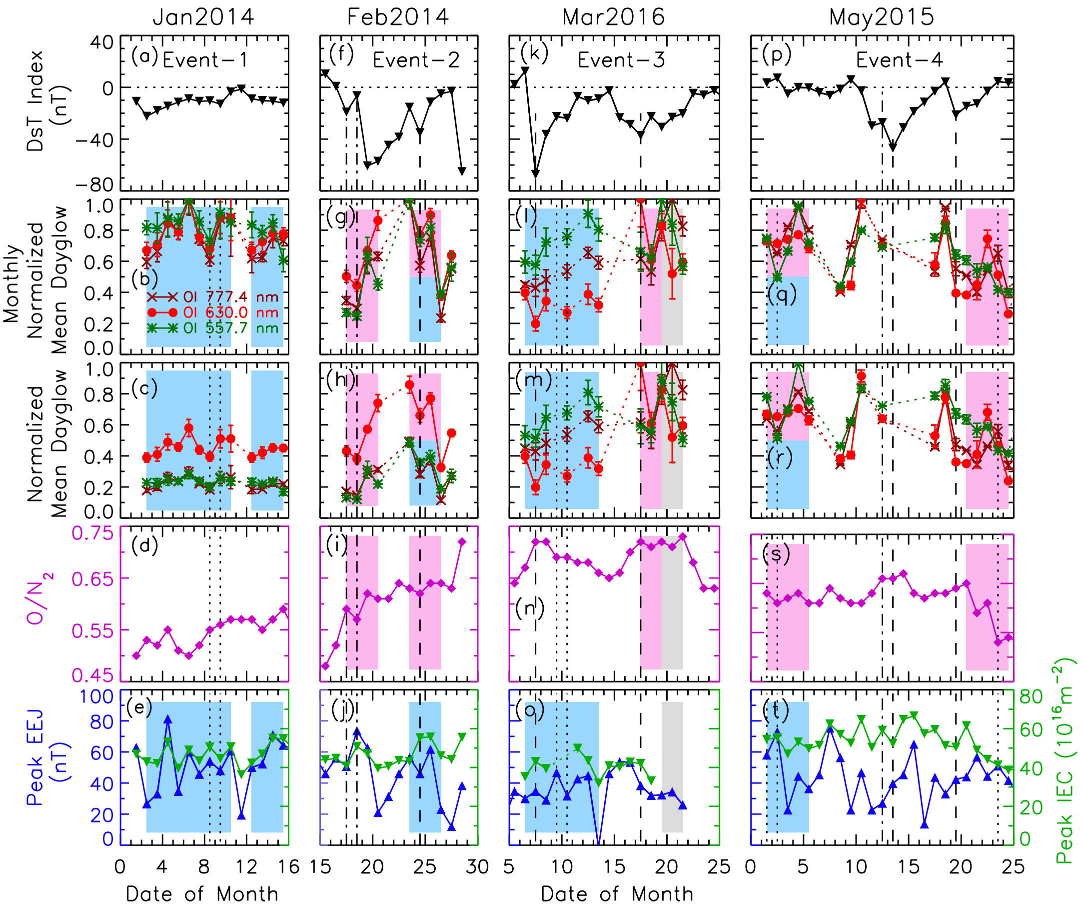

Figure 5.2: Variations of daily mean of the D$_{st}$ index (Figures 5.2a,f,k,p), monthly normalized daily mean dayglow emission intensity in the three wavelengths (Figures 5.2b,g,l,q), normalized daily mean dayglow emission intensity during the four events in the three wavelengths (Figures 5.2c,h,m,r), daily averaged O/N_2 (Figures 5.2d,i,n,s), variation of the peak EEJ and the peak IEC (Figures 5.2e,j,o,t) are shown for various durations: January 2014 (Figures 5.2a-e), February 2014 (Figures 5.2f-j), March 2016 (Figures 5.2k-o), and May 2015 (Figures 5.2p-t). The X-axis shows the dates in each month. The duration in which both the dayglow emission intensities and EEJ show similar variations are shaded in blue color, whereas, the duration in which both the dayglow emission intensities and O/N_2 show similar variations are shaded in pink color. On the days marked by grey shaded region, the behavior of dayglow at different wavelengths showed a mixed response to the variation of O/N2 and EEJ.

EEJ for this period. Excluding a couple of days as shown by the vertical dotted lines in Figures 5.2b,e, the average of correlation coefficients of all the three individual values (for correlation between OI 777.4 nm to peak EEJ, OI 630.0

nm to peak EEJ, and OI 557.7 nm to peak EEJ) turn out to be 0.8. The days on which both the dayglow emission intensities and EEJ show similar variations are shaded in blue color in Figure 5.2. Independent ionospheric measurements of IEC over the crest region of the EIA vary hand-in-hand with those of the EEJ (Figure 5.2e), which is due to the effect of equatorial electric field on the EIA process [*Raghavarao et al.*, 1978]. On the days with larger EEJ value, due to stronger ($\vec{E} \times \vec{B}$) up-drifting of plasma over the geomagnetic equator, more plasma are transported to the off-equatorial regions. This thereby increases the electron densities and the production of the dayglow emission intensities over low-latitude regions. Such similar variations between the dayglow emission intensities and the EEJ indicates the influence of equatorial electrodynamics from day-to-day on the low-latitude thermospheric optical emission intensities and are consistent with earlier findings as reported in the literature [e.g., *Sridharan et al.*, 1999]. Specifically, it had been explained in the earlier studies that the temporal variations in the OI 630.0 nm dayglow emission intensity are due to the dissociative recombination mechanism, which, in turn, depends on the ambient electron densities [*Pallam Raju et al.*, 1996] and equatorial electric fields [*Karan et al.*, 2016]. It may be noted that the dayglow emission intensities do not show any similarity with the variations in O/N_2 during this period.

Now let us compare the variation of the dayglow emission intensities with the peak EEJ and O/N_2 during the three geomagnetically disturbance events. Similar type of data presentation as shown for the Event-1 (Figures 5.2a-e) is maintained for the Events-2, 3, and 4. During the Event-2, the D_{st} values continued to decrease from around 9.5 LT on 16 February to 2.5 LT on 17 February 2014 (Figure 5.1b) and then recovered to its zero value by 19.5 LT on 18 February. As a consequence, the O/N_2 over low-latitudes increased on 17 February and decreased on 18 February, shown by vertical dashed-dot lines (Figure 5.2i). The D_{st} value again started decreasing from around 19.5 LT on 18 February and the main phase continued till 21 February (Figure 5.1b). The Ap value reached a maximum of 94 on 19 February. An increased transport of the neutral densities from high-latitudes could be responsible for the rise of O/N_2 observed on 19 and 20 February (Figure 5.2i). During this period (17-20 February), the dayglow emission intensities showed a similar variation to that of the thermospheric O/N_2. As discussed above an average value of R obtained for each of the three dayglow emission wavelengths (except for the 630.0 nm dayglow emissions on 20 February 2014) (Figures 5.2g,i) with O/N_2 is 0.8. The days on which both the dayglow emission intensities and O/N_2 showed similar variations are shaded in pink color. On the other hand, correlation between variations of the dayglow emission intensities and EEJ showed negative (-0.5) values during these days (Figures 5.2g,j). Further, this is also in contrast to the behavior (+ve correlation) noted in the case of Event-1. Moreover, during the recovery phase of the storm, the IMF B_z once again becomes southward which results in another disturbed phase of the event during 23-27 February 2014 (Figure 5.1b). The main phase of this storm continued from around 15.5 LT on 23 February 2014 to 4.5 LT on 24 February 2014. During this period (23-26 February), dayglow emission intensities showed a similar variations with the EEJ strength with an average R value of 0.9. Also, the dayglow emission intensities showed similar variation with the O/N_2 with an average R value of 0.45. Hence, effect of the EEJ in the variation of the dayglow emission intensities seem to be stronger than the O/N_2. This could be due to the weaker strength of the storm during this period when compared with the previous one. These effects can cause a decrease of the dayglow emission intensities in all the three wavelengths observed on 24 February 2014 (Figure 5.2g).

Event-3 depicts the geomagnetically disturbance period during 6-23 March 2016 (Figures 5.2k-o). During this event, the main phase of the storm continued from around 21.5 LT on 6 March to 2.5 LT on 7 March 2016 (Figure 5.1c). The Ap value (94) peaked on 7 Mar 2016. On this day, both O/N_2 and EEJ strength showed an increase in their values. However, a decrease in the dayglow emission intensities is observed in all the three emission wavelengths on 7 March 2016, shown by vertical dashed line (Figure 5.2l). The possible cause(s) for this behavior could be some of the localized effects which require further investigations. During the recovery phase of the storm (8-12 March), the dayglow emission intensities rose along with the EEJ with an average R value of 0.88 (Figure 5.2l,o) (blue shaded region). The decrease of the dayglow emission intensities in all the wavelengths on 13 March (geomagnetically quiet) is due to the counter electrojet occurrence on that day. During this period (8-12 March), an opposite behavior is observed between the variations of the dayglow emission intensities and O/N_2 (Figure 5.2n) indicating a seemingly stronger effect of equatorial electrodynamics on the dayglow emission intensities during equinoxes even during geomagnetically disturbed periods. The vertical dashed lines in Figure 5.2o correspond to the days on which the IEC data were not available.

Another moderate storm occurred during 14-22 March 2016. The dayglow data are available on the days (17-21 March 2016) which are during the main phase of this storm. During 17-19 March, the dayglow emission intensities showed similar variations with those of the O/N_2 with an average R value of 0.72, which are shaded in pink color (Figures 5.2l,n), while the EEJ strength showed an opposite behavior with the variation of the dayglow emission intensities (Figures 5.2l,o). On the rest of the days (marked by grey shaded region), the behavior of the dayglow emission intensities at different wavelengths showed a mixed response to the variation of the O/N_2 and the EEJ strength. The IEC data were not available for these days. Thus, based on these measurements during geomagnetic storm periods in the equinoxes, it seems that the low-latitude variations of the dayglow emission intensities are influenced to a greater extent by the equatorial electrodynamics than the effects of the neutral dynamics of high-latitude origin.

Further, we have considered a geomagnetic disturbance period during May 2015 as Event-4 (Figures 5.2p-t). The geomagnetic condition was quiet during 1-5 May 2015 (Figure 5.1d). On these days, the dayglow emission intensities showed similar variations with the O/N_2 with an average R value of 0.7 (Figures 5.2q,s). Except for the first two days (shown by vertical dotted lines in Figure 5.2t) during this period, the dayglow emission intensities in all the wavelengths showed similar type of variations with the EEJ strength and the IEC, as shown in the blue color shaded region with an average value of R = 0.8 (Figures 5.2q,t). The main phase of the storm started around 11.5 LT on 10 May and continued till 11.5 LT of 13 May 2015. No simultaneous optical data were available, except for 12 May

2015 (Figures 5.2q,r) to enable comparison in case of this storm. The dayglow emission intensities on 12 May 2015 are found to decrease in comparison to that on 10 May 2015, shown by vertical dashed-dot line. This could be attributed to the weaker electrodynamical strength as observed in both the EEJ strength and IEC (Figures 5.2q,s,t). Another moderate storm occurred during 18 to 22 May 2016 when simultaneous dayglow data were available. The main phase of this disturbance continued during 16.5 LT of 18 May to 4.5 LT of 19 May. The effect of which was observed as a decrease in the dayglow emission intensities at each emission wavelengths on 19 May 2015, shown by vertical dashed line. During the recovery phase (20-24 May) of the storm, variation of the dayglow emission intensities showed a good correlation with the O/N_2 (Figures 5.2q,s) with an average R value of 0.7 (except for 23 May; shown by dotted line). Whereas, variations of the EEJ strength do not show any similarity with the dayglow emission intensities (Figures 5.2q,t).

5.3.2 Geomagnetic storm effect on the GW scale sizes over the low-latitudes

For the analysis so far, we have considered only the daily averaged zenith dayglow emission intensity variations as obtained from Hyderabad. It is clear that there are distinct changes in them between the geomagnetically quiet and disturbed periods. It is obvious that these effects are spread over large spatial locations. As MISE has a large FOV, it has the capability to simultaneously obtain the dayglow variability over a large spatial extent. This enables us to carry out analysis in greater details to obtain the spatial scale sizes in the GW domain that are set up during geomagnetic disturbances at the emission altitudes of 557.7, 630.0, and 777.4 nm dayglow emission intensities.

The slit of MISE was oriented along the zonal direction on most of the days considered in the present work to obtain the dayglow emission intensity variation along the zonal directions and hence, the zonal GW scale sizes. The method of obtaining the spatial distribution of the dayglow emission intensities for all the three emission wavelengths at a given time have been discussed in detail in section

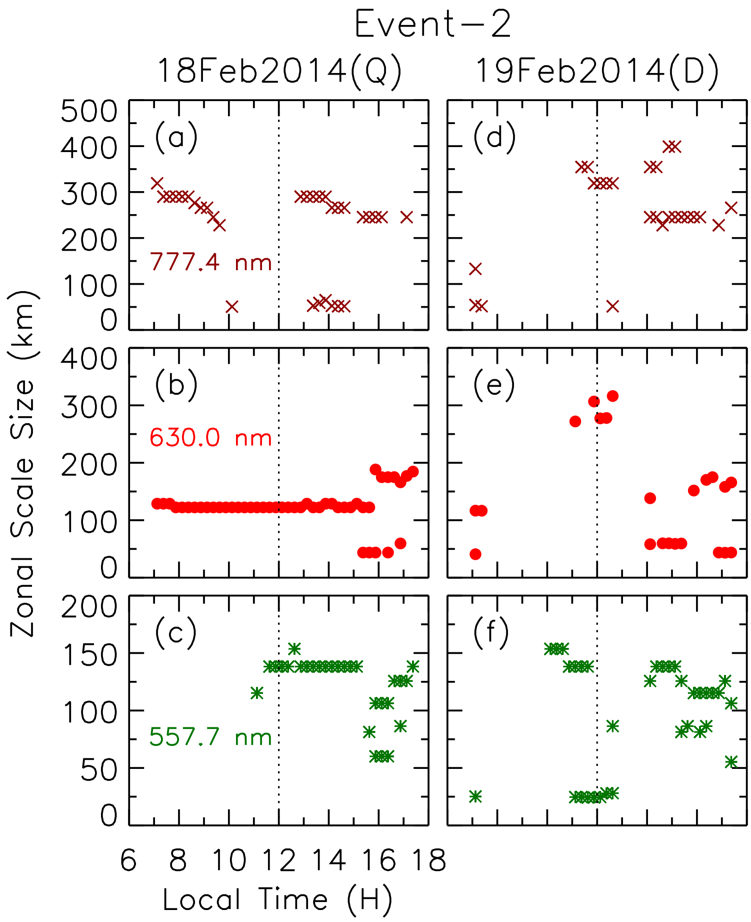

Figure 5.3: Local time (LT) distribution of the zonal scale sizes at the emission altitudes of 777.4 (upper panel, Figures 5.3a,d), 630.0 (middle panel Figures 5.3b,e), and 557.7 nm (bottom panel Figures 5.3c,f) dayglow emission intensities on 18 February 2014 (left column) and 19 February 2014 are shown. The vertical dashed line is drawn at local noon. The LT distribution in the zonal scale sizes is different on the geomagnetically quiet and disturbed days.

2.5.5. This method has been followed to calculate the dominant GW zonal scale sizes in all the three dayglow emission wavelengths for a whole day at a data cadence of 15 minutes.

We have obtained the diurnal distribution of the significant zonal scale sizes for all the three dayglow emissions and compare them between geomagnetically quiet and disturbed days. For this study, we have considered the three geomagnetically disturbed events (Events-2,3,4) as depicted in Figures 5.1, 5.2 above. The couple of days considered in each of the events are marked by two vertical arrows in the upper side of the plots in Figures 5.1b,c,d. In the Event-2, we have considered the data for 18 February 2014 (geomagnetically quiet) (Figures 5.3a-c) and 19 February 2014 (geomagnetically disturbed) (Figures 5.3d-f). The X- and Y-axes show the local time in hours and the zonal scale sizes in km. The vertical dotted line corresponds to local noon. A notable contrast is observed in the diurnal distribution pattern of the zonal scale sizes between these two days. At 777.4 nm emission altitude, the zonal scale sizes of around 200-300 km are seen during forenoon on the quiet day (Figure 5.3a). In afternoon, along with these values, additional zonal scale sizes with smaller values (50 km) are seen. Contrary to this, on the disturbed day no significant zonal scale sizes are seen during forenoon (Figure 5.3d) and during afternoon larger scale sizes of greater than 250 km are seen. A finite possibility does exist that the scale sizes in forenoon on the disturbed day are much larger (beyond the cut-off limit of 425 km). At the emission altitude of 630.0 nm dayglow, 120 km zonal scale sizes are seen throughout the quiet day. After 15 h, the zonal scale sizes of 45 km and 175 km are observed (Figure 5.3b). Surprisingly, on the disturbed day (Figure 5.3e), the 120 km zonal scale sizes are not seen. Rather, larger zonal scale sizes of around 300 km are seen during noon which seem to decrease to smaller scale sizes of around 50 and 150 km in afternoon on the disturbed day. At 130 km altitude, zonal scale sizes of around 140 km are seen during 11-15 h on the quiet day (Figure 5.3c). After 15 h, values of these scale sizes decrease. While on the disturbed day (Figure 5.3f), along with the 140 km scale size, smaller scale sizes of around 25 km are seen during noon and the larger scale sizes seem to decrease in afternoon. On these two days, no contrasting difference is seen in the zonal scale sizes after 15 h at this altitude.

Figures 5.4 and 5.5 are plotted in the same way as explained for Figure 5.3. Figure 5.4 shows the comparison of the zonal scale sizes on 6 March (geomagnetically quiet) and 7 March (geomagnetically disturbed) 2016 (Event-3). At 300 km altitude, 60 km zonal scale sizes are seen during the morning hours (7-10 h) on the quiet day (Figure 5.4a). Whereas, on the disturbed day (Figure 5.4d), along with the 60 km zonal scale sizes, 130 km scale sizes are also seen in the morning hours. On both the days, values of the zonal scale sizes increase during

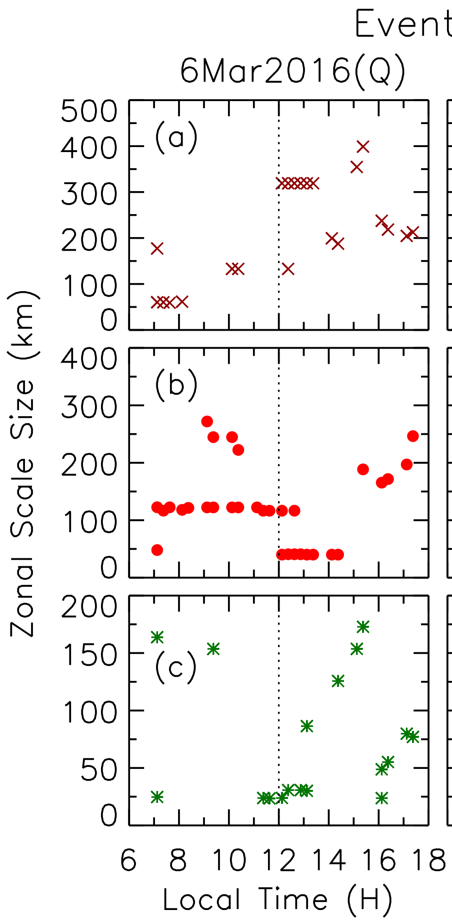

Figure 5.4: Same as in Figure 5.3, but for 6 and 7 March 2016.

afternoon. At 230 km altitude, 120 km zonal scale sizes are seen during forenoon and 50 and 200 km scale sizes are seen during afternoon on both the days. It is to be noted that in addition to these scales, additional scale sizes of 250 km are found to be more significant during forenoon on the disturbed day. At 130 km altitude on both the days, during forenoon no significant scale sizes are seen, whereas, both smaller and larger scale sizes are seen during afternoon. Smaller scale sizes of around 30 km are seen during noon on the quiet day but not on the disturbed day (Figures 5.4c,f).

In the Event-4 (Figure 5.5), we have compared the diurnal distribution of the zonal scale sizes on 10 May (geomagnetically quiet day) and 12 May (geomagnetically disturbed day) 2015. Due to the unfavorable sky conditions, the optical dayglow data could not be obtained on 13 and 14 May 2015, when the geomagnetic disturbance was at its peak. Therefore, we have considered 12 May

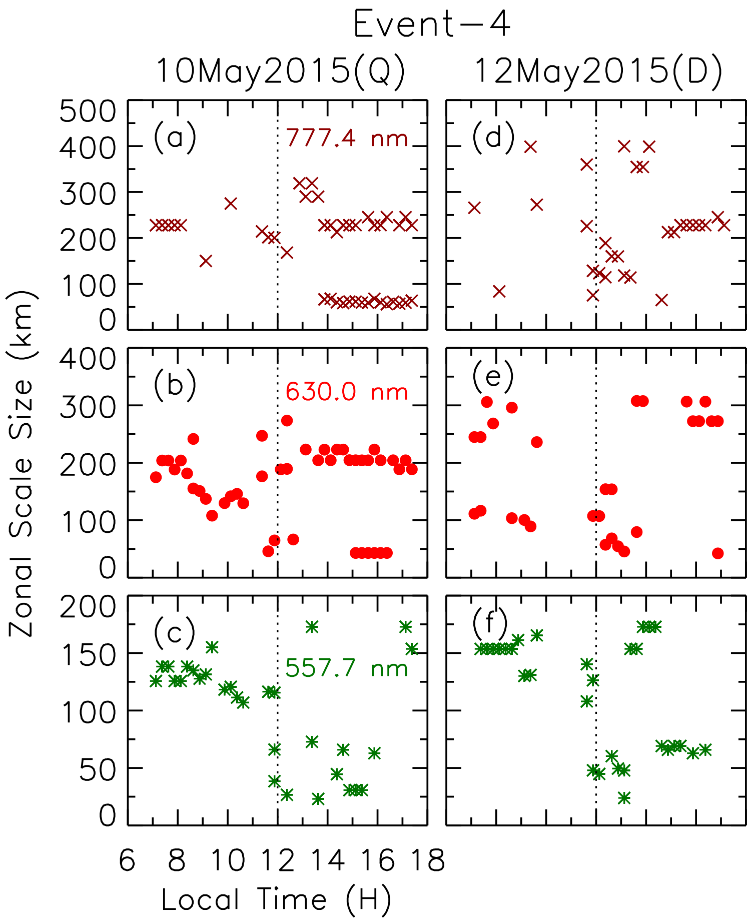

Figure 5.5: Same as in Figure 5.3, but for 10 and 12 May 2015.

2015 as the disturbed day for the comparison. Even though this is not the most geomagnetically disturbed day, this day is within the main phase of the geomagnetic disturbance. The contrast in the distribution of the zonal scale sizes on the two days are clearly noticeable. At the emission altitude of 777.4 nm dayglow, 230 km scale sizes are seen during the morning and afternoon on the quiet day but only during afternoon on the disturbed day. Interestingly, the smaller scale sizes of around 60 km are present during afternoon on the quiet day but not on the disturbed day (Figures 5.5a,d). It is to be noted that on the disturbed day, significant scale sizes are sparse during forenoon. On this day, larger scale sizes are present during afternoon, which are not seen on the quiet day. At the emission altitude of 630.0 nm dayglow, zonal scale sizes decrease from 200 km to 100 km during forenoon and again increase to 200 km during afternoon on the quiet day, whereas, on the disturbed day this type of trend in zonal scale sizes is not seen (Figures 5.5b,e). On the disturbed day, zonal scale sizes of around 100 and 300 km are observed during forenoon. Smaller scale sizes (around 50-150 km) are seen during noon and these scale sizes increase to around 300 km during afternoon (Figure 5.5e). At the emission altitude of 557.7 nm dayglow, on both the days, zonal scale sizes of around 150 km are seen during forenoon (Figures 5.5c,f) and seem to decrease during afternoon. Not much difference is observed in the zonal scale size distribution between these two days at this emission altitude.

Lack of contrast in the diurnal distribution of the zonal scale sizes at the emission altitude of 557.7 nm dayglow between the geomagnetically quiet and disturbed days for all the events considered, could be due to the contributions from dual heights (both upper and lower thermosphere) to the production of 557.7 nm dayglow emission. Although the zenith OI 557.7 nm dayglow emission intensity respond to the neutral density (O/N_2) variations as shown earlier in Figure 5.2, with regard to the GWs in the zonal direction, it may, however, be possible that the lower atmospheric contribution overwhelms the column integrated intensities.

5.4 Discussion

From the results of the three disturbed events (Events-2, 3 and 4 as shown in Figure 5.2) discussed above, it is clear that the dayglow emission intensities at all the three wavelengths show variations with the D_{st} index during geomagnetically disturbed periods. It is to be remembered that these are two independent parameters and therefore, their interdependency has been investigated to understand the process through which they are related. In order to do that both the neutral and the electrodynamic variations that existed on those days have been looked into in greater details.

The optical dayglow emission intensities over low-latitude regions are affected by both the neutral winds and the equatorial electrodynamics. The behavior of the dayglow emission intensities depends both on the nature of ambient neutral winds (magnitude and direction) and strength of the equatorial zonal electric fields. These effects show seasonal variations. During geomagnetic disturbances, the ambient background conditions change when compared to the quiet times. During geomagnetically quiet conditions, variations of low-latitude dayglow emission intensities are primarily governed by the equatorial electrodynamics and hence, the day-to-day averaged intensity variations showed similarity with that of the EEJ strength (Figures 5.2b,e; Event-1). This is because, an increase in the EEJ strength causes an increase in the strength of the plasma fountain, thereby bringing in greater electron densities (reactants for OI dayglow) to the off-equatorial latitudes, such as Hyderabad. This contributes to greater dayglow emission intensities. If a geomagnetic disturbance occurs, TADs and TIDs are set up at high-latitudes. Due to the high- to low-latitude wind circulation, the relative atomic to molecular nitrogen contribution (O/N_2) varies globally. Such variations of O/N_2 over low-latitudes seem to govern the oxygen dayglow emission intensities and hence, during this period, they show similar type of variations with O/N_2 instead of the EEJ strength (as seen in Event-2). During equinoxes, when the meridional wind speeds are small, significant similarities are observed between the dayglow emission intensities and the EEJ strengths (Figures 5.2l,q) and is also consistent with our earlier observations [*Karan et al.*, 2016], which is discussed in detail in Chapter-3. It is to be noted that during the moderate storm in solstice period of May 2015 (Event-4), the dayglow emission intensities vary with O/N_2. However, during geomagnetically quiet period in May 1 to 5, the dayglow emission intensities showed similar variation with the O/N_2, the EEJ strength and the IEC. It is to be noted that during the present investigation, the daily mean value of the dayglow emission intensities are compared with the other parameters to get a broad disturbed time picture of the equatorial- and low-latitude thermosphere. However, investigations of the daily variations in the dayglow emission intensities will give more insights into the process of the effect of geomagnetic disturbances on the thermospheric behavior. Such investigations will be carried out in future.

The day-to-day variations in the optical dayglow emission intensities over low-latitudes are observed to be affected by the interplay between the neutral dynamics and the equatorial electrodynamics under varying geophysical conditions. However, a broad systematic variations between the dayglow emission intensities at all the three wavelengths and the O/N_2 during all these four months of observations can be seen in Figure 5.2. Both the dayglow emission intensities and the O/N_2 gradually increase from January to March and again decrease towards May. But, EEJ strength does not show such type of variations in all these four months.

The EEJ strength and IEC are expected to show similar variations during geomagnetically quiet periods, as indeed observed during the quiet periods of all the events described in Figures 5.2e,j,o,t. On the days with peak geomagnetic disturbances (i.e. minimum D_{st} value) in the months of February (24) and May (13 and 19), as shown by vertical dashed lines, the EEJ strength and IEC do not show similar variation. Whereas, on the days with peak disturbances in March (7 and 17) the EEJ strength and IEC showed similar variations, which is also consistent with the variations in the dayglow emission intensities as discussed above. It is known that during geomagnetic disturbances, the equatorial zonal electric field can be modified because of the prompt penetration electric field and disturbance dynamo electric field effects which do affect the daytime upper atmospheric behavior [e.g., *Richmond and Matsushita*, 1975; *Pallamraju et al.*, 2004b; *Chakrabarty et al.*, 2010]. Thus, an enhancement or decrement of the equatorial zonal electric field under the influence of prompt and/or disturbance dynamo electric fields over the equatorial region can be understood to be the cause for the dissimilar behavior of the dayglow emission intensity with the EEJ strength. Hence, in different seasons the effect of the geomagnetic disturbances on the optical neutral dayglow emissions are different as they depend on the ambient conditions.

As discussed above and also in Chapter-3 that the neutral optical dayglow emission intensities over low-latitude regions are sensitive to the equatorial electrodynamics. It was extensively discussed that the diurnal behavior of the dayglow emission intensities are symmetric/asymmetric with respect to the local noon on the days with weak/strong equatorial electric field strength. The extent of symmetric or asymmetric diurnal behavior of the dayglow emission intensity was estimated by a parameter called Asymmetricity in Time (AT). The diurnal behavior of dayglow was considered as symmetric or asymmetric for AT $\leq$ 0.4h or AT $>$ 0.4h, respectively (Discussed in detail in Chapter-3. In Chapter-4 of the thesis, the diurnal distribution in the zonal scale sizes on geomagnetically quiet days (Ap values smaller than 22) with symmetric and asymmetric diurnal behavior during December 2013 to March 2014 is shown in Figure 4.10. Figures 4.10(a,b,c) and (d,e,f) show the diurnal distribution of the zonal scale sizes on two sample days, with symmetric and asymmetric diurnal behavior in the zenith emission intensities at all the three emission wavelengths. The contrast in the distribution of the zonal scale sizes on these two days is clearly noticeable. The zonal scale size distributions on all the days with symmetric/asymmetric diurnal emission intensity behavior are overlaid and shown in Figures 4.10(g,h,i) and (j,k,l), respectively. As discussed in earlier results, for geomagnetic quiet times, it can be seen that the diurnal distribution in the scale sizes are (i) conspicuously similar on the days with a particular (symmetric/asymmetric) diurnal behavior, and (ii) distinctly different on the days with symmetric diurnal behavior as compared to the days with asymmetric diurnal behavior [*Karan and Pallamraju*, 2017]. In the present work, the diurnal behavior of the three dayglow emission intensities on the two days considered in Event-2 (Figure 5.3), are asymmetric in nature (the AT values for 777.4, 630.0, and 557.7 nm dayglow emission intensities are 0.5 h, 0.9 h, and 1.7 h on 18 February 2014 and 1.0 h, 1.6 h, and 0.6 h on 19 February 2014, respectively). It is interesting to compare the results of zonal scale sizes for days with asymmetric diurnal dayglow behavior for geomagnetically quiet days (Figure 4.10) with those of present results of geomagnetically disturbed days (Figure 5.3). The diurnal distribution of the scale sizes for all the dayglow emissions on 18 February (Figures 5.3a,b,c) show similar pattern as seen for the days with asymmetric diurnal behavior in Figures 4.10g,h,i. Contrary to this, diurnal distribution in the zonal scale sizes on 19 February 2014 show altogether a different pattern. Even though both these days showed asymmetric diurnal pattern in their zenith intensities, the contrast seen in the diurnal pattern of the gravity wave zonal scale sizes between these two days (as discussed before in Figures 5.3, 5.4, 5.5) is attributed to the effect of geomagnetic disturbances on the thermospheric neutral wave dynamics. On the dates of the optical data considered in Events-3 and 4, not all the emissions show a common (symmetric/asymmetric) diurnal behavior to enable such a comparison as carried out for Event-2. The diurnal distribution in the GW zonal scale sizes show contrast in the quiet and disturbed day in the three events (Figures 5.3, 5.4, 5.5) as described above.

However, it is to be noted that the scale size distribution pattern on the disturbed days in different seasons do not show a common type of pattern. The scale sizes and propagation directions of the GWs depend on the thermospheric ambient neutral winds [*Hines*, 1960], which has a seasonal dependence. Thus, the effect of the geomagnetic disturbances on the low-latitude thermospheric wave dynamics is unlikely to be the same in different seasons. Moreover, localized effects, if any, can also be modified due to the propagation of TADs during geomagnetically disturbed periods. Such compositional variations that are brought in due to the meridional circulations during the disturbance periods over the low-latitudes will also affect the thermospheric wave dynamics over the equatorial- and low-latitudes. The tides also play an important role in bringing the diurnal and seasonal variations in the composition of the atmosphere. Thus, it can have an effect on both the optical dayglow emission intensities and the thermospheric O/N_2 simultaneously over low-latitudes. However, it is difficult to decipher the relative contribution of the tides and O/N_2 in the dayglow. The intricacies of the effects due to various sources on the upper atmospheric GWs need further investigations. The effect of the compositional variations due to the geomagnetic disturbances on the low-latitude thermospheric neutral wave dynamics is observed to be more during the solstices (Events-2 and 4) than during the equinoxes (Event-3).

During geomagnetic disturbances, the TADs and TIDs move from the polar to the equatorial- and low-latitude regions. As a result, the neutral waves *en route* get modified. Moreover, sometimes the equatorial electric field also changes because of both prompt penetration and disturbance dynamo electric fields. These electric fields re-distribute the ion densities over the equatorial- and low-latitude regions through processes such as, EIA and ETWA. The transported ion densities alter the neutral densities through the ion-neutral collisions. Thereby, changes are brought in the wave structure also. The modification of the neutral wave dynamics depends on the ambient thermospheric conditions. As the ambient conditions vary from season to season, accordingly the effect of the storm on the equatorial neutral wave dynamics will vary. In some seasons, during the SSW events, new meridional circulation from the pole to the equator is set up in the MLT altitudes [*Laskar and Pallamraju*, 2014]. Any geomagnetic disturbances during this period may affect the neutral wave dynamics at the low-latitude regions differently than in the case of non-SSW events, and it is difficult to assess their relative contribution to the changes in the GW regime. It is to be noted that the geomagnetic disturbance will bring changes in the zonal, meridional, and vertical scale sizes along with their path of propagation in the thermospheric waves over the equatorial- and low-latitude regions. In order to study this, large FOV optical dayglow measurements along both the zonal and meridional directions are required [*Pallamraju et al.*, 2016]. However, in the present study, we have investigated the behavior of zonal scale sizes only.

5.5 Conclusion

To investigate the effect of the geomagnetic disturbances on the equatorial- and low-latitude upper atmosphere, neutral optical oxygen dayglow emission intensities at three wavelengths were obtained by using a large FOV high resolution spectrograph, MISE. The mean zenith dayglow emission intensities showed different types of variations with those of the D_{st} index during geomagnetic disturbances in different seasons. Such similarity between these two independently measured parameters points to a clear coupling between the magnetosphere-thermosphere-ionosphere system. Further, variations of the mean zenith dayglow emission intensities, EEJ strength, IEC, and the thermospheric O/N_2 have been studied during three geomagnetic disturbance events, which occurred in different seasons. During winter and summer solstices, dayglow emission intensities show similar variations with O/N_2. This is attributed to the effect of the geomagnetic disturbances over equatorial- and low-latitude thermosphere. During equinox period, the dayglow emission intensities show similar variations with the EEJ strength indicating a dominance of the equatorial electric fields over the storm influenced neutral wave dynamics during the equinoxes. This clearly shows that there is a seasonal dependence of the electrodynamic vs. neutral dynamics over the equatorial- and low-latitudes. Moreover, from this large FOV dayglow measurements, wave number spectral analyses have been carried out to obtain the GW zonal scale sizes at three multiple altitudes. Diurnal distribution in the GW zonal scale sizes are studied in different seasons on a case-by-case basis by comparing the behavior of the quiet and the disturbed days in each season. Contrasting distributions in the diurnal variations of the zonal scale sizes were noticed in different seasons. This shows that changes are brought-in in the zonal GW scale sizes during geomagnetic disturbances irrespective of the season of the storm occurrence. Such first of the kind results on the effect of geomagnetic disturbances on the equatorial- and low-latitude thermospheric zonal wave dynamics as inferred from large FOV dayglow measurements have brought to light new information on the neutral wave dynamics that exists in the daytime thermosphere. To extend the capability, we have carried out further analysis to obtain the scale size information along both horizontal and vertical directions, which will be discussed in the next chapter.

Chapter 6

Daytime Three Dimensional Wave Characteristics Over Low-Latitudes

6.1 Introduction

Importance of the neutral wind and the wave dynamics in contributing to the day-to-day, diurnal, and seasonal behavior of the upper atmosphere both during geomagnetically quiet and disturbed periods is well-known [e.g., *Mayr et al.*, 1978]. The inter-hemispheric winds in solstices, westward/eastward winds during the daytime/nighttime, and equatorward winds and waves due to the Joule heating at high-latitudes during geomagnetic storms are of great interest to the research community as these alter the composition, and bring about the latitudinal changes in the neutral densities [*Mayr et al.*, 1978; *Immel et al.*, 2001]. Effect of the thermospheric wind and waves in bringing variations on the coupling process of the thermosphere and ionosphere during various space weather conditions have been discussed in previous chapters of this thesis. Satellite-based measurements have provided a broad picture of the neutral winds [e.g., *Herrero et al.*, 1988; *Shepherd et al.*, 1993a] which in combination with the ground-based measurements have formed the basis for empirical wind models [e.g., *Hedin et al.*, 1996; *Drob et al.*, 2015]. It can be appreciated that, unlike winds which can be measured by both the ground-based [e.g., *Meriwether et al.*, 1986; *Makela et al.*, 2013] and satellite-based platforms [e.g., *Spencer et al.*, 1981; *Shepherd et al.*, 1993b; *Killeen et al.*, 2006], the neutral wave scale sizes (scale size is a different terminology used for the wavelength of the atmospheric waves) and periodicities in the daytime can only be measured by the ground-based observations of the optical airglow emissions that are carried out over a large FOV. It is shown that the density fluctuations due to the waves alter the reactants that produce the nightglow/dayglow and thus, contribute to the modulations in their intensities [*Teitelbaum et al.*, 1981; *Shepherd et al.*, 1993b; *Pallamraju et al.*, 2010]. While nightglow imaging has been possible to obtain the wave features in two-dimensions [e.g., *Taylor et al.*, 1995; *Mendillo et al.*, 1997; *Shiokawa et al.*, 2009; *Lakshmi Narayanan et al.*, 2010], measurements during the daytime, however, remain a challenge. This is essentially due to the difficulty of using two-dimensional optical imaging techniques in the daytime as direct incidence of sunlight renders the images unusable.

In terms of two dimensional information on the daytime thermospheric behavior obtained from the ground-based measurements, to the best our knowledge there has been only one report in peer reviewed literature on the observations of the OI 630.0 nm dayglow emission intensities and its response to the equatorial processes, and was carried out using the daytime photometric technique [*Pallamraju and Sridharan*, 1998a]. In that experiment, a mirror scanner attached to the dayglow photometer sequentially rotated in the azimuth and elevation angles in a programmed manner to obtain the two-dimensional intensity maps of OI 630.0 nm dayglow emissions. For an integration time of 20 sec per datum point, a two-dimensional map was obtained in 12 minute. It was assumed that the wave dynamics remains constant between the successive scans. These maps clearly showed the movement of the large scale features, such as the EIA, in low-latitudes. However, as the measurements along the zonal and meridional directions were not obtained simultaneously, it was not possible to obtain information on the scale sizes of the neutral waves using such a method.

However, using the high spectral resolution spectrograph MISE, it is now possible to obtain the simultaneous dayglow emission intensity data at multiple wavelengths (OI 557.7, 630.0, and 777.4 nm) over a large FOV. The details about these three dayglow emission intensities, MISE and the method of extraction of dayglow emission intensities have been explained in sections 2.2 and 2.3. The method of obtaining the scale sizes from the space varying dayglow emission intensities have been explained in detail in section 2.5.5. Using this method, scale sizes along the zonal directions have been obtained at the emanating altitudes of the three dayglow emissions of our interest (i.e. OI 557.7, 630.0, and 777.5 nm) as measured by MISE. Many new and exciting results have come out from the zonal scale size information of the thermospheric waves over the low-latitudes. Distribution pattern of the zonal scale sizes are found to be different on the days with strong and weaker equatorial electrodynamics, which is discussed in detail in Chapter-4. Also, behavior of the zonal scale sizes and their diurnal distribution patterns are affected during geomagnetic disturbance periods, which is discussed in Chapter-5.

The waves in the atmosphere propagate along an inclined plane with respect to the horizontal due to the vertical and horizontal gradients in the density, temperature, and pressure. Thus, the atmospheric waves have both horizontal and vertical components and are three dimensional in nature. In this work, we have carried out analysis to obtain three dimensional daytime thermospheric wave dynamics. For this we have obtained the dayglow emission intensities along both the zonal and meridional directions in a specially organized observational campaign. From this spatial varying information of the dayglow emission intensities in the orthogonal directions, the wave features in the horizontal directions (e.g. horizontal scale sizes, time periods, phase speed, horizontal phase propagation direction etc.) at the three altitudes of oxygen emissions have been obtained through wave number spectral analysis. Such measurements on horizontal scale sizes (in two dimensions) have hitherto been not reported. Moreover, the measured values have been used in conjunction with the GW dispersion relation [*Hines*, 1960] to calculate the plausible wave features in the vertical direction. Thus, this study reports the first results on the three-dimensional wave characteristics at different altitudes in the daytime upper atmosphere.

6.2 Measurement Technique And Data Analysis

Details about the three types of dayglow emission intensities and MISE are discussed in sections 2.2 and 2.3. As MISE is a large FOV slit spectrograph, spatial information of the dayglow emission intensities can be obtained along the slit orientation as shown in Chapters-4 and 5. For the present investigation, it is required that the dayglow emission intensity be obtained along both the zonal and meridional directions. Hence, orientation of MISE was changed between the orthogonal directions in each half an hour and the dayglow data were obtained. This was repeated throughout the day. The spatial coverage at the emission altitude of 557.7, 630.0, and 777.4 nm dayglow emissions are 3^0, 5.5^0, and 7.3^0 (~340, 600, and 800 km) in latitude/longitude for MISE (depending on its orientation along meridional/zonal direction).

The description of the spatial resolution and spatial uncertainties possible for each emission wavelength, along with the spectral analysis to obtain the scale sizes in the zonal direction has been described in detail in section 2.5.5. For the present work reported in this chapter, after around 30 minutes of operation in a particular orientation, the spectrograph is rotated to its orthogonal position. The data cadence for obtaining information on the dayglow emission intensities along a given orientation is 5 minutes, however, data are averaged for 15 minutes. Spectral analyses have been carried out for each of the 15-minutes of data along a spatial orientation and values of wave numbers k_x (zonal) and k_y (meridional) (and hence, scale sizes λ_x and λ_y) that are statistically significant (greater than 90% false-alarm-limit, FAL) are obtained. Out of all the dominant scale sizes, the lower cut-offs are taken to be 22, 40, and 50 km considering the 2-pixel resolution as discussed in section 2.5.5, for 557.7, 630.0, and 777.4 nm emission wavelengths. To ensure that at least two waves exist in the observed spatial extent, scale sizes which are greater than half the spatial extent have not been considered for the analysis. Taking the spatial uncertainties (due to 2-pixel resolution) into account, the higher cut-offs turn out to be 181, 320, and 425 km at the emission altitude of 557.7, 630.0, and 777.4 nm dayglow emissions. The horizontal wave vector k_H, and hence, the horizontal scale size λ_H, is estimated using the values of k_x and k_y measured alternatively ($k_H^2 = k_x^2 + k_y^2$). The phase propagation angle of these waves, (θ_H), is given as $tan^{-1}(k_y/k_x)$.

6.3 Results

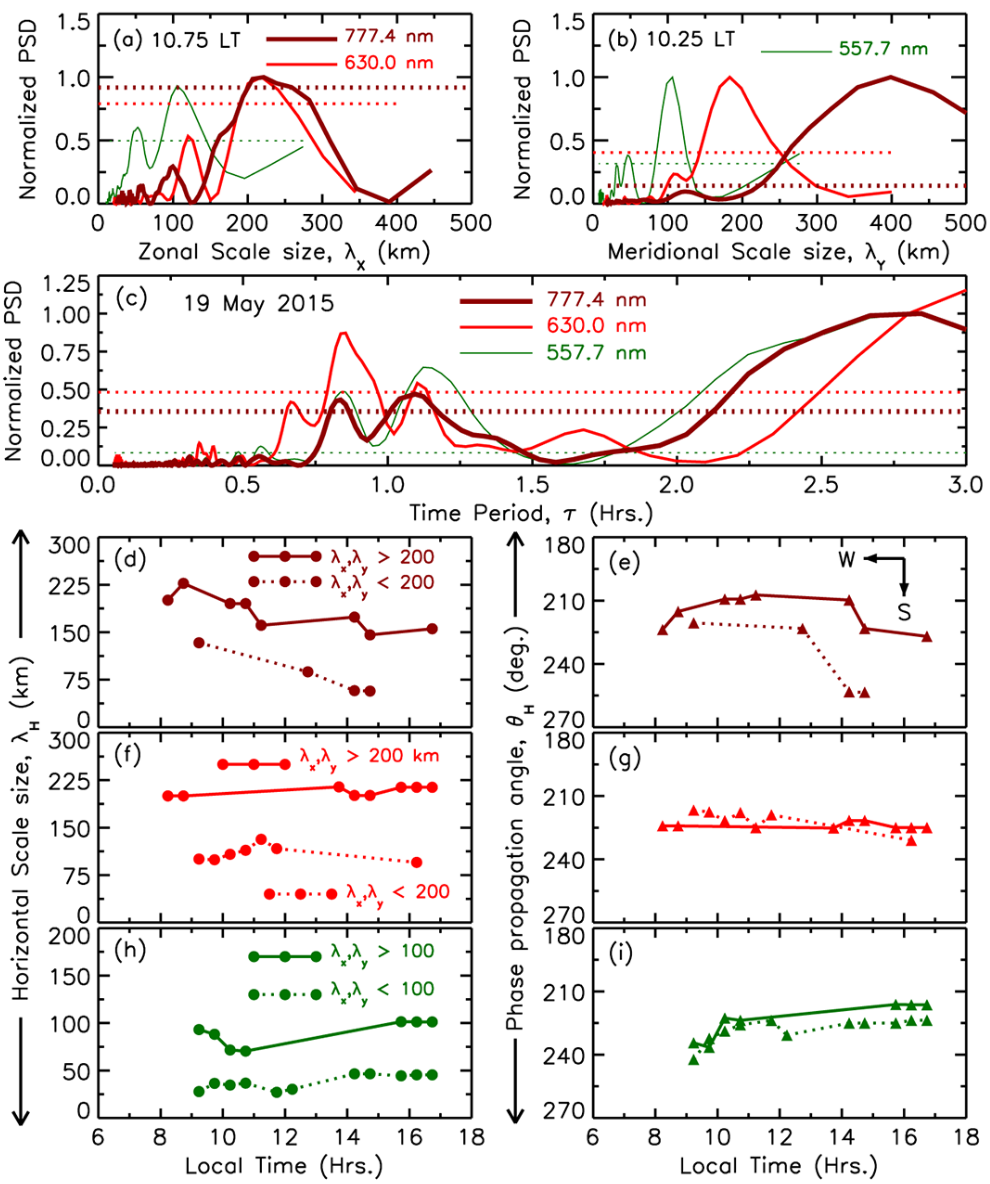

Figure 6.1: Wavenumber spectral analysis showing (a and b) λ_x, λ_y, (c) time period, τ, (d,f, and h) horizontal scale size, λ_H, and (e,g, and i) the phase propagation angle, θ_H counterclockwise from west.

Figures 6.1a and b show sample results of the wave number spectral analysis carried out of the dayglow intensities at the three emission wavelengths obtained along the zonal and meridional orientations at two times on 19 May 2015. The X- and Y-axes show the scale sizes in km and the normalized power spectral density for each of the wavelengths. The dotted lines show the 90% FAL. Using the data cadence of 5 min for zenithal dayglow emission intensities for all the three emission wavelengths, Lomb-Scargle periodogram analysis [*Lomb*, 1976; *Scargle*, 1982] has been carried out to arrive at the prominent periodicities (τ) of GWs for this day. These values are 32.8 ± 1.9, 51.1 ± 5.3 and 69.1 ± 13.9 min for the emissions corresponding to 557.7 nm; 51.2 ± 1.9 and 66.1 ± 6.7 min for 630.0 nm; and 50.2 ± 5.1 and 65.6 ± 11.6 min for 777.4 nm emissions (Figure 6.1c). As the variations in all the emission intensities show a prominent common time period of around 51 min, the information on the values of λ_x and λ_y arrived at within a gap of just 30 min is considered together for estimating the horizontal scale sizes. Thus, the values of λ_H [$= \lambda_x \lambda_y/(\lambda_x^2+\lambda_y^2)^{1/2}$] for 10.5 LT turn out to be 74, 142, and 185 km at the heights corresponding to the emission altitude of 557.7, 630.0, and 777.4 nm dayglow. It should be noted that a smaller scale size of 53 and 46 km in 557.7 nm emission at 10.75 and 10.25 LT in the zonal and meridional directions will contribute to another value of λ_H. The zonal/meridional scale sizes obtained at a given time are used twice in conjunction with the preceding and succeeding values of meridional/zonal scale sizes to yield the λ_H at a cadence of half an hour.

Such analyses as described above have been carried out for all the times of this day at all the emission wavelengths, and the resulting behavior is shown in Figures 6.1d-i for λ_H (in km; left column) and the phase propagation angle (θ_H, in degrees; right column) for 777.4 nm (Figures 6.1d and e), 630.0 nm (Figures 6.1f and g), and 557.7 nm (Figures 6.1h and i) dayglow. To maintain the fidelity of wave modes, the larger scale sizes in λ_x have been combined with the larger values of λ_y and the smaller λ_x with smaller λ_y to calculate the values of λ_H and θ_H. In doing so, arbitrary boundaries of 200 and 100 km are considered for 777.4 nm and 630.0 nm; and 557.7 nm dayglow emission altitudes (Figures 6.1d, f, and h). It can be noted that on this day the magnitudes of λ_H progressively decrease with local time at 777.4 nm emission altitude while those at 557.7 nm increase with local time and the ones at 630.0 nm emission altitude stay reasonably unchanged throughout the day. Interestingly, the corresponding propagation angles (in the range of 207^0-253^0, counterclockwise from east) seem to indicate a rotation in the wave orientations with altitude as a function of LT. That is, at higher/lower altitudes the waves seem to be moving away from/closer to the west. The cause for such new aspects is to be investigated.

During the nighttime conditions, propagation characteristics of the waves are inferred by comparing subsequent two-dimensional airglow images. For daytime conditions, however, this process is ineffective as generally there exist more production mechanisms for dayglow emissions in comparison to usually one for nightglow. For 557.7 nm and 630.0 nm dayglow, the photoelectron and photodissociation production mechanisms can contribute up to 70% of the total emission intensities. Although these mechanisms do not vary in the GW/tidal time scales [*Solomon and Abreu*, 1989; *Sridharan et al.*, 1992b], they contribute to a dc shift in the emission intensity, and as a consequence, the wave motion is not apparent in the column integrated emissions. The 777.4 nm dayglow emission is also affected by such an effect as the background electron densities in the F region too increase with rise in solar elevation angle. Therefore, to remove the dc contribution and to discern the propagation direction of the waves at each of the emission altitudes during the daytime, we have considered the power in the dominant scale sizes at a given time by using a band-pass filter of widths of 22, 40, and 50 km for 557.7, 630.0, and 777.4 nm, respectively, centered at the peak scale sizes greater than the FAL, as described in [*Hocke and Kämpfer*, 2009]. The power thus isolated in the Fourier domain is subjected to inverse fourier transform to obtain the emission intensity modulations caused by these waves. Independent keograms of the emission intensity modulations due to both the smaller and the larger scale sizes as mentioned above were generated for 777.7, 630.0 and 557.7 nm emission wavelengths and are shown in Figures 6.2, 6.3, and 6.4, respectively.

In all these figures the left/right columns correspond to the meridional/zonal

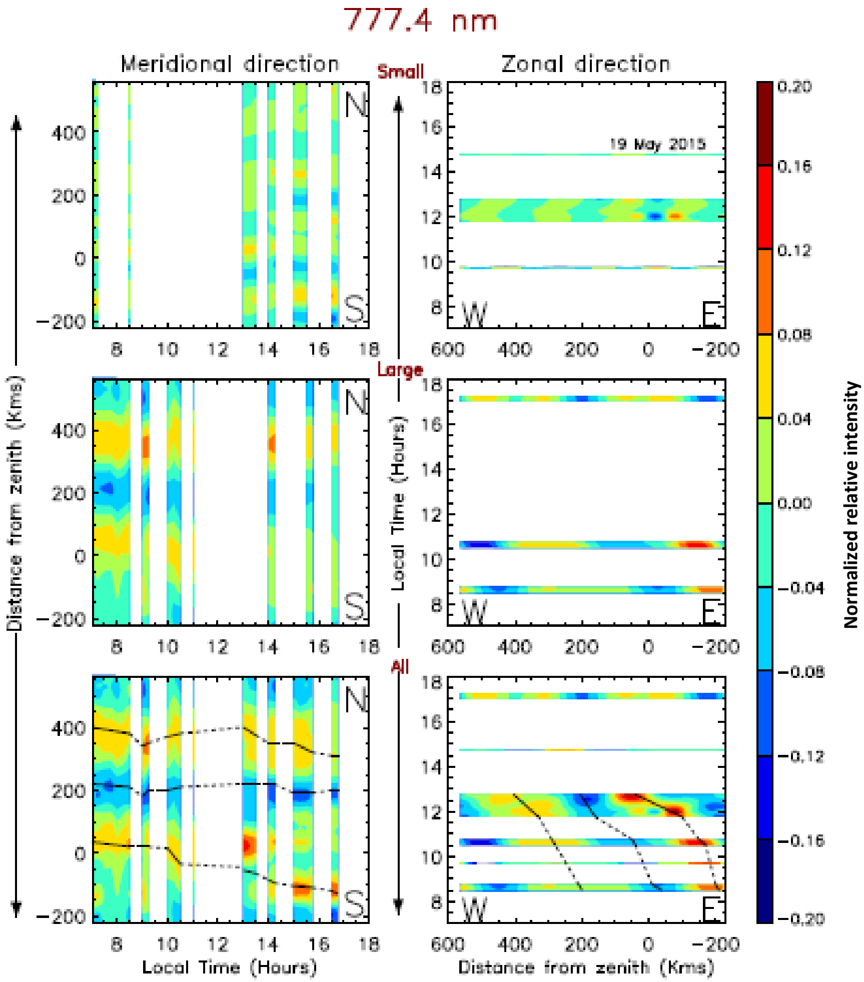

Figure 6.2: Normalized relative dayglow emission intensity variations at 777.4 nm wavelength obtained using band-pass filter centered on the dominant scale sizes shown in Figure 6.1 for 19 May 2015. Top row: (Smaller scale sizes <200 km), Middle row: (larger scale sizes >200 km), Bottom row: All the scale sizes combined. Left/right columns show the meridional/zonal scale sizes.

scale sizes. The X- and Y-axes on the left column show the local time and the distance from the zenith in the meridional direction, whereas, on the right column they show the distance from the zenith along the zonal direction and the local time, respectively. Here, the local time is considered corresponding to the zenith longitude. The colors indicate the normalized relative emission intensity variations. Due to the technical difficulties in the viewing geometry, the data in the southern/eastern directions extend to smaller distances from the zenith compared to the northern/western directions as also mentioned earlier in Chapter-4. The whites in between the scans indicate gaps due to alternating nature of data

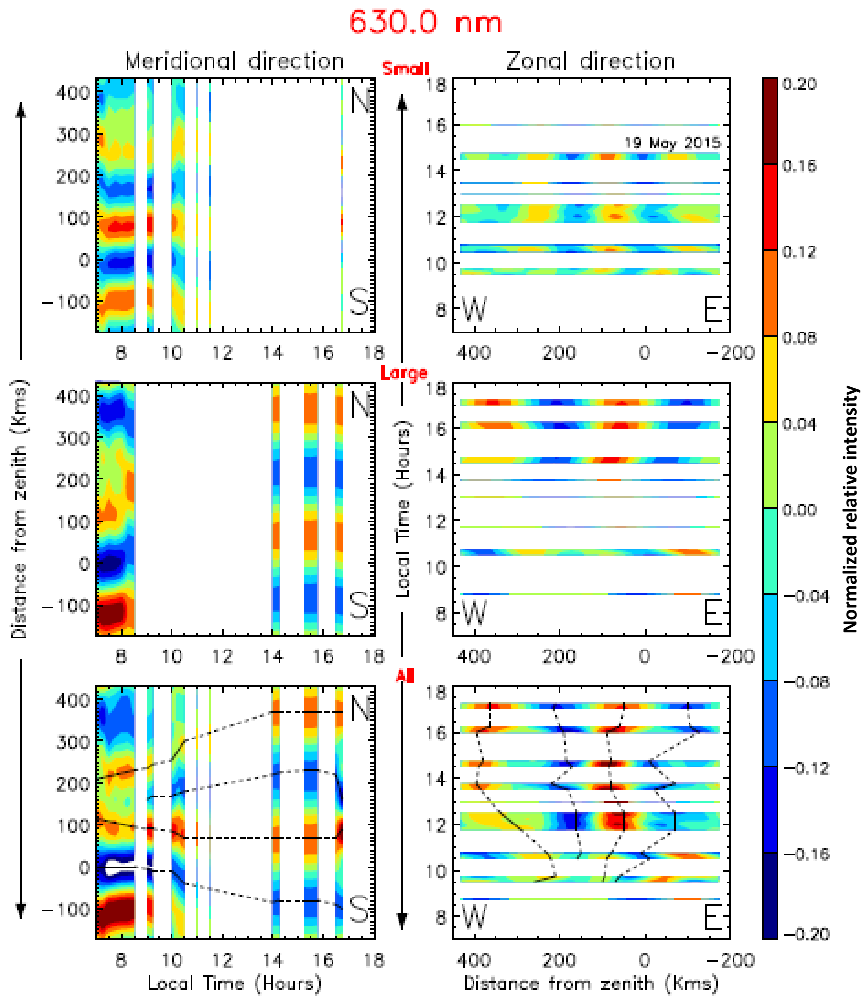

Figure 6.3: Same as Figure 6.2 but for 630.0 nm dayglow emission wavelength.

acquisition and/or to the absence of statistically significant power in any of the scales at that time. The upper/middle panels show the keograms of the intensity modulations due to smaller/larger scale sizes, respectively. As the propagation angles between the smaller/larger scale sizes at each of the emission heights were similar (can be seen in Figures 6.1e,g,i), they have been combined and shown in the bottom panels of Figures 6.2, 6.3 and 6.4. For better comparison and visualization of the movement of the crests and troughs in the emission intensity modulation at all the three wavelengths, plots in the bottom panels of Figures 6.2, 6.3 and 6.4 are combined and shown in Figure 6.5. Figures 6.5(a,b), (c,d) and (e,f) show the keograms for 777.4, 630.0, and 557.7 nm emission wavelengths, respectively. Attention is drawn to the movement of crests and troughs through the dotted line. The yellow/blue color represents the crest/trough of the waves.

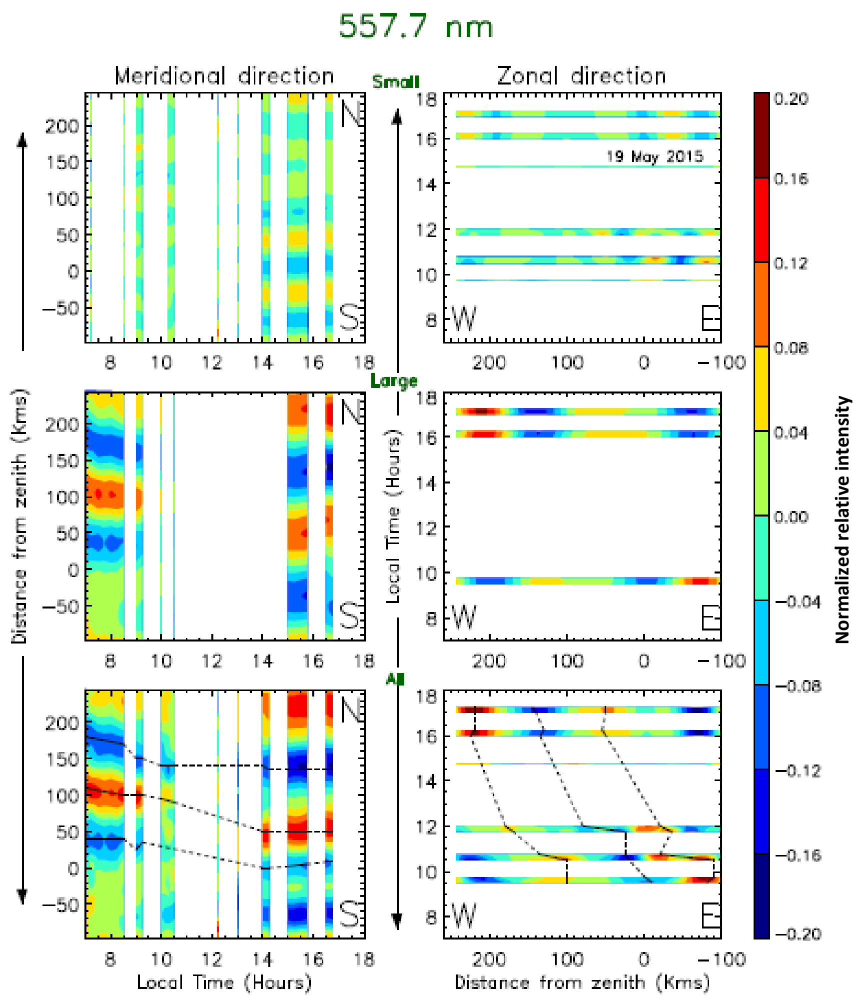

Figure 6.4: Same as Figure 6.2 but for 557.7 nm dayglow emission wavelength. Here the small/large scales correspond to smaller/greater than 100 km.

The keograms show that broadly there is a westward movement of waves at all the emission heights which are more prominent in the 777.4 nm and 557.7 nm emissions. Further, there is a southward movement of waves which is prominent in the 557.7 nm (during forenoon) and 777.4 nm emissions (during afternoon). The resultant propagation angle, θ_H, is shown in Figure 6.6. In 630.0 nm emissions, the power in the smaller/larger scale sizes were less than the FAL in afternoon/forenoon and so, when the daily behavior is seen, it gives an appearance of expansion in scale sizes from forenoon to afternoon (the inter crest separation increases with time). Another intriguing observation is that the waves seen in 630.0 nm dayglow emission intensities west of zenith move westward and those on the east move eastward. In similar way, for 630.0 nm dayglow emission in-

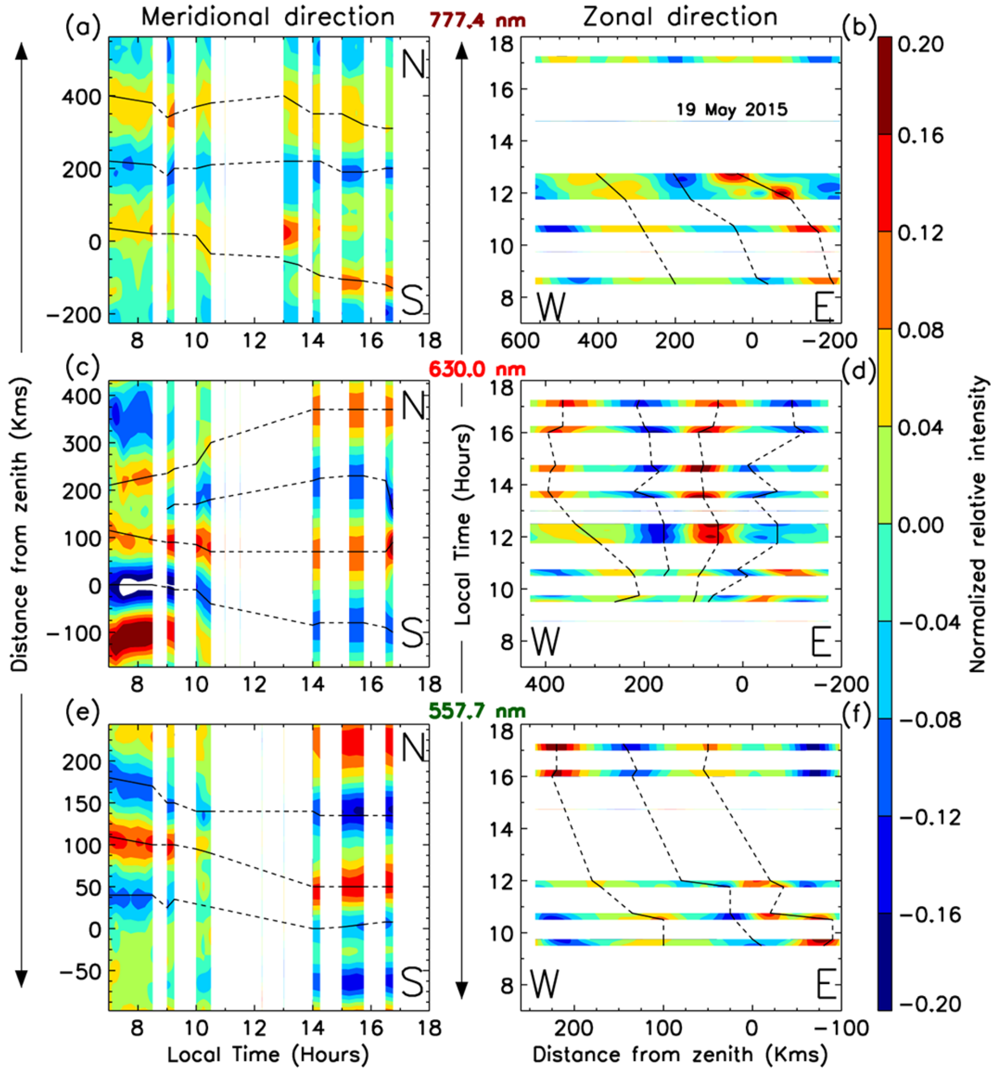

Figure 6.5: Normalized relative dayglow emission intensity variations obtained using band-pass filter centered on the dominant scale sizes shown in Figure 6.1 for 19 May 2015. Left/right columns show the meridional/zonal scale sizes. Westward and southward phase propagations can be seen.

tensities, the waves seen in the north of the zenith move northward, whereas, the waves seen in the south of the zenith move southward. The cause for such a movement is being investigated. Thus, a net southwestward propagation of the wave is observed at the emission altitudes of the three dayglow emissions.

Figures 6.6a and 6.6b shows the measured horizontal scale sizes, λ_H, and the corresponding phase velocities ($c_H = \omega/k_H$) as a function of the local time. The propagation angles, θ_H (solid arrows), and the propagation angles of the model neutral wind, θ_U (dotted arrows), at the emission altitudes of the three

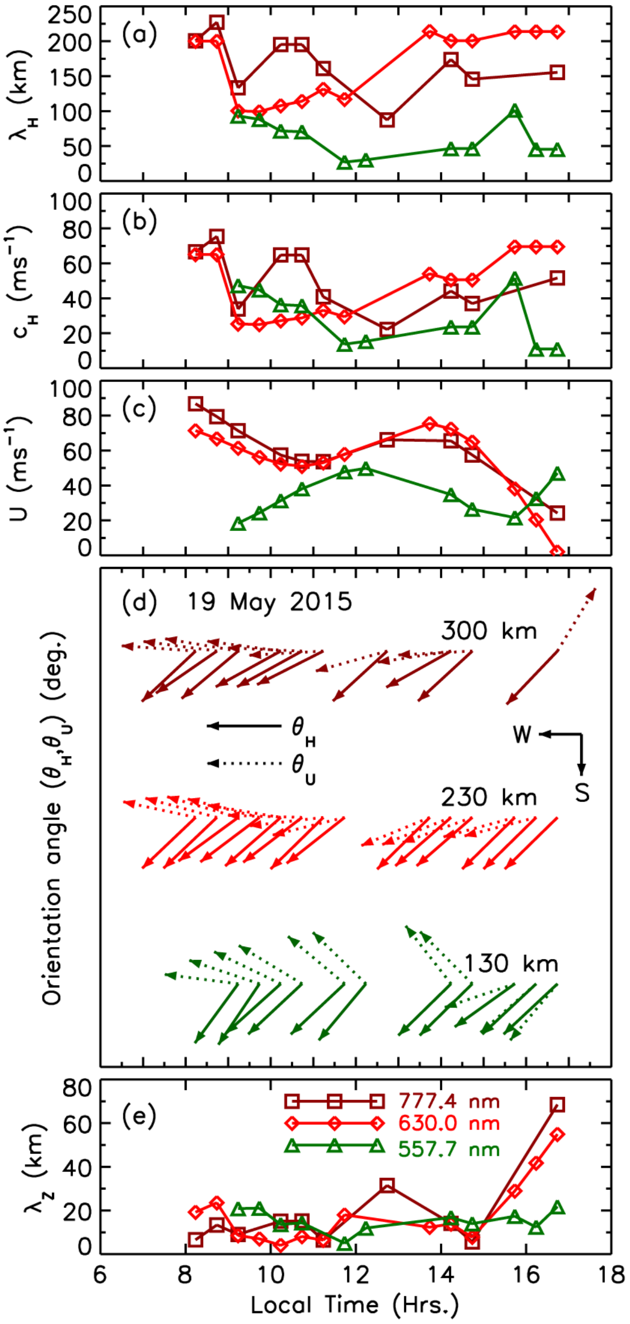

Figure 6.6: (a) the horizontal scale sizes (b) phase speeds (c) HWM14 model wind speeds, (d) wave propagation (solid lines) and the neutral wind (dashed) directions at the three emission altitudes, (e) vertical scale sizes calculated with above values as inputs into GW dispersion relationship.

dayglow emissions are shown in Figure 6.6d). These are the first results on the characteristics (λ_H, θ_H, τ, and c_H) of the two-dimensional wave behavior in the daytime upper atmosphere.

6.4 Discussion

In order to appreciate the results on the daytime wave dynamics better, they are compared with the known characteristics that exist in the nighttime. From the OH and O_2 nightglow imaging measurements, the horizontal scale sizes and the phase speeds have been found to be in the range of 10-60 km and 20-100 ms^{-1}, with a predominant northeastward/southwestward motion (depending on season) [*Nakamura et al.*, 1998; *Taylor et al.*, 1995; *Shiokawa et al.*, 2009; *Lakshmi Narayanan et al.*, 2010], which were obtained from the middle- and low-latitudes. These parameters as seen from the present study for 557.7 nm dayglow emission intensities (which emanate from around 40 km above the OH/O_2 emission altitudes) are 27-101 km and 7-52 ms^{-1}. With regard to the thermospheric emissions, the nightglow 630.0 nm imager data reveal the scale sizes to be 100-400 km, periodicities of 30-150 min, and phase speeds of 50-150 ms^{-1} with a predominant movement in south/southwestern direction [*Taylor et al.*, 1998; *Shiokawa et al.*, 2009]. For 19 May 2015, these values were found to be 95-214 km, 51-66 min, and 24-70 ms^{-1}. (In general, the GW time periods in these dayglow emission intensities are found to be in the range of BV period to ∼3 h [*Laskar et al.*, 2015]). The peak values of the phase speeds on this day are, in general, lower than those reported for the nighttime. This could be understood to be due to (i) an increase in the neutral densities at a given altitude with temperatures in the daytime, which thereby offer greater resistance to the propagation of the waves, and (ii) the increase in the BV time period with increase in temperatures in the daytime, which contribute to a decrease in the daytime phase speeds.

Figure 6.7a shows the variation of the neutral temperature obtained from the NRLMSISE-00 model at the peak emission latitude of 557.7, 630.0, and 777.4 nm dayglow emission intensities on 19 May 2015. It can be noted that depending on the altitudes, there is about 18-36% increase in the neutral temperature in the daytime as compared to the nighttime. The scale height and the BV time periods are calculated for the same day and are shown in Figures 6.7b,c. The BV time period increases by about 9-16% in the daytime than the nighttime and so will contribute to the observed decrease in the phase speeds in the daytime.

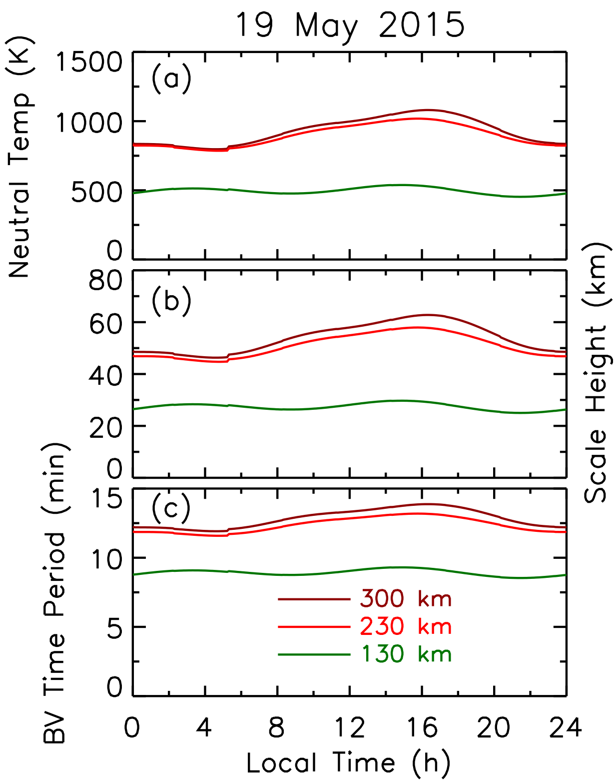

Figure 6.7: Local time variation of (a) the neutral temperature obtained from the NRLMSISE-00 model, (b) the scale height, and (c) the BV time period at the peak emission altitudes of 557.7, 630.0, and 777.4 nm dayglow emissions on 19 May 2015 are shown. The green, red and dark red colored lines correspond to 130, 230, and 300 km altitude.

The largest scale sizes obtained in the daytime seem smaller in comparison to the largest scale sizes obtained in the nighttime, which could, in all possibility, be due to the smaller FOV of observation in the present daytime experiment as opposed to much larger FOV, in general, of nighttime imaging studies. As shown in Figure 6.5, the movement of the waves is mostly in the west/southwestward direction. During nighttime, both eastward/westward propagations have been noted in the equatorial latitudes and southward propagation in middle latitudes [*Shiokawa et al.*, 2006].

In an earlier work, measurements of daytime waves in the zonal direction present in the MLT altitudes were carried out using UV OI 297.2 nm emissions from on-board a balloon on 8 March 2010 [*Pallamraju et al.*, 2014]. For that experiment, a large FOV ultraviolet spectrograph was flown on balloon from the

National Balloon Facility in Hyderabad, India (same location where MISE is installed for the present experiment) to observe the OI 297.2 nm emissions. MISE was operated from the ground along with a nighttime OI 557.7 nm photometer. It was observed that the daytime waves and the zenith intensity fluctuations of around 20 minutes on that day continuing on into the nighttime as observed by the nightglow photometer operated at that location [*Pallamraju et al.*, 2014]. However, for varying latitudes, it is envisaged that the daytime periodicities, phase speeds, scale sizes, and propagation directions would be different. Simultaneous, collocated day and night measurements in the future will provide greater insights into these aspects.

The characteristic scale sizes, time periods, and the phase speeds of 777.4 nm in the daytime are 57-227 km, 50-66 min, and 14-75 ms^{-1}. To the best of our knowledge, there are no reports of such information in the published literature for the nighttime conditions obtained at this emission wavelength to enable comparison.

Further, as the horizontal wave characteristics obtained are in the class of acoustic GWs, the linear dispersion relation (equation 6.1) as given by [*Hines*, 1960] has been used to derive the vertical scale sizes (λ_z).

$$(k_z)^2 = \frac{N^2}{(u^* - c_H)^2} - k_H^2 - \frac{1}{4H^2} \tag{6.1}$$

Here, k_z is the vertical wave number ($2\pi/\lambda_z$), N is the BV frequency, c_H is the measured phase speed obtained from the present experiment (Figure 6.6b), u^* is the component of the ambient neutral wind along the phase front, and H is the scale height.

Neutral thermospheric temperatures for 19 May 2015 from NRLMSISE-00 model have been considered to calculate the values of H, which, on an average are 39, 55, and 60 km at the emission altitudes of 130, 230, and 300 km, respectively. The BV frequency, N, (given as $(2g^*/5H)^{1/2}$, where g^* is the acceleration due to gravity at a given altitude) has been calculated to be 11×10^{-3}, 8×10^{-3}, and 7×10^{-3} rad.s^{-1}, respectively, at the altitudes under consideration. Ambient neutral wind magnitudes, u, and their directions, θ_U, play an important role

Table 6.1: Summary of the 3-D Daytime Thermospheric GW Characteristics Obtained for 19 May 2015.

Wavelength, λ(nm)	Zonal Scale Size, λ_x(km)	Meridional Scale Size, λ_y(km)	Horizontal Scale Size, λ_H(km)	Horizontal Phase Angle, θ_H(deg), Counter clockwise From East	Time Period, τ(min)	Phase Speed, c_H $=\omega/k_H$, (ms^{-1})	Vertical Scale Size, $\lambda_z^{a,b}$(km)	Resultant 3-D Scale Size, $\lambda_v^{a,b}$	Vertical Phase Angle With Respect to k_H,θ_v^b(deg.)
OI 777.4	159-278	54-398	155-227 57-133	207-226 220-253	65.6±11.6; 50.2±5.1	37.0-75.4; 14.6-44.2	0.3-68.4 0.2-31.4	0.3-62.6; 0.2-29.6	66.2-89.9; 70.2-89.7
OI 630.0	125-304	47-302	200-214; 95-131	221-225; 216-231	66.1±6.7; 51.2±1.9	50.4-69.7; 23.9-42.7	0.1-54.9 0.9-18.0	0.1-53.2; 0.9-17.8	75.5-89.9; 81.2-89.5
OI 557.7	37-160	25-172	70-101; 27-46	216-236; 223-242	69.1±13.9; 51.1±5.3 32.8±1.9	16.9-51.5; 6.5-23.6	2.1-21.0 0.1-21.7	2.1-20.5; 0.1-19.6	76.5-88.8; 64.4-89.7

[a] Small λ_z and λ_v derived will be evanescent. [b] Calculated using the dispersion relation given by [*Hines*, 1960].

in influencing the magnitudes of λ_z of GWs. The HWM14 winds [*Drob et al.*, 2015] (Figure 6.6c) and their angles at the three emission altitudes are depicted as arrows (dashed lines) in Figure 6.6d. The relative angles between θ_H and θ_U have been used to calculate the component of wind, u^*, along the direction of c_H. These values along with the model H, N, and measured c_H, λ_H from the present experiment have been used to calculate the λ_z (shown in Figure 6.6e) which vary from 0 to 70 km. From the measured λ_H and the derived λ_z, the magnitudes of the resultant scale size (λ_v) [$= \lambda_H \lambda_z/(\lambda_H^2 + \lambda_z^2)^{1/2}$ (as $k_v^2 = k_H^2 + k_z^2$)] and the vertical phase angles of GWs, θ_v [$= tan^{-1}(k_z/k_H)$] (with respect to the horizontal) have also been calculated. Thus, this approach gives as realistic a picture as possible of the characteristics of GWs in the vertical direction (scale sizes and phase angles) existing at a given time in the daytime. The θ_v seem to be greater than 60^0 which can have important consequences with regard to the vertical coupling of atmospheres. At the same time, it should also be noted that the waves with smaller magnitudes in λ_z and λ_v may be incapable of propagating to greater heights. It can be seen from equation 6.1 that the magnitudes of λ_z vary not only due to the changes in the wind magnitudes, u, and their directions, θ_U, but also due to the changes in the phase speeds, c_H, and the phase angles, θ_H, of the measured waves. It is known that the winds along/opposite to the direction of the phase propagation reduce/enhance the magnitudes of λ_z [*Fritts and Alexander*, 2003]. Also, larger λ_H could result in larger magnitudes of λ_z. It can be appreciated that in addition to day-to-day variability, the variation in the relative angles between the θ_H and θ_U that changes with seasons and geomagnetic activity will result in different values of λ_z. Therefore, measurements of the horizontal characteristics of waves as presented here are essential in understanding the three-dimensional wave dynamics during the daytime. It is to be noted that the vertical scale sizes are not measurable using the daytime optical emissions due to the thickness of the emission layer. Using these measured horizontal wave characteristics, the vertical wave characteristics (λ_z, θ_v) have been derived. Table 6.1 summarizes all values of the thermospheric wave characteristics in three dimensions (λ_x, λ_y, λ_H, θ_H, τ, c_H, λ_z, λ_v, and θ_v) during the daytime for 19 May

2015 that have been made possible through this work for the first time.

It is known that the 557.7 nm dayglow emissions peak at two altitudes. One at around 100 km (94-104 km) and the other at around 160 km (140-180 km). The emissions at lower peak are known to be affected by the dynamical motion of the lower thermosphere [*Shepherd et al.*, 1997]. In comparison to the emissions originating at the lower altitude, those at the higher altitudes are known to vary with respect to the solar zenith angle as shown by the empirical modeling studies [*Zhang and Shepherd*, 2005]. It was revealed that the emission intensities of higher altitude of the green line emission show a smooth variability with respect to the solar zenith angle. The approach followed in obtaining the horizontal scale sizes of waves was based on these considerations. The same approach have been used to obtain the meridional scale sizes of the waves at 557.7 nm dayglow emission altitude [*Pallamraju et al.*, 2014]. At this point, it is to be remembered that the integration along the layer thickness will reduce the contrast making it difficult to observe the propagation of the waves in the raw integrated emission intensities most of the times. However, they reveal tidal, semi-diurnal and diurnal periodicities for 630.0 nm dayglow emission intensities [*Pallamraju et al.*, 2010]. For smaller-scale (GW regime) periodicities, spectral analysis of the residuals (obtained by subtracting the 3-h running mean from the total intensities) have been carried out and the results give a clear signature of the GWs ([*Pallamraju et al.*, 2010; *Laskar et al.*, 2015]). *Laskar et al.* [2015] shows the GW periodicities at the emission altitude of all the three dayglow emission wavelengths obtained by MISE. Moreover, as shown in Figure 6.5, using the method explained above, the horizontal scale sizes and the phase propagation angle of the waves at multiple altitudes are distinguishably obtained.

The last three parameters in Table 6.1 (i.e. λ_z, λ_v, and θ_v) are derived using [*Hines*, 1960] dispersion relationship for the GWs by using the measured horizontal wave characteristics as inputs. Such a new capability of deriving the three-dimensional wave characteristics of the waves in the daytime opens up new possibilities of investigations of vertical coupling through waves in the daytime. Further, in addition to enhance our understanding of the processes related to the vertical coupling of atmospheres and modeling of the thermospheric wave dynamics in the daytime, such studies can also provide insights into the role of the wave sources from lower below in the generation of the ionospheric equatorial plasma irregularities in the nighttime.

6.5 Conclusion

There are methods available to infer information on the neutral winds such as satellite-based optical interferometry and spectrometry, triangulation of vapor cloud releases from rockets, and from radars and Doppler shifts of the optical emissions from the ground. However, investigations on the neutral wave dynamics in the daytime can be carried out only by ground-based dayglow measurements over a large FOV, as presented in this work, wherein dayglow emission intensities at 557.7 nm, 630.0 nm, and 777.4 nm wavelengths were measured along the orthogonal directions to obtain the components λ_x (zonal) and λ_y (meridional) of the horizontal waves. These were used to calculate the horizontal scale sizes, λ_H of waves and their propagation angles, θ_H, in the daytime and are first results of their kind. Not only the wave parameters in two dimensions but also the characteristics of the waves in the vertical dimension have been arrived at in this study using the dispersion relation of GWs. Measurements such as these now present us with a new capability of investigating the thermospheric wave dynamics in three dimensions during the daytime.

Chapter 7

Summary and Future Scope

7.1 Summary of The Thesis Work

In this thesis work, focus of study has been the coupled nature of the daytime ionosphere-thermosphere system (ITS) over equatorial- and low-latitudes. The effect of these coupling processes along with forcing on the low-latitude thermospheric GW dynamics during various geophysical conditions are investigated. Conventionally, by using data set for a longer duration, temporal variations of the thermospheric GW dynamics are studied. In this thesis work, GW characteristics have been investigated both in temporal and spatial domain.

The necessary background information is given in detail, in the Chapter-1 of the thesis. The structure of different layers (particularly in the upper atmosphere) of the Earth's atmosphere, in terms of its composition, energetics and dynamics (e.g. neutral winds, waves and solar forcing), are presented. The geomagnetically quiet and disturbed time picture of the equatorial- and low-latitude thermospheric behavior is also discussed. Various methods that have been used to study the upper atmospheric behavior are also reviewed.

To carry out the investigations of this thesis work, the neutral optical dayglow emission intensities at three wavelengths (OI 557.7, 630.0, and 777.4 nm) are obtained by using a large FOV high spectral resolution spectrograph called MISE. These dayglow data are used as the primary data set for this thesis work. To substantiate the results and to draw inferences, other supporting data sets, such as the EEJ strength, ionospheric data, D_{st} index, thermospheric O/N_2 along with model driven outputs are also used. Detailed discussion on all these data sets, their measurement techniques, and analysis methodology are carried out in Chapter-2.

Several new and exciting results have been obtained during this thesis work. The diurnal behavior of the dayglow emission intensities obtained at all the three emission wavelengths showed both symmetric and asymmetric behavior with respect to noon. The extent of asymmetric behavior in the dayglow emission intensity is defined by Asymmetricity in Time (AT). The days with AT ≤ 0.4 h and AT > 0.4 h are considered to be the days with symmetric and asymmetric diurnal behavior in the emission intensities. To the first order, considering purely the photochemical production mechanisms of the dayglow emission intensities, the asymmetric diurnal behavior in the dayglow emission intensities is not expected. The cause for the asymmetric diurnal behavior is investigated in terms of the neutral dynamics vs. the equatorial electrodynamics. Comparing the AT values with the neutral winds and the EEJ strength, it is conclusively shown that the dayglow emission intensities over the off-equatorial thermosphere are predominantly affected by the equatorial electrodynamics which causes the asymmetric diurnal behavior in the dayglow emission intensities. The equatorial electrodynamics is stronger on the days with asymmetric diurnal behavior in the dayglow emission intensity. Independent ionospheric measurements assest this finding. It has also been noted that during the low solar activity, the diurnal variability in the oxygen dayglow emission intensities were predominantly symmetric, while they were asymmetric during the high solar activity. This again gives a broader picture to the behavior of ITS. This result is shown schematically in Figure 7.1 and is discussed in Chapter-3 of the thesis.

For the investigations discussed in Chapter-3, only the zenith measurements of the dayglow emission intensities have been considered. In the work discussed in Chapter-3 of the thesis, both the temporal and spatial variations of the dayglow emission intensities are investigated. By carrying out the periodogram analysis of the dayglow data at all the three emission wavelengths over three

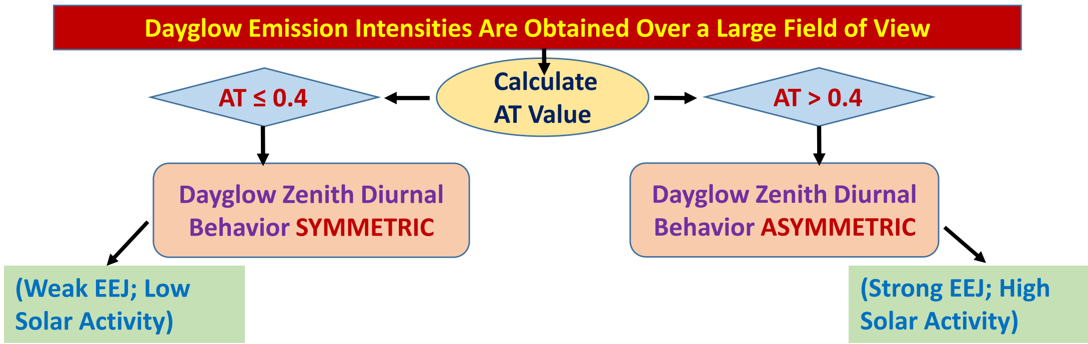

Figure 7.1: Results obtained from the thesis work as discussed in Chapter-3, is shown schematically.

distinctly different directions (west, zenith and east), the GW time periods are obtained. Presence/absence of the similar time periods in these three directions suggests to a common/different source driving the wave features indicating the non-existence/existence of longitudinal differences in the GW features within the spatial extent possible by the present measurement. Such observational results from this study, revealed for the first time that longitudinal differences can exist in small spatial separations of $\sim 3^0$-8^0. Until now, the reports presented in the published literature showed the existence of longitudinal difference in 10^0 separations. Moreover, the diurnal behavior of the dayglow emission intensity are found be symmetric/asymmetric on the days when the similar time periods are present/absent. The non-existence of the similar time periods on the days with asymmetric diurnal behavior was attributed to the stronger equatorial electrodynamics, which seems to show variations even within a $\sim 3^0$ longitudinal separation. This gives a clear and broader picture of the coupling processes between the equatorial electrodynamics and the off-equatorial neutral wave dynamics. Moreover, the GW features in terms of the zonal scale sizes and the propagation directions also show different behavior on the days with symmetric and asymmetric diurnal dayglow emission intensity behavior. The cause for this longitudinal differences has been attributed to that in the equatorial electrodynamical processes. This result is explained in Chapter-4 of the thesis. Figure 7.2 depicts the schematic presentation of the results discussed in Chapters-3 and 4 of the thesis. The (*)s in the Figure 7.2 indicate to the results that have been possible due to the large

FOV measurement of the dayglow emission intensities by the present measurement technique.

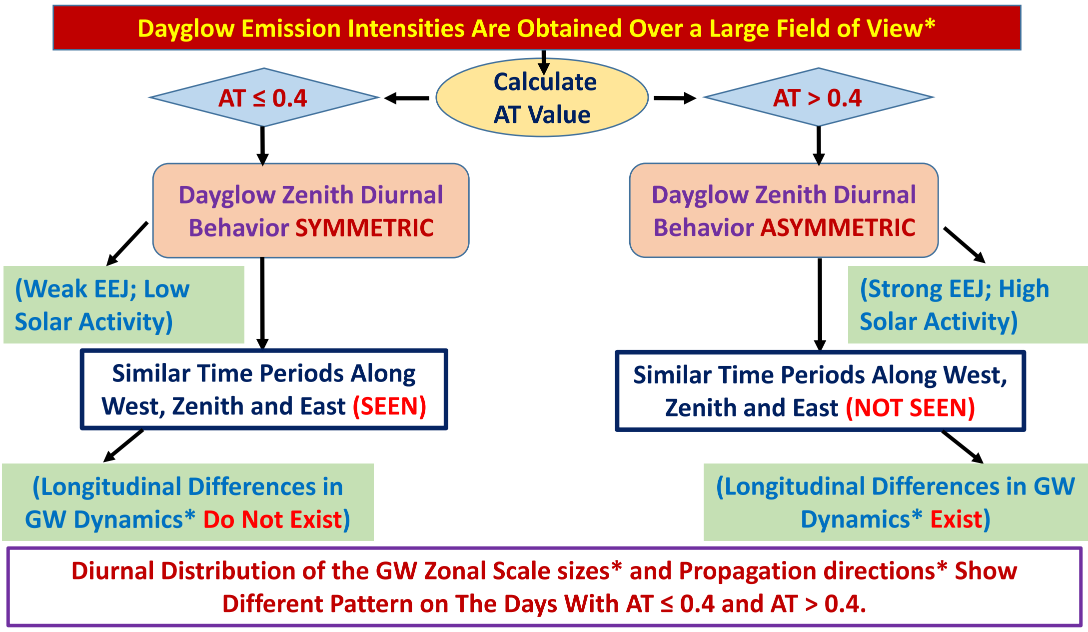

Figure 7.2: Results obtained from the thesis work as discussed in Chapters-3 and 4, is shown schematically.

The zonal GW characteristics discussed in the previous result is geomagnetically quiet time picture, which get affected by the geomagnetic disturbances. Investigations of the variations of the dayglow emission intensities with D_{st}, EEJ strength, thermospheric O/N_2, and IEC have been carried out during three geomagnetic disturbance periods which occurred in three different seasons, in order to get information on the broad effect of the geomagnetic disturbances on the low-latitude thermosphere. It is found that the dayglow emission intensities show similar variations with the O/N_2 during geomagnetic disturbances on solstices. This is attributed to the effect of the geomagnetic disturbances over low-latitude thermosphere. However, during the equinox, the dayglow emission intensities show similar variations with the EEJ. This shows the dominance of the equatorial electric field over the storm influenced neutral wave dynamics over low-latitudes during the equinoxes. This indicates that there is a seasonal dependence of the electrodynamic vs. neutral dynamics over the equatorial- and low-latitudes. Moreover, contrasting distributions of the GW zonal scale sizes are observed on the geomagnetically quiet and disturbed days in different seasons. This shows that changes are brought-in in the zonal GW scale sizes during geomagnetic disturbances irrespective of the season of the storm occurrence. This result is discussed in Chapter-5 of the thesis. Figure 7.3 depicts the schematic presentation of the results discussed in Chapters-3, 4, and 5 of the thesis.

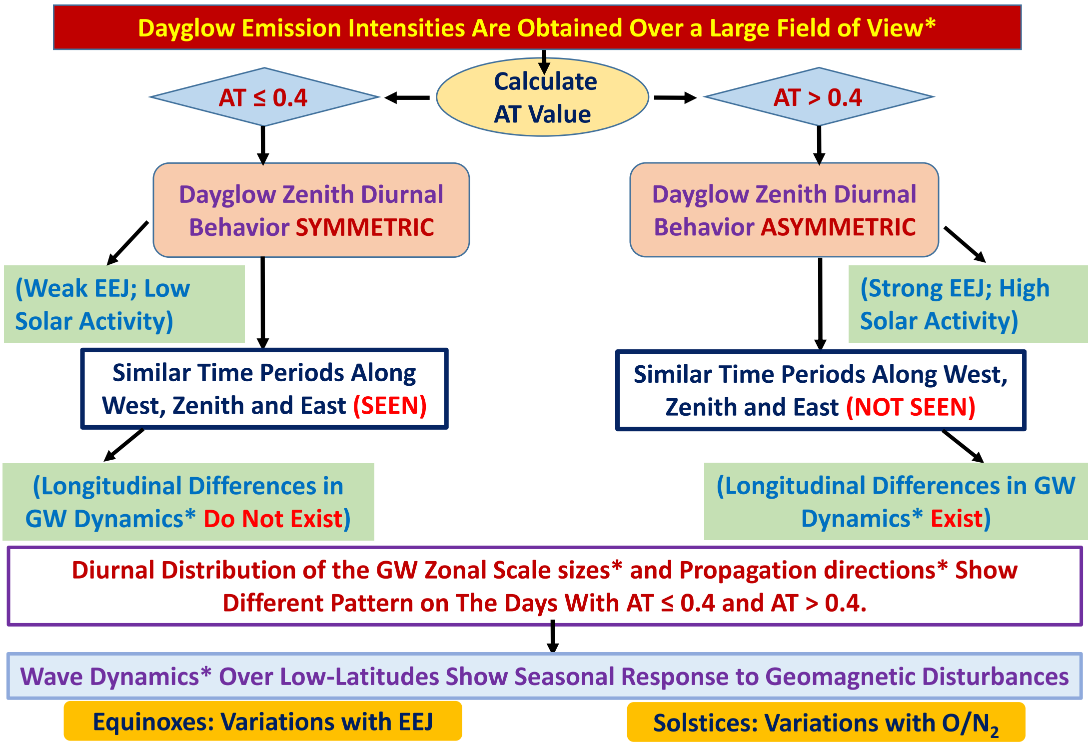

Figure 7.3: Results obtained from the thesis work as discussed in Chapters-3, 4, and 5 is shown schematically.

Till now, the GW characteristics along the zonal directions over the low-latitude thermosphere have been discussed both during geomagnetically quiet and disturbed periods. In this work, near-simultaneous measurements of the spatial varying dayglow intensity at the three emission wavelengths along both the zonal and meridional directions are obtained. From the wave number spectral analysis of these data, λ_x (zonal) and λ_y (meridional) component of the horizontal waves are obtained. These values are used to calculate the horizontal scale sizes, λ_H of the waves and their propagation angles, θ_H. Such measurements on the horizontal scale sizes (in two dimensions) are first results of their kind. Moreover, the measured values have been used in conjunction with the GW dispersion relation

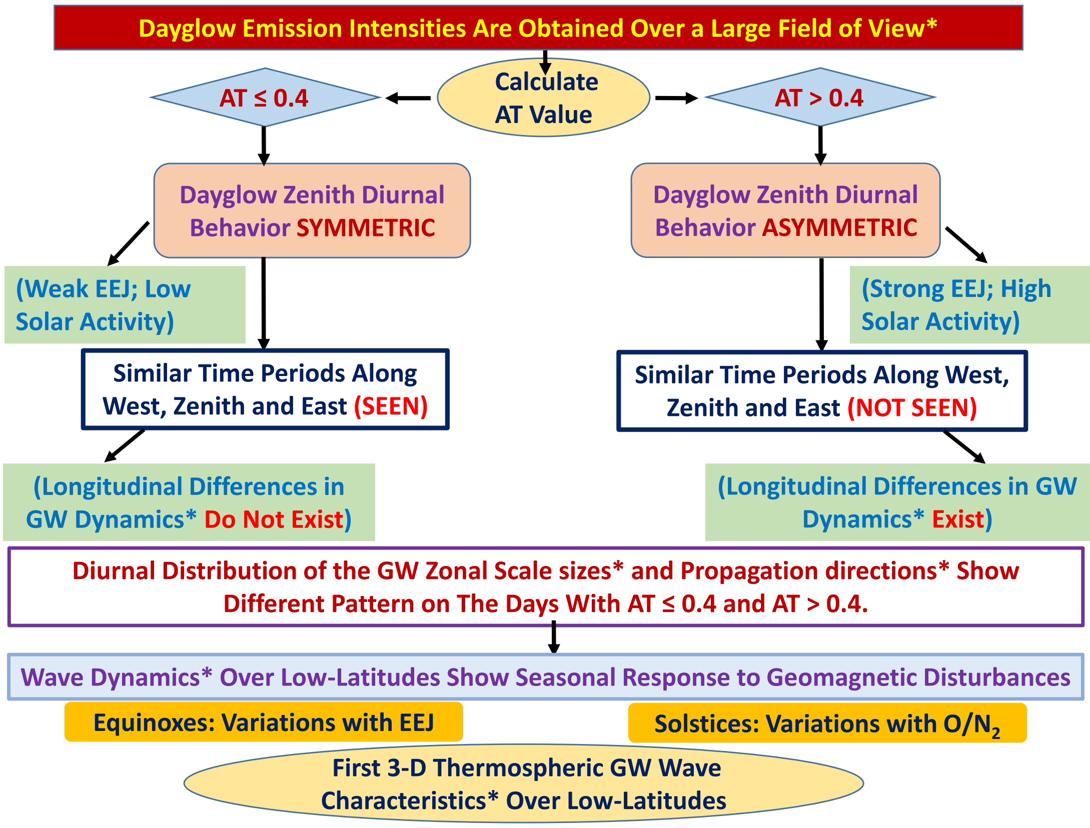

Figure 7.4: Results obtained from the thesis work as discussed in Chapters-3, 4, 5, and 6 is shown schematically.

to calculate the plausible wave features in the vertical direction. Thus, the first three dimensional GW characteristics in the daytime upper atmosphere is derived. This technique opens up new possibilities in the investigations of the daytime wave dynamics. This result is discussed in Chapter-6 of the thesis. Figure 7.4 depicts the schematic presentation of all the results discussed in Chapters-3, 4, 5, and 6 of the thesis.

7.2 Future Scope of The Thesis Work

The results obtained in this thesis work have provided lot of insights and at the same time generated a large number of problems which need further detailed investigation in future. Some of these are discussed below.

The equatorial electrodynamics has a strong influence on the optical neutral dayglow emission intensities over the off-equatorial regions. Hence, on the days with stronger equatorial electrodynamics, the diurnal behavior of the dayglow intensities at all the three emissions are observed to be asymmetric. However, there are days on which not all the three dayglow emission intensities show a common type of behavior. This indicates to the altitudinal variations of the effect of the equatorial electrodynamics which needs thorough detailed investigation. Also, there are some days, on which the AT values turned out to be negative i.e. the peak emission intensity occurred during forenoon. This could be possibly due to the weaker EEJ strength during forenoon or a change in the wind pattern. Further detailed investigations are required to understand this behavior.

Depending on the strength of the equatorial electrodynamics, its effect on the off-equatorial thermospheric dayglow emission intensities will have a latitudinal variation. Thus, on a given day, the AT values will be different for observations at different latitudes. Hence, the characterization of AT value as has been done in the present work (AT $\leq$ 0.4 h and AT $>$ 0.4 h for days with symmetric and asymmetric diurnal behavior of the dayglow emission intensities), is valid for observations at this latitude. Similar type of dayglow observations from different latitudes are required to investigate the latitudinal variation of the effect of equatorial electrodynamics more comprehensively.

During the investigations, it is found that the AT values showed a solar activity dependence. During the high solar activity periods, the increase of solar flux results in an increase of the ionization in the upper atmosphere. As a result, more plasma is transported to the off-equatorial latitudes for the same value of electric fields as in the low solar activity periods. However, along with the solar cycle variation, the AT values also show a day-to-day variations, which could be due to the daily variations of the equatorial electric field, when the solar flux does not show significant daily variations from one day to another. At this point, it will be of interest to explore if any information on the equatorial electric field can be obtained from the AT values obtained by optical neutral dayglow measurements from Hyderabad. In order to do that comparison with physics based model, EEJ strength, and diurnal behavior of the dayglow emission intensity will be carried out in near future.

This thesis work reported the first time, systematic longterm zonal scale size measurements of the GWs at three different altitudes as seen in the variations of the optical dayglow emission intensities. These new results presented here hold lot of promise on various aspects of coupling of the atmospheres that vary as a function of time. The local time distribution of the zonal scale sizes at different altitudes need greater attention to address the causative mechanisms responsible for the observed pattern and to understand the vertical coupling of different layers in the upper atmosphere. Such investigations are challenging since the production mechanisms of the three dayglow emission intensities and the daytime dynamics are quiet complex and require measured plasma parameters for theoretical estimations of the emission rates. Modeling/simulations of such observations would provide greater insights on these aspects of coupling.

The observed GW features during the investigations, such as, (i) the existence of the longitudinal variations of the GWs more during equinoxes and less during the solstices, (ii) eastward/westward movements of the crest and trough of the GWs present in the east/west of the zenith, particularly at the emission altitude of 630.0 nm dayglow needs a more detailed investigation.

Further, it is to be noted that all the GW characteristics obtained during the investigations of this thesis work are carried out for the days on which the dayglow emission intensities at all the three wavelengths showed a common (either symmetric/asymmetric) diurnal behavior. However, there are days in which a couple of emission wavelengths show symmetric/asymmetric diurnal behavior while the remaining one shows an opposite behavior. Characterization of the dayglow emission intensity data on these days will provide information on the nature of inter-coupling behavior among the thermosphere and new insights to the GWs at different altitudes.

Effect of geomagnetic storms on the low-latitude thermospheric GW scale sizes along the zonal directions have been investigated during three disturbed events which occurred during different seasons. The zonal scale size distribution pattern on the disturbed days are found to be different in all the seasons. The intricacies of the effects due to the various sources on the upper atmospheric GWs needs further detailed investigations.

GWs are three dimensional in nature with different projections in zonal, meridional and vertical directions as shown in one of the results of this thesis work. A long term study of the three dimensional daytime thermospheric GWs over low-latitudes during both geomagnetically quiet and disturbed days will give clear understanding and new insights of the daytime thermospheric wave characteristics. Simultaneous, collocated day and night measurements of this kind in the future will provide greater insights into these aspects.

Bibliography

Abdu, M. A., J. A. Bittencourt, and I. S. Batista (1981), Magnetic declination control of the equatorial F region dynamo electric field development and spread F, *J. Geophys. Res.*, *86*(A13), 11,443–11,446, doi:10.1029/JA086iA13p11443.

Abdu, M. A., J. H. A. Sobral, E. R. de Paula, and I. S. Batista (1991), Magnetospheric disturbance effects on the equatorial ionization anomaly (EIA) : An overview, *J. Atmos. Terr. Phys.*, *53*(8), 757 – 771, doi:https://doi.org/10.1016/0021-9169(91)90126-R.

Abdu, M. A., M. Takashi, I. S. Batista, S. Saito, and M. Nakamura (2007), Ionospheric responses to the october 2003 superstorm: Longitude/local time effects over equatorial low and middle latitudes, *J. Geophys. Res.*, *112*(A10), doi:10.1029/2006JA012228.

Anandarao, B. G. (1976), Effects of gravity wave winds and wind shears on equatorial electrojet, *Geophys. Res. Lett.*, *3*(9), 545–548, doi:10.1029/GL003i009p00545.

Anandarao, B. G., and R. Raghavarao (1987), Structural changes in the currents and fields of the equatorial electrojet due to zonal and meridional winds, *J. Geophys. Res.*, *92*(A3), 2514–2526, doi:10.1029/ja092ia03p02514.

Anderson, D. N. (1973), A theoretical study of the ionospheric F region equatorial anomaly—I. Theory, *Planet. Space Sci.*, *21*(3), 409–419, doi:10.1016/0032-0633(73)90040-8.

Andrews, D. G. (2010), *An Introduction to Atmospheric Physics*, Cambridge University Press.

Appleton, E. V. (1946), Two anomalies in the ionosphere, *Nature*, *157*(3995), 691–691, doi:10.1038/157691a0.

Appleton, E. V., and L. J. Ingram (1935), Magnetic storms and upper atmospheric ionization, *Nature*, *136*, 548–549.

Bagiya, M. S., K. N. Iyer, H. P. Joshi, S. V. Thampi, T. Tsugawa, S. Ravindran, R. Sridharan, and B. M. Pathan (2011), Low-latitude ionospheric-thermospheric response to storm time electrodynamical coupling between high and low latitudes, *J. Geophys. Res.*, *116*(A1), doi:10.1029/2010JA015845.

Balan, N., G. J. Bailey, R. J. Moffett, Y. Z. Su, and J. E. Titheridge (1995), Modelling studies of the conjugate-hemisphere differences in ionospheric ionization at equatorial anomaly latitudes, *J. Atmos. Terr. Phys.*, *57*(3), 279 – 292, doi:https://doi.org/10.1016/0021-9169(94)E0019-J.

Balan, N., G. J. Bailey, M. A. Abdu, K. I. Oyama, P. G. Richards, J. MacDougall, and I. S. Batista (1997), Equatorial plasma fountain and its effects over three locations: Evidence for an additional layer, the F3 layer, *J. Geophys. Res.*, *102*(A2), 2047–2056, doi:10.1029/95JA02639.

Barmore, F. E. (1977), High resolution observations of the 6300 $\AA$ oxygen line in the day airglow, *Planet. Space Sci.*, *25*(2), 185–191, doi:10.1016/0032-0633(77)90023-X.

Barth, C. A. (1964), Three-body reactions, *Ann. de Geophys.*, *20*, 182.

Barth, C. A., and A. F. Hildebrandt (1961), The 5577 $\AA$ airglow emission mechanism, *J. Geophys. Res.*, *66*(3), 985–986, doi:10.1029/JZ066i003p00985.

Basu, S., S. Basu, K. M. Groves, H. C. Yeh, S. Y. Su, F. J. Rich, P. J. Sultan, and M. J. Keskinen (2001a), Response of the equatorial ionosphere in the south atlantic region to the great magnetic storm of July 15, 2000, *Geophys. Res. Lett.*, *28*(18), 3577–3580, doi:10.1029/2001GL013259.

Basu, S., et al. (2001b), Ionospheric effects of major magnetic storms during the international space weather period of September and October 1999: Gps observations, VHF/UHF scintillations, and in situ density structures at middle and equatorial latitudes, *J. Geophys. Res.*, *106*(A12), 30,389–30,413, doi:10.1029/2001JA001116.

Beer, T. (1974), *Atmospheric Waves*, Wiley.

Bens, A. R., L. L. Cogger, and G. G. Shepherd (1965), Upper atmospheric temperatures from Doppler line widths-III: Observation of the OI dayglow emission at 6300 Å, *Planet. Space Sci.*, *13*(6), 551–563, doi:10.1016/0032-0633(65)90168-6.

Biondi, M. A., and D. P. Sipler (1985), Horizontal and vertical winds and temperatures in the equatorial thermosphere: Measurements from Natal, Brazil during August-September, *Planet. Space Sci.*, *33*, 817–823.

Blanc, M., and A. D. Richmond (1980), The ionospheric disturbance dynamo, *J. Geophys. Res.*, *85*(A4), 1669–1686, doi:10.1029/JA085iA04p01669.

Burnside, R. G., and C. A. Tepley (1989), Optical observations of thermospheric neutral winds at Arecibo between 1980 and 1987, *J. Geophys. Res.*, *94*(A3), 2711–2716, doi:10.1029/JA094iA03p02711.

Chakrabarti, S., D. Pallamraju, and J. Baumgardner (2001), HiTIES: A High Throughput Imaging Echelle Spectrogragh for ground-based visible airglow and auroral studies, *J. Geophys. Res.*, *106*(A12), 30,337–30,348.

Chakrabarty, D., R. Sekar, H. Chandra, R. Narayanan, B. M. Pathan, and K. S. V. Subbarao (2002), Characterizations of the diurnal shapes of OI 630.0 nm dayglow intensity variations: inferences, *Ann. Geophys.*, *20*(11), 1851–1855, doi:10.5194/angeo-20-1851-2002.

Chakrabarty, D., R. Sekar, R. Narayanan, C. V. Devasia, and B. M. Pathan (2005), Evidence for the interplanetary electric field effect on the OI 630.0 nm airglow over low latitude, *J. Geophys. Res.*, *110*(A11), doi:10.1029/2005JA011221.

Chakrabarty, D., R. Sekar, J. H. Sastri, B. M. Pathan, G. D. Reeves, K. Yumoto, and T. Kikuchi (2010), Evidence for OI 630.0 nm dayglow variations over low latitudes during onset of a substorm, *J. Geophys. Res.*, *115*(A10), doi:10.1029/2010JA015643.

Chakrabarty, D., D. Rout, R. Sekar, R. Narayanan, G. D. Reeves, T. K. Pant, B. Veenadhari, and K. Shiokawa (2015), Three different types of electric field disturbances affecting equatorial ionosphere during a long-duration prompt penetration event, *J. Geophys. Res.*, *120*(6), 4993–5008, doi:10.1002/2014JA020759.

Chamberlain, J. W. (1961), *Physics of the Aurora and Airglow*, 704 pp., Academic Press.

Chapman, S. (1931), Bakerian lecture. Some phenomena of the upper atmosphere, *Proc. R. Soc. London. Ser. A*, *132*(820), 353–374, doi:10.1098/rspa.1931.0105.

Chimonas, G., and C. O. Hines (1971), Atmospheric gravity waves induced by a solar eclipse, 2, *J. Geophys. Res.*, *76*(28), 7003–7005, doi:10.1029/JA076i028p07003.

Christensen, A. B., et al. (2003), Initial observations with the Global Ultraviolet Imager (GUVI) in the NASA TIMED satellite mission, *J. Geophys. Res.*, *108*(A12), doi:10.1029/2003JA009918.

Cocks, T. D., D. F. Creighton, and F. Jacka (1980), Application of a dual fabry-perot spectrometer for daytime airglow studies, *J. Atmos. Terr. Phys.*, *42*(5), 499 – 511, doi:10.1016/0021-9169(80)90010-0.

Culot, F., C. Lathuillère, J. Lilensten, and O. Witasse (2004), The OI 630.0 and 557.7nm dayglow measured by WINDII and modeled by TRANSCAR, *Ann. Geophys.*, *22*(6), 1947–1960, doi:10.5194/angeo-22-1947-2004.

Culot, F., C. Lathuillre, and J. Lilensten (2005), Influence of geomagnetic activity on the o i 630.0 and 557.7 nm dayglow, *J. Geophys. Res.*, *110*(A1), doi:10.1029/2004JA010667, a01304.

Dabas, R. S., D. R. Lakshmi, and B. M. Reddy (1989), Effect of geomagnetic disturbances on the VHF nighttime scintillation activity at equatorial and low latitudes, *Radio Science*, *24*(4), 563–573, doi:10.1029/RS024i004p00563.

Das, U., D. Pallamraju, and S. Chakrabarti (2010), Effect of an X-Class solar flare on the OI 630 nm dayglow emissions, *J. Geophys. Res.*, *115*(A8), doi:10.1029/2010JA015370.

Daubechies, I. (1988), Orthonormal bases of compactly supported wavelets, *Commun. Pure Appl. Math.*, *41*(7), 909–996, doi:10.1002/cpa.3160410705.

Deeming, T. J. (1975), Fourier analysis with unequally-spaced data, *Astrophys. Space Sci.*, *36*(137D), 137–158, doi:10.1007/BF00681947.

Dougherty, J. P., and D. T. Farley (1963), A theory of incoherent scattering of radio waves by a plasma: 3. Scattering in a partly ionized gas, *J. Geophys. Res.*, *68*(19), 5473–5486, doi:10.1029/JZ068i019p05473.

Drob, D. P., et al. (2008), An empirical model of the Earth's horizontal wind fields: HWM07, *J. Geophys. Res.*, *113*(A12), doi:10.1029/2008JA013668.

Drob, D. P., et al. (2015), An update to the Horizontal Wind Model (HWM): The quiet time thermosphere, *Earth and Space Science*, *2*(7), 301–319, doi: 10.1002/2014EA000089.

Emmert, J. T., D. P. Drob, G. G. Shepherd, G. Hernandez, M. J. Jarvis, J. W. Meriwether, R. J. Niciejewski, D. P. Sipler, and C. A. Tepley (2008), DWM07 global empirical model of upper thermospheric storm-induced disturbance winds, *J. Geophys. Res.*, *113*(A11), doi:10.1029/2008JA013541.

England, S. L., S. Maus, T. J. Immel, and S. B. Mende (2006), Longitudinal variation of the E-region electric fields caused by atmospheric tides, *Geophys. Res. Lett.*, *33*(21), doi:10.1029/2006GL027465.

Farley, D. T. (1969), Faraday rotation measurements using incoherent scatter, *Radio Science*, *4*(2), 143–152, doi:10.1029/RS004i002p00143.

Fejer, B. G., and L. Scherliess (1995), Time dependent response of equatorial ionospheric electric fields to magnetospheric disturbances, *Geophys. Res. Lett.*, *22*(7), 851–854, doi:10.1029/95GL00390.

Fejer, B. G., and L. Scherliess (1997), Empirical models of storm time equatorial zonal electric fields, *J. Geophys. Res.*, *102*(A11), 24,047–24,056, doi:10.1029/97JA02164.

Fejer, B. G., C. A. Gonzales, D. T. Farley, M. C. Kelley, and R. F. Woodman (1979), Equatorial electric fields during magnetically disturbed conditions 1. The effect of the interplanetary magnetic field, *J. Geophys. Res.*, *84*(A10), 5797–5802, doi:10.1029/JA084iA10p05797.

Floyd, L., J. Newmark, J. Cook, L. Herring, and D. McMullin (2005), Solar EUV and UV spectral irradiances and solar indices, *J. Atmos. Sol. Terr. Phys.*, *67*(1-2), 3–15, doi:10.1016/j.jastp.2004.07.013.

Forbes, J. M. (1981), The equatorial electrojet, *Rev. Geophys.*, *19*(3), 469–504, doi:10.1029/RG019i003p00469.

Forbes, J. M., R. G. Roble, and F. A. Marcos (1987), Thermospheric dynamics during the March 22, 1979, magnetic storm: 2. Comparisons of model predictions with observations, *J. Geophys. Res.*, *92*(A6), 6069–6081, doi: 10.1029/JA092iA06p06069.

Forbes, J. M., S. L. Bruinsma, Y. Miyoshi, and H. Fujiwara (2008), A solar terminator wave in thermosphere neutral densities measured by the CHAMP satellite, *Geophys. Res. Lett.*, *35*(14), doi:10.1029/2008GL034075.

Frederick, J. E., D. W. Rusch, G. A. Victor, W. E. Sharp, P. B. Hays, and H. C. Brinton (1976), The O I (λ5577 Å) airglow: Observations and excitation mechanisms, *J. Geophys. Res.*, *81*(22), 3923–3930, doi:10.1029/JA081i022p03923.

Fritts, D. C., and M. J. Alexander (2003), Gravity wave dynamics and effects in the middle atmosphere, *Rev. Geophys.*, *41*(1), doi:10.1029/2001RG000106.

Fujiwara, H., S. Maeda, H. Fukunishi, T. J. Fuller-Rowell, and D. S. Evans (1996), Global variations of thermospheric winds and temperatures caused by substorm energy injection, *J. Geophys. Res.*, *101*(A1), 225–239, doi:10.1029/95JA01157.

Fuller-Rowell, T. J., M. V. Codrescu, R. J. Moffett, and S. Quegan (1994), Response of the thermosphere and ionosphere to geomagnetic storms, *J. Geophys. Res.*, *99*(A3), 3893–3914, doi:10.1029/93JA02015.

Geisler, J. (1967), A numerical study of the wind system in the middle thermosphere, *J. Atmos. Terr. Phys.*, *29*(12), 1469 – 1482, doi:http://dx.doi.org/10.1016/0021-9169(67)90100-6.

Gerrard, A. J., and J. W. Meriwether (2011), Initial daytime and nighttime SOFDI observations of thermospheric winds from Fabry-Perot Doppler shift measurements of the 630-nm OI line-shape profile, *Ann. Geophys.*, *29*(9), 1529–1536, doi:10.5194/angeo-29-1529-2011.

Gilman, D. L., F. J. Fuglister, and J. M. Mitchell (1963), On the Power Spectrum of "Red Noise", *J. Atmos. Sci.*, *20*(2), 182–184, doi:10.1175/1520-0469(1963)020⟨0182:OTPSON⟩2.0.CO;2.

Gonzales, C. A., M. C. Kelley, B. G. Fejer, J. F. Vickrey, and R. F. Woodman (1979), Equatorial electric fields during magnetically disturbed conditions 2. Implications of simultaneous auroral and equatorial measurements, *J. Geophys. Res.*, *84*(A10), 5803–5812, doi:10.1029/JA084iA10p05803.

Gouin, P., and P. N. Mayaud (1967), A propos de Ixistence possible dn contre electrojet aux latitudes magnetiques equatorials, *Ann. Geophys.*, *23*, 41–47.

Goupillaud, P., A. Grossmann, and J. Morlet (1984), Cycle-octave and related transforms in seismic signal analysis, *Geoexploration*, *23*(1), 85–102, doi:10.1016/0016-7142(84)90025-5.

Grainger, J. F., and J. Ring (1962), Anomalous Fraunhofer line profiles, *Nature*, *193*, 762, doi:10.1038/193762a0.

Greenhow, J. S. (1954), A radio echo method for the investigation of atmospheirc winds at altitudes of 80-100 km, using radio echoes from meteor trails, *Philosophical Magazine*, *7*(45), 471–490.

Grossmann, A., and J. Morlet (1984), Decomposition of Hardy functions into square integrable wavelets of constant shape, *SIAM J. Math. Anal.*, *15*(4), 723–736, doi:10.1137/0515056.

Gurubaran, S. (2002), The equatorial counter electrojet: Part of a worldwide current system?, *Geophys. Res. Lett.*, *29*(9), 511–514, doi:10.1029/2001GL014519.

Hagan, M. E., R. G. Roble, and J. Hackney (2001), Migrating thermospheric tides, *J. Geophys. Res.*, *106*(A7), 12,739–12,752, doi:10.1029/2000JA000344.

Hajkowicz, L. (1991), Global onset and propagation of large-scale travelling ionospheric disturbances as a result of the great storm of 13 march 1989, *Planet. Space Sci.*, *39*(4), 583 – 593, doi:http://dx.doi.org/10.1016/0032-0633(91)90053-D.

Hargreaves, J. K. (1992), *The Solar-Terrestrial Environment*, Cambridge University Press.

Harris, F. J. (1978), On the use of windows for harmonic analysis with the discrete fourier transform, *Proceedings of the IEEE*, *66*, 51–83.

Hays, P. B., G. Carignan, B. C. Kennedy, G. G. Shepherd, and J. C. G. Walker (1973), The visible-airglow experiment on Atmosphere Explorer, *Radio Science*, *8*(4), 369–377, doi:10.1029/RS008i004p00369.

Hays, P. B., D. W. Rusch, R. G. Roble, and J. C. G. Walker (1978), The O-I (6300 Å) airglow, *Rev. Geophys.*, *16*(2), 225–232, doi:10.1029/RG016i002p00225.

Hays, P. B., V. J. Abreu, M. E. Dobbs, D. A. Gell, H. J. Grassl, and W. R. Skinner (1993), The high-resolution doppler imager on the Upper Atmosphere Research Satellite, *J. Geophys. Res.*, *98*(D6), 10,713–10,723, doi:10.1029/93JD00409.

Hedin, A. E., and H. G. Mayr (1973), Magnetic control of the near equatorial neutral thermosphere, *J. Geophys. Res.*, *78*(10), 1688–1691, doi:10.1029/JA078i010p01688.

Hedin, A. E., P. Bauer, H. G. Mayr, G. R. Carignan, L. H. Brace, H. C. Brinton, A. D. Parks, and D. T. Pelz (1977), Observations of neutral composition and related ionospheric variations during a magnetic storm in February 1974, *J. Geophys. Res.*, *82*(22), 3183–3189, doi:10.1029/JA082i022p03183.

Hedin, A. E., N. W. Spencer, and T. L. Killeen (1988), Empirical global model of upper thermosphere winds based on Atmosphere and Dynamics Explorer satellite data, *J. Geophys. Res.*, *93*(A9), 9959–9978, doi:10.1029/JA093iA09p09959.

Hedin, A. E., et al. (1996), Empirical wind model for the upper, middle and lower atmosphere, *J. Atmos. Terr. Phys.*, *58*(13), 1421 – 1447, doi:http://dx.doi.org/10.1016/0021-9169(95)00122-0.

Heelis, R. A., P. C. Kendall, R. J. Moffett, D. W. Windle, and H. Rishbeth (1974), Electrical coupling of the E- and F-regions and its effect on F-region drifts and winds, *Planet. Space Sci.*, *22*(5), 743–756, doi:10.1016/0032-0633(74)90144-5.

Hernandez, G., and R. G. Roble (1976), Direct measurements of nighttime thermospheric winds and temperatures, 2. Geomagnetic storms, *J. Geophys. Res.*, *81*(28), 5173–5181, doi:10.1029/JA081i028p05173.

Herrero, F., H. Mayr, and N. Spencer (1988), Low latitude thermospheric meridional winds between 250 and 450 km altitude: AE-E satellite data, *J. Atmos. Terr. Phys.*, *50*(10), 1001 – 1006, doi:http://dx.doi.org/10.1016/0021-9169(88)90087-6.

Hickey, D. A., C. R. Martinis, F. S. Rodrigues, R. H. Varney, M. A. Milla, M. J. Nicolls, A. Strmme, and J. F. Arratia (2015), Concurrent observations at the magnetic equator of small-scale irregularities and large-scale depletions associated with equatorial spread F, *J. Geophys. Res.*, *120*(12), 10,883–10,896, doi:10.1002/2015JA021991.

Hines, C. O. (1960), Internal atmospheric gravity waves at ionospheric heights, *Can. J. Phys.*, *38*(11), 1441–1481, doi:10.1139/p60-150.

Hines, C. O. (1974), *The upper atmosphere in motion: A selection of papers with annotation*, Geophys. Monogr.

Hinteregger, H. E. (1976), EUV Fluxes in the solar spectrum below 2000 *Å*, *J. Atmos. Terr. Phys.*, *38*(8), 791 – 806, doi:http://dx.doi.org/10.1016/0021-9169(76)90020-9.

Hocke, K., and N. Kämpfer (2009), Gap filling and noise reduction of unevenly sampled data by means of the Lomb-Scargle periodogram, *Atmos. Chem. Phys.*, *9*(12), 4197–4206, doi:10.5194/acp-9-4197-2009.

Hocke, K. K. S. (1996), A review of atmospheric gravity waves and travelling ionospheric disturbances: 1982-1995, *Ann. Geophys.*, *14*(9), 917–940, doi:10.1007/s00585-996-0917-6.

Horne, J. H., and S. L. Baliunas (1986), A prescription for period analysis of unevenly sampled time series, *Astrophys. J.*, *302*, 757–763, doi:10.1086/164037.

Hsu, V. W., J. P. Thayer, J. Lei, and W. Wang (2014), Formation of the equatorial thermosphere anomaly trough: Local time and solar cycle variations, *J. Geophys. Res.*, *119*(12), 10,456–10,473, doi:10.1002/2014JA020416, 2014JA020416.

Huba, J. D., D. P. Drob, T.-W. Wu, and J. J. Makela (2015), Modeling the ionospheric impact of tsunami-driven gravity waves with SAMI3: Conjugate effects, *Geophys. Res. Lett.*, *42*(14), 5719–5726, doi:10.1002/2015GL064871.

Hunsucker, R. D. (1982), Atmospheric gravity waves generated in the high-latitude ionosphere: A review, *Rev. Geophys.*, *20*(2), 293–315, doi:10.1029/RG020i002p00293.

Immel, T. J., G. Crowley, J. D. Craven, and R. G. Roble (2001), Dayside enhancements of thermospheric O/N_2 following magnetic storm onset, *J. Geophys. Res.*, *106*(A8), 15,471–15,488, doi:10.1029/2000JA000096.

Immel, T. J., S. B. Mende, H. U. Frey, N. stgaard, and G. R. Gladstone (2003), Effect of the 14 July 2000 solar flare on Earth's FUV emissions, *J. Geophys. Res.*, *108*(A4), doi:10.1029/2001JA009060.

Immel, T. J., E. Sagawa, S. L. England, S. B. Henderson, M. E. Hagan, S. B. Mende, H. U. Frey, C. M. Swenson, and L. J. Paxton (2006), Control of equatorial ionospheric morphology by atmospheric tides, *Geophys. Res. Lett.*, *33*(15), doi:10.1029/2006GL026161.

Jarrett, A. H., and M. J. Hoey (1963), A ground-level photographic observation of the day airglow emission of atomic oxygen at 6300 Å, *Planet. Space Sci.*, *11*(10), 1251–1252, doi:10.1016/0032-0633(63)90256-3.

Jones, A. V., and A. W. Harrison (1955), Rotational temperatures of the auroral N_2^+ bands, *J. Atmos. Terr. Physics*, *6*(1), 336 – 343, doi:https://doi.org/10.1016/0021-9169(55)90051-9.

Karan, D. K., and D. Pallamraju (2017), Small-scale longitudinal variations in the daytime equatorial thermospheric wave dynamics as inferred from oxygen dayglow emissions, *J. Geophys. Res.*, pp. 6528–6542, doi:10.1002/2017JA023891.

Karan, D. K., D. Pallamraju, K. A. Phadke, T. Vijayalakshmi, T. K. Pant, and S. Mukherjee (2016), Electrodynamic influence on the diurnal behaviour of neutral daytime airglow emissions, *Ann. Geophys.*, *34*(11), 1019–1030, doi:10.5194/angeo-34-1019-2016.

Kelley, M. C. (2009), *The Earth's Ionosphere: Plasma Physics and Electrodynamics*, vol. 96, Academic press.

Kelley, M. C., and J. J. Makela (2002), By-dependent prompt penetrating electric fields at the magnetic equator, *Geophys. Res. Lett.*, *29*(7), 571–573, doi:10.1029/2001GL014468.

Kikuchi, T., K. K. Hashimoto, and K. Nozaki (2008), Penetration of magnetospheric electric fields to the equator during a geomagnetic storm, *J. Geophys. Res.*, *113*(A6), doi:10.1029/2007JA012628.

Killeen, T. L., Q. Wu, S. C. Solomon, D. A. Ortland, W. R. Skinner, R. J. Niciejewski, and D. A. Gell (2006), TIMED Doppler Interferometer: Overview and recent results, *J. Geophys. Res.*, *111*(A10), doi:10.1029/2005JA011484.

Kivelson, M. G., and C. T. Russell (1995), *Introduction to Space Physics*, Cambridge University Press.

Kohl, H., and J. W. King (1967), Atmospheric winds between 100 and 700 km and their effects on the ionosphere, *J. Atmos. Terr. Phys.*, *29*(9), 1045–1062, doi:10.1016/0021-9169(67)90139-0.

Kovács, G. (1981), Frequency shift in fourier analysis, *Astrophys. Space Sci.*, *78*(1), 175–188, doi:10.1007/BF00654032.

Kulkarni, P. V. (1976), Rocket study of 5577$\mathring{A}$ OI emission at night over the magnetic equator, *J. Geophys. Res.*, *81*(22), 3740–3744, doi:10.1029/JA081i022p03740.

Lakshmi Narayanan, V., S. Gurubaran, and K. Emperumal (2010), Airglow imaging observations of small-scale structures driven by convective instability in the upper mesosphere over Tirunelveli (8.7^{0}N), *J. Geophys. Res.*, *115*(D19), doi:10.1029/2009JD012937.

Laskar, F. I. (2015), Effect of lower atmospheric and solar forcings on daytime upper atmospheric dynamics, Ph.D. thesis, Indian Institute of Technology, Gandhinagar.

Laskar, F. I., and D. Pallamraju (2014), Does sudden stratospheric warming induce meridional circulation in the mesosphere thermosphere system?, *J. Geophys. Res.*, *119*(12), 10,133–10,143, doi:10.1002/2014JA020086.

Laskar, F. I., D. Pallamraju, T. V. Lakshmi, M. A. Reddy, B. M. Pathan, and S. Chakrabarti (2013), Investigations on vertical coupling of atmospheric regions using combined multiwavelength optical dayglow, magnetic, and radio measurements, *J. Geophys. Res.*, *118*(7), 4618–4627, doi:10.1002/jgra.50426.

Laskar, F. I., D. Pallamraju, and B. Veenadhari (2014), Vertical coupling of atmospheres: dependence on strength of sudden stratospheric warming and solar activity, *Earth, Planets and Space*, *66*(1), 94, doi:10.1186/1880-5981-66-94.

Laskar, F. I., D. Pallamraju, B. Veenadhari, T. V. Lakshmi, M. A. Reddy, and S. Chakrabarti (2015), Gravity waves in the thermosphere: Solar activity dependence, *Adv. Space Res.*, *55*(6), 1651 – 1659, doi:https://doi.org/10.1016/j.asr.2014.12.040.

Lau, K. M., and H. Y. Weng (1995), Climate signal detection using wavelet transform: How to make a time series sing, *Amer. Meteor. Soc.*, *76*, 2391–2402.

Le, G., J. A. Slavin, and R. J. Strangeway (2010), Space technology 5 observations of the imbalance of regions 1 and 2 field-aligned currents and its implication to the cross-polar cap pedersen currents, *J. Geophys. Res.*, *115*(A7), doi:10.1029/2009JA014979.

Lean, J. (1997), The Suns's variable radiation and its relevance for Earth, *Annu. Rev. Astron. Astrophys.*, *35*(1), 33–67, doi:10.1146/annurev.astro.35.1.33.

Lei, J., J. P. Thayer, W. Wang, A. D. Richmond, R. Roble, X. Luan, X. Dou, X. Xue, and T. Li (2012), Simulations of the equatorial thermosphere anomaly: Field-aligned ion drag effect, *J. Geophys. Res.*, *117*(A1), n/a–n/a, doi:10.1029/2011JA017114, a01304.

Lindzen, R. S. (1990), *Dynamics in atmospheric physics*, Cambridge University Press.

Liu, H., H. Lhr, S. Watanabe, W. Khler, and C. Manoj (2007), Contrasting behavior of the thermosphere and ionosphere in response to the 28 october 2003 solar flare, *J. Geophys. Res.*, *112*(A7), doi:10.1029/2007JA012313.

Lomb, N. R. (1976), Least-squares frequency analysis of unequally spaced data, *Astrophys. Space Sci.*, *39*(2), 447–462, doi:10.1007/BF00648343.

Maharaj-Sharma, R., and G. G. Shepherd (2004), Solar variability of the day-time atomic oxygen O(1S) emission in the middle and lower thermosphere, *J. Geophys. Res.*, *109*(A3), doi:10.1029/2003JA010183.

Makela, J. J., and Y. Otsuka (2011), Overview of nighttime ionospheric instabilities at low- and mid-latitudes: Coupling aspects resulting in structuring at the mesoscale, *Space. Sci. Rev.*, *168*(1-4), 419–440, doi:10.1007/s11214-011-9816-6.

Makela, J. J., et al. (2011a), Imaging and modeling the ionospheric airglow response over hawaii to the tsunami generated by the tohoku earthquake of 11 march 2011, *Geophys. Res. Lett.*, *38*(24), doi:10.1029/2011GL047860.

Makela, J. J., J. W. Meriwether, Y. Huang, and P. J. Sherwood (2011b), Simulation and analysis of a multi-order imaging Fabry–Perot interferometer for the study of thermospheric winds and temperatures, *Appl. Opt.*, *50*(22), 4403–4416, doi:10.1364/ao.50.004403.

Makela, J. J., D. J. Fisher, J. W. Meriwether, R. A. Buriti, and A. F. Medeiros (2013), Near-continual ground-based nighttime observations of thermospheric neutral winds and temperatures over equatorial Brazil from 2009 to 2012, *J. Atmos. Sol. Terr. Phys.*, *103*, 94 – 102, doi:https://doi.org/10.1016/j.jastp.2012.11.019.

Mallat, S. G. (1989), A theory for multiresolution signal decomposition: the wavelet representation, *IEEE Trans. Pattern Anal. Mach. Intell.*, *11*(7), 674–693, doi:10.1109/34.192463.

Marshall, R. A., S. Smith, J. Baumgardner, and S. Chakrabarti (2011), Continuous ground-based multiwavelength airglow measurements, *J. Geophys. Res.*, *116*(A11), doi:10.1029/2011JA016901.

Martinis, C., J. Baumgardner, M. Mendillo, J. Wroten, A. Coster, and L. Paxton (2015), The night when the auroral and equatorial ionospheres converged, *J. Geophys. Res.*, *120*(9), 8085–8095, doi:10.1002/2015JA021555.

Maruyama, N., A. D. Richmond, T. J. Fuller-Rowell, M. V. Codrescu, S. Sazykin, F. R. Toffoletto, R. W. Spiro, and G. H. Millward (2005), Interaction between direct penetration and disturbance dynamo electric fields in the storm-time equatorial ionosphere, *Geophys. Res. Lett.*, *32*(17), doi:10.1029/2005GL023763.

Maruyama, T., G. Ma, and M. Nakamura (2004), Signature of TEC storm on 6 November 2001 derived from dense GPS receiver network and ionosonde chain over Japan, *J. Geophys. Res.*, *109*(A10), doi:10.1029/2004JA010451.

Mayr, H. G., and H. Volland (1973), Magnetic storm characteristics of the thermosphere, *J. Geophys. Res.*, *78*(13), 2251–2264, doi:10.1029/JA078i013p02251.

Mayr, H. G., I. Harris, and N. W. Spencer (1978), Some properties of upper atmosphere dynamics, *Rev. Geophys.*, *16*(4), 539–565, doi:10.1029/RG016i004p00539.

Mendillo, M., and J. Baumgardner (1982), Airglow characteristics of equatorial plasma depletions, *J. Geophys. Res.*, *87*(A9), 7641, doi:10.1029/JA087iA09p07641.

Mendillo, M., J. Baumgardner, D. Nottingham, J. Aarons, B. Reinisch, J. Scali, and M. Kelley (1997), Investigations of thermospheric-ionospheric dynamics with 6300$\mathring{A}$ images from the arecibo observatory, *J. Geophys. Res.*, *102*(A4), 7331–7343, doi:10.1029/96JA02786.

Meriwether, J. (2006), Studies of thermospheric dynamics with a Fabry–Perot interferometer network: A review, *68*(13), 1576–1589, doi:10.1016/j.jastp.2005.11.014.

Meriwether, J. W., P. Shih, T. L. Killeen, V. B. Wickwar, and R. G. Roble (1984), Nighttime thermospheric winds over Sondre Stromfjord, Greenland, *Geophys. Res. Lett.*, *11*(9), 931–934, doi:10.1029/GL011i009p00931.

Meriwether, J. W., J. W. Moody, M. A. Biondi, and R. G. Roble (1986), Optical interferometric measurements of nighttime equatorial thermospheric winds at Arequipa, Peru, *J. Geophys. Res.*, *91*(A5), 5557–5566, doi:10.1029/JA091iA05p05557.

Meriwether, J. W., J. J. Makela, Y. Huang, D. J. Fisher, R. A. Buriti, A. F. Medeiros, and H. Takahashi (2011), Climatology of the nighttime equatorial thermospheric winds and temperatures over Brazil near solar minimum, *J. Geophys. Res.*, *116*(A4), doi:10.1029/2011JA016477.

Moffett, R. J. (1979), The Equatorial Anomaly in the electron distribution of the terrestrial F-region, *Fundam. Cosm. Phys.*, *4*, 313–391.

Morlet, J., G. Arens, E. Fourgeau, and D. Glard (1982), Wave propagation and sampling theoryPart I: Complex signal and scattering in multilayered media, *Geophysics*, *47*(2), 203–221, doi:10.1190/1.1441328.

Nakamura, T., T. Tsuda, H. Miyagawa, Y. Matsushita, H. Fukunishi, Y. Takahashi, and Y. Yamada (1998), Propagation directions of gravity wave patterns observed in OH CCD images during the SEEK Campaign, *Geophys. Res. Lett.*, *25*(11), 1793–1796, doi:10.1029/98GL01064.

Narayanan, R., J. N. Desai, N. K. Modi, R. Raghavarao, and R. Sridharan (1989), Dayglow photometry: a new approach, *Appl. Opt.*, *28*, 2138–2142, doi:10.1364/AO.28.002138.

Nishida, A. (1968a), Geomagnetic DP 2 fluctuations and associated magnetospheric phenomena, *J. Geophys. Res.*, *73*(5), 1795–1803, doi:10.1029/JA073i005p01795.

Nishida, A. (1968b), Coherence of geomagnetic DP 2 fluctuations with interplanetary magnetic variations, *J. Geophys. Res.*, *73*(17), 5549–5559, doi:10.1029/JA073i017p05549.

Noxon, J. F. (1968), Day airglow, *Sp. Sci. Rev.*, *8*(1), 92–134, doi:10.1007/BF00362572.

Noxon, J. F., and R. M. Goody (1962), Observation of day airglow emission, *J. Atmos. Sci.*, *19*(4), 342–343, doi:10.1175/1520-0469(1962)019⟨0342:OODAE⟩2.0.CO;2.

Onwumechilli, A. (1967), Geomagnetic variations in the equatorial zone, in *Phys. of Geomagnetic Phenomena*, p. 426.

Owens, R. J., Mathew J.and Forsyth (2013), The heliospheric magnetic field, *Living Reviews in Solar Physics*, *10*(1), 5, doi:10.12942/lrsp-2013-5.

Pallam Raju, D., R. Sridharan, R. Narayanan, N. K. Modi, R. Raghavarao, and B. H. Subbaraya (1995), Ground-based optical observations of daytime auroral emissions from Antarctica, *J. Atmos. Terr. Phys.*, *57*(13), 1591–1597, doi:10.1016/0021-9169(95)00089-K.

Pallam Raju, D., R. Sridharan, S. Gurubaran, and R. Raghavarao (1996), First results from ground-based daytime optical investigation of the development of the equatorial ionization anomaly, *Ann. Geophys.*, *14*(2), 238–245, doi:10.1007/s00585-996-0238-9.

Pallamraju, D. (1996), Studies of daytime upper atmospheric phenomena using ground-based optical techniques, Ph.D. thesis, Devi Ahilya Vishwa Vidyalaya of Indore.

Pallamraju, D., and S. Chakrabarti (2005), First ground-based measurements of OI 6300 daytime aurora over Boston in response to the 30 October 2003 geomagnetic storm, *Geophys. Res. Lett.*, *32*(3), doi:10.1029/2004GL021417.

Pallamraju, D., and S. Chakrabarti (2006), Contributions of imaging Echelle spectrographs to daytime optical aeronomy, *J. Atmos. Sol. Terr. Phys.*, *68*(13), 1459 – 1471, doi:10.1016/j.jastp.2005.05.013.

Pallamraju, D., and R. Sridharan (1998a), High resolution 2-D maps of OI 630.0 nm thermospheric dayglow from equatorial latitudes, *Ann. Geophys.*, *16*(8), 997–1006, doi:10.1007/s00585-998-0997-6.

Pallamraju, D., and R. Sridharan (1998b), Ground-based optical measurements of daytime auroral emissions: A new means of investigating space-weather related processes, *Proceedings of the Indian Academy of Sciences - Earth and Planetary Sciences*, *107*(3), 203–211, doi:10.1007/BF02840480.

Pallamraju, D., J. Baumgardner, and S. Chakrabarti (2000), A multiwavelength investigation of the ring effect in the day sky spectrum, *Geophys. Res. Lett.*, *27*(13), 1875–1878, doi:10.1029/1999gl010961.

Pallamraju, D., J. Baumgardner, S. Chakrabarti, and T. R. Pedersen (2001), Simultaneous ground based observations of an auroral arc in daytime/twilighttime OI 630.0 nm emission and by incoherent scatter radar, *J. Geophys. Res.*, *106*(A4), 5543–5549, doi:10.1029/2000JA000244.

Pallamraju, D., J. Baumgardner, and S. Chakrabarti (2002), HIRISE: A ground-based high-resolution imaging spectrograph using echelle grating for measuring daytime airglow/auroral emissions, *J. Atmos. Sol. Terr. Phys.*, *64*(12-14), 1581–1587, doi:10.1016/S1364-6826(02)00095-0.

Pallamraju, D., S. Chakrabarti, R. Doe, and T. Pedersen (2004a), First ground-based oi 630 nm optical measurements of daytime cusplike and f-region auroral precipitation, *Geophys. Res. Lett.*, *31*(8), doi:10.1029/2003GL019173.

Pallamraju, D., S. Chakrabarti, and C. E. Valladares (2004b), Magnetic storm-induced enhancement in neutral composition at low latitudes as inferred by $O(^1D)$ dayglow measurements from Chile, *Ann. Geophys.*, *22*(9), 3241–3250, doi:10.5194/angeo-22-3241-2004.

Pallamraju, D., U. Das, and S. Chakrabarti (2010), Short- and long-timescale thermospheric variability as observed from OI 630.0 nm dayglow emissions from low latitudes, *J. Geophys. Res.*, *115*(A6), doi:10.1029/2009JA015042.

Pallamraju, D., S. Chakrabarti, and S. C. Solomon (2011), On deriving incident auroral particle fluxes in the daytime using combined ground-based optical and radar measurements, *J. Geophys. Res.*, *116*(A4), doi:10.1029/2010JA015934.

Pallamraju, D., F. I. Laskar, R. P. Singh, J. Baumgardner, and S. Chakrabarti (2013), MISE: A multiwavelength imaging spectrograph using echelle grating for daytime optical aeronomy investigations , *J. Atmos. Sol. Terr. Phys.*, *103*(0), 176 – 183, doi:10.1016/j.jastp.2012.12.003.

Pallamraju, D., et al. (2014), Daytime wave characteristics in the mesosphere lower thermosphere region: Results from the Balloon-borne Investigations of Regional-atmospheric Dynamics experiment, *J. Geophys. Res.*, *119*(3), 2229–2242, doi:10.1002/2013JA019368.

Pallamraju, D., D. K. Karan, and K. A. Phadke (2016), First three dimensional wave characteristics in the daytime upper atmosphere derived from ground-based multiwavelength oxygen dayglow emission measurements, *Geophys. Res. Lett.*, *43*(11), 5545–5553, doi:10.1002/2016GL069074.

Pandey, K., R. Sekar, B. Anandarao, S. Gupta, and D. Chakrabarty (2016), Estimation of nighttime dip-equatorial E-region current density using measurements and models, *J. Atmos. Sol. Terr. Phys.*, *146*, 160–170, doi:https://doi.org/10.1016/j.jastp.2016.06.002.

Pant, T. K., and R. Sridharan (1998), A case-study of the low-latitude thermosphere during geomagnetic storms and its new representation by improved MSIS model, *Ann. Geophys.*, *16*(11), 1513–1518, doi:10.1007/s00585-998-1513-8.

Parker, E. N. (1958), Dynamics of the interplanetary gas and magnetic fields., *Astrophys. J.*, *128*, 664, doi:10.1086/146579.

Phadke, K. A., R. Narayanan, R. P. Singh, and D. Pallamraju (2014), An Automated CCD-based multi-wavelength airglow photometer (CMAP) for Optical Aeronomy Studies, *PRL Tech. Note*, *PRL-TN-2014-107*.

Phani Chandrasekhar, N., K. Arora, and N. Nagarajan (2014), Characterization of seasonal and longitudinal variability of EEJ in the Indian region, *J. Geophys. Res.*, *119*(12), 10,242–10,259, doi:10.1002/2014JA020183.

Pitteway, M. L. V., and C. O. Hines (1963), The viscous damping of atmospheric gravity waves, *Can. J. Phys.*, *41*(12), 1935–1948, doi:10.1139/p63-194.

Pramitha, M., M. Venkat Ratnam, A. Taori, B. V. Krishna Murthy, D. Pallamraju, and S. Vijaya Bhaskar Rao (2015), Evidence for tropospheric wind shear excitation of high-phase-speed gravity waves reaching the mesosphere using the ray-tracing technique, *Atmos. Chem. Phys.*, *15*(5), 2709–2721, doi:10.5194/acp-15-2709-2015.

Prolss, G. W. (1980), Magnetic storm associated perturbations of the upper atmosphere: Recent results obtained by satellite-borne gas analyzers, *Rev. Geophys.*, *18*(1), 183–202, doi:10.1029/RG018i001p00183.

Prolss, G. W., M. Roemer, and J. W. Slowey (1988), Dissipation of solar wind energy in the earth's upper atmosphere: The geomagnetic activity effect, *Adv. Space Res.*, *8*(5), 215 – 261, doi:https://doi.org/10.1016/0273-1177(88)90043-9.

Raghavarao, R., and B. G. Anandarao (1980), Vertical winds as a plausible cause for equatorial counter electrojet, *Geophys. Res. Lett.*, *7*(5), 357–360, doi:10.1029/GL007i005p00357.

Raghavarao, R., P. Sharma, and M. R. Sivaraman (1978), Correlation of ionization anomaly with the intensity of the electrojet, *Space Res.*, *18*, 277–280, doi:10.1016/B978-0-08-022021-5.50063-X.

Raghavarao, R., S. Gupta, R. Sekar, R. Narayanan, J. Desai, R. Sridharan, V. Babu, and V. Sudhakar (1987), In situ measurements of winds, electric fields and electron densities at the onset of equatorial spread-F, *J. Atmos. Terr. Phys.*, *49*(5), 485 – 492, doi:http://dx.doi.org/10.1016/0021-9169(87)90042-0.

Raghavarao, R., R. Sridharan, J. H. Sastri, V. V. Agashe, B. C. N. Rao, P. B. Rao, and V. V. Somayajulu (1988), *The equatorial ionosphere; WITS handbook. World Ionosphere/Thermosphere Study, vol 1.*, 48–93 pp., SCOSTEP Secretariat, University of Illinois, Urbana.

Raghavarao, R., L. E. Wharton, N. W. Spencer, H. G. Mayr, and L. H. Brace (1991), An equatorial temperature and wind anomaly (ETWA), *Geophys. Res. Lett.*, *18*(7), 1193–1196, doi:10.1029/91GL01561.

Raghavarao, R., W. R. Hoegy, N. W. Spencer, and L. E. Wharton (1993), Neutral temperature anomaly in the equatorial thermosphere- A source of vertical winds, *Geophys. Res. Lett.*, *20*(11), 1023–1026, doi:10.1029/93GL01253.

Rajaram, G. (1977), Structure of the equatorial F region, topside and bottomside-A review, *J. Atmos. Terr. Phys.*, *39*, 1125–1177.

Rees, M. H. (1989), *Physics and Chemistry of the Upper Atmosphere*, 289 pp., Cambridge University Press.

Richards, P. I. (1967), Computing reliable power spectra, *IEEE Spectrum*, *4*, 83–90.

Richmond, A. D., and S. Matsushita (1975), Thermospheric response to a magnetic substorm, *J. Geophys. Res.*, *80*(19), 2839–2850, doi:10.1029/JA080i019p02839.

Rishbeth, H. (1972), Thermospheric winds and the F-region: A review, *J. Atmos. Terr. Phys.*, *34*(1), 1 – 47, doi:http://dx.doi.org/10.1016/0021-9169(72)90003-7.

Rishbeth, H. (1997), The ionospheric E-layer and F-layer dynamos: A tutorial review, *J. Atmos. Sol. Terr. Phys.*, *59*(15), 1873 – 1880, doi:http://dx.doi.org/10.1016/S1364-6826(97)00005-9.

Rishbeth, H., and O. K. Garriott (1969), *Introduction to Ionospheric Physics*, 331 pp., Academic Press.

Roble, R. G., and R. E. Dickinson (1973), Is there enough solar extreme ultraviolet radiation to maintain the global mean thermospheric temperature?, *J. Geophys. Res.*, *78*(1), 249–257, doi:10.1029/JA078i001p00249.

Roble, R. G., J. M. Forbes, and F. A. Marcos (1987), Thermospheric dynamics during the march 22, 1979, magnetic storm: 1. model simulations, *J. Geophys. Res.*, *92*(A6), 6045–6068, doi:10.1029/JA092iA06p06045.

Rush, C. M., and A. D. Richmond (1973), The relationship between the structure of the equatorial anomaly and the strength of the equatorial electrojet, *J. Atmos. Terr. Physics*, *35*(6), 1171 – 1180, doi:https://doi.org/10.1016/0021-9169(73)90013-5.

Sagawa, E., T. J. Immel, H. U. Frey, and S. B. Mende (2005), Longitudinal structure of the equatorial anomaly in the nighttime ionosphere observed by IMAGE/FUV, *J. Geophys. Res.*, *110*(A11), doi:10.1029/2004JA010848.

Salah, J. E., and J. M. Holt (1974), Midlatitude thermospheric winds from incoherent scatter radar and theory, *Radio Science*, *9*(2), 301–313, doi:10.1029/RS009i002p00301.

Sampath, S., and T. S. G. Sastry (1979), Results from in situ measurements of ionospheric currents in the equatorial region-I, *J. Geomag. Goelect.*, *31*(3), 373–379, doi:10.5636/jgg.31.373.

Sastri, J. H. (1990), Equatorial anomaly in F region- A review, *Indian. J. Radio Space Phys*, *19*, 225–240.

Sastri, J. H., K. Niranjan, and K. S. V. Subbarao (2002), Response of the equatorial ionosphere in the Indian (midnight) sector to the severe magnetic storm of July 15, 2000, *Geophys. Res. Lett.*, *29*(13), 291–294, doi:10.1029/2002GL015133.

Scargle, J. D. (1982), Studies in astronomical time series analysis. II - Statistical aspects of spectral analysis of unevenly spaced data, *Astrophys. J.*, *263*, 835–853, doi:10.1086/160554.

Seaton, M. J. (1956), A possible explanation of the drop in F-region critical densities accompanying major ionospheric storms, *J. Atmos. Terr. Phys.*, *8*, 122 – 124.

Sekar, R., and R. Raghavarao (1987), Role of vertical winds on the Rayleigh-Taylor mode instabilities of the night-time equatorial ionosphere, *J. Atmos. Terr. Phys.*, *49*(10), 981 – 985, doi:http://dx.doi.org/10.1016/0021-9169(87)90104-8.

Sekar, R., D. Chakrabarty, and D. Pallamraju (2012), Optical signature of shear in the zonal plasma flow along with a tilted structure associated with equatorial spread F during a space weather event, *J. Atmos. Sol. Terr. Phys.*, *75–76*, 57 – 63, doi:https://doi.org/10.1016/j.jastp.2011.05.009.

Sharma, P., and R. Raghavarao (1989), Simultaneous occurrence of ionization ledge and counterelectrojet in the equatorial ionosphere: observational evidence and its implications, *Can. J. Phys.*, *67*(2-3), 166–172, doi:10.1139/p89-028.

Shepherd, G. G., W. A. Gault, D. W. Miller, Z. Pasturczyk, S. F. Johnston, P. R. Kosteniuk, J. W. Haslett, D. J. W. Kendall, and J. R. Wimperis (1985), WAMDII: wide-angle Michelson Doppler imaging interferometer for Spacelab, *Appl. Opt.*, *24*(11), 1571, doi:10.1364/AO.24.001571.

Shepherd, G. G., et al. (1993a), WINDII, the wind imaging interferometer on the Upper Atmosphere Research Satellite, *J. Geophys. Res.*, *98*(D6), 10,725–10,750, doi:10.1029/93JD00227.

Shepherd, G. G., et al. (1993b), Longitudinal structure in atomic oxygen concentrations observed with WINDII on UARS, *Geophys. Res. Lett.*, *20*(12), 1303–1306, doi:10.1029/93GL01105.

Shepherd, G. G., N. J. Siddiqi, R. H. Wiens, and S. Zhang (1997), Airglow measurements of possible changes in the ionosphere and middle atmosphere, *Adv. Space Res.*, *20*(11), 2127 – 2135, doi:http://dx.doi.org/10.1016/S0273-1177(97)00605-4.

Shepherd, G. G., R. G. Roble, C. McLandress, and W. E. Ward (1997), WINDII observations of the 558 nm emission in the lower thermosphere: the influence of dynamics on composition, *J. Atmos. Sol. Terr. Phys.*, *59*, 655–667, doi:10.1016/S1364-6826(96)00142-3.

Shepherd, G. G., et al. (2012), The Wind Imaging Interferometer (WINDII) on the Upper Atmosphere Research Satellite: A 20 year perspective, *Rev. Geophys.*, *50*(2), doi:10.1029/2012RG000390.

Shiokawa, K., Y. Katoh, M. Satoh, M. K. Ejiri, T. Ogawa, T. Nakamura, T. Tsuda, and R. H. Wiens (1999), Development of Optical Mesosphere Thermosphere Imagers (OMTI), *Earth, Planets and Space*, *51*(7-8), 887–896, doi:10.5636/eps.51.887.

Shiokawa, K., et al. (2003), Thermospheric wind during a storm-time large-scale traveling ionospheric disturbance, *J. Geophys. Res.*, *108*(A12), doi:10.1029/2003JA010001.

Shiokawa, K., Y. Otsuka, and T. Ogawa (2006), Quasiperiodic southward moving waves in 630-nm airglow images in the equatorial thermosphere, *J. Geophys. Res.*, *111*(A6), doi:10.1029/2005JA011406.

Shiokawa, K., Y. Otsuka, and T. Ogawa (2009), Propagation characteristics of nighttime mesospheric and thermospheric waves observed by optical mesosphere thermosphere imagers at middle and low latitudes, *Earth, Planets and Space*, *61*(4), 479–491, doi:10.1186/BF03353165.

Singh, R. P., and D. Pallamraju (2015), On the latitudinal distribution of mesospheric temperatures during sudden stratospheric warming events, *J. Geophys. Res.*, *120*(4), 2926–2939, doi:10.1002/2014JA020355.

Singh, R. P., and D. Pallamraju (2016), Effect of cyclone Nilofar on mesospheric wave dynamics as inferred from optical nightglow observations from Mount Abu, India, *J. Geophys. Res.*, *121*(6), 5856–5867, doi:10.1002/2016JA022412.

Singh, R. P., and D. Pallamraju (2017), Near infrared imaging spectrograph (NIRIS) for ground-based mesospheric OH (6-2) and O2 (0-1) intensity and temperature measurements, *J. Earth Syst. Sci.*, *126*, doi:10.1007/s12040-017-0865-4.

Singh, V., I. McDade, G. Shepherd, B. Solheim, and W. Ward (1996), The O(1D) dayglow emission as observed by the WIND Imaging Interferometer on UARS, *Adv. Space Res.*, *17*(11), 11 – 14, doi:http://dx.doi.org/10.1016/0273-1177(95)00725-T.

Smith, S. M., C. R. Martinis, J. Baumgardner, and M. Mendillo (2015), All-sky imaging of transglobal thermospheric gravity waves generated by the March

2011 Tohoku Earthquake, *J. Geophys. Res.*, *120*(12), 10,992–10,999, doi:10.1002/2015JA021638.

Solomon, S. C., and V. J. Abreu (1989), The 630 nm dayglow, *J. Geophys. Res.*, *94*(A6), 6817–6824, doi:10.1029/JA094iA06p06817.

Somayajulu, V. V., L. Cherian, K. Rajeev, G. Ramkumar, and C. R. Reddi (1993), Mean winds and tidal components during counter electrojet events, *Geophys. Res. Lett.*, *20*(14), 1443–1446, doi:10.1029/93GL00088.

Spencer, N. W., L. Wharton, H. Niemann, A. Hedin, G. Carignan, and J. Maurer (1981), The Dynamics Explorer wind and the temperature spectrometer, *Space Science Instrumentation*, *5*(4), 417–428.

Sridharan, R., S. Gurubaran, R. Raghavarao, and R. Suhasini (1991a), Coordinated thermospheric and F-region measurements from low latitudes, *J. Atmos. Terr. Phys.*, *53*(6-7), 515–519, doi:10.1016/0021-9169(91)90078-L.

Sridharan, R., R. Raghavarao, S. Gurubaran, and R. Narayanan (1991b), First results of OI 630.0 nm dayglow measurements from equatorial latitudes, *J. Atmos. Sol.-Terr. Phy.*, *53*, 521–528.

Sridharan, R., R. Narayanan, and N. K. Modi (1992a), Improved chopper mask for the dayglow photometer, *Appl. Opt.*, *31*(4), 425–426, doi:10.1364/AO.31.000425.

Sridharan, R., S. A. Haider, S. Gurubaran, R. Sekar, and R. Narayanan (1992b), OI 630.0-nm dayglow in the region of equatorial ionization anomaly: Temporal variability and its causative mechanism, *J. Geophys. Res.*, *97*(A9), 13,715–13,721, doi:10.1029/92JA00674.

Sridharan, R., R. Narayanan, N. K. Modi, and D. P. Raju (1993a), A Novel mask design for multiwavelength dayglow photometry, *Appl. Opt.*, *32*(22), 4178–80, doi:10.1364/AO.32.004178.

Sridharan, R., R. Sekar, and S. Gurubaran (1993b), Two-dimensional high-resolution imaging of the equatorial plasma fountain, *J. Atmos. Terr. Phys.*, *55*(13), 1661 – 1665, doi:http://dx.doi.org/10.1016/0021-9169(93)90170-4.

Sridharan, R., D. P. Raju, R. Raghavarao, and P. V. S. Ramarao (1994), Precursor to equatorial spread-F in OI 630.0 nm dayglow, *Geophys. Res. Lett.*, *21*(25), 2797–2800, doi:10.1029/94GL02732.

Sridharan, R., D. Pallam Raju, R. Narayanan, N. K. Modi, B. H. Subbaraya, and R. Raghavarao (1995), Daytime measurements of optical auroral emissions from Antarctica, *Current science*, *68*(8), 830–834.

Sridharan, R., N. K. Modi, D. P. Raju, R. Narayanan, T. K. Pant, A. Taori, and D. Chakrabarty (1998), A multiwavelength daytime photometer - a new tool for the investigation of atmospheric processes, *Meas. Sci. Technol.*, *9*(4), 585.

Sridharan, R., D. P. Raju, V. Somayajulu, A. Taori, D. Chakrabarty, and R. Raghavarao (1999), Imprint of equatorial electrodynamical processes in the OI 630.0 nm dayglow, *J. Atmos. Sol. Terr. Phys.*, *61*(15), 1143 – 1155, doi:https://doi.org/10.1016/S1364-6826(99)00064-4.

Stening, R. J., C. E. Meek, and A. H. Manson (1996), Upper atmosphere wind systems during reverse equatorial electrojet events, *Geophys. Res. Lett.*, *23*(22), 3243–3246, doi:10.1029/96GL02611.

Stolarski, R. S., P. B. Hays, and R. G. Roble (1975), Atmospheric heating by solar EUV radiation, *J. Geophys. Res.*, *80*(16), 2266–2276, doi:10.1029/JA080i016p02266.

Strickland, D. J., J. S. Evans, and L. J. Paxton (1995), Satellite remote sensing of thermospheric O/N_2 and solar EUV: 1. Theory, *J. Geophys. Res.*, *100*(A7), 12,217–12,226, doi:10.1029/95JA00574.

Strickland, D. J., R. J. Cox, R. R. Meier, and D. P. Drob (1999), Global O/N_2 derived from DE-1 FUV dayglow data: Technique and examples from two storm periods, *J. Geophys. Res.*, *104*(A3), 4251–4266, doi:10.1029/98JA02817.

Sumod, S. G., T. K. Pant, C. Vineeth, and M. M. Hossain (2014), On the ionospheric and thermospheric response of solar flare events of 19 January 2005: An investigation using radio and optical techniques, *J. Geophys. Res.*, *119*(6), 5049–5059, doi:10.1002/2013JA019714.

Sunda, S., and B. M. Vyas (2013), Local time, seasonal, and solar cycle dependency of longitudinal variations of TEC along the crest of EIA over India, *J. Geophys. Res.*, *118*(10), 6777–6785, doi:10.1002/2013JA018918.

Sutton, E. K., J. M. Forbes, R. S. Nerem, and T. N. Woods (2006), Neutral density response to the solar flares of October and November, 2003, *Geophys. Res. Lett.*, *33*(22), doi:10.1029/2006GL027737.

Taori, A., R. Sridharan, D. Chakrabarty, N. Modi, and R. Narayanan (2003), Significant upper thermospheric contribution to the O (1S) 557.7 nm dayglow emission: first ground based evidence, *J. Atmos. Sol. Terr. Phys.*, *65*(1), 121 – 128, doi:https://doi.org/10.1016/S1364-6826(02)00289-4.

Taylor, M. J., M. B. Bishop, and V. Taylor (1995), All-sky measurements of short period waves imaged in the OI(557.7 nm), Na(589.2 nm) and near infrared OH and O2(0,1) nightglow emissions during the ALOHA-93 Campaign, *Geophys. Res. Lett.*, *22*(20), 2833–2836, doi:10.1029/95GL02946.

Taylor, M. J., J.-M. Jahn, S. Fukao, and A. Saito (1998), Possible evidence of gravity wave coupling into the mid-latitude F region ionosphere during the SEEK Campaign, *Geophys. Res. Lett.*, *25*(11), 1801–1804, doi:10.1029/97GL03448.

Teitelbaum, H., M. Massebeuf, J. L. Fellous, M. Petitdidier, J. Christophe, and F. Blanco (1981), Simultaneous measurements of meteor winds and green line intensity variations: Gravity waves and planetary waves, *J. Geophys. Res.*, *86*(A9), 7767–7770, doi:10.1029/JA086iA09p07767.

Thome, G. D., and L. S. Wagner (1971), Electron density enhancements in the E and F regions of the ionosphere during solar flares, *J. Geophys. Res.*, *76*(28), 6883–6895, doi:10.1029/JA076i028p06883.

Tinsley, B. A., A. B. Christensen, J. Bittencourt, H. Gouveia, P. D. Angreji, and H. Takahashi (1973), Excitation of oxygen permitted line emissions in the tropical nightglow, *J. Geophys. Res.*, *78*(7), 1174–1186, doi:10.1029/JA078i007p01174.

Torr, M. R., and D. G. Torr (1982), The role of metastable species in the thermosphere, *Rev. Geophys. Sp. Phys.*, *20*(1), 91–144.

Torrence, C., and G. P. Compo (1998), A practical guide to wavelet analysis, *Bull. Amer. Meteor. Soc.*, *79*(1), 61–78, doi:10.1175/1520-0477(1998)079⟨0061:APGTWA⟩2.0.CO;2.

Troshichev, O. A. (1982), Polar magnetic disturbances and field-aligned currents, *Space Science Reviews*, *32*(3), 275–360, doi:10.1007/BF00167945.

Tsugawa, T., A. Saito, Y. Otsuka, M. Nishioka, T. Maruyama, H. Kato, T. Nagatsuma, and K. T. Murata (2011), Ionospheric disturbances detected by GPS total electron content observation after the 2011 off the Pacific coast of Tohoku Earthquake, *Earth, Planets and Space*, *63*(7), 66, doi:10.5047/eps.2011.06.035.

Tsunoda, R. T. (1985), Control of the seasonal and longitudinal occurrence of equatorial scintillations by the longitudinal gradient in integrated e region pedersen conductivity, *J. Geophys. Res.*, *90*(A1), 447–456, doi:10.1029/JA090iA01p00447.

Tsurutani, B., et al. (2004), Global dayside ionospheric uplift and enhancement associated with interplanetary electric fields, *J. Geophys. Res.*, *109*(A8), doi:10.1029/2003JA010342.

Tsurutani, B. T., et al. (2005), The October 28, 2003 extreme EUV solar flare and resultant extreme ionospheric effects: Comparison to other Halloween events and the Bastille Day event, *Geophys. Res. Lett.*, *32*(3), doi:10.1029/2004GL021475.

Tyagi, S., and V. Singh (1998), The morphology of oxygen greenline dayglow emission, *Ann. Geophys.*, *16*(12), 1599–1606, doi:10.1007/s00585-998-1599-z.

Upadhayaya, A. K., and V. Singh (2002), Effects of temperature dependence of reaction $N_2(A^3\ S^+{}_u)$ + O on greenline dayglow emission, *Ann. Geophys.*, *20*(12), 2039–2045, doi:10.5194/angeo-20-2039-2002.

Vadas, S. L., and D. C. Fritts (2005), Thermospheric responses to gravity waves: Influences of increasing viscosity and thermal diffusivity, *J. Geophys. Res.*, *110*(D15), D15,103, doi:10.1029/2004JD005574.

Walker, G. O., J. H. K. Ma, and E. Golton (1994), The equatorial ionospheric anomaly in electron content from solar minimum to solar maximum for South East Asia, *Ann. Geophys.*, *12*(2/3), 195–209, doi:10.1007/s00585-994-0195-0.

Wallace, L. (1961), An attempt to observe the day airglow, *J. Geophys. Res.*, *66*(5), 1585–1586, doi:10.1029/JZ066i005p01585.

Wallace, L. (1963), Observation of the day airglow, *J. Geophys. Res.*, *68*(5), 1559–1560, doi:10.1029/JZ068i005p01559.

Wallace, L., and M. B. McElroy (1966), The visual dayglow, *Planet. Space Sci.*, *14*(8), 677–708, doi:10.1016/0032-0633(66)90100-0.

Witasse, O., J. Lilensten, C. Lathuillre, and P.-L. Blelly (1999), Modeling the OI 630.0 and 557.7 nm thermospheric dayglow during EISCAT-WINDII coordinated measurements, *J. Geophys. Res.*, *104*(A11), 24,639–24,655, doi: 10.1029/1999JA900260.

Yadav, S., and D. Pallamraju (2015), On the coupled interactions between ring current intensity and high-latitude ionospheric electron density variations, *J. Atmos. Sol. Terr. Phys.*, *125126*, 50–58, doi:https://doi.org/10.1016/j.jastp.2015.02.006.

Yigit, E., A. D. Aylward, and A. S. Medvedev (2008), Parameterization of the effects of vertically propagating gravity waves for thermosphere general circulation models: Sensitivity study, *J. Geophys. Res.*, *113*(D19), D19,106, doi: 10.1029/2008JD010135.

Zhang, S. P., and G. G. Shepherd (2000), Neutral winds in the lower thermosphere observed by WINDII during the April 45th, 1993 storm, *Geophys. Res. Lett.*, *27*(13), 1855–1858, doi:10.1029/2000GL000034.

Zhang, S. P., and G. G. Shepherd (2004), Solar influence on the O(^{1}D) dayglow emission rate: Global-scale measurements by WINDII on UARS, *Geophys. Res. Lett.*, *31*(7), L07,804, doi:10.1029/2004GL019447.

Zhang, S. P., and G. G. Shepherd (2005), On the response of the O(^{1}S) dayglow emission rate to the sun's energy input: An empirical model deduced from WINDII/UARS global measurements, *J. Geophys. Res.*, *110*(A3), A03,304, doi:10.1029/2004JA010887.

Zhang, Y., L. J. Paxton, D. Morrison, B. Wolven, H. Kil, C.-I. Meng, S. B. Mende, and T. J. Immel (2004), O/N_2 changes during 14 October 2002 storms: IMAGE SI-13 and TIMED/GUVI observations, *J. Geophys. Res.*, *109*(A10), doi:10.1029/2004JA010441.

Zhang, Y., L. Paxton, D. Morrison, D. Marsh, and H. Kil (2014), Storm-time behaviors of O/N_2 and NO variations, *J. Atmos. Sol. Terr. Phys.*, *114*, 42–49, doi:https://doi.org/10.1016/j.jastp.2014.04.003.

Zhao, B., W. Wan, and L. Liu (2005), Responses of equatorial anomaly to the October-November 2003 superstorms, *Ann. Geophys.*, *23*(3), 693–706, doi:10.5194/angeo-23-693-2005.

List of Publications

Publications in Journals

1. Pallamraju, D., **D. K. Karan**, K. A. Phadke (2016), First three dimensinal wave characteristics in the daytime upper atmosphere derived from ground-based multiwavelength oxygen dayglow emisison measurements, Geophys. Res. Lett., 42, 5545-5553, doi:10.1002/2016GL069074.

2. **Karan, D. K.**, D. Pallamraju, K. A. Phadke, T. Vijayalakshmi, T. K. Pant, and S. Mukherjee (2016), Electrodynamic influence on the diurnal behaviour of neutral daytime airglow emissions, Ann. Geophys., 34, 1019-1030, doi:10.5194/angeo-34-1019-2016.

3. **Karan, D. K.**, and D. Pallamraju (2017), Small-scale longitudinal variations in the daytime equatorial thermospheric wave dynamics as inferred from oxygen dayglow emissions, J. Geophys. Res. Space Physics, 122, 6528-6542, doi:10.1002/2017JA023891.

4. **Karan, D. K.**, and D. Pallamraju (2018), Effect of geomagnetic storms on the daytime low-latitude thermospheric wave dynamics, J. Atmos. Sol. Terr. Phys., https://doi.org/10.1016/j.jastp.2018.02.003

Conference Papers

1. Pallamraju, D., **D. K. Karan**, F. I. Laskar, K. A. Phadke, T. Vijaya Lakshmi, M. Anji Reddy, "Zonal behaviour of optical daytime airglow emission intensities from low latitudes." (Paper No.: PS3 - 80) Presented at 18th

National Space Science Symposium held during 29 January - 1 February 2014 at Dibrugarh University, Dibrugarh, Assam. [Poster by DKK]

2. Pallamraju, D., **D. K. Karan**, F. I. Laskar, K. A. Phadke, T. Vijaya Lakshmi, M. Anji Reddy, "Wave dynamical coupling in the daytime as obtained from optical oxygen airglow emission intensities over low latitudes." (Presenatation No.: C2.2 - 0052 - 14), 40th COSPAR Scientific Assembly, 2 - 10 August 2014, Moscow, Russia. [Oral by DP]

3. **Karan, D. K.**, D. Pallamraju, K. A. Phadke, T. Vijaya Lakshmi, "Coordinated, optical, radio, and magnetic investigations of wave dynamics in the daytime upper atmosphere." (Session 4: Coupling processes), United Nations / Japan Workshop on Space Weather "Science and Data Products from ISWI Instruments", 2 - 6 March 2015, Fukuoka, Japan. [Oral by DKK]

4. Pallamraju, D., **D. K. Karan**, K. A. Phadke, "Investigations on wave dynamics of daytime upper atmosphere over low-latitude," Session-S4, 14th ISEA meeting, Bahir-Dar, Ethiopia, 19-23 October, 2015. [Oral by DP]

5. Pallamraju, D., **D. K. Karan**, F. I. Laskar, "Upper atmospheric dynamics: influence of solar radiation versus forcing from below," Science for space weather, Goa, 24-29 January, 2016. [Oral by DP]

6. **Karan, D. K.**, D. Pallamraju, K. A. Phadke, T. Vijaya Lakshmi, and M. Anji Reddy, "Effect of equatorial electrodynamical process on the optical neutral dayglow emission intensities over low latitudes." (Paper No.: PS3 - 136). Presented at 19th National Space Science Symposium, Space Physics Laboratory, VSSC, Trivandrum, India, 9-12 February, 2016. [Poster by DKK]

7. Pallamraju, D., **D. K. Karan**, K. A. Phadke, T. Vijaya Lakshmi, and M. Anji Reddy,"Recent results from the investigations of daytime uper atmospheric wavedynamics over low-latitudes."Presented at 19th National Space Science Symposium held during 9-12 February, 2016, Space Physics Laboratory, VSSC, Trivandrum, India. [Oral by DP]

8. Pallamraju, D., **D. K. Karan**,"The changes in the ionospheric-thermo spheric behaviour during varying solar activity levels." Presented at 9th IAGA - ICMA/IAMAS-ROSMIC/VarSITI/SCOSTEP workshop on Long-Term Changes and Trends in the Atmosphere, Khlungsborn, 19-23 September, 2016. [Oral by DP]

9. Pallamraju, D., S. Mandal, K. A. Phadke, **D. K. Karan**, R. P. Singh,"Gravity waves in the ionosphere as derived from digisonde measurements at Ahmedabad, India."- 3rd URSI-Regional Conference on Radio Science, NARL, Tirupati, March 1-4, 2017. [Oral by DP]

10. Pallamraju, D., **D. K. Karan**,"Effect Of Equatorial Electrodynamics And Lower Atmospheric Forcing On Optical Neutral Dayglow Emission As A Function Of Solar Activity."- ST08-A007 - Presented at 14th annual meeting Asia Oceania Geosciences Society, 6-11 August 2017. [Oral by DP]

11. Pallamraju, D., **D. K. Karan**, S. Mandal, and R. P. Singh,"Results from the first three dimensional waves in the daytime obtained from dayglow emissions and their comparison with those derived from ionospheric measurements "- ST26-27-A018 - Presented at 14th annual meeting Asia Oceania Geosciences Society, 6-11 August 2017. [Oral by DP]

12. **Karan, D. K.** and D. Pallamraju, "Effect of equatorial electrodynamics on low-latitude thermosphere as inferred from neutral optical dayglow emission observations "- SA34A-07 - Presented at 2017 American Geophysical Union Fall Meeting, 13 December 2017. [Oral by DKK]

13. Pallamraju, D. and **D. K. Karan**, "Small-scale longitudinal variations in the daytime equatorial wave dynamics as inferred from oxygen dayglow emissions "- SA51A-2368 - Presented at 2017 American Geophysical Union Fall Meeting, 15 December 2017. [Poster by DKK]

Publications Attached With Thesis

1. Pallamraju, D., **D. K. Karan**, K. A. Phadke (2016), First three dimensinal wave characteristics in the daytime upper atmosphere derived from ground-based multiwavelength oxygen dayglow emisison measurements, Geophys. Res. Lett., 42, 5545-5553, doi:10.1002/2016GL069074.

2. **Karan, D. K.**, D. Pallamraju, K. A. Phadke, T. Vijayalakshmi, T. K. Pant, and S. Mukherjee (2016), Electrodynamic influence on the diurnal behaviour of neutral daytime airglow emissions, Ann. Geophys., 34, 1019-1030, doi:10.5194/angeo-34-1019-2016.

3. **Karan, D. K.**, and D. Pallamraju (2017), Small-scale longitudinal variations in the daytime equatorial thermospheric wave dynamics as inferred from oxygen dayglow emissions, J. Geophys. Res. Space Physics, 122, 6528-6542, doi:10.1002/2017JA023891.

AGU PUBLICATIONS

Geophysical Research Letters

RESEARCH LETTER
10.1002/2016GL069074

Key Points:
- Technique to derive daytime thermospheric 3-D wave characteristics presented
- Large field-of-view ground-based multiwavelength dayglow measurements enable estimation of wave parameters
- New method of deriving propagation characteristics of waves in horizontal and vertical directions

Correspondence to:
D. Pallamraju,
raju@prl.res.in

Citation:
Pallamraju, D., D. K. Karan, and K. A. Phadke (2016), First three dimensional wave characteristics in the daytime upper atmosphere derived from ground-based multiwavelength oxygen dayglow emission measurements, *Geophys. Res. Lett.*, *43*, 5545–5553, doi:10.1002/2016GL069074.

Received 11 APR 2016
Accepted 16 MAY 2016
Accepted article online 18 MAY 2016
Published online 4 JUN 2016

First three dimensional wave characteristics in the daytime upper atmosphere derived from ground-based multiwavelength oxygen dayglow emission measurements

Duggirala Pallamraju[1], Deepak K. Karan[1,2], and Kedar A. Phadke[1]

[1]Space and Atmospheric Sciences Division, Physical Research Laboratory, Ahmedabad, India, [2]Indian Institute of Technology, Gandhinagar, India

Abstract First results on the three-dimensional wave characteristics in the daytime upper atmosphere have been derived using measurements of oxygen dayglow emissions at 557.7, 630.0, and 777.4 nm that originate at around 130, 230, and 300 km (peak of the *F* region). The horizontal scale sizes of gravity waves (GWs), their time periods, phase propagation angle (counterclockwise from east), and phase speeds are found to vary in the range of 27–227 km, 32–70 min, 207°–253°, and 6–76 ms^{-1}, respectively. Two-dimensional measurements on the horizontal scale sizes in the daytime have not been reported before. Further, using Hines' (1960) dispersion relation for GWs, vertical scale sizes and phase angles have also been derived. This technique opens up new possibilities in the investigations of daytime wave dynamics in three dimensions in the upper atmosphere.

1. Introduction

The importance of neutral wind and wave dynamics in contributing to the day-to-day, diurnal, and seasonal behavior of the upper atmosphere is well known [e.g., *Mayr et al.*, 1978]. Satellite-based measurements have provided a broad picture of neutral winds [e.g., *Herrero et al.*, 1988; *Shepherd et al.*, 1993a] which, in combination with ground-based measurements, have formed the basis for empirical wind models [e.g., *Hedin et al.*, 1996; *Drob et al.*, 2015]. It can be appreciated that, unlike winds which can be measured by both ground-based [e.g., *Meriwether et al.*, 1986; *Makela et al.*, 2013] and satellite-based platforms [e.g., *Spencer et al.*, 1981; *Shepherd et al.*, 1993a, 1993b; *Killeen et al.*, 2006], neutral wave scale sizes and periodicities in the daytime can only be measured by ground-based observations of optical airglow emissions that are carried out over a large field of view (FOV). It is shown that the density fluctuations due to waves alter the reactants that produce nightglow/dayglow and thus contribute to modulations in their intensities [*Teitelbaum et al.*, 1981; *Shepherd et al.*, 1993b; *Pallamraju et al.*, 2010]. While nightglow imaging has been possible to obtain wave features in two dimensions [e.g., *Taylor et al.*, 1995; *Mendillo et al.*, 1997; *Shiokawa et al.*, 2009; *Lakshmi Narayanan et al.*, 2010], measurements during daytime, however, remain a challenge. This is essentially due to the difficulty of using two-dimensional optical imaging techniques in the daytime as direct incidence of sunlight renders the images unusable.

The nearest attempt on two-dimensional maps in the daytime was made using an azimuth and elevation mirror scanning arrangement to the dayglow photometer [*Pallam Raju and Sridharan*, 1998]; however, as the measurements were not simultaneous over a large FOV, it was not possible to obtain information on scale sizes using such method. In the present study, we have used a high spectral resolution imaging slit spectrograph in zonal and meridional directions and obtained thermospheric daytime airglow emission intensities simultaneously at multiple wavelengths over a large FOV. From this information on the dayglow intensities in the orthogonal directions, the wave features in the horizontal directions at the three altitudes of oxygen emissions have been obtained through spectral analysis. Such measurements on horizontal scale sizes (in two dimensions) have hitherto been not reported. Moreover, the measured values have been used in conjunction with the gravity wave (GW) dispersion relation [*Hines*, 1960] to calculate the plausible wave features in the vertical direction as well. Thus, this paper reports the first results on the three-dimensional wave characteristics at different altitudes in the daytime upper atmosphere.

2. Measurement Technique

It is a challenge to make ground-based measurements of thermospheric dayglow emission intensities as these are buried in the strong solar scattered background continuum. However, innovations in the recent past have enabled unambiguous measurements of daytime optical emissions from the ground [e.g., *Narayanan et al.*, 1989; *Sridharan et al.*, 1993, 1998; *Chakrabarti et al.*, 2001; *Pallamraju et al.*, 2002, 2013; *Gerrard and Meriwether*, 2011; *Marshall et al.*, 2011].

In this study, wave characteristics in terms of their scale sizes, periodicities, orientations, and phase speeds, have been obtained as a function of local time (LT) using a multiwavelength imaging echelle spectrograph, MISE. MISE is an ideal technique for simultaneously obtaining the daytime thermospheric airglow emission intensities originating at multiple altitudes over a large FOV [*Pallamraju et al.*, 2013]. Dayglow intensity variations at 557.7, 630.0, and 777.4 nm that originate at around 130, 230 km, and peak height of the *F* region (considered at 300 km), respectively, are used to infer the wave characteristics at those altitudes as a function of time. For a FOV of 100°, the spatial coverage at those emission altitudes is 3°, 5.5°, and 7.3° (~340, 600, and 800 km) in latitude/longitude (depending on MISE's orientation along meridional/zonal direction). Information from all these three spectra obtained at a high resolution (~0.015 nm) is imaged onto a 1 k × 1 k CCD detector. On-chip binning of 8 pixels along the spatial direction (results in an image of size 1024 (spectral) × 128 pixels (spatial)) is carried out to increase the signal-to-noise-ratio. Different segments of the image on the CCD correspond to different spatial regions. Spectra from each of the spatial segments are compared with the normalized solar spectrum [*Delbouille et al.*, 1973] to obtain the dayglow emissions by removing the contribution of atmospheric scattering (Ring effect) [*Pallamraju et al.*, 2000, 2002, 2013].

With regard to the production mechanisms, the 630.0 nm dayglow originates at the base of the *F* region (~230 km) and is produced due to a cumulative effect of photoelectron impact on atomic oxygen, photodissociation of molecular oxygen, and dissociative recombination of O_2^+ [*Solomon and Abreu*, 1989]. Similar to 630.0 nm emissions, 557.7 nm dayglow also has multiple production sources but peaks at two altitudes, 100 and 160 km. Here an average value of 130 km has been considered as a representative height for 557.7 nm emissions, which is produced due to quenching of N_2, electron impact excitation of O, dissociative recombination of O_2^+, and charge exchange of O_2^+ with N [*Witasse et al.*, 1999]. The 777.4 nm emissions originate from radiative recombination of O^+ and e^- [*Tinsley et al.*, 1973]. As the densities of both species maximize at the peak height (h_{max}) of the *F* region, this emission emanates from ~300 km. Daytime 777.4 nm emission measurements have been possible only after the emergence of MISE [*Pallamraju et al.*, 2013] which have contributed to a greater understanding of upper atmospheric behavior due to waves from gravity to planetary scales in the recent times [e.g., *Laskar et al.*, 2013, 2015; *Laskar and Pallamraju*, 2014].

3. Data Analysis

The measurements presented here have been obtained during 13–25 May 2015 from Hyderabad (17.3°N, 78.5°E), a low-latitude location in India. The maximum spatial extent of data possible at the 557.7, 630.0, and 777.4 nm emission altitudes is 340, 600, and 800 km, respectively. In the present experiment, an 11 pixel running average of the spectral image is obtained along spatial direction. By design, in a size of 128 pixels along the spatial direction, 89 useful segments of data exist leaving out ~20 pixels on either side of the image which correspond to locations that form very low elevation angles and so are susceptible to large scattering in the lower atmosphere. The maximum spatial dispersion for the three emission wavelengths considering the varying nature of spatial distance with view angle corresponds to 11, 20, and 25 km pixel^{-1}, respectively. Considering a 2 pixel resolution to ascertain the position, the spatial uncertainty for each of these emission altitudes is 22, 40, and 50 km. The data cadence for obtaining information on dayglow emission intensities along a given orientation is 5 min; however, data are averaged for 15 min in the present study to smooth out the highly fluctuating components of the order of Brunt-Väisälä (BV) period. Further, after around 30 min of operation in a certain orientation, the spectrograph is rotated to its orthogonal position. This is repeated throughout the day. Spectral analyses have been carried out for each of the 15 min of data along a spatial orientation and values of wave numbers k_x (zonal) and k_y (meridional) (and hence scale sizes λ_x and λ_y) that are statistically significant (greater than 90% false alarm limit (FAL)) are obtained. Out of all the dominant scale sizes, the lower cutoffs are taken to be 22, 40, and

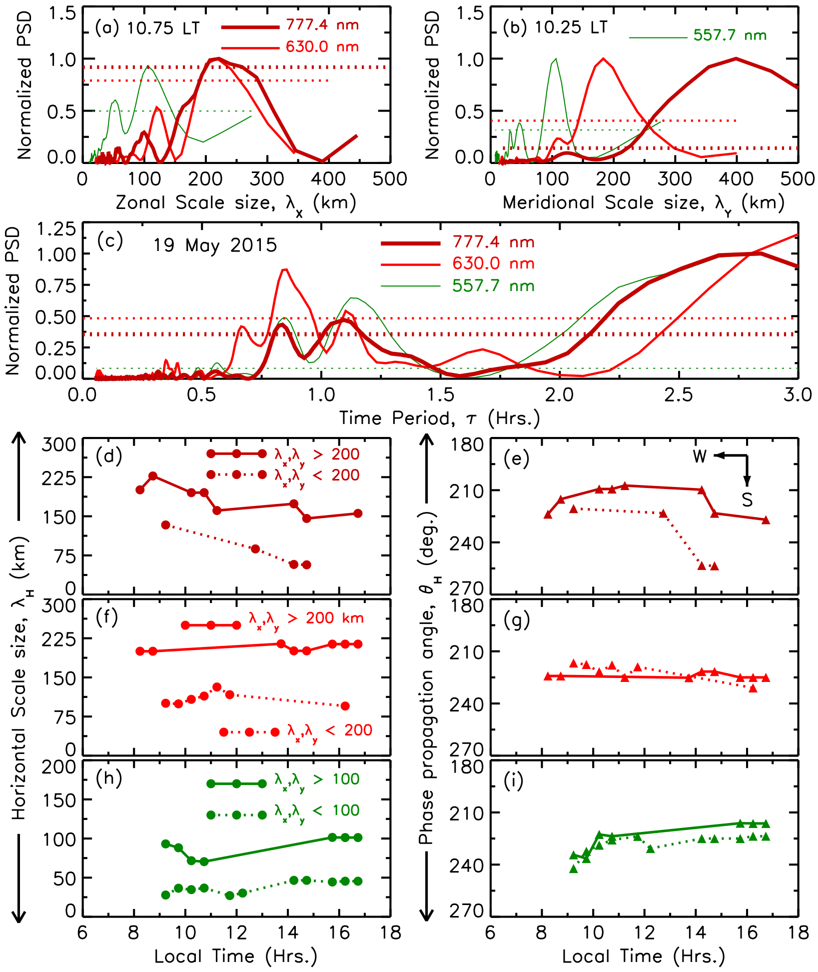

Figure 1. Wave number spectral analysis showing (a and b) λ_x, λ_y, (c) τ, (d, f, and h) λ_H, and (e, g, and i) θ_H counterclockwise from west.

50 km considering the 2 pixel resolution as mentioned above for 557.7, 630.0, and 777.4 nm. The higher cutoffs are estimated according to the Nyquist criterion and so the scale sizes greater than half the spatial extent have not been considered for further analysis. Taking also into account the spatial uncertainties (due to 2 pixel resolution) the higher cutoffs are 181, 320, and 425 km for the three emission altitudes considered. The horizontal wave vector k_H, and hence scale size λ_H, is calculated using the values of k_x and k_y measured alternatingly ($k_H^2 = k_x^2 + k_y^2$). The phase propagation angle of these waves, θ_H, is given as $\tan^{-1}(k_y/k_x)$.

4. Results

Figures 1a and 1b show sample results of wave number spectra as obtained for zonal (λ_x) and meridional (λ_y) orientations for the three emission wavelengths of investigations at two times on 19 May 2015. The *x* and *y* axes show the scale sizes in kilometer and normalized power spectral density for each of the wavelengths. The dotted lines show the 90% FAL. Using the data cadence of 5 min for zenithal dayglow emission intensities for all the emission wavelengths, Lomb-Scargle periodogram analysis [*Lomb*, 1976; *Scargle*, 1982] has been carried out to arrive at the prominent periodicities (τ) of GWs for this day. These values are 32.8 ± 1.9, 51.1 ± 5.3, and 69.1 ± 13.9 min for the emissions corresponding to 557.7 nm; 51.2 ± 1.9 and 66.1 ± 6.7 min for 630.0 nm; and 50.2 ± 5.1 and 65.6 ± 11.6 min for 777.4 nm emissions (Figure 1c). As the variation in all the emission intensities shows a prominent common time period of around 51 min, the information on the values

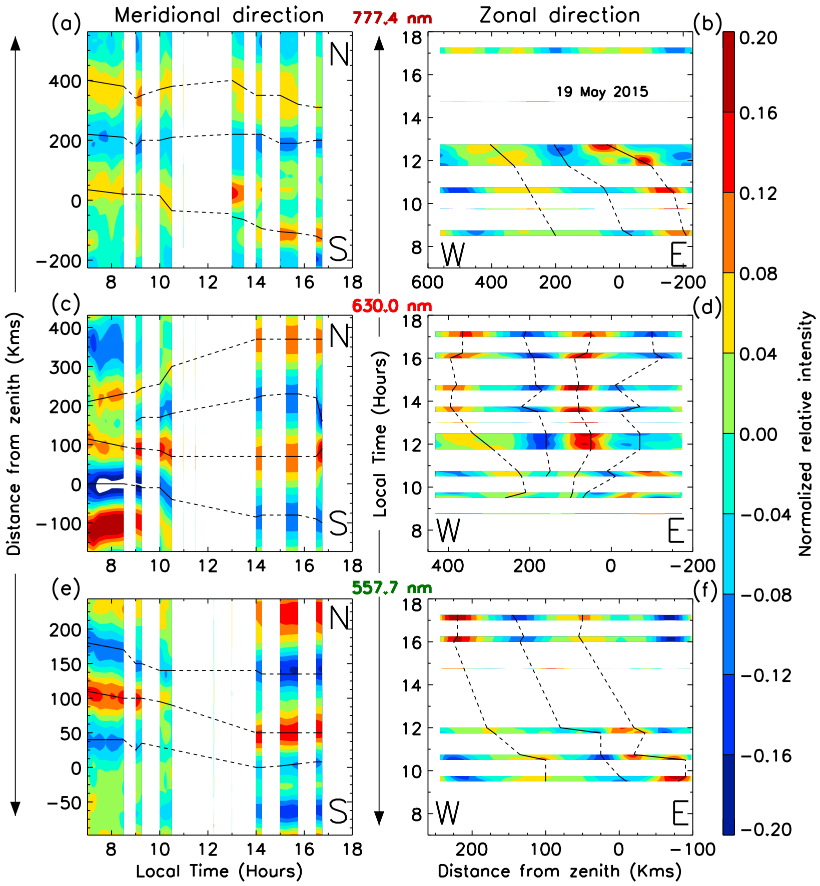

Figure 2. Normalized relative dayglow intensity variations obtained using band-pass filter centered on the dominant scale sizes shown in Figure 1 for 19 May 2015. (left and right columns) The meridional/zonal scales. Westward and southward phase propagations can be seen.

of λ_x and λ_y arrived at within a gap of just 30 min is considered together for estimating the horizontal scale sizes. Thus, the values of $\lambda_H = \left[\lambda_x\lambda_y/\sqrt{\lambda_x^2+\lambda_y^2}\right]$ for 10.5 LT turn out to be 74, 142, and 185 km for the heights at the emission wavelengths of 557.7, 630.0, and 777.4 nm. It should be noted that a smaller scale size of 53 and 46 km in the 557.7 nm emission at 10.75 and 10.25 LT in the zonal and meridional directions will contribute to another value of λ_H. The zonal/meridional scale sizes obtained at a given time are used twice in conjunction with the preceding and succeeding values of meridional/zonal scale sizes to yield λ_H at a cadence of half hour.

Such analyses as described above have been carried out for all the times of this day at all emission wavelengths, and the resulting behavior is shown in Figures 1d–1i for λ_H (in km; left column) and the phase propagation angle (θ_H, in degrees; right column) for 777.4 nm (Figures 1d–1e), 630.0 nm (Figures 1f and 1g), and 557.7 nm (Figures 1h and 1i). To maintain the fidelity of wave modes, the larger scale sizes in λ_x have been combined with the larger values of λ_y and the smaller λ_x with smaller λ_y to calculate the values of λ_H and θ_H. In doing so, arbitrary boundaries of 200 and 100 km are considered for 777.4 nm and 630.0 nm and 557.7 nm emission altitudes (Figures 1d, 1f, and 1h). It can be noted that on this day the magnitudes of λ_H progressively decrease with local time at 777.4 nm emission altitude while those at 557.7 nm increase with time and the ones at 630.0 nm altitude stay reasonably unchanged throughout the day. Interestingly, the corresponding propagation angles (in the range of 207°–253°, counterclockwise from east) seem to indicate a rotation in the wave orientations with altitude as a function of LT. That is, at higher/lower altitudes the waves seem to be moving away from/closer to the west. The cause for such new aspects is currently under investigation.

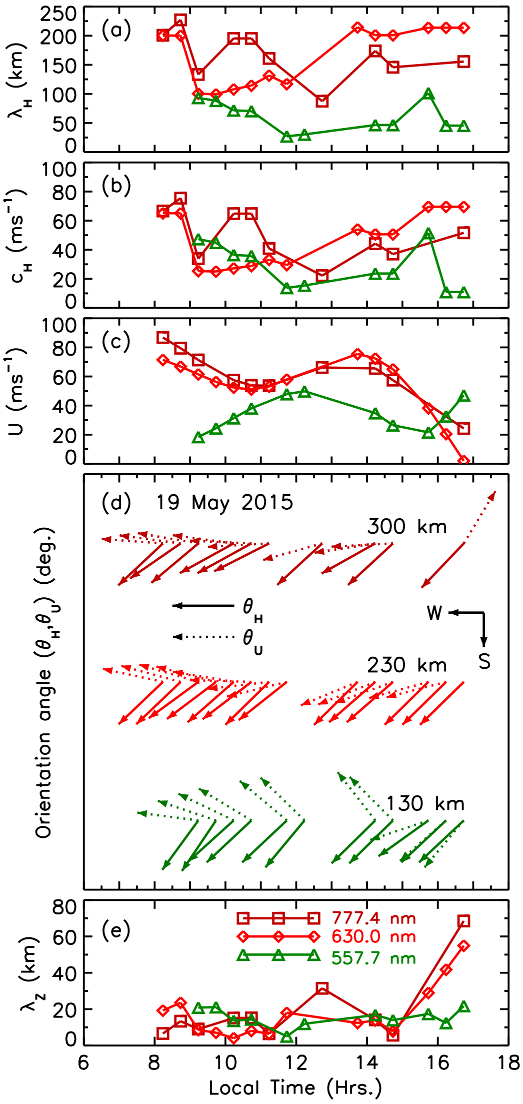

Figure 3. (a) Horizontal scale sizes, (b) phase speeds, (c) HWM14 model wind speeds, (d) wave propagation (solid lines), and neutral wind (dashed) directions at the three emission altitudes. (e) Vertical scale sizes calculated with above values as inputs into GW dispersion relationship.

During nighttime conditions, propagation characteristics of waves are inferred by comparing subsequent two-dimensional airglow images. For daytime conditions, however, this process is ineffective as generally there exist more production mechanisms for dayglow emissions in comparison to usually one for nightglow. For 557.7 nm and 630.0 nm dayglow, the photoelectron and photodissociation production mechanisms can contribute up to 70% of the total emission intensities. Although these mechanisms do not vary in the GW/tidal time scales [*Solomon and Abreu*, 1989; *Sridharan et al.*, 1992], they contribute to a dc shift in emission intensity, and as a consequence, the wave motion is not apparent in the column-integrated emissions. The 777.4 nm dayglow emission is also affected by such an effect as the background electron densities in the *F* region too increase with increase in solar elevation angle. Therefore, to remove the dc contribution and to discern the propagation direction of the waves at each of the emission altitudes during daytime, we have considered the power in the dominant scale sizes at a given time by using a band-pass filter of widths of 22, 40, and 50 km for 557.7, 630.0, and 777.4 nm centered at the peak scale sizes greater than the FAL (as described in *Hocke and Kampfer* [2009]). The power thus isolated in the Fourier domain is subjected to inverse transform to obtain intensity modulations caused by these waves. Independent keograms of the intensity modulations due to both smaller and larger scale sizes as mentioned above were generated for all the emission wavelengths (not shown here). As propagation angles between them at each of the emission heights were similar, they have been combined. The resulting keograms are shown in Figure 2 for 777.4 nm (Figures 2a and 2b), 630.0 nm (Figures 2c and 2d), and 557.7 nm (Figures 2e and 2f) emissions. The left/right columns correspond to meridional/zonal scale sizes. The colors indicate the normalized relative intensity variations. Due to technical difficulties in the viewing geometry, the data in the southern/eastern directions extend to smaller distances from zenith compared to northern/western directions. The whites in between the scans indicate gaps due to alternating nature of data acquisition and/or to the absence of statistically significant power in any of the scales at that time. Attention is drawn to the movement of crests and troughs through the dotted line.

The keograms show that broadly there is a westward movement of waves at all the emission heights which are more prominent in the 777.4 nm and 557.7 nm emissions. Further, there is a southward movement of waves which is prominent in the 557.7 nm (during forenoon) and 777.4 nm emissions (during afternoon). The resultant propagation angle, θ_H, is shown in Figure 3. In 630.0 nm emissions, the power in the smaller/larger scale sizes was less than the FAL in the afternoon/forenoon hours and so, when the daily behavior is seen, it gives an appearance of expansion in scale sizes from prenoon to postnoon (the intercrest separation increases with time). Another intriguing observation is that the waves seen in 630.0 nm intensities west of zenith move westward and those on the east move eastward. The cause for such a movement is being investigated.

Figures 3a and 3b shows the measured horizontal scale sizes, λ_H, and the corresponding phase velocities ($c_H = \omega/k_H$) as a function of LT. The propagation angles, θ_H, at the different emission altitudes are shown as arrows with solid lines in Figure 3d). These are the first results on the characteristics (λ_H, θ_H, τ, and c_H) of the two-dimensional wave behavior in the daytime upper atmosphere.

5. Discussion

In order to appreciate the results on daytime wave dynamics better, they are compared with the known characteristics that exist in the nighttime. From OH and O_2 nightglow imaging measurements, the horizontal scale sizes and phase speeds have been found to be in the range of 10–60 km and 20–100 m s^{-1}, with a predominant northeastward/southwestward motion (depending on season) [*Nakamura et al.*, 1998; *Taylor et al.*, 1995; *Shiokawa et al.*, 2009; *Lakshmi Narayanan et al.*, 2010], which were obtained from middle and low latitudes. These parameters as seen from the present study for 557.7 nm emission dayglow intensities (which emanate from around 40 km above the OH/O_2 emission altitudes) are 27–101 km and 7–52 m s^{-1}. With regard to the thermospheric emissions, the nightglow 630.0 nm imager data reveal the scale sizes to be 100–400 km, periodicities of 30–150 min, and phase speeds of 50–150 m s^{-1} with a predominant movement in south/southwestern direction [*Taylor et al.*, 1998; *Shiokawa et al.*, 2009]. For 19 May 2015, these values were found to be 95–214 km, 51–66 min, and 24–70 m s^{-1}. (In general, the GW periods in these dayglow emissions have been found to be in the range of BV period to ~3 h [*Laskar et al.*, 2015]). The peak values of phase speeds on this day are, in general, lower than those reported for the nighttime. This could be understood to be due to (i) an increase in neutral densities at a given altitude with temperatures in the daytime, which thereby offer greater resistance to the propagation of waves and (ii) the increase in the BV period with increase in temperatures in the daytime, which contributes to a decrease in the daytime phase speeds.

The largest scale sizes obtained in the daytime seem smaller in comparison to the largest scale sizes obtained in the nighttime, which could in all possibility be due to the smaller FOV of observation in the present daytime experiment as opposed to much larger FOV, in general, of nighttime imaging studies. As shown in Figure 2, the movement of waves is mostly in the west/southwestward direction. During nighttime, both eastward/westward propagations have been noted in equatorial latitudes and southward propagation in middle latitudes [*Shiokawa et al.*, 2006]. It was seen in an earlier experiment that the periodicity of waves continues to remain the same from day to night at a given location [*Pallamraju et al.*, 2014]; however, for varying latitudes, it is envisaged that the daytime periodicities, phase speeds, scale sizes, and propagation directions would be different. Simultaneous, collocated day and night measurements in the future will provide greater insights into these aspects.

The characteristic scale sizes, time periods, and phase speeds of 777.4 nm in the daytime are 57–227 km, 50–66 min, and 14–75 m s^{-1}. To the best of our knowledge, there are no reports of such information in the published literature for the nighttime conditions obtained at this emission wavelength to enable comparison.

Further, as the horizontal wave characteristics obtained are in the class of acoustic GWs, the linear dispersion relation as given by *Hines* [1960] has been used to derive the vertical scale sizes (λ_z).

$$(k_z)^2 = \frac{N^2}{(u^* - c_H)^2} - (k_H)^2 - \frac{1}{4H^2} \tag{1}$$

Here k_z is the vertical wave number ($2\pi/\lambda_z$), N is the BV frequency, c_H is the phase speed (in the west/southwest direction), u^* is the component of ambient wind along the phase front, and H is the scale height.

Neutral thermospheric temperatures for 19 May 2015 from NRLMSISE-00 model have been considered to calculate the values of H, which on an average are 39, 55, and 60 km at the emission altitudes of 130, 230, and 300 km, respectively. The BV frequency, N, (given as $(2g^*/5H)^{1/2}$, where g^* is the acceleration due to gravity at a given altitude) has been calculated to be 11×10^{-3}, 8×10^{-3}, and 7×10^{-3} rad s^{-1}, respectively, at the altitudes under consideration. Ambient wind magnitudes, u, and their directions, θ_u, play an important role in

Table 1. Summary of the 3-D Daytime Thermospheric GW Characteristics Obtained for 19 May 2015

Wavelength, λ (nm)	Zonal Scale Size, λ_x (km)	Meridional Scale Size, λ_y (km)	Horizontal Scale Size, λ_H (km)	Horizontal Phase Angle, θ_H (deg), Counterclockwise From East	Time Period, τ (min)	Phase Speed, $c_H = \frac{\omega}{k_H}$, (m s^{-1})	Vertical Scale Size, λ_z [a,b] (km)	Resultant 3-D Scale Size, λ_v [a,b] (km)	Vertical Phase Angle With Respect to k_H, θ_v [b] (deg.)
OI 777.4	59–278	54–398	155–227;	207–226;	65.6 ± 11.6,	37.0–75.4;	0.3–68.4;	0.3–62.6;	66.2–89.9;
			57–133	220–253	50.2 ± 5.1	14.6–44.2	0.2–31.4	0.2–29.6	70.2–89.7
OI 630.0	125–304	47–302	200–214;	221–225;	66.1 ± 6.7,	50.4–69.7;	0.1–54.9;	0.1–53.2;	75.5–89.9;
			95–131	216–231	51.2 ± 1.9	23.9–42.7	0.9–18.0	0.9–17.8	81.2–89.5
OI 557.7	37–160	25–172	70–101;	216–236;	69.1 ± 13.9,	16.9–51.5;	2.1–21.0;	2.1–20.5;;	76.5–88.8;
			27–46	223–242	51.1 ± 5.3,	6.5–23.6	0.1–21.7	0.1–19.6	64.4–89.7
					32.8 ± 1.9				

[a]Small λ_z and λ_v derived will be evanescent.
[b]Calculated using the dispersion relation given by *Hines* [1960].

influencing the magnitudes of λ_z of GWs. The HWM14 winds [*Drob et al.*, 2015] (Figure 3c) and their angles at the three emission altitudes are depicted as arrows (dashed lines) in Figure 3d. The relative angles between θ_H and θ_u have been used to calculate the component of wind, u^*, along the direction of c_H. These values along with model *H*, *N*, and measured c_H, λ_H from the present experiment have been used to calculate λ_z (shown in Figure 3e) which vary from 0 to 70 km. From the measured λ_H and derived λ_z, the magnitudes of the resultant scale size $(\lambda_v)\left[= \lambda_H\lambda_z/\sqrt{\lambda_H^2+\lambda_z^2}\ (\text{as } k_v^2 = k_H^2 + k_z^2)\right]$ and the vertical phase angles of GWs, θ_v [=$\tan^{-1}(k_z/k_H)$] (with respect to horizontal) have also been calculated. Thus, this approach gives as realistic a picture as possible of the characteristics of GWs in the vertical dimension (scale sizes and phase angles) existing at a given time in daytime. The θ_v seem to be greater than 60° which can have important consequences with regard to vertical coupling of atmospheres. At the same time, it should also be noted that the waves with smaller magnitudes in λ_z and λ_v may be incapable of propagating to greater heights. It can be seen from equation (1) that magnitudes of λ_z vary not only due to changes in wind magnitudes, *u*, and their directions, θ_u, but also due to changes in the phase speeds, c_H, and phase angles, θ_H, of the measured waves. It is known that winds along/opposite to the direction of the phase propagation reduce/enhance the magnitudes of λ_z [*Fritts and Alexander*, 2003]. Also, larger λ_H could result in larger magnitudes of λ_z. It can be appreciated that in addition to day-to-day variability, the variation in the relative angles between the θ_H and θ_u that changes with seasons and geomagnetic activity will result in different values of λ_z. Therefore, measurements of horizontal characteristics of waves as presented here are essential in understanding the three-dimensional wave dynamics during daytime. Table 1 summarizes all values of the thermospheric wave characteristics in three dimensions (λ_x, λ_y, λ_H, θ_H, τ, c_H, λ_z, λ_v, and θ_v) during daytime for 19 May 2015 that have been made possible through this work for the first time. It is to be noted that the vertical scale sizes are not measureable using the daytime optical emissions due to the thickness of the emission layer. Thus, the last three parameters (λ_z, λ_v, and θ_v) are derived using *Hines*'s [1960] dispersion relationship for gravity waves by using the measured horizontal wave characteristics as inputs. Such a new capability of deriving three-dimensional wave characteristics of waves in the daytime opens up new possibilities of investigations of vertical coupling through waves in the daytime. Further, in addition to enhancing our understanding the processes related to vertical coupling of atmospheres and modeling of thermospheric wave dynamics in daytime, such studies can also provide insights into the role of wave sources from lower below in the generation of ionospheric equatorial plasma irregularities in the nighttime.

6. Conclusion

There are methods available to infer information on neutral winds such as satellite-based optical interferometry and spectrometry, triangulation of vapor cloud releases from rockets, and from radars and Doppler shifts of optical emissions from the ground. However, investigations on neutral wave dynamics in the daytime can be carried out only by ground-based dayglow measurements over a large FOV, as presented in this paper, wherein intensities at 557.7 nm, 630.0 nm, and 777.4 nm were measured along orthogonal directions to obtain the components λ_x (zonal) and λ_y (meridional) of the horizontal waves. These were used to calculate the horizontal scale sizes of waves, λ_H, and their propagation angles, θ_H, in the daytime and are first results of their kind. Not only the wave parameters in two dimensions but also the characteristics of waves in the vertical dimension have been arrived at in this study using the dispersion relation of GWs. Measurements such as these now present us with a new capability of investigating thermospheric wave dynamics in three dimensions during daytime.

Acknowledgments
The data used in this work were obtained by Physical Research Laboratory and can be made available by contacting the corresponding author. NRLMSISE-00 Model neutral temperature values have been obtained from http://ccmc.gsfc.nasa.gov/modelweb/models/nrlmsise00.php. The logistic support with regard to operation of MISE provided by T. Vijaya Lakshmi and her team at the Jawaharlal Nehru Technological University at Hyderabad, India, is duly acknowledged. The authors thank R. Sekar for discussions. We gratefully acknowledge the critical comments provided by the reviewers which greatly improved the clarity of this paper. This work is supported by Department of Space, Government of India.

References

Chakrabarti, S., D. Pallamraju, J. Baumgardner, and J. Vaillancourt (2001), HiTIES: A high throughput imaging echelle spectrograph for ground-based visible airglow and auroral studies, *J. Geophys. Res.*, *106*, 30,337–30,348, doi:10.1029/2001JA001105.

Delbouille, L., L. Neven, and G. Roland (1973), *Photometric Atlas of the Solar Spectrum From Lambda 3000 to Lambda 10000*, vol. 1, pp. 2994–6455, Inst. d'Astrophysique de L'Univ, Cointe-Ougreé, Belgium.

Drob, D. P., et al. (2015), An update to the Horizontal Wind Model (HWM): The quiet time thermosphere, *Earth Space Sci.*, *2*, 301–319, doi:10.1002/2014EA000089.

Fritts, D. C., and M. J. Alexander (2003), Gravity wave dynamics and effects in the middle atmosphere, *Rev. Geophys.*, *41*(1), 1003, doi:10.1029/2001RG000106.

Gerrard, A., and J. Meriwether (2011), Initial daytime and nighttime SOFDI observations of thermospheric winds from Fabry–Perot Doppler shift measurements of the 630 nm OI line-shape profile, *Ann. Geophys.*, *29*, 1529–1536.

Hedin, A. E., et al. (1996), Emperical wind model for the upper, middle and lower atmosphere, *J. Atmos. Terr. Phys.*, *58*, 1421–1447.

Herrero, F. A., H. G. Mayr, and N. W. Spencer (1988), Low-latitude thermospheric meridional winds between 250 and 450 km altitude, AE-E satellite data, *J. Atmos. Terr. Phys.*, *50*, 1001–1006.

Hines, C. O. (1960), Internal atmospheric gravity waves at ionospheric heights, *Can. J. Phys.*, *38*, 1441–1481.

Hocke, K., and N. Kampfer (2009), Gap filling and noise reduction of unevenly sampled data by means of the Lomb-Scarge periodogram, *Atmos. Chem. Phys.*, *9*, 4197–4208.

Killeen, T. L., Q. Wu, S. C. Solomon, D. A. Ortland, W. R. Skinner, R. J. Niciejewski, and D. A. Gell (2006), TIMED Doppler interferometer: Overview and recent results, *J. Geophys. Res.*, *111*, A10S01, doi:10.1029/2005JA011484.

Lakshmi Narayanan, V., S. Gurubaran, and K. Emperumal (2010), Airglow imaging observations of small-scale structures driven by convective instability in the upper mesosphere over Tirunelveli (8.7°N), *J. Geophys. Res.*, *115*, D19119, doi:10.1029/2009JD012937.

Laskar, F. I., and D. Pallamraju (2014), Does sudden stratospheric warming induce meridional circulation in the mesosphere thermosphere system?, *J. Geophys. Res. Space Physics*, *119*, 10,133–10,143, doi:10.1002/2014JA020086.

Laskar, F. I., D. Pallamraju, T. V. Lakshmi, M. A. Reddy, B. M. Pathan, and S. Chakrabarti (2013), Investigations on vertical coupling of atmospheric regions using combined multiwavelength optical dayglow, magnetic, and radio measurements, *J. Geophys. Res. Space Physics*, *118*, 4618–4627, doi:10.1002/jgra.50426.

Laskar, F. I., D. Pallamraju, B. Veenadhari, T. Vijaya Lakshmi, M. Anji Reddy, and S. Chakrabarti (2015), Gravity waves in the thermosphere: Solar activity dependence, *Adv. Space Res.*, *55*, 1651–1659.

Lomb, N. R. (1976), Least-squares frequency analysis of unequally spaced data, *Astrophys. Space Sci.*, *39*, 447–462.

Makela, J. J., D. J. Fisher, J. W. Meriwether, R. A. Buriti, and A. F. Medeiros (2013), Near-continual ground-based nighttime observations of thermospheric neutral winds and temperatures over equatorial Brazil from 2009 to 2012, *J. Atmos. Sol. Terr. Phys.*, *103*, 94–102.

Marshall, R. A., S. Smith, J. Baumgardner, and S. Chakrabarti (2011), Continuous ground-based multiwavelength airglow measurements, *J. Geophys. Res.*, *116*, A11304, doi:10.1029/2011JA016901.

Mayr, H. G., I. Harris, and N. W. Spencer (1978), Some properties of upper atmosphere dynamics, *Rev. Geophys. Space Phys.*, *16*, 539–565.

Mendillo, M., J. Baumgardner, D. Nottingham, J. Aarons, B. Reinisch, J. Scali, and M. Kelley (1997), Investigations of thermospheric-ionospheric dynamics with 6300 A images from the Arecibo Observatory, *J. Geophys. Res.*, *102*, 7331–7343, doi:10.1029/96JA02786.

Meriwether, J. W., J. W. Moody, M. A. Biondi, and R. G. Roble (1986), Optical interferometric measurements of nighttime equatorial thermospheric winds at Arequipa, Peru, *J. Geophys. Res.*, *91*, 5557–5566, doi:10.1029/JA091iA05p05557.

Nakamura, T., T. Tsuda, H. Miyagawa, Y. Matsushita, H. Fukunishi, Y. Takahashi, and Y. Yamada (1998), Propagation directions of gravity wave patterns observed in OH CCD images during SEEK campaign, *Geophys. Res. Lett.*, *25*, 1793–1796, doi:10.1029/98GL01064.

Narayanan, R., J. N. Desai, N. K. Modi, R. Raghavarao, and R. Sridharan (1989), Dayglow photometry: A new approach, *Appl. Opt.*, *28*, 2138–2142.

Pallam Raju, D., and R. Sridharan (1998), High-resolution 2-D maps of OI 630.0 nm thermospheric dayglow from equatorial latitudes, *Ann. Geophys.*, *16*, 997–1006.

Pallamraju, D., J. Baumgardner, and S. Chakrabarti (2000), A multiwavelength investigation of the Ring effect in the day sky spectrum, *Geophys. Res. Lett.*, *27*, 1875–1878, doi:10.1029/1999GL010961.

Pallamraju, D., J. Baumgardner, and S. Chakrabarti (2002), HIRISE: A ground-based high-resolution imaging spectrograph using echelle grating for measuring daytime airglow/auroral emissions, *J. Atmos. Sol. Terr. Phys.*, *64*, 1581–1587.

Pallamraju, D., U. Das, and S. Chakrabarti (2010), Short- and long-time scale thermospheric variability as observed from OI 630.0 nm dayglow emissions from low latitudes, *J. Geophys. Res.*, *115*, A06312, doi:10.1029/2009JA015042.

Pallamraju, D., F. I. Laskar, R. P. Singh, J. Baumgardner, and S. Chakrabarti (2013), MISE: A multiwavelength imaging spectrograph using echelle grating for daytime optical aeronomy investigations, *J. Atmos. Sol. Terr. Phys.*, *103*, 176–183.

Pallamraju, D., J. Baumgardner, R. P. Singh, F. I. Laskar, C. Mendillo, T. Cook, S. Lockwood, R. Narayanan, T. K. Pant, and S. Chakrabarti (2014), Daytime wave characteristics in the mesosphere lower thermosphere region: Results from the Balloon-borne Investigations of Regional-atmospheric Dynamics experiment, *J. Geophys. Res. Space Physics*, *119*, 2229–2242, doi:10.1002/2013JA019368.

Scargle, J. D. (1982), Studies in astronomical time series analysis. II. Statistical aspects of spectral analysis of unevenly spaced data, *Astrophys. J.*, *263*(2), 835–853.

Shepherd, G. G., et al. (1993a), WINDII, the Wind Imaging Interferometer on the Upper Atmosphere Research Satellite, *J. Geophys. Res.*, *98*, 10,725–10,750, doi:10.1029/93JD00227.

Shepherd, G. G., et al. (1993b), Longitudinal structure in atomic oxygen concentrations observed with WINDII on UARS, *Geophys. Res. Lett.*, *20*, 1303–1306, doi:10.1029/93GL01105.

Shiokawa, K., Y. Otsuka, and T. Ogawa (2006), Quasiperiodic southward moving waves in 630 nm airglow images in the equatorial thermosphere, *J. Geophys. Res.*, *111*, A06301, doi:10.1029/2005JA011406.

Shiokawa, K., Y. Otsuka, and T. Ogawa (2009), Propagation characteristics of nighttime mesospheric and thermospheric waves observed by optical mesosphere thermosphere imagers at middle and low latitudes, *Earth Planets Space*, *61*, 479–491.

Solomon, S. C., and V. Abreu (1989), The 630.0 nm dayglow, *J. Geophys. Res.*, *94*, 6817–6824, doi:10.1029/JA094iA06p06817.

Spencer, N. W., L. E. Wharton, H. B. Hiemann, A. E. Hedin, G. R. Carignan, and J. C. Maurer (1981), The Dynamics Explorer wind and temperature spectometer, *Space Sci. Instrum.*, *5*, 417–428.

Sridharan, R., S. A. Haider, S. Gurubaran, R. Sekar, and R. Narayanan (1992), OI 630.0 nm dayglow in the region of equatorial ionization anomaly: Temporal variability and its causative mechanisms, *J. Geophys. Res.*, *97*, 13,715–13,721, doi:10.1029/92JA00674.

Sridharan, R., R. Narayanan, N. K. Modi, and D. Pallam Raju (1993), A novel mask design for multiwavelength dayglow photometry, *Appl. Opt.*, *32*, 4178–4180.

Sridharan, R., N. K. Modi, D. Pallam Raju, R. Narayanan, T. K. Pant, A. Taori, and D. Chakrabarty (1998), A multiwavelength daytime photometer: A new tool for the investigation of atmospheric processes, *Meas. Sci. Technol.*, *9*, 585–591.

Taylor, M. J., M. B. Bishop, and V. Taylor (1995), All-sky measurements of short period waves imaged in the OI(557.7 nm), Na(589.2 nm) and near infrared OH and O2(0,1) nightglow emissions during the ALOHA-93 campaign, *Geophys. Res. Lett.*, *22*, 2833–2836, doi:10.1029/95GL02946.

Taylor, M. J., J.-M. Jahn, S. Fukao, and A. Saito (1998), Possible evidence of gravity wave coupling into the midlatitude *F* region ionosphere during the SEEK campaign, *Geophys. Res. Lett.*, *25*, 1801–1804, doi:10.1029/97GL03448.

Teitelbaum, H., M. Massebeuf, J. L. Fellous, M. Petitdidier, J. Christophea, and F. Blanco (1981), Simultaneous measurements of meteor winds and greenline intensity variations: Gravity waves and planetary waves, *J. Geophys. Res.*, *86*, 7767–7770, doi:10.1029/JA086iA09p07767.

Tinsley, B. A., A. B. Christensen, J. Bittencourt, H. Gouveia, P. D. Angreji, and H. Takahashi (1973), Excitation of oxygen permitted line emissions in the tropical nightglow, *J. Geophys. Res.*, *78*(7), 1174–1186, doi:10.1029/JA078i007p01174.

Witasse, O., J. Lilensten, C. Lathuillère, and P.-L. Blelly (1999), Modeling the OI 630.0 and 557.7 nm thermospheric dayglow during EISCAT-WINDII coordinated measurements, *J. Geophys. Res.*, *104*, 24,639–24,655, doi:10.1029/1999JA900260.

Ann. Geophys., 34, 1019–1030, 2016
www.ann-geophys.net/34/1019/2016/
doi:10.5194/angeo-34-1019-2016

Annales Geophysicae Open Access EGU

Electrodynamic influence on the diurnal behaviour of neutral daytime airglow emissions

Deepak K. Karan[1,2], Duggirala Pallamraju[1], Kedar A. Phadke[1], Tatiparti Vijayalakshmi[3], Tarun K. Pant[4], and Shyamoli Mukherjee[5]

[1]Physical Research Laboratory, Navrangpura, Ahmedabad, India
[2]Indian Institute of Technology, Gandhinagar, Ahmedabad, India
[3]Jawaharlal Nehru Technological University, Kukatpally, Hyderabad, India
[4]Space Physics Laboratory, Trivandrum, India
[5]Indian Institute of Geomagnetism, Navi Mumbai, India

Correspondence to: Duggirala Pallamraju (raju@prl.res.in)

Received: 11 June 2016 – Revised: 20 October 2016 – Accepted: 26 October 2016 – Published: 16 November 2016

Abstract. The diurnal variations in daytime airglow emission intensity measurements at three wavelengths OI 777.4 nm, OI 630.0 nm, and OI 557.7 nm made from a low-latitude location, Hyderabad (17.5° N, 78.4° E; 8.9° N MLAT) in India have been investigated. The intensity patterns showed both symmetric and asymmetric behaviour in their respective diurnal emission variability with respect to local noon. The asymmetric diurnal behaviour is not expected considering the photochemical nature of the production mechanisms. The reason for this observed asymmetric diurnal behaviour has been found to be predominantly the temporal variation in the equatorial electrodynamics. The plasma that is transported across latitudes due to the action of varying electric field strengths over the magnetic equator in the daytime contributes to the asymmetric diurnal behaviour in the neutral daytime airglow emissions. Independent magnetic and radio measurements support this finding. It is also noted that this asymmetric diurnal behaviour in the neutral emission intensities has a solar cycle dependence with a greater number of days during high solar activity period showing asymmetric diurnal behaviour compared to those during a low solar activity epoch. These intensity variations over a long timescale demonstrate that the daytime neutral optical emissions are extremely sensitive to the changes in the eastward electric field over low and equatorial latitudes.

Keywords. Atmospheric composition and structure (airglow and aurora) – ionosphere (equatorial ionosphere; ionosphere–atmosphere interactions)

1 Introduction

It is known that optical airglow emissions act as tracers of atmospheric behaviour that exists at the altitudes of their origin. In the earth's upper atmosphere, optical emissions originate when atomic or molecular constituents or their ions de-excite from their higher energy states to the lower ones. The emissions emanate at different altitudes depending on the constituents and type of chemical/photochemical reactions that produces them at those altitudes. Understandably, the variability of the reactants that participate in these reactions has a role in the overall variability of the airglow emissions. In that regard, the Doppler shifts and widths of the neutral 630.0 nm nightglow emissions have been used to obtain information on thermospheric winds and neutral thermospheric temperatures. With the knowledge that dissociative recombination is responsible for the 630.0 nm nightglow, the all-sky images of this emission yielded unique signatures of the reversal of the equatorial ionization anomaly (EIA) in the nighttime (Sridharan et al., 1993a). The all-sky images also provide information on the dynamics of large-scale plasma bubbles (e.g. Taylor et al., 1995; Makela et al., 2013). The mesospheric (OH, O_2 band) and lower thermospheric (OI 557.7 nm) emission variability has been used to derive information on the mesospheric temperatures (e.g. Taylor et al., 1995; Singh and Pallamraju, 2015), atmospheric gravity waves (Shiokawa et al., 2009; Singh and Pallamraju, 2016), tides, and planetary-scale waves (Nakamura et al., 1998).

With regard to the daytime airglow, predominantly OI 630.0 nm emissions have been used to derive the effect of coronal mass ejection on the thermosphere (Pallamraju and Chakrabarti, 2005), solar flares (Das et al., 2010), and magnetospheric cusps (Pallamraju et al., 2004) and to understand the upper-atmospheric behaviour due to solar activity. Similar variations between daily averaged 630.0 nm dayglow emission intensity and the daily sunspot number indicated the influence of solar flux on the optical dayglow emissions (Pallamraju et al., 2010). With the addition of OI 557.7 nm for daytime measurements, investigations have been extended to study various aspects such as gravity wave dynamics in the lower thermosphere (Laskar et al., 2013, 2015), the effect of tidal and solar flux variations on mesosphere and lower-thermosphere (MLT) dynamics from onboard the Upper Atmosphere Research Satellite (UARS; e.g. Maharaj-Sharma et al., 2004; Zhang and Shepherd, 2004, 2005), and three-dimensional daytime wave characteristics (Pallamraju et al., 2016). In all these measurements it was seen that the diurnal behaviour of daytime intensity broadly varied as a function of solar zenith angle. In fact, the empirical models for OI 557.7 nm and OI 630.0 nm dayglow emissions that were developed (Zhang and Shepherd, 2004, 2005) do have solar zenith angle as one of the inputs. This is not unexpected, as the solar photons through the processes of photodissociation, photoelectron production, and ionization at a given location do affect the volume emission rates of the daytime airglow emissions. This gives rise to a broad solar zenith-angle-dependent behaviour for the diurnal emission intensity distribution (Solomon and Abreu, 1989). Thus, one would expect that with the decreasing/increasing of the solar zenith angle, the dayglow emission intensities will increase/decrease giving rise to maximum dayglow emission intensities around local noon resulting in a symmetric pattern in the diurnal variation of emission intensities with respect to local noon. However, the high temporal resolution ground-based measurements that we have carried out do show that the diurnal behaviour of dayglow emission intensities does not follow a symmetric pattern with respect to local noon on several days. This non-symmetric or asymmetric diurnal behaviour in the intensity pattern with respect to the local noon on a given day has been investigated at greater depths in this work. The influence of neutral winds vs. that of equatorial electrodynamics on the daytime airglow production mechanisms and, thereby, the resulting emission intensities have been assessed. It is found that the electrodynamic behaviour is mainly responsible for such disparity that is seen in the diurnal behaviour of neutral dayglow emission intensities. Moreover, the extent of asymmetricity in the diurnal behaviour in the dayglow emission intensities is found to show a solar activity dependence with a greater number of days showing asymmetric diurnal behaviour during high solar activity periods.

2 Observational technique and data analysis

2.1 Oxygen dayglow emissions

Ground-based optical instruments are now available that provide opportunities to measure the thermospheric dayglow emissions buried in the strong solar background continuum. A few methods have been put forth in the past (e.g. Narayanan et al., 1989; Sridharan et al., 1993b, 1998; Chakrabarti et al., 2001; Pallamraju et al., 2002, 2013; Gerard and Meriwether, 2011) to measure these emission intensities, which used low- and high-resolution Fabry–Pérot etalons, echelle and normal gratings, with varying fields of view.

In the present work the thermospheric optical dayglow OI emission intensities measured have been obtained by using a high spectral resolution Multiwavelength Imaging Spectrograph using Echelle grating (MISE) (Pallamraju et al., 2013) from a low-latitude station, Hyderabad, India (17.5° N, 78.4° E; 8.9° N MLAT). MISE obtains dayglow emission intensities over a large field of view ($\sim 100°$) along the slit direction, simultaneously at three wavelengths: OI 557.7, OI 630.0, and OI 777.4 nm (without any need to change the grating angle). Both photochemical and chemical reactions are responsible for the production of these three optical dayglow emissions. The availability of the reactants, such as photoelectrons, and atmospheric constituents responsible for an emission decide the altitudes of emissions, which are around 130 km (average of the two peak emission altitudes at ~ 100 and ~ 160 km), 230, and 300 km for the $O(^1S)$ (557.7 nm), $O(^1D)$ (630.0 nm), and $O(^5S)$ (777.4 nm) emissions, respectively. The $O(^1S)$ state is produced due to photoelectron impact on the ground state of O, collisional deactivation of N_2, photodissociation of O_2 in 90–120 nm of the solar radiation, and dissociative recombination of O_2^+ (e.g. Tyagi and Singh, 1998; Witasse et al., 1999; Zhang and Shepherd, 2005). Also, a three-body reaction (Barth mechanism) is responsible for the production of 557.7 nm emissions at lower altitudes below 120 km (which peak at ~ 100 km). The dissociative recombination of O_2^+, which depends on the electron densities, contributes significantly to the production of 557.7 nm dayglow emissions at higher altitudes, especially in low and equatorial latitudes (e.g. Tyagi and Singh, 1998; Upadhayaya et al., 2002; Taori et al., 2003). Rocket-borne $O(^1S)$ 557.7 nm measurements (Wallace and McElroy, 1966), nightglow measurements from the Wind Imaging Interferometer (WINDII; Shepherd et al., 1997), and ground-based optical dayglow measurements (Taori et al., 2003) reported a dominant F region contribution as compared to that of lower altitudes. The 630.0 nm is produced due to the de-excitation of $O(^1D)$ to $O(^3P)$ state. The $O(^1D)$ state is produced by photoelectron impact on the ground state O, photodissociation of O_2 in the Schumann–Runge continuum (135–175 nm) of the solar radiation, a dissociative recombination of O_2^+, and a cascade from the loss of $O(^1S)$, with the last one being a minor contributor (Solomon and Abreu, 1989; Witasse et al., 1999). The photoelectron impact mechanism contributes most to the 630.0 nm dayglow emissions followed by the photodissociation mechanism. Dissociative recombination contribution to the 630.0 nm dayglow emission is around 20–30 % (Hays et al., 1978; Singh et al., 1996). However, the dissociative recombination contributes significantly to the temporal variability of the emissions (Sridharan et al., 1992, 1994; Pallam Raju et al., 1996). The de-excitation of $O(^5S)$ to $O(^5P)$ yields 777.4 nm dayglow emissions. The $O(^5S)$ state is produced due to the radiative recombination of O^+ and e^- (Tinsley et al., 1973). This emission maximizes at the peak of the F layer where the densities of both O^+ and e^- are maximal.

The variation in intensities at these three optical thermospheric dayglow emissions carries the information of the dynamical behaviour occurring at the respective altitudes of emissions. The dayglow emission intensities at the three wavelengths are imaged onto a 1 k × 1 k charge coupled device (CCD) detector to form a high-resolution (0.012 nm at 630.0 nm) spectral image. On-chip binning of eight pixels along the spatial direction is carried out to increase the signal-to-noise ratio. The spectra obtained from MISE are compared with the normalized standard solar spectrum in order to calibrate them in the wavelength domain. These are then compared at the continuum level to obtain the contributions of total dayglow emissions and the atmospheric scattering (Ring effect) (Pallamraju et al., 2000). The dayglow emission intensities are obtained by removing the scattering contribution with a data cadence of 5 min. This method of retrieval of dayglow is well-established and is described in detail in the literature (Pallamraju et al., 2002, 2013). The technical details of MISE have been described by Pallamraju et al. (2013). Further, in order to make a comparison of our findings with earlier dayglow measurements, we have made use of the OI 630.0 nm data as presented in the published literature.

2.2 EEJ data

Equatorial electrojet (EEJ) refers to the intense narrow jet of current in the eastward direction that flows in the daytime over the dip equator. EEJ strength can be obtained by measuring the induced magnetic field using magnetometers placed on the surface of earth. Over Indian longitudes the horizontal component of the earth's magnetic field is obtained from two stations. One station is at Tirunelveli (TIR) (8.7° N, 77.8° E; 0.15° N MLAT), in a magnetic equatorial region which records the influence of currents induced due to the EEJ, and the other is at Alibag (ABG) (18.6° N, 72.9° E; 10.5° N MLAT), magnetically an off-equatorial station, that is not influenced by the EEJ currents. From each station, variations relative to their nighttime base values are subtracted so that the contribution from magnetospheric currents, if any, is removed. Thus, the difference between the magnetic data at Tirunelveli and Alibag yields information on the strength of the EEJ current. The high temporal resolution (1 min data cadence) EEJ data from December 2013 to March 2014 have been used in the present work.

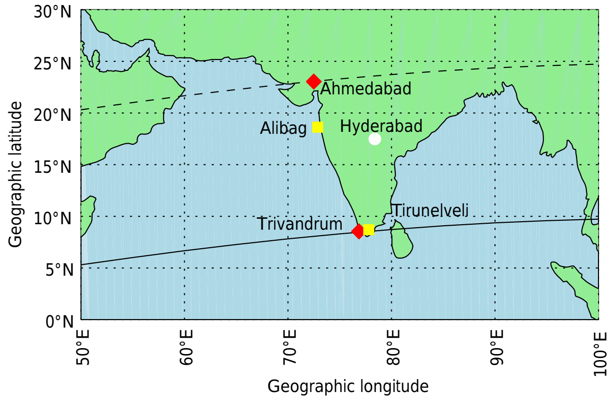

Figure 1. The geographic locations of the stations from which data have been obtained are shown. Neutral optical dayglow emission data have been obtained by MISE commissioned at Hyderabad (white dot). The ionospheric data obtained from digisondes located at Trivandrum and Ahmedabad are shown as red diamonds. Stations from which the magnetic data are obtained to calculate the EEJ strengths are marked as yellow squares. The solid and dashed dark lines represent the geomagnetic equator (obtained from IGRF-12) (Emmert et al., 2010) and the EIA crest location in the Northern Hemisphere (+15°), respectively, for the year 2014.

2.3 Ionospheric data

Ionospheric behaviour from two stations, Trivandrum (8.5° N, 76.9° E; 0.07° N MLAT), a geomagnetically equatorial location, and Ahmedabad (23.0° N, 72.5° E; 14.9° N MLAT), typically the northern crest location of the EIA, has been used. The data cadence for the ionospheric information is 7.5 min.

Figure 1 shows the geophysical locations of all the stations from which the data are used for the present work. The x and y axes show the geographic longitude and latitude, respectively. Neutral optical dayglow emission data are obtained from the location Hyderabad, marked as a white solid circle on the map. The red diamonds and yellow squares show the stations from which ionospheric information and the EEJ data are obtained. The dark solid line represents the geomagnetic equator (obtained from the International Geomagnetic Reference Field (IGRF-12) model for 2014.0), whereas the dashed line shows the typical northern crest region (15° N MLAT) of the EIA.

In the present work the optical dayglow emission data obtained from December 2013 to March 2014 have been used to address this issue. Independent ionospheric data and the EEJ data obtained during this period have been used to substantiate our findings.

3 Results

Figure 2 depicts examples of diurnal variability on 2 days for OI 630.0 nm dayglow emissions, with the x and y axes showing local time (LT) in hours and intensity in rayleighs. The black solid line shows the 11-point running average. A dotted vertical line is drawn at local noon to aid the eye in bringing out the contrast between the pre- and post-noon behaviour in the emission intensity variability. It can be readily noted that on 5 January 2014 (Fig. 2a), the intensity variability is symmetric with peak intensity around noontime, which seems almost like an inflexion point. This behaviour is contrary to that obtained on 19 December 2013 (Fig. 2b), when the peak intensity was reached in the afternoon hours. As discussed above, the photochemical production is expected to peak around noontime, and, therefore, this asymmetric diurnal behaviour in the dayglow emission intensities seems anomalous. It may also be noted that the rate of rise in intensities is different on these 2 days. The extent of asymmetry can be quantified as the product of difference in times between those of peak intensity and local noon and the ratios of the intensities at those times. Mathematically, the asymmetricity in time (AT) is given as

$$\mathrm{AT} = \left(\frac{I_{\mathrm{peak}}}{I_{\mathrm{noon}}}\right) \times \left(T_{\mathrm{peak}} - T_{\mathrm{noon}}\right), \qquad (1)$$

where T_{peak} and T_{noon} are the times of peak emission intensity and local noon. I_{peak} and I_{noon} are the intensity values corresponding to T_{peak} and T_{noon}, respectively. If the peak intensity occurs in pre-noon hours, it can be seen from Eq. (1) that the AT becomes negative. The diurnal emission intensity pattern is considered to be symmetric or asymmetric for $\mathrm{AT} \leq 0.4$ h. and $\mathrm{AT} > 0.4$ h, respectively. The AT values for 5 January 2014 and 19 December 2013 are calculated to be 0.4 h (symmetric diurnal behaviour) and 1.1 h (asymmetric diurnal behaviour), respectively.

Such behaviour in the diurnal intensity pattern is seen not only in the OI 630.0 nm emissions but also in the emissions at OI 777.4 nm and OI 557.7 nm that emanate from altitudes above and below that of the OI 630.0 nm dayglow. Figure 3 shows the diurnal intensity behaviour, according to which the x axes represent the local time and the y axes show the intensity of the optical emissions. The vertical dotted line represents the local noontime. All the data included here correspond to magnetically quiet days ($\mathrm{Ap} < 23$). The total number of days plotted in each panel may be noted on the top right corner of each figure. The upper (Fig. 3a, d), middle (Fig. 3b, e), and lower (Fig. 3c, f) panels show the diurnal behaviour of dayglow emission intensities at 777.4, 630.0, and 557.7 nm wavelengths, respectively. Figure 3a–c and d–f show the behaviour on several days when the diurnal intensity pattern was symmetric ($\mathrm{AT} \leq 0.4$ h) and asymmetric ($\mathrm{AT} > 0.4$ h), respectively. Note the difference in the timings of the occurrence peaks with respect to local noon, which are different for different days. The yellow line shows the average of all the days of data, which is essentially drawn to show the contrasting diurnal behaviour in each emission. The difference in the pattern of the emission intensities on the days with symmetric/asymmetric diurnal behaviour is clearly contrasting in many ways. (1) It may be noted that the intensity variability in the days with symmetric diurnal behaviour is not as much as that seen in the days with asymmetric diurnal behaviour. (2) The post-noon spread in intensities on the days with asymmetric diurnal behaviour is much greater as compared with that in the pre-noon. (3) The pattern of rise in intensity is different between these two types, with a slow rate of rise on the days with asymmetric diurnal behaviour, while it is relatively faster on the days that show symmetric diurnal behaviour. (4) While the emission intensity pattern seems skewed towards post-noon on the days with asymmetric diurnal behaviour, it seems slightly skewed towards forenoon, especially in the 630.0 nm and OI 557.7 nm emissions, on the days with symmetric diurnal behaviour. In Fig. 3 we collated the days with symmetric/asymmetric diurnal behaviour in emission intensities at each of the wavelengths, obtained from December 2013 to March 2014. There are days when only one or two emission intensities show symmetric diurnal behaviour but the others show asymmetric behaviour. There are also common days when all the oxygen emission intensities show symmetric/asymmetric diurnal behaviour. All these features make this very interesting and intriguing at the same time, as there seems to be a combination of atmospheric processes, the constituents/reactants available at a given time, neutral dynamics (winds), and electrodynamic forces operative at different altitudes on these days.

To begin with, let us look at the production mechanisms for these emissions as discussed in the earlier section. It is clear that the 557.7 and 630.0 nm dayglow emissions depend on both neutral and electron densities, whereas the 777.4 nm emissions depend only on the ion and electron densities. Thus, the production of all three dayglow emission intensities depends on the available solar flux, temperature-dependent reaction rates, and densities of neutrals and ions. It can be readily seen that photoelectrons, extreme ultraviolet (EUV) flux for photodissociation, and ionization at any location vary with respect to the solar zenith angle. So the diurnal pattern of the three dayglow emission intensities is expected to be symmetric with respect to local noontime. Thus, the asymmetric diurnal behaviour observed in the three optical dayglow emission intensities (Fig. 3) can mainly be due to the variation of either the neutral densities or the electron densities, which can be engendered by neutral dynamics or electrodynamics or both.

Firstly, we consider the changes in electron densities due to winds, especially the meridional wind, as it is known that the wind-assisted movement of electrons along the magnetic field lines does alter the electron densities at a given location. An increase/decrease of the electron number densities results in a corresponding increase/decrease in the optical emission intensities. A poleward wind moves the ionospheric layer to

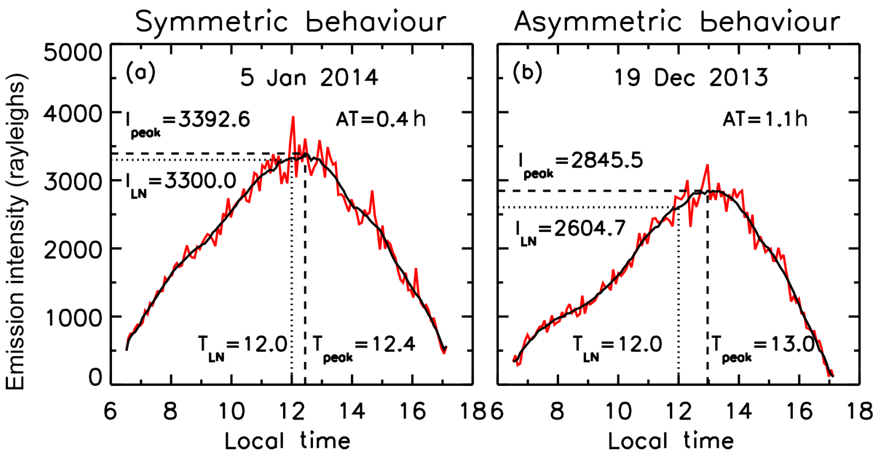

Figure 2. Sample of the diurnal behaviour of OI 630.0 nm dayglow emissions. **(a)** Symmetric diurnal behaviour in intensities with respect to local noon. The behaviour shows solar zenith-angle-dependent variation. Note that with respect to noon the rise and fall in intensities seem symmetric. **(b)** Asymmetric diurnal behaviour in intensities with respect to local noon. The peak in intensities is achieved after about 1 h from noon. Note the rise in intensities is more gradual than the decrease. The product of ratio of intensities at the peak to those at noon and the difference in times between the peak reached and local noon yield the value of asymmetricity in time (AT), which is also shown in both the panels.

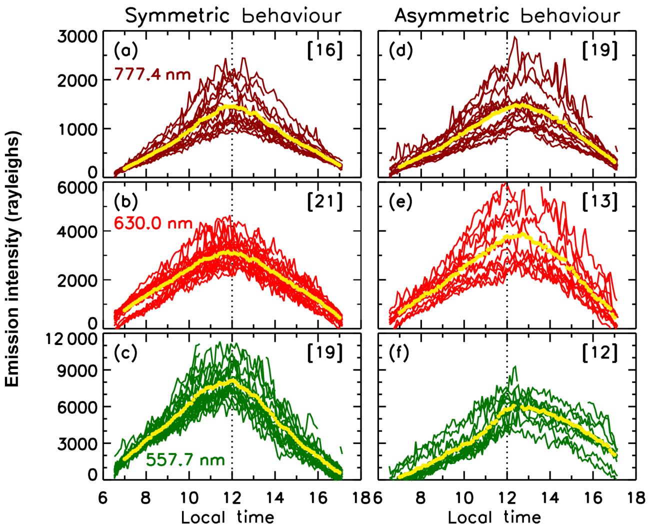

Figure 3. The diurnal behaviour in optical dayglow emission intensities at **(a, d)** OI 777.4 nm, **(b, e)** OI 630.0 nm, and **(c, f)** OI 557.7 nm is shown. The plots in the left column **(a, b, c)** show the plots with symmetric diurnal behaviour in intensities with respect to local noon. Plots **(d, e, f)** show asymmetric diurnal behaviour in intensities with respect to local noon. The yellow line shows the average of all the days of the data. The number of days of data that exist for a given diurnal behaviour is shown in square brackets.

lower altitudes where the dissociative recombination mechanism can be significant, thereby increasing the yield of OI 630.0 nm and OI 557.7 nm dayglow emissions. Similarly, the yield of the OI 777.4 nm dayglow emission is also expected to show an enhancement through the radiative recombination mechanism. An equatorward wind will move the ionospheric layer to higher altitudes, thereby reducing the potential yield of the dayglow emissions. In a similar manner, poleward winds, especially from the winter hemisphere, bring additional plasma into the summer hemisphere and so give rise to a greater yield in all the daytime airglow emissions.

Other than meridional winds, the equatorial electrodynamic forcing is another potential cause which is capable of bringing plasma to low latitudes. In the equatorial region, due to the horizontal nature of the magnetic field lines, several interesting phenomena take place. In the daytime, the formation of the equatorial electrojet is one of them, the strength of which can be used to infer the effectiveness of the electrodynamic processes operative on that day in the low latitudes. Under the action of the equatorial F region electric fields and the northward directed magnetic field lines of the earth, the plasma undergoes an $\boldsymbol{E} \times \boldsymbol{B}$ drift, which moves it to higher altitudes, from where the plasma follows the magnetic field lines and is transported to latitudes farther away due to the pressure gradient forces. This action forms the well-known EIA. Such excess ionization that is brought in to a given off-equatorial location results in greater emission intensities through the dissociative recombination and radiative recombination mechanisms. Moreover, in off-equatorial low-latitude regions, the westward zonal wind can produce an eastward E region electric field which gets mapped to the equatorial F region through magnetic field lines and can contribute to the $\boldsymbol{E} \times \boldsymbol{B}$ plasma drifts, thereby increasing the EIA strength. Thus, the effect of the zonal winds on the optical dayglow emission intensities can also be brought about through the equatorial electrodynamics. The relative importance of these two sources, namely neutral winds and electrodynamics, in making the diurnal emission behaviour to be asymmetric in the dayglow emission intensities is evaluated below.

Figure 4 shows 2 individual days (columns) of data for all the OI emissions, thermospheric neutral winds, and EEJ strengths (rows). The left column shows the day with a symmetric diurnal pattern (26 December 2013), and the one on the right shows the day with an asymmetric diurnal pattern (7 February 2014) in all the dayglow emission intensities. The x axes show local time, while the y axes (in the top three rows) show the dayglow intensity and (fourth row) the thermospheric zonal wind, U_x (dotted line, positive eastward), and meridional wind, U_y (solid line, positive northward), at all three emission altitudes on both the days as obtained by the Horizontal Wind Model (HWM14) (Drob et al., 2015). The bottommost row shows EEJ strength in nanotesla, and the horizontal dashed line drawn corresponds to 0 nT value. The solid lines in the dayglow emission intensities represent an 11-point running average of the data. The vertical dotted lines are drawn at local noontime. The dates of data and the values of AT of each of the emissions are shown in the plots. For these days, panels d and i show the zonal and meridional wind at 130, 230, and 300 km altitudes from where the OI 557.7 nm, OI 630.0 nm, and OI 777.4 nm emissions originate. It is expected that larger meridional winds bring the ionospheric layer to lower altitudes, which give rise to larger dayglow emissions, as discussed above. The meridional wind magnitudes were large on 26 December 2013 at all the altitudes, which, expectedly, are favourable for giving rise to an asymmetric diurnal pattern in emission intensities; however, the observations do not show such a behaviour. Conversely, on the day (7 February 2014) with lower meridional wind magnitudes, asymmetric diurnal behaviour was observed in all the dayglow emission intensities. Therefore, the meridional wind hypothesis as the cause of the asymmetric diurnal behaviour is not supported by observations.

In this context, the possibility of electrodynamic influence in bringing about the asymmetric diurnal behaviour in the intensities is examined using the equatorial electrojet strength as the reference. It is known that the EEJ dynamics have a significant role to play not only in influencing the distribution of electron densities in low-latitude regions (Moffett, 1979) but also in influencing the zonal winds and temperatures (Raghavarao et al., 1993). It should be noted that the peak EEJ strengths on these 2 days were different (40 and 75 nT); however, the peak emission intensities on these days were similar, and therefore it is apparent that the peak EEJ strengths have no direct relationship with the magnitudes of the peak dayglow intensities. However, it has been shown in earlier works (Raghavarao et al., 1978) that the integrated EEJ strength until noontime has a direct one-to-one correlation with the strength of the EIA. Although ionization is not measured through optical measurements, it has been shown by earlier studies that the ionization brought in from equatorial latitudes contributes to the OI 630.0 nm dayglow emissions through a dissociative recombination mechanism (Sridharan et al., 1992; Pallam Raju et al., 1996; Pallamraju et al., 2002). Thus, the asymmetricity in time observed in optical measurements at all the emission wavelengths is compared with the values of the EEJ strengths (A_{EEJ}) integrated over 07:00–12:00 LT. On these days with symmetric and asymmetric diurnal patterns in dayglow emission intensities, the values of A_{EEJ} were 147 and 214 nT h. As discussed above in this section, the larger value of A_{EEJ} on the day with asymmetric diurnal behaviour enhances the strength of the EIA and results in higher values of AT. The values of AT on the day with asymmetric diurnal behaviour were calculated to be 1.2, 1.1, and 1.4 h for 777.4, 630.0, and 557.7 nm emissions, respectively, whereas on the day with symmetric diurnal behaviour, these values were −0.1, −0.2, and −0.3 h for these emissions. The zonal wind magnitudes show nearly similar behaviour on both these days. In any case, the zonal winds

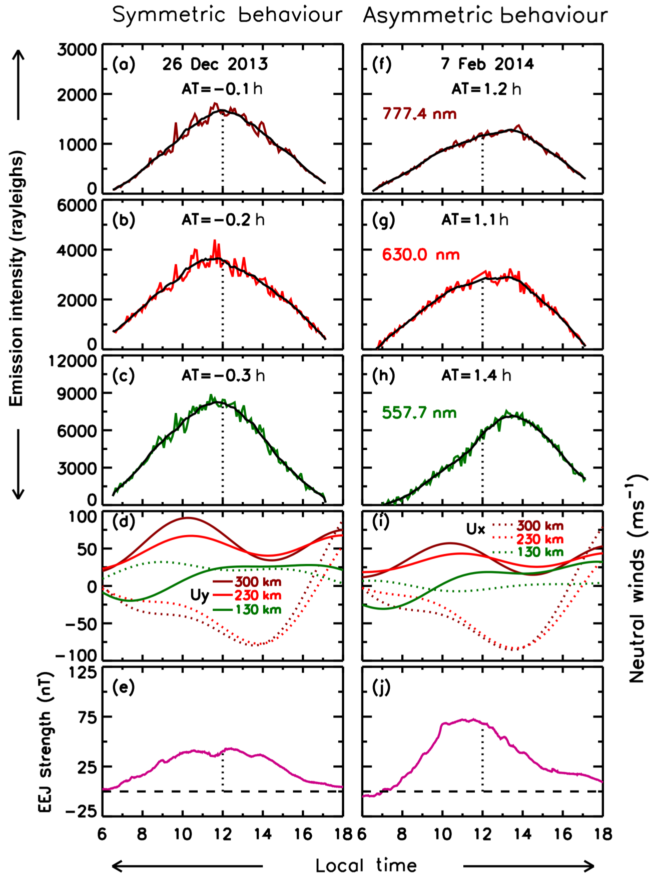

Figure 4. Top row **(a, f)** shows the diurnal variability in OI 777.4 nm on 2 selected days. Plots **(b, g)** and **(c, h)** show the diurnal behaviour of OI 630.0 nm and OI 557.7 nm emissions on the same days as of OI 777.4 nm emissions. Plots **(d, i)** show the HWM14 neutral wind magnitudes. Plots **(e, j)** show the electrojet strengths. The plots in the left column show the symmetric diurnal behaviour in all three oxygen dayglow emission intensities, while those on the right represent the day with asymmetric diurnal behaviour in all the dayglow emission intensities.

affect the equatorial electrodynamics, and, therefore, their effect will be implicit in the integrated EEJ strength.

Figure 5 comprehensively summarizes the results of the present investigation. The x axis shows the day number beginning on 1 December 2013. Figure 5a shows the peak meridional wind, U_y (solid line), and the corresponding zonal wind, U_x (dotted line), magnitudes obtained from the HWM14 model (Drob et al., 2015) for the three emission altitudes. It can be seen that the meridional wind reduces in magnitude, expectedly, from December to March, which is consistent with the seasonal wind behaviour as one moves from the solstice to the equinox, whereas the variation in zonal winds is not significant. Figure 5b shows the AT values for all these three emissions, which over this period varied from -1.5 to $+1.5$ h. From the uncorrelated behaviour between the values of AT and the meridional winds, it is clear that meridional winds are not the cause of the observed asymmetric diurnal behaviour in the optical emission intensities. Figure 5c shows the EEJ strengths, A_{EEJ}, integrated in the pre-noon hours (07:00–12:00 LT), which display a similar behaviour to that in the AT values in the optical dayglow emission intensities at all three wavelengths. The optical dayglow emissions are affected by both neutral dynamics and electrodynamics; both of these show seasonal dependence. So their contributions in the observed dayglow fluctuations are different in different seasons. The strength of equatorial electrodynamics decides the latitudinal extent of the EIA. Also, the effect of the EIA can first be seen at lower altitudes in off-equatorial latitudes and then at higher altitudes. Thus, on a given day this can result in better agreement between A_{EEJ} and values of AT in 557.7 nm emission intensity but not in 630.0/777.4 nm emissions. In Fig. 5, AT values are calculated for all the clear-sky days irrespective of symmetric or asymmetric diurnal patterns at all three emission wavelengths, which shows a broad similarity with the values of A_{EEJ} at different wavelengths of emissions. This clearly indicates that electrodynamic variations primarily govern the diurnal behaviour of the neutral dayglow emission intensities.

For the sake of completeness, it should however be mentioned that the thermospheric winds used in this study are model driven, whereas the EEJ values were obtained from measurements. Model values of winds have been used as measurements of winds in the daytime are not available for comparison. Nevertheless, as they are driven primarily by solar heating, it is not expected that the measured winds (had they been available) would yield any different result, as they are not expected to show significant variations from one day to another during magnetically quiet times, to which the data in this study corresponds.

To further confirm the role of electrodynamic influence on the daytime airglow intensities, we have investigated the ionospheric behaviour at two different locations, Trivandrum (magnetic equatorial location) and Ahmedabad (typically the northern crest location of the EIA). These independent ionospheric measurements were segregated into two categories: those corresponding to the days when all the dayglow emission intensities showed symmetric diurnal behaviour (AT $\leq$ 0.4 h) and those that showed asymmetric diurnal behaviour (AT $>$ 0.4 h). Figure 6a and b show the peak F region height (hmF2) over Trivandrum on the days with symmetric and asymmetric intensity distribution in dayglow emission intensities, respectively (ionosonde data corresponding to the days with symmetric diurnal behaviour in optical emission intensities are not available from Trivandrum during December 2013). The variation in the values of hmF2 is considered to be representative of the F region electric field over the dip equator. It can be seen in Fig. 6a that the peak hmF2 decreases in the afternoon on the days with symmetric diurnal behaviour. However, on the days with asymmetric diurnal behaviour (Fig. 6b), the hmF2 shows an increasing trend, indicating that the equatorial electrodynamics are active in the afternoon. Figure 6c and d show the ionospheric electron content (IEC) obtained from the digisonde mea-

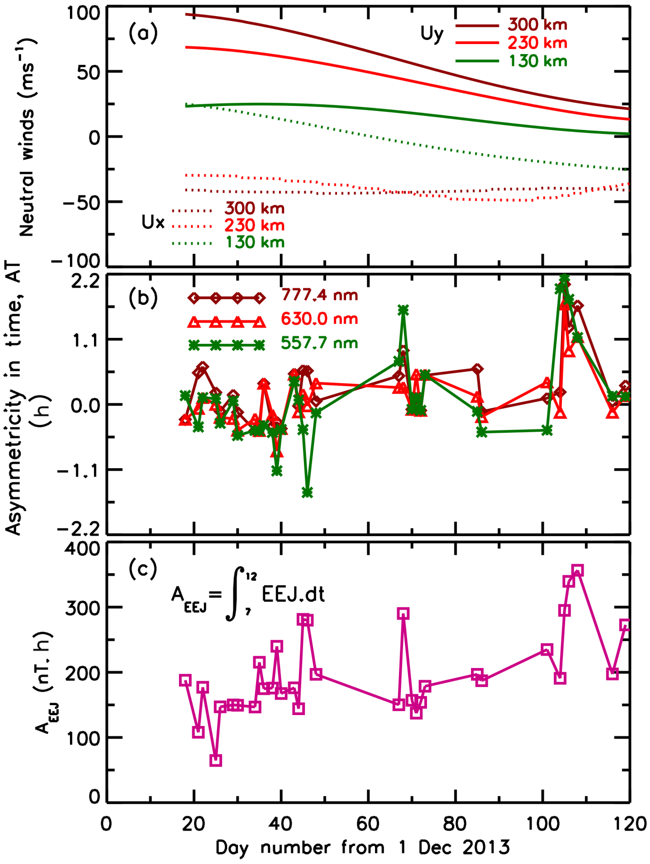

Figure 5. The variation in **(a)** neutral winds at the three different emission altitudes, **(b)** the asymmetricity in time (AT) at the three dayglow emission intensities on different days, and **(c)** EEJ strength integrated over 07:00–12:00 LT (A_{EEJ}) on the days corresponding to optical data are shown. The x axis shows the day number starting from 1 December 2013.

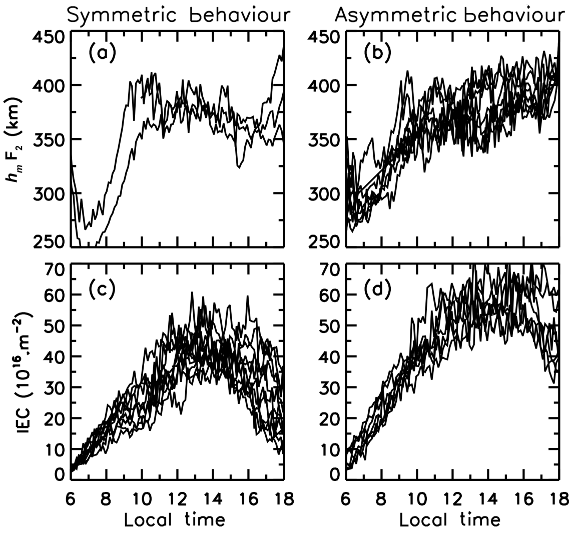

Figure 6. Variation of peak height of F2 layer over Trivandrum (equatorial station) and ionospheric electron content (IEC) over Ahmedabad (station typically under the northern crest of the EIA) on the days with **(a, c)** symmetric and **(b, d)** asymmetric diurnal dayglow intensity behaviour, respectively, are depicted.

surements over Ahmedabad on these days. It is very clear from these figures that the electron density over Ahmedabad peaked at around 14:00 LT on the days with symmetric diurnal behaviour, whereas on the days with asymmetric diurnal behaviour the electron density keeps increasing and its peak occurs later than 15:00 LT. It also indicates that the electrodynamics had been active in the late afternoon hours on the days with an asymmetric diurnal pattern observed in the dayglow emission intensities. Further, the IEC values are of greater magnitudes on the days with asymmetric diurnal behaviour (Fig. 6d) as compared to the days with symmetric diurnal behaviour (Fig. 6c). It is striking to note that the optical dayglow measurements obtained over Hyderabad (a location between Trivandrum and Ahmedabad; Fig. 1) show peak emission intensities at around 13:00 LT on the days with asymmetric diurnal behaviour in comparison to 15:00 LT in IEC over Ahmedabad, which can be attributed to the movement of the crest of the EIA. These independent measurements add credence to our interpretation that the temporal behaviour seen in the optical neutral dayglow emission intensities are governed by electrodynamic forces that originate at the magnetic equator.

4 Discussion

The nighttime airglow intensities vary purely as a function of densities of reactants, and their behaviour does not show any set pattern, whereas the daytime emission intensities show a broad solar zenith-angle-dependent variation primarily due to the solar control of several of the production mechanisms. However, it is quite interesting to note the clear changes that are brought in in the diurnal intensity variation of neutral daytime airglow emission intensities. For OI 630.0 nm dayglow emission, the data obtained during 2001 from a low-latitude location, Carmen Alto, in Chile (Pallamraju and Chakrabarti, 2006) showed such asymmetric diurnal behaviour as seen in the present study. However, later in a low solar activity epoch such an asymmetric diurnal pattern in the dayglow emission intensities was not noted. In Fig. 7 we reproduce Fig. 1 from Laskar et al. (2015), where the data that were obtained from Hyderabad, India, over the years of 2011–2013 are shown. The diurnal behaviour in intensities in all these years shows a broadly symmetric nature as seen in Fig. 3a, b, and c of the present study. The optical data obtained from that epoch did not show any asymmetric diurnal behaviour in the emission intensities. It is important to note that for the days of optical data that exist in the years 2001, 2011, 2012, 2013, and 2014, the average sunspots numbers were 160, 35, 52, 53, and 144, respectively, and so there seems to be a solar activity dependence in the observed AT values in optical dayglow emissions.

In order to characterize the solar activity effect, we have looked at the 630.0 nm optical dayglow emission intensity pattern as presented in the literature at different times and locations. The 630.0 nm dayglow emission is chosen due to the availability of a large set of observations at this emission (for over 25 years, although not continuous) in the published literature. The AT values were calculated for each day, and their mean values in different years are shown in Fig. 8. The x axis shows the year, and the y axis (on the left) shows the mean AT values (red dots) (the relevant literature which has been considered for these data is shown in the figure). We have also plotted (on the right side of the y axis) the monthly average sunspot numbers (dark dots). Observations by Laskar et al. (2015) during 2011–2013 show a symmetric diurnal pattern at all three wavelength emissions and in the absence of any possibility to calculate the AT values for these days (as the emission peak occurs around noontime; however, as the solar glare enters directly over the slit, no data were obtainable), the values of AT are approximated to zero during these years. It should be mentioned here that in the present experimental setup, the slit of MISE is oriented in the zonal direction (for the study of longitudinal variations) due to which the direct entry of solar glare during noontime is avoided, enabling us to obtain continuous dayglow data throughout the day without any gap. Also, some of the earlier results published in the literature that are used in this study to estimate the AT values plotted in Fig. 8 had a smaller field of view of $\sim 4°$ (Sridharan et al., 1999) because of which direct entry of solar glare was not an issue. The mean AT values calculated from the present observations at the three emission wavelengths are shown in different colours. It is striking to note that the variations of AT values go almost hand-in-hand with those in sunspot numbers. This clearly shows that the asymmetricity in time observed in optical neutral dayglow

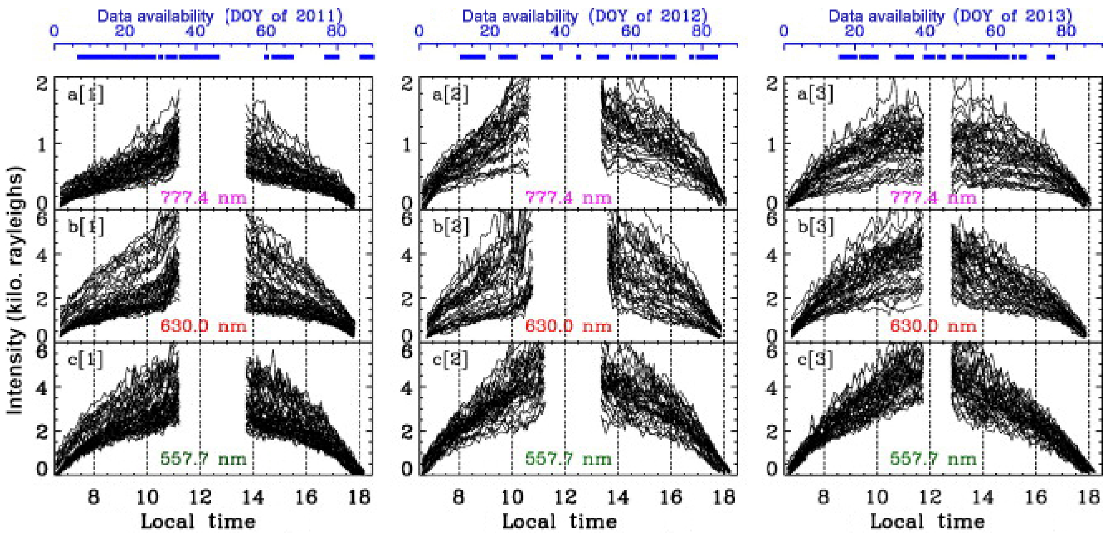

Figure 7. Reproduced from Fig. 1 of Laskar et al. (2015). The diurnal variations of the dayglow emission intensities for the 3 years 2011–2013 (left to right) and for the three wavelengths (top to bottom) are shown. The additional axes at the top represent the day of the year (DOY) on which dayglow data are available. It can be noted that the diurnal intensity pattern of all the emissions show a symmetric, broad solar zenith angle dependence in these years unlike the ones reported in the present data from the year 2014, in which deviations from solar zenith angle dependence seem to exit (Fig. 3d, e, f).

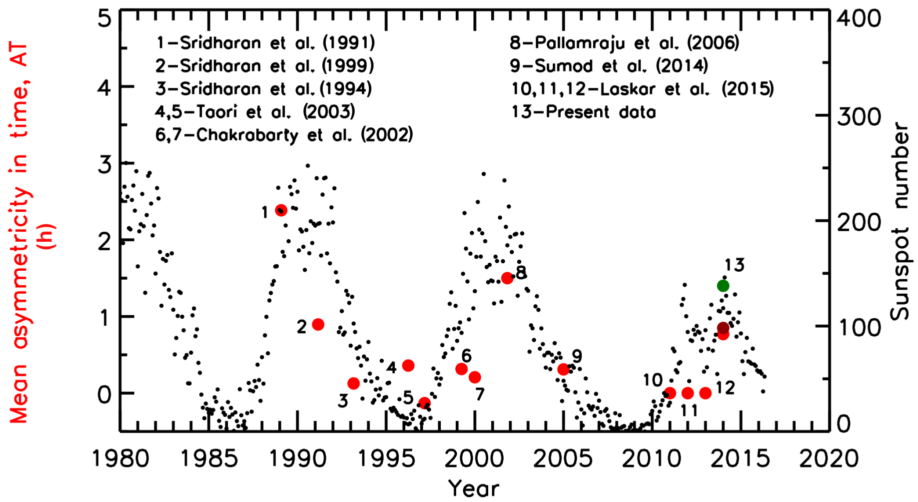

Figure 8. Variation of mean asymmetricity in time (AT) at OI 630.0 nm emissions in different years as obtained from the published literature is shown. The monthly averaged sunspot number is also plotted. A striking similarity between them indicates that the equatorial electric field has a direct role in the observed diurnal behaviour of the neutral optical dayglow emission intensities.

emissions has a solar activity dependence. This is interpreted to be due to the increase in equatorial electric field strengths with solar activity.

It thus shows the dominance of electrodynamic processes over the photochemical processes in bringing about temporal variations in the neutral dayglow emissions and is also a good example of E and F region coupling in the equatorial- and low-latitude ionosphere–thermosphere system. A consequence of this effect is shown in Fig. 6, where a movement of F region height in the afternoon to higher altitudes on some days over Trivandrum (equatorial station) (Fig. 6b) and a corresponding increase in the IEC over Ahmedabad (station near the northern crest of the EIA) is seen (Fig. 6d). The strength of this phenomenon varies with respect to local time, season, and solar activity. In the low solar activity period (2011–2013), the electric field strengths are smaller (Fejer and Scherliess, 1995) and apparently not sufficient to move the ionization to regions far away from the magnetic equator. Hence, the dayglow emission intensities measured from Hyderabad showed a symmetric photochemical emission behaviour in their respective intensities. This can also be seen in the present study wherein the negative AT values on some days correlate with smaller integrated electrojet strengths (Fig. 5b and c) and, hence, weaker electrodynamics (Fig. 6a and c). Further, the results from midlatitudes (Boston), where equatorial electrodynamic effects do not exist, do show a symmetric type of behaviour in OI 630.0 nm diurnal emission intensities (Pallamraju and Chakrabarti, 2006) as seen in the present study with weaker electrodynamics. These issues add credence to the inference regarding the influence of an electrodynamic effect in the neutral daytime airglow emissions.

To appreciate this issue further, attention is drawn to another study wherein the dayglow OI 630.0 nm emissions were measured from the magnetic equatorial station Thumba in India. It was seen that the shape of the diurnal pattern of the 630.0 nm dayglow was similar to that of the EEJ with a time shift (Sridharan et al., 1999). This time gap had been interpreted to be the time taken for the plasma to move from the E to F region under the influence of $\boldsymbol{E} \times \boldsymbol{B}$ drifts. The fact that it was indeed so was also confirmed by the simultaneously operating VHF doppler radar, where the $\boldsymbol{E} \times \boldsymbol{B}$ drifts obtained by the measured eastward electric fields were consistent with the observed time gaps between the EEJ and 630.0 nm dayglow variation. This result indicated the imprint of electrodynamic effect on the 630.0 nm dayglow emission intensities, both of which were obtained from the same location. Observations from an EIA crest region, Mt Abu (24.6° N, 72.8° E) in India, during high solar activity showed different behaviour in the OI 630.0 nm emission intensities on the equatorial electrojet and counter electrojet days (Chakrabarty et al., 2002). All these results corroborate our conclusion that the asymmetric diurnal behaviour of the optical dayglow emission intensities seen in the low latitudes is mainly due to the equatorial electrodynamic variations. However, the effect of neutral winds on the dayglow emissions cannot be ruled out completely. Ultimately, a comprehensive model is needed to fully understand the complex coupled behaviour of the thermosphere/ionosphere and the underlying processes at equatorial and off-equatorial low-latitude regions.

In this study it is shown that not only the OI 630.0 nm dayglow intensity variations but also those at OI 777.4 nm and OI 557.7 nm show asymmetric diurnal behaviour. It should be remembered that the peak dayglow emission intensities at any of the wavelengths are not correlated with EEJ strengths; they are related with the asymmetricity in time, indicating that it is not the total emission intensities but their temporal variability that is governed by the EEJ strength.

5 Conclusion

Oxygen-neutral dayglow emissions at multiple wavelengths measured during 2013–2014 showed that the emissions' diurnal behaviour in intensities was both symmetric and asymmetric with respect to local noon. While the symmetric diurnal behaviour can be understood in terms of solar zenith angle variation of the production mechanisms, the cause of asymmetric behaviour in diurnal emission intensities is not apparent. Against this background, its possible causes have been investigated in terms of neutral winds and equatorial electrodynamics. Using the equatorial electrojet strength data and ionospheric behaviour on all these days, it has been conclusively shown that the equatorial electrodynamics that are operative on a given day give rise to the observed asymmetric diurnal behaviour in the neutral oxygen dayglow emission variability. This aspect has been discussed in a wider context. It has been noted that in the low solar activity period, the diurnal variability in the oxygen emission intensities was predominantly symmetric with respect to local noon, while they were asymmetric during high solar activity periods. This again gives a broader picture to the ionosphere–thermosphere systemic behaviour as the neutral dayglow emission intensities are sensitive to the electrodynamic changes that happen over a solar cycle.

6 Data availability

For this study, the optical dayglow data from Hyderabad and ionospheric data from Ahmedabad were obtained by the Physical Research Laboratory and can be made available on request. The EEJ data can be obtained from the Indian Institute of Geomagnetism. The ionosonde data from Trivandrum can be obtained from the Space Physics Laboratory. The sunspot number data are obtained from the daily solar dataset maintained by NOAA (ftp://ftp.swpc.noaa.gov/pub/indices).

Acknowledgements. The authors acknowledge the assistance provided by Abdul Moid, Sambasivam Rao, and Abhilash Maryada in the operation of MISE at Jawaharlal Nehru Technological University, Hyderabad, India. This work is supported by the Department of Space, Government of India.

The topical editor, J. Makela, thanks the three anonymous referees for help in evaluating this paper.

References

Chakrabarty, D., Sekar, R., Chandra, H., Narayanan, R., Pathan, B. M., and Subbarao, K. S. V.: Characterizations of the diurnal shapes of OI 630.0 nm dayglow intensity variations: inferences, Ann. Geophys., 20, 1851–1855, doi:10.5194/angeo-20-1851-2002, 2002.

Chakrabarti, S., Pallamraju, D., Baumgardner, J., and Vaillancourt, J.: HiTIES: a high throughput imaging echelle spectrograph for ground-based visible airglow and auroral studies, J. Geophys. Res., 106, 30337–30348, 2001.

Das, U., Pallamraju, D., and Chakrabarti, S.: Effect of an X-Class solar flare on the OI 630 nm dayglow emissions, J. Geophys. Res., 115, A08302, doi:10.1029/2010JA015370, 2010.

Drob, D. P., Emmert, J. T., Meriwether, J. W., Makela, J. J., Doornbos, E., Conde, M., Hernandez, G., Noto, J., Zawdie, K. A., McDonald, S. E., Huba, J. D., and Klenzing, J. H.: An update to the Horizontal Wind Model (HWM): The quiet time thermosphere, Earth and Space Science, 2, 301–319, doi:10.1002/2014EA000089, 2015.

Emmert, J. T., Richmond, A. D., and Drob D. P.: A computationally compact representation of Magnetic-Apex and Quasi-Dipole coordinates with smooth base vectors, J. Geophys. Res., 115, A08322, doi:10.1029/2010JA015326, 2010.

Fejer, B. G. and Scherliess, L.: Time dependent response of equatorial ionospheric electric fields to magnetospheric disturbances, Geophys. Res. Lett., 22, 851–854, doi:10.1029/95GL00390, 1995.

Gerrard, A. J. and Meriwether, J. W.: Initial daytime and nighttime SOFDI observations of thermospheric winds from Fabry-Perot Doppler shift measurements of the 630-nm OI line-shape profile, Ann. Geophys., 29, 1529–1536, doi:10.5194/angeo-29-1529-2011, 2011.

Hays, P. B., Rusch, D. W., Roble, R. G., and Walker, J. C. G.: The OI (6300 A) airglow, Rev. Geophys., 16, 225–232, 1978.

Laskar, F. I., Pallamraju, D., Lakshmi, T. V., Reddy, M. A., Pathan, B. M., and Chakrabarti, S.: Investigations on vertical coupling of atmospheric regions using combined multiwavelength optical dayglow, magnetic, and radio measurements, J. Geophys. Res.-Space, 118, 4618–4627, doi:10.1002/jgra.50426, 2013.

Laskar, F. I., Pallamraju, D., Veenadhari, B., Lakshmi, T. V., Reddy, M. A., and Chakrabarti, S.: Gravity waves in the thermosphere: Solar activity dependence, Adv. Space. Res., 55, 1651–1659, 2015.

Maharaj-Sharma, R. and Shepherd, G. G.: Solar variability of the day-time atomic oxygen $O(^1S)$ emission in the middle and lower thermosphere, J. Geophys. Res., 109, A03303, doi:10.1029/2003JA010183, 2004.

Makela, J. J., Fisher, D. J., Meriwether, J. W., Buriti, R. A., and Medeiros, A. F.: Near-continual ground-based nighttime observations of thermospheric neutral winds and temperatures over equatorial Brazil from 2009 to 2012, J. Atmos. Sol.-Terr. Phy., 103, 94–102, 2013.

Moffett, R. J.: The equatorial anomaly in the electron distribution of the Terrestrial F region, Fund. Cosmic. Phys., 4, 313–387, 1979.

Nakamura, T., Tsuda, T., Miyagawa, H., Matsushita, Y., Fukunishi, H., Takahashi, Y., and Yamada, Y.: Propagation directions of gravity wave patterns observed in OH CCD images during SEEK campaign, Geophys. Res. Lett., 25, 1793–1796, 1998.

Narayanan, R., Desai, J. N., Modi, N. K., Raghavarao, R., and Sridharan, R.: Dayglow photometry: a new approach, Appl. Optics, 28, 2138–2142, 1989.

Pallam Raju, D., Sridharan, R., Gurubaran, S., and Raghavarao, R.: First results from ground-based daytime optical investigation of the development of the equatorial ionization anomaly, Ann. Geophys., 14, 238–245, doi:10.1007/s00585-996-0238-9, 1996.

Pallamraju, D., Baumgardner, J., and Chakrabarti, S.: A multiwavelength investigation of the Ring effect in the day sky spectrum, Geophys. Res. Lett., 27, 1875–1878, 2000.

Pallamraju, D., Baumgardner, J., and Chakrabarti, S.: HIRISE: A ground-based high-resolution imaging spectrograph using echelle grating for measuring daytime airglow/auroral emissions, J. Atmos. Sol.-Terr. Phy., 64, 1581–1587, 2002.

Pallamraju, D., Chakrabarti, S., Doe, R., and Pederson, T.: First ground-based OI 630 nm optical measurements of daytime cusp-like and F-region auroral precipitation, Geophys. Res. Lett., 31, L08807, doi:10.1029/2003GL019173, 2004.

Pallamraju, D. and Chakrabarti, S.: First ground-based measurements of OI 6300 A daytime aurora over Boston in response to the 30 October 2003 geomagnetic storm, Geophys. Res. Lett., 32, L03S10, doi:10.1029/2004GL021417, 2005.

Pallamraju, D. and Chakrabarti, S.: Contributions of Imaging Echelle spectrographs to daytime optical aeronomy, J. Atmos. Sol.-Terr. Phy., 68, 1459–1471, 2006.

Pallamraju, D., Das, U., and Chakrabarti, S.: Short- and long-timescale thermospheric variability as observed from OI 630.0 nm dayglow emissions from low latitudes, J. Geophys. Res.-Space, 115, A06312, doi:10.1029/2009JA015042, 2010.

Pallamraju, D., Laskar, F. I., Singh, R. P., Baumgardner, J., and Chakrabarti S.: MISE: A multiwavelength imaging spectrograph using echelle grating for daytime optical aeronomy investigations, J. Atmos. Sol.-Terr. Phy., 103, 176–183, 2013.

Pallamraju, D., Karan, D. K., and Phadke, K. A.: First three dimensional wave characteristics in the daytime upper atmosphere derived from ground-based multiwavelength oxygen dayglow emission measurements, Geophys. Res. Lett., 43, 5545–5553, doi:10.1002/2016GL069074, 2016.

Raghavarao, R., Sharma, P., and Sivaraman, M. R.: Correlation of Ionization anomaly with the intensity of the electrojet, Space Res., XVIII, 277–280, 1978.

Raghavarao, R., Hoegy, W. R., Spencer, N. W., and Wharton, L. E.: Neutral temperature anomaly in the equatorial thermosphere – A source of vertical winds, Geophys. Res. Lett., 20, 1023–1026, 1993.

Shepherd, G. G., Siddiqi, N. J., Wiens, R. H., and Zang, S.: Airglow measurements of possible changes in the ionosphere and middle atmosphere, Adv. Space Res., 20, 2127–2135, 1997.

Shiokawa, K., Otsuka, Y., and Ogawa, T.: Propagation characteristics of nighttime mesospheric and thermospheric waves observed by optical mesosphere thermosphere imagers at middle and low latitudes, Earth Planets Space, 61, 479–491, 2009.

Singh, R. P. and Pallamraju, D.: On the latitudinal distribution of mesospheric temperatures during sudden stratospheric warming events, J. Geophys. Res.-Space, 120, 2926–2939, doi:10.1002/2014JA020355, 2015.

Singh, R. P. and Pallamraju, D.: Effect of cyclone Nilofar on mesospheric wave dynamics as inferred from optical nightglow observations from Mt. Abu, India, J. Geophys. Res.-Space, 121, 5856–5867, doi:10.1002/2016JA022412, 2016.

Singh, V., McDade, I. C., Shepherd, G. G., Solheim, B. H., and Ward, W. E.: The O(1D) dayglow emission as observed by the wind imaging interferometer on UARS, Adv. Space Res., 17, 11–14, 1996.

Solomon, S. C. and Abreu, V.: The 630.0nm dayglow, J. Geophys. Res., 94, 6817–6824, 1989.

Sridharan, R., Raghavarao, R., Gurubaran, S., and Narayanan, R.: First results of OI 630.0 nm dayglow measurements from equatorial latitudes, J. Atmos. Sol.-Terr. Phy., 53, 521–528, 1991.

Sridharan, R., Haider, S. A., Gurubaran, S., Sekar, R., and Narayanan, R.: OI 630.0-nm dayglow in the region of equatorial ionization anomaly: Temporal variability and its causative mechanism, J. Geophys. Res., 97, 13715–13721, 1992.

Sridharan, R., Sekar, R., and Gurubaran, S.: Two dimensional high resolution imaging of the equatorial plasma fountain, J. Atmos. Sol.-Terr. Phy., 55, 1661–1665, 1993a.

Sridharan, R., Narayanan, R., Modi, N. K., and Pallamraju, D.: A novel mask design for multiwavelength dayglow photometry, Appl. Optics, 32, 4178–4180, 1993b.

Sridharan, R., Pallamraju, D., Raghavarao, R., and Ramarao, P. V. S.: Precursor to equatorial spread-F in 0I 630.0 nm dayglow, Geophys. Res. Lett., 21, 2797–2800, 1994.

Sridharan, R., Modi, N. K., Pallam Raju, D., Narayanan, R., Pant, T. K., Taori, A., and Chakrabarty, D.: A Multiwavelength daytime photometer – a new tool for the investigation of atmospheric processes, Meas. Sci. Technol., 9, 585–591, 1998.

Sridharan, R., Pallamraju, D., Somayajulu, V. V., Taori, A., Chakrabarty, D., and Raghavarao, R.: Imprint of equatorial electrodynamical processes in the OI 630.0 nm dayglow, J. Atmos. Sol.-Terr. Phy., 61, 1143–1155, 1999.

Sumod, S. G., Pant, T. K., Vineeth, C., and Hossain, M. M.: On the ionospheric and thermospheric response of solar flare events of 19 January 2005: An investigation using radio and optical techniques, J. Geophys. Res.-Space, 119, 5049–5059, doi:10.1002/2013JA019714, 2014.

Taori, A., Sridharan, R., Chakrabarty, D., Modi, N. K., and Narayanan, R.: Significant upper thermospheric contribution to the O (^{1}S) 557.7 nm dayglow emission: first ground based evidence, J. Atmos. Sol.-Terr. Phy., 65, 121–128, 2003.

Taylor, M. J., Bishop, M. B., and Taylor, V.: All-sky measurements of short period waves imaged in the OI (557.7 nm), Na (589.2 nm) and near infrared OH and O_2 (0,1) nightglow emissions during the ALOHA-93 campaign, Geophys. Res. Lett., 22, 2833–2836, 1995.

Tinsley, B. A., Christensen, A. B., Bittencourt, J., Gouveia, H., Angreji, P. D., and Takahashi, H.: Excitation of oxygen permitted line emissions in the tropical nightglow, J. Geophys. Res., 78, 1174–1186, 1973.

Tyagi, S. and Singh, V.: The morphology of oxygen greenline dayglow emission, Ann. Geophys., 16, 1599–1606, doi:10.1007/s00585-998-1599-z, 1998.

Upadhayaya, A. K. and Singh, V.: Effects of temperature dependence of reaction $N_2(A^3\ S_u^+) + O$ ongreenline dayglow emission, Ann. Geophys., 20, 2039–2045, doi:10.5194/angeo-20-2039-2002, 2002.

Wallace, L. and McElroy, M. B.: The visual dayglow, Planet. Space Sci., 14, 677–708, 1966.

Witasse, O., Lilensten, J., Lathuillere, C., and Blelly, P. L.: Modeling the OI 630.0 and 557.7 nm thermospheric dayglow during EISCAT-WINDII coordinated measurements, J. Geophys. Res., 104, 24639–24655, 1999.

Zhang, S. P. and Shepherd, G. G.: Solar influence on the O(1D) dayglow emission rate: Global scale measurements by WINDII on UARS, Geophys. Res. Lett., 31, L07804, doi:10.1029/2004GL019447, 2004.

Zhang, S. P. and Shepherd, G. G.: On the response of the O(1S) dayglow emission rate to the Sun's energy input: An empirical model deduced from WINDII/UARS global measurements, J. Geophys. Res., 110, A03304, doi:10.1029/2004JA010887, 2005.

AGU PUBLICATIONS

JGR

Journal of Geophysical Research: Space Physics

RESEARCH ARTICLE
10.1002/2017JA023891

Key Points:
- Ground-based large FOV dayglow measurements along zonal direction reveal the existence of spatial differences in thermospheric wave dynamics
- Longitudinal differences in the gravity wave time periods, scale sizes, and propagation directions exist within 3°–8° spatial extent
- Findings point to variations in the equatorial electrodynamics as the cause for longitudinal differences observed in neutral wave dynamics

Correspondence to:
D. Pallamraju,
raju@prl.res.in

Citation:
Karan, D. K., and D. Pallamraju (2017), Small-scale longitudinal variations in the daytime equatorial thermospheric wave dynamics as inferred from oxygen dayglow emissions, *J. Geophys. Res. Space Physics*, *122*, 6528–6542, doi:10.1002/2017JA023891.

Received 12 JAN 2017
Accepted 15 MAY 2017
Accepted article online 16 MAY 2017
Published online 5 JUN 2017

Small-scale longitudinal variations in the daytime equatorial thermospheric wave dynamics as inferred from oxygen dayglow emissions

Deepak K. Karan[1,2] and Duggirala Pallamraju[1]

[1]Space and Atmospheric Sciences Division, Physical Research Laboratory, Ahmedabad, India, [2]Indian Institute of Technology, Gandhinagar, India

Abstract The equatorial upper atmospheric dynamic processes show both latitudinal and longitudinal variabilities. While the variability in latitudes can exist over small distances (approximately hundreds of kilometers), the longitudinal behavior has been shown to be existing mainly over large spatial separations (approximately thousands of kilometers). In the present work we have used variations in thermospheric optical dayglow emissions at OI 557.7, 630.0, and 777.4 nm, as tracers of neutral dynamics. These emissions are obtained simultaneously from a high-resolution slit spectrograph, Multi wavelength Imaging Spectrograph using Echelle grating, from a low-latitude location, Hyderabad (17.5°N, 78.4°E; 8.9°N magnetic latitude) in India, to investigate the longitudinal differences in the upper atmospheric processes over short separations. Spectral analyses of gravity waves carried out on the dayglow emission intensity variations for different independent viewing directions on some days show dissimilar periodicities suggesting the existence of longitudinal differences. Gravity wave scale sizes and the propagation characteristics on these days are different from those in which longitudinal differences are not seen. Further, the zenith diurnal emission intensity patterns are different on the days with and without the observed longitudinal variability. This work shows for the first time that longitudinal differences in upper atmospheric processes can exist at even as small as 3° longitude separations. Such longitudinal differences seen in the neutral dayglow emission intensities are attributed to the zonal variation in the daytime equatorial electrodynamics.

Plain Language Summary The longitudinal variability in the upper atmospheric phenomena has been reported over large distances in the literature that span greater than several thousands of kilometer. However, nothing is known as to what happens on the smaller distances. Using large field of view optical dayglow emission measurements obtained along zonal direction, we discovered that longitudinal variations do exist in as small longitudinal separations as 300–800 km. We inferred that this is due to changes in the equatorial electrodynamics. These results have implications for comprehensive understanding of the variations in the atmospheric dynamics which can many a times be localized.

1. Introduction

Earth's upper atmosphere consists of both neutrals as well as plasma, and hence, it is affected by both neutral and electrodynamic processes. These processes vary in both zonal and meridional directions. Owing to the horizontal nature of the Earth's magnetic field lines above the geomagnetic equator, many interesting upper atmospheric phenomena, such as equatorial electrojet (EEJ), equatorial ionization anomaly (EIA), and equatorial temperature and wind anomaly, are formed over the equatorial/low latitudes during daytime. These coupled processes bring about variations in both neutral and plasma densities across the latitudes. The details on the formation mechanism of these phenomena and their effects in bringing about changes across latitudes are now well understood [e.g., *Moffett*, 1979; *Raghavarao et al.*, 1978, 1991, 1993]. During daytime, the zonal wind across the magnetic field lines gives rise to a dynamo action, wherein the EEJ currents are formed above the geomagnetic equator. The strength of the EEJ has been shown to be directly proportional to strength of the EIA [*Raghavarao et al.*, 1978], and therefore, it plays an important role in bringing about changes in the meridional variations in the development of equatorial upper atmospheric processes. Moreover, during geomagnetic disturbances due to the precipitation of highly energetic particles and the enhancement of auroral electrojet current, joule heating occurs over polar regions which sets in winds and waves. These winds and waves move away from the high-latitudes, and the large-scale motion in neutrals and plasmas is referred to as traveling atmospheric disturbances (TADs) and traveling ionospheric disturbances (TIDs). The TADs and TIDs alter the densities of the upper atmospheric constituents bringing about latitudinal variations from high-to-low latitudes [e.g., *Richmond and Matsushita*, 1975; *Hajkowicz*, 1991; *Hocke and Schlegel*, 1996; *Pallamraju et al.*, 2004].

In addition to the meridional variations, these neutral and electrodynamic processes also show zonal variations. Many studies have been carried out on the zonal variations of the ionosphere and thermosphere at different longitude sectors. Variation in geomagnetic field strength and magnetic declination angle at different longitudinal sectors can bring about changes in the strengths of dynamo action and thereby cause longitudinal variations in the equatorial electrodynamics. For example, the magnetic field strength over the Indian sector is greater than that over the American sector. Therefore, the vertical drifts (v_d) of equatorial plasma over the Indian sector are smaller than those over the American sector [*Kelley*, 2009] (as $v_d = \frac{\vec{E} \times \vec{B}}{\left|\vec{B}\right|^2}$, where $\vec{E}$ is the zonal electric field and $\vec{B}$ is the geomagnetic field intensity). This further contributes to the differences in the extents of the EIA crests at these two longitude sectors [*Raghavarao et al.*, 1988]. Changes in the declination angle with respect to longitude also contribute to longitudinal variability in the electrodynamics, which is most prominent over the Brazilian sector (South Atlantic anomaly region) in comparison to that over the Chilian longitudes. As the Earth's axis of rotation is tilted, the relative angle between the magnetic declination and solar terminator keeps changing at a given location in a year. The preferential occurrence of the plasma irregularities across longitudes was shown to be matching with the periods of alignment of the solar terminator with that of the north-south plane of magnetic field lines [e.g., *Abdu et al.*, 1981], as it enables simultaneous sunset in both the hemispheres, thereby preventing the shorting of the *F* region electric fields by the highly conducting *E* region.

In the recent past analysis of far ultraviolet (FUV) emissions (OI 135.6 nm) obtained onboard the IMAGE satellite showed the existence of a significant longitudinal structure in the emission intensities [e.g., *England et al.*, 2006; *Immel et al.*, 2006; *Sagawa et al.*, 2005]. The ionospheric densities as inferred in the nightglow emissions were found to be peaking at some fixed longitudes and were attributed to be due to the *E* region dynamo being governed by neutral winds associated with nonmigrating diurnal tides [*England et al.*, 2006; *Immel et al.*, 2006]. Such fixed locations of the global wave 4 structure were interpreted to be due to the latent heat release from the lower atmosphere due to the prevalent convective processes [*Immel et al.*, 2006]. In an earlier work carried out using ISIS 2 satellite measurements of electron densities at two different longitudes (51°E and 80°E) separated by ~30°, the EIA strengths were reported to be behaving differently from one another [*Sharma and Raghavarao*, 1989]. Now we know that the two longitudes happen to be over different convective regions on the ground that coincide with the crest and trough regions of the FUV airglow intensities as reported by *Immel et al.* [2006]. Using GPS Aided Geo Augmented Navigation network-derived measurements, differences in the values of total electron content over Indian longitudes (70°E to 95°E) were reported which seem consistent with the global wave number 4 structure [*Sunda and Vyas*, 2013]. More recently, from magnetic measurements at two different Indian longitude regions (separated by 15°) the existence of longitudinal variations in equatorial electric fields and current density was reported [*Chandrasekhar et al.*, 2014].

To summarize, all the measurements/results reported in the literature over the years show that the zonal differences are localized over fixed longitudinal sectors. These could be due to differing conditions in geomagnetic anomalies, geomagnetic field line geometry, or tropospheric convective zones. The longitudinal differences in the dynamical process thus obtained using satellite observations, ground-based measurements, and through simulations give information on the existence of variability in the electrodynamic processes over longitudinal separations greater than 1000 km. However, it is not known if any longitudinal difference exists over smaller distances that are shorter than 1000 km. If they do, then what are the mechanisms responsible for such small-spatial scale changes in the zonal direction? To the best of our knowledge, longitudinal differences of the daytime electrodynamic processes within separations smaller than 10° (over South American sector) have not been reported in the literature. In other sectors where such drastic differences in geomagnetic conditions as in South Atlantic anomaly region do not exist, the minimum separation in longitudinal differences has been on the order of 15° [*Chandrasekhar et al.*, 2014].

10.1002/2017JA023891

Satellites with high-inclination orbit can yield information on the small-scale meridional variations but are not well suited for the studies of the temporal variation of any phenomenon over a given longitudinal region which may possibly have zonal structures. Measurements from ground-based instruments in close separation (e.g., 1° latitude × 1° longitude) could be useful to study such small-scale zonal differences. However, in the absence of such measurements in grids of such fine spacing, optical measurements with high spatial resolution are best suited for such studies. Optical emission intensity variations can be used as tracers of the dynamic processes that occur at the respective altitude of emissions. In the present work, by using multiwavelength oxygen optical dayglow emission intensity data obtained over a large field of view (FOV) of around 100°, for the first time, we have found the existence of small-scale zonal (along east-west) differences in the neutral wave dynamics. These are attributed to the variations in the equatorial electrodynamics. This dependence varies from day to day and is shown to be intricately coupled with the EEJ strength. Further, we also show that the daytime wave characteristics in terms of the wave periods, scale sizes, and propagation direction are clearly different on the days that show longitudinal variations in comparison with those that do not show any longitudinal variation.

2. Experimental Technique and Data Analysis

The dayglow emissions are buried in the strong solar scattered background continuum. In the present work, neutral optical oxygen dayglow emission intensity data at 557.7, 630.0, and 777.4 nm wavelengths over a FOV of around 100° are obtained by using the high-resolution spectrograph, Multi wavelength Imaging Spectrograph using Echelle grating (MISE) [*Pallamraju et al.*, 2013]. These emissions originate at 130, 230, and 300 km altitudes, respectively. The data used in the present work were obtained during December 2013 to March 2014. MISE is commissioned at Hyderabad (17.5°N, 78.4°E; 8.9°N magnetic latitude) which is a low-latitude location in India. The spectral information around these three wavelengths is imaged onto a 1 k × 1 k pixel charge coupled device detector. An on-chip binning of 8 pixels is carried out along the spatial direction to increase the signal-to-noise ratio of the measurement. The spectral resolution of MISE is 0.012 nm at 630.0 nm. The day-sky spectra are compared with the normalized solar spectrum for wavelength calibration. Further, the solar spectrum is scaled with the sky spectra at the continuum levels, and therefore, the difference between them gives information on the atmospheric contributions (both emissions and scattering). The atmospheric scattering contribution (Ring effect) at a Fraunhofer absorption line (free from atmospheric emissions and telluric absorptions) very close to the emission line is considered and subtracted from the atmospheric contribution at the emission line of interest to yield the dayglow emission intensities. A data cadence of 5 min is considered as it is typically half of the Brunt Väisälä period in the altitudes considered in this work. This process is well established and has been described in detail in the literature [*Pallamraju et al.*, 2000, 2002, 2013]. This process of obtaining dayglow emission intensity at each wavelength is repeated continuously to obtain information on its diurnal variability. An example of OI 630.0 nm dayglow intensities obtained for 1 day is shown as a solid red line in Figure 1a.

The slit of MISE was oriented along the zonal direction for the present study. The maximum spatial extent covered for the given FOV at the emission altitudes of 557.7, 630.0, and 777.4 nm dayglow emission intensities are ~340, ~600, and ~800 km, respectively. The spectra of MISE have 128 pixels along the spatial direction. Data from pixel numbers 10 to 109 are considered for analyses which correspond to the light incident from the 100° FOV. The remaining pixels on either side correspond to lower elevation angles of the sky which are susceptible to be affected by scattering effect in the lower atmosphere and hence, have not been considered for the analysis. An 11-pixel running average of the spectral image is obtained along the spatial direction, which smooth out very fine spatial scales that may not have any physical significance. The nonlinear nature of the relation between FOV and the distance covered in space results in pixel-to-pixel variation in the spatial extent as imaged on the detector. Spatial resolution over zenith corresponds to 0.4, 0.7, and 0.9 km pixel^{-1} for the emission heights of 130, 230, and 300 km, respectively, whereas it is 11, 20, and 25 km pixel^{-1}, at higher view angles for the 557.7, 630.0, and 777.4 nm emission wavelengths. Considering a 2-pixel resolution to ascertain the position, the maximum spatial uncertainty for each of these emissions is 22, 40, and 50 km, respectively. The dayglow emission intensities along the FOV are obtained simultaneously. The spectra from different spatial segments of an image are independently analyzed to obtain the emission intensities along the zonal direction. A sample of such result is shown in Figure 1c.

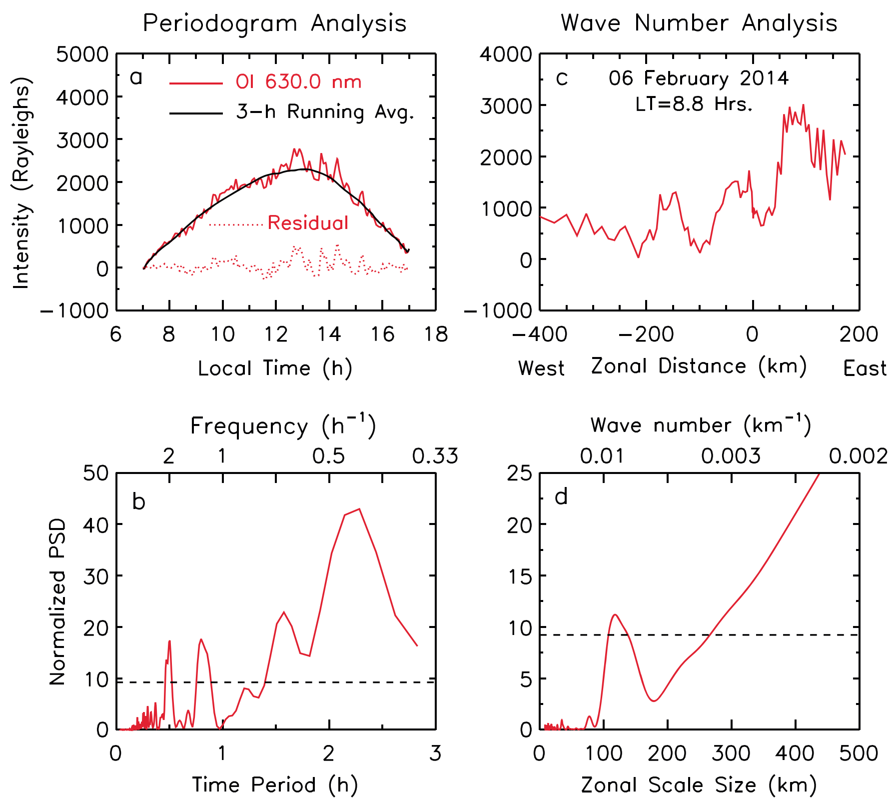

Figure 1. (a) The diurnal pattern of the OI 630.0 nm dayglow emission intensity over zenith on 06 February 2014 is shown (red). The 3 h running average (dark line) is subtracted from the dayglow to obtain the residuals (dotted red line). (b) The result of Lomb-Scargle periodgram analysis obtained from the residuals is shown. The horizontal dashed line represents the 90% FAL. On this day, time periods of 2.28, 1.57, 0.8, and 0.5 h are found to be significant. (c) The OI 630.0 nm dayglow emission intensity along the zonal direction at 8.8 LT on the same day is shown. Ranges covered toward east and west from the zenith are shown as positive and negative values. (d) The result of wave number spectral analysis on the spatial dayglow data in Figure 1c is shown. The horizontal dashed line shows the 90% FAL level. A significant scale size of 118 km is found to be present on this day.

The optical dayglow emission intensities are produced due to various photochemical and chemical reactions occurring in the atmosphere. The OI 557.7, 630.0, and 777.4 nm dayglow emissions occur due to the transitions as shown below:

$$O(^1S) \rightarrow O(^1D) + h\nu(\lambda = 557.7\,\mathrm{nm}) \tag{1}$$

The $O(^1S)$ state can be produced due to collisional deactivation of N_2, dissociative recombination of O_2^+ and e^-, photoelectron impact excitation of O, and photo dissociation of O_2 at 100–120 nm of the solar radiation [*Witasse et al.*, 1999; *Upadhayaya and Singh*, 2002; *Zhang and Shepherd*, 2005]. These reactions contribute to the emission of 557.7 nm that peak at around 160 km. Along with these reactions the three body mechanism (Barth mechanism) contributes to the emission of OI 557.7 nm from a lower altitude with a peak at around 100 km. In this work an average of around 130 km is considered to be the representative altitude for the 557.7 nm emission, which is found to appropriately describe the overall behavior of the OI 557.7 nm dayglow emission variability [e.g., *Pallamraju et al.*, 2014; *Laskar et al.*, 2015; *Karan et al.*, 2016].

$$O(^1D) \rightarrow O(^3P) + h\nu(\lambda = 630.0\,\mathrm{nm}) \tag{2}$$

Production of $O(^1D)$ state depends on photoelectron impact excitation of O, photodissociation of O_2 at Schumann Runge continuum at 135–175 nm of solar radiation, and dissociative recombination of

O_2^+ and e^- [*Solomon and Abreu*, 1989; *Witasse et al.*, 1999; *Pallamraju et al.*, 2004]. The 630.0 nm dayglow emissions peak at an altitude of around 230 km.

$$O(^5P) \rightarrow O(^5S) + h\nu(\lambda = 777.4\,\text{nm}) \tag{3}$$

Radiative recombination of O^+ and e^- produces 777.4 nm dayglow emissions [*Tinsley et al.*, 1973; *Pallamraju et al.*, 2013] which emanates from the peak height of *F* layer (~300 km).

3. Results

As mentioned above, the slit of MISE was oriented along the zonal (E-W) direction. Due to the imaging property of MISE, information on the spatial variations (across longitudes) in the dayglow emission intensities is obtained simultaneously. Diurnal variation in the three dayglow emission intensities are obtained along three independent segments toward the west, zenith, and east directions for each image as a function of time. As the altitudes of emanation of the three optical emissions are different, the zonal distances to which the emission intensity data correspond are also different. The dayglow emission intensity patterns at all the three wavelengths are linear superposition of waves of different periodic behavior, such as gravity waves (GWs), tidal oscillations, diurnal, and semidiurnal modulations. Figure 1a shows a sample diurnal behavior of OI 630.0 nm dayglow emission intensity obtained from zenith on 6 February 2014 as a function of local time (LT). Figures 1a and 1b depict the steps involved in obtaining the spectral information. The diurnal pattern of the 630.0 nm dayglow emission intensity (solid red) (Figure 1a) shows a broad solar zenith angle-dependent variation along with other small period fluctuations, which are attributed to GWs. Since, in the present work, our focus is on the fluctuations in the GW regime, time periods in this range are obtained from the dayglow intensities for the three directions (west, zenith, and east) at all the three emission wavelengths by subtracting a 3 h smoothed line (solid dark) from the dayglow intensities. As the large time scale variations are subtracted, the residuals (red dotted line) now correspond to time periods that are smaller than 3 h. Periodgram analysis has been carried out using the Lomb-Scargle technique [*Lomb*, 1976; *Scargle*, 1982] to obtain the GW time periods, the result of which is shown in Figure 1b. Here the *x* and *y* axes represent the time periods in hours and normalized power spectral density (PSD), respectively. The frequency (in h^{-1}) of the PSD is noted in the *x* axis on the top. The horizontal dotted line shows the 90% false alarm limit (FAL) value. On this day time periods of 2.28, 1.57, 0.8, and 0.5 h are found to be significant ($>$ 90% FAL) in the 630.0 nm dayglow emissions in zenith. Such analysis is carried out for the optical emissions from other view angles as well. Coherency in time periods in all the three directions was assessed with respect to the time period(s) obtained over zenith within a range of ±0.25 h (which is equal to the maximum Brunt Väisälä period among the altitudes considered in the present study). Existence of a common time period in the emission intensity variability at all these three well-separated spatial regions signifies to the likelihood of the same source driving the wave features in all these directions. Hence, it is assumed that on such days no longitudinal differences exist in the neutral wave dynamics over the given spatial extent. On the other hand, absence of coherent time period(s) in the emission intensity variations at all the three directions indicates that the sources of waves prevalent in these three directions are different, and hence, there exist longitudinal differences in the zonal wave features within this spatial extent.

Periodgram analyses as described for a sample of diurnal OI 630.0 nm intensity variations for zenith have been carried out at all the three wavelengths of dayglow emissions for all the three directions. Figure 2 shows the result of such periodgram analyses over west, zenith, and east for four sample days, with the *x* and *y* axes showing the time period and normalized PSD (similar to that shown in Figure 1b for 630.0 nm emission). Periodgrams in the top (Figures 2a, 2d, 2g, and 2j), middle (Figure 2b, 2e, 2h, and 2k), and bottom (Figure 2c, 2f, 2i, and 2l) rows represent those that were obtained for 777.4, 630.0, and 557.7 nm wavelength emission intensities, respectively. This type of depiction is maintained for all the figures that follow. Periodgrams at west, zenith, and east are shown by different line styles. The blue shaded regions correspond to the coherent time periods in all the three directions. The vertical arrows on the top of each panel points to the values of time periods which are coherent in any of the two directions. On 30 December 2013, significant time periods of 0.9 h (Figure 2a), 1.6 h (Figure 2b), and 1.2, 0.9, 0.7, and 0.5 h (Figure 2c) are found to be coherent in all the three directions at the emission altitudes of 777.4, 630.0, and 557.7 nm wavelengths, respectively. On 20 January 2014, although no coherent time periods were found along the three directions at

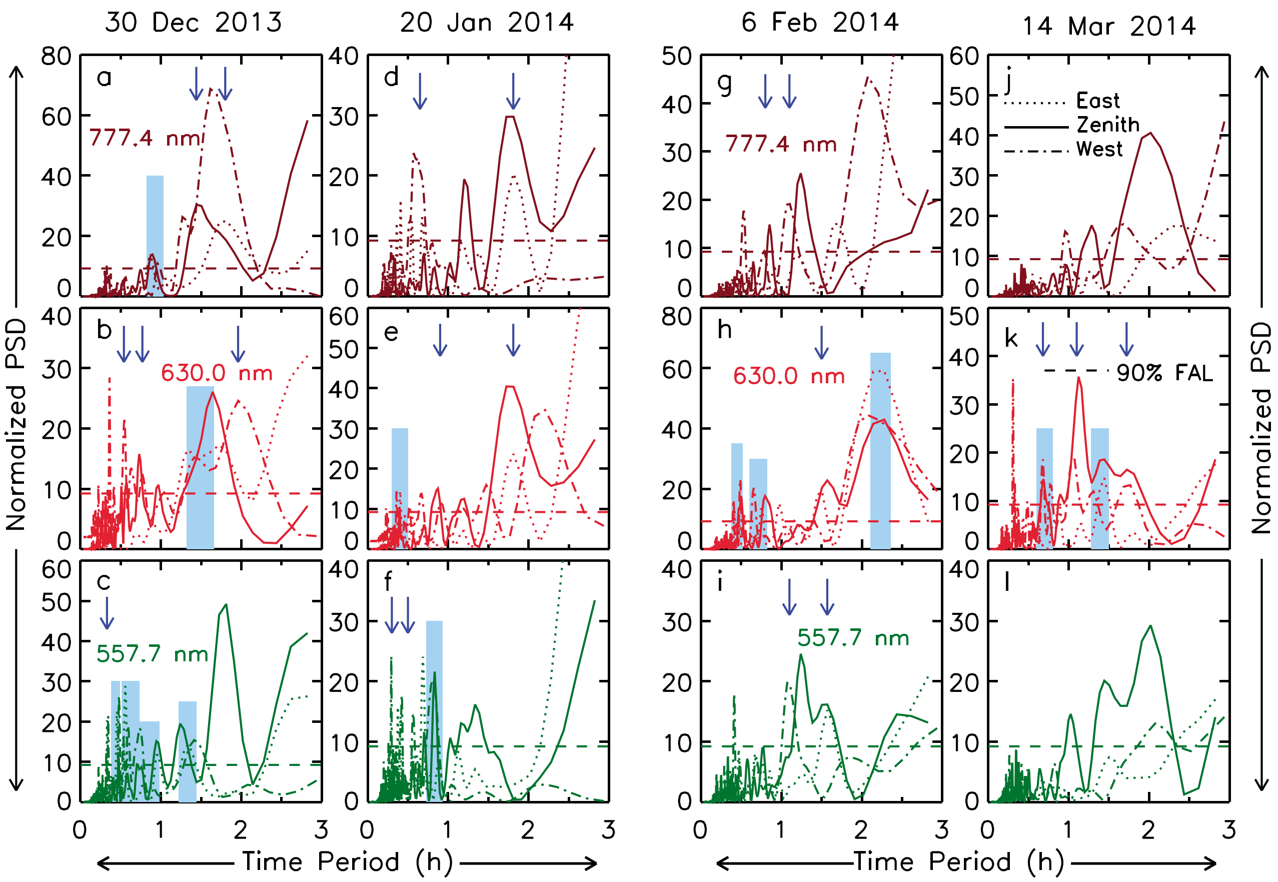

Figure 2. Results of the periodgram analyses carried out in the dayglow emission intensity data at all the three wavelengths obtained over west, zenith, and east directions on four sample days are shown. Periodgrams in the top (Figures 2a, 2d, 2g, and 2j), middle (Figures 2b, 2e, 2h, and 2k), and bottom (Figures 2c, 2f, 2i, and 2l) rows represent those that were obtained for 777.4, 630.0, and 557.7 nm wavelengths, respectively. The shaded portion in blue corresponds to the time period in which gravity waves obtained from all the three directions are coherent. The blue arrows on the top indicate the values of time periods in which GWs are coherent in any two directions. It may be noted that coherency in GW periodicities at heights of all emission wavelengths and in two directions is seen more readily on the two days on the left as compared with the two on the right. The two days on the left/right correspond to symmetric/asymmetric diurnal pattern in dayglow emission intensities and are illustrated in Figure 3.

the 777.4 nm emission altitude, coherency in time periods in all the three directions was found at 630.0 and 557.7 nm emission altitudes for 0.4 h (Figure 2e) and 0.8 h (Figure 2f), respectively. As described above, existence of coherent time periods in all the three directions at a given altitude indicates the existence of a similar behavior in the thermosphere, thereby most probably to the existence of a common source driving the wave dynamics. This suggests that no significant longitudinal differences exist in the neutral wave dynamics within the longitudinal extent of 3°–8° on these two days. This, however, is not the case always. On 6 February 2014 and 14 March 2014, no coherent time periods were found in all the three directions at the emission altitudes of 777.4 and 557.7 nm wavelengths (Figures 2g–2l). The poor availability/nonavailability of coherent time periods on these days points to a nonuniform or nonidentical behavior of sources in these three well-separated zonal locations that drive the thermospheric neutral wave mechanisms. Thus, these days indicate the existence of longitudinal differences in the neutral wave features within the spatial extent of 3°–8° longitudes (spatial extents covered corresponding to the altitudes of the three dayglow emissions). An exception has been noticed for 630.0 nm dayglow emissions wherein coherent time periods at 1.4 and 0.9 h were found on these two days.

The zenith diurnal patterns of the dayglow emission intensities at all the three emission wavelengths on the 4 days considered for periodgram analyses (depicted in Figure 2) are shown in Figure 3. The *x* axis shows the LT in hours. The *y* axes for all these plots indicate the dayglow emission intensities in Rayleigh. An 11-point running average of the dayglow emission intensities is over plotted as a continuous line for a clear

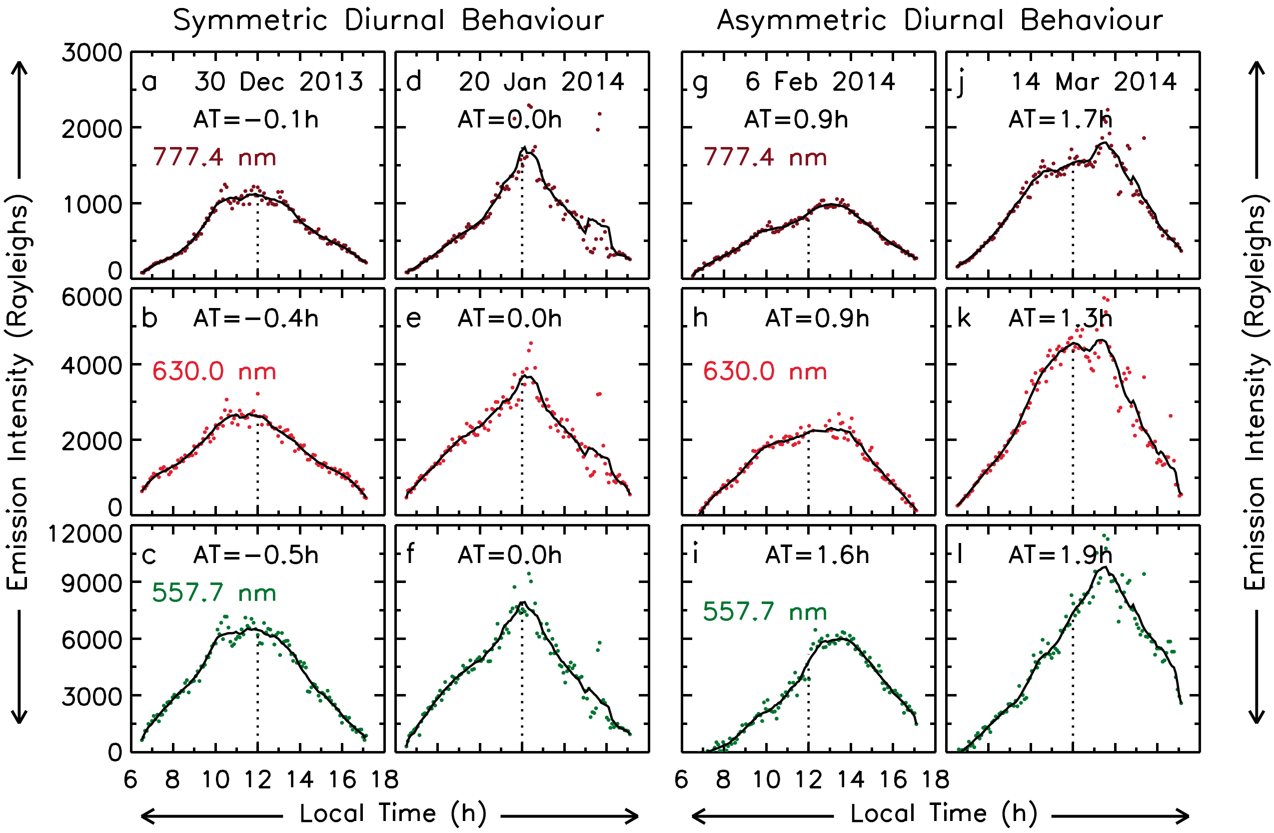

Figure 3. Zenith diurnal emission intensity variability along with the respective AT values for (a, d, g, and j) OI 777.4 nm, (b, e, h, and k) OI 630.0 nm, and (c, f, i, and l) OI 557.7 nm are shown on the four days considered for the periodgram analyses in Figure 2. The dark sold line in each of the figures represents the 11-point running average of the dayglow emission intensities. A vertical dotted line is drawn at the local noon to aid the eye for appreciating the symmetric/asymmetric pattern in the diurnal dayglow emission intensities. Figures 3a–3f/3g–3l correspond to two days on which the diurnal pattern of the dayglow emission intensities was symmetric/asymmetric in all the three emission wavelengths.

visualization of the diurnal pattern. A vertical dotted line is drawn at local noon to aid the eye for comparing the diurnal emission intensity pattern between forenoon and afternoon. The dayglow emission intensities at each of the wavelengths in Figures 3a–3c and 3d–3f (representing the behavior for 30 December 2013 and 20 January 2014) peak around local noon, and therefore, they show a symmetric diurnal pattern (with respect to local noon). In Figures 3g–3i and 3j–3l (6 February 2014 and 14 Mar 2014), the dayglow emission intensities at all emission wavelengths peak in the afternoon hours, which make the diurnal emission intensity pattern to be asymmetric with respect to local noon. Considering purely the photochemical nature of the dayglow emissions, an asymmetric diurnal pattern is not expected. Such type of asymmetric diurnal patterns at all the three optical dayglow emission intensities was characterized and explained in detail in one of our earlier studies [*Karan et al.*, 2016]. The extent of asymmetricity in time (AT) in the diurnal emission intensity pattern is estimated as

$$\mathrm{AT} = \left(\frac{I_{\mathrm{peak}}}{I_{\mathrm{noon}}}\right) \times \left(T_{\mathrm{peak}} - T_{\mathrm{noon}}\right) \tag{4}$$

where T_{peak} and T_{noon} are the times of peak emission intenisty and local noon. I_{peak} and I_{noon} are the intensities at T_{peak} and T_{noon}, respectively. The diurnal emission intensity pattern was characterized as symmetric and asymmetric for values of AT $\leq$ 0.4 h and AT $>$ 0.4 h, respectively. The AT values for each diurnal pattern are noted in their corresponding panels in Figure 3, and according to this characterization, emission variabilities at all the wavelengths on 30 December 2013 and 20 January 2014 show symmetric diurnal pattern, whereas on 6 February 2014 and 14 March 2014 the diurnal pattern is asymmetric in nature. It is striking to note that coherent time periods (as shown in Figure 2) over west, zenith, and east were found to exist

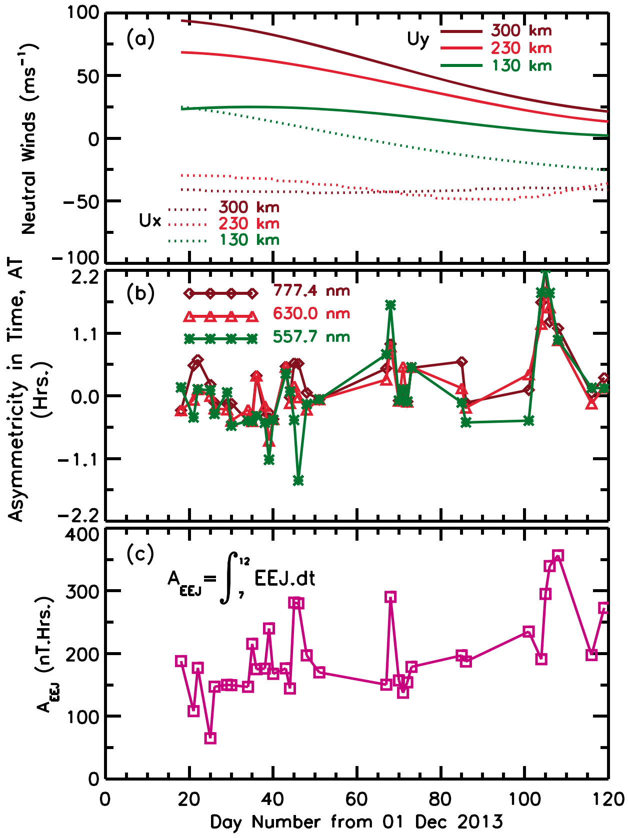

Figure 4. The variations in (a) model neutral winds at the three oxygen emission altitudes, (b) the asymmetricity in time (AT) for the three dayglow emission intensities on different days, and (c) EEJ strength integrated over 7–12 LT (A_{EEJ}) on the days corresponding to optical data are shown. The *x* axis shows the day number starting from 1 December 2013. [from *Karan et al.*, 2016, Figure 5].

on the days when the diurnal pattern of the dayglow emission intensities over zenith were symmetric. On the other hand, no coherent time periods were found on the days when the diurnal pattern of the dayglow emission intensities were asymmetric. *Karan et al.* [2016] showed that the neutral optical dayglow emission intensities at low-latitudes are generally sensitive to the equatorial electrodynamics. This was based on systematic investigations of the EEJ and the diurnal variability of the three dayglow emissions. It was shown that on the day when the electrodynamic forcing is large/small (as seen in the EEJ), the diurnal pattern of the optical emission intensity is asymmetric/symmetric. Such imprints of the electric field effect in the neutral dayglow have been shown in earlier studies as well [e.g., *Sridharan et al.*, 1999; *Pallamraju et al.*, 2004, 2010, 2014]. For the days being discussed in this study the integrated EEJ strengths (A) between 7 to 12 h ($A = \int_7^{12}$EEJ.dt) values are 149.5, 169.7, 290.3, and 190.8 nTh on 30 December 2013, 20 January 2014, 6 February 2014, and 14 March 2014, respectively [*Karan et al.*, 2016]. It may be noted that the values of A are larger on the days with asymmetric diurnal pattern than on the days with symmetric diurnal pattern. Figure 4 shows the effect of equatorial electrodynamics on the dayglow emission intensity pattern as characterized by "A" and "AT" values [*Karan et al.*, 2016, Figure 5]. Figures 4a–4c show the variation of (HWM14) model neutral winds at the altitudes of emanation of the three dayglow emissions, asymetricity in time (AT) in all the three dayglow emissions, and the integrated EEJ strength (A), respectively. It was shown in that study that to a first order the equatorial electrodynamics, and not the meridional winds, to be the cause for the observed asymmetricity in the dayglow emission intensities. The broadly similar behavior of AT and A (Figures 4b and 4c) clearly indicates that the asymmetric diurnal pattern of the dayglow emissions are predominantly due to the effect of electrodynamics. Independent ionospheric observations confirmed the clear relation between EEJ and AT not only during a few months but also from the reconstructed data for over two solar cycles [*Karan et al.*, 2016]. We thus use the dayglow behavior over this low-latitude location as a qualitative indicator of the variation of the equatorial electrodynamics.

Further, we have investigated the coherency in time periods in all the three directions on all the days with symmetric (17 days) and asymmetric (8 days) diurnal pattern in the zenith emission intensities at the three wavelenghts. Table 1 shows the percentage of coherency in GW periodicites, range, and mean values of coherent time periods. It may be noted that the coherency in periodicities in different directions are observed in more number of days with symmetric diurnal pattern in comparison to those on the days with asymmetric diurnal pattern. Correspondingly, the percentage occurrence of days with coherent time periods on "symmetric days" is greater than those on "asymmetirc days," mainly at 777.4 and 557.7 nm emission wavelengths. The range of values of the coherent time periods is from 0.4 to 2.1 h for all the three emission intensities for all the days. The values of integated EEJ strengths (A) on the days (considered here) with symmetric diurnal

Table 1. Summary of the GW Characteristics (Coherency in Time Periods and Zonal Scale Sizes) on the Days With a Similar Type of Diurnal Pattern (Either Symmetric or Asymmetric) in All the Three Dayglow Emissions is Given Below

Emission Wavelength (nm)	Diurnal Pattern in All the Three Emissions	No. of Days Which Showed Coherency in GW Time Period(s)	% of Coherency in GW Periodicities	Range and Mean of Coherent Time Periods (h)	Zonal Scale Sizes (km)
OI 777.4	Symmetric	11	64	0.4–2.1; 1.2	Before 10 LT: ----; ---- After 10 LT: ----; 227-638
	Asymmetric	2	25	2.0–2.1; 2.0	Before 10 LT: ----; 265-290 After 10 LT: 50–66; 240–638
OI 630.0	Symmetric	7	41	0.4–1.9; 1.1	Before 12 LT: 40–128; 244–490 After 12 LT: 47–165; ----
	Asymmetric	4	50	0.5–2.2; 0.9	Before 12 LT: 116–135; ---- After 12 LT: 42–185; 201–306
OI 557.7	Symmetric	14	82	0.5–2.0; 0.9	Before 11 LT: 86–98; 106–115 After 11 LT: 23–99; 106–230
	Asymmetric	5	62	0.6–2.0; 1.0	Before 11 LT: 25–98; 274–276 After 11 LT: 23–81; 115–197

emission intensity pattern range from 64 to196 nTh, whereas on the days with asymmetric diurnal emission intensity pattern the values of *A* range from 124 to 295 nTh. This clearly indicates that the equatorial electrodynamics is, in general, stronger on the days with asymmetric diurnal emission intensity pattern in which longitudinal differnces are found to exist.

At this point, it is to be appreciated that longitudinal differences in the GW time periods are observed in the optical dayglow emission intensity variations which is a neutral phenomena. We have seen above that when the diurnal pattern of the dayglow emission intensities over zenith are asymmetric, there is a strong equatorial electrodynamic forcing on that day. This is a good example of electrodynamic and neutral coupling in the low- and equatorial-latitude upper atmosphere. The contrast in symmetric and asymmetric diurnal pattern in 630.0 nm dayglow emissions is poorer than in 557.7 and 777.4 nm dayglow emissions [*Karan et al.*, 2016]. This is most probably due to the combined effect of equatorial electrodynamics and neutral winds to the 630.0 nm dayglow emissions, and thus, this seems to be resulting in the observed coherency in time periods even on the days with an asymmetric diurnal pattern as seen in Figure 2.

As discussed above, the EEJ strengths have a strong influence on the diurnal pattern of dayglow emission intensities. This suggests that the varying equatorial electrodynamic processes at different longitudes would have their imprint on the neutral dayglow emissions at different longitudes, just as reflected in our optical observations over zenith. If that be the case, the zonal gravity wave characteristics would be different on all these days. In order to understand the different nature of thermospheric wave characteristics in greater detail, we have carried out wave number spectral analyses for these days. Figures 1c and 1d illustrate a sample of the method for wave number spectral analysis used for 630.0 nm dayglow emission intensity at 8.8 LT on 6 February 2014. The *x* and *y* axes in Figure 1c show the zonal distance (positive eastward from zenith) and dayglow emission intensity, respectively. The spatial variation of 630.0 nm dayglow emission intensity is shown as the solid red line. The *x* and *y* axes in Figure 1d show the values of scale sizes (in kilometer) and their normalized PSD. The upper *x* axis shows the wave number (in km^{-1}). The 90% FAL is shown as the horizontal dashed line. A significant zonal scale size of 118 km is found to be present at the altitude of origin of the OI 630.0 nm emissions at 8.8 LT. This method has been followed to obtain the diurnal behavior of the statistically significant scale sizes for all the days at all the emission wavelengths at a cadence of 15 min. Out of all the significant scale sizes obtained, the lower cutoffs are taken to be 22, 40, and 50 km considering the 2-pixel resolution as mentioned above for 557.7, 630.0, and 777.4 nm, respectively. In a recent study [*Pallamraju et al.*, 2016], this method has been demonstrated to yield neutral gravity wave characteristics (both in space and time) and the first three-dimensional wave structure in the daytime upper atmosphere had been obtained.

Diurnal distribution of the scale sizes obtained for two sample days, with symmetric and asymmetric diurnal emission intensity pattern for all the three wavelengths are shown on the two left columns of Figure 5. Figures 5a–5c/Figures 5d–5f show the diurnal variations of the zonal scale sizes on 30 December 2013/6 February 2014, which were the days with symmetric/asymmetric pattern in the diurnal emission intensity at all the three wavelengths. The *x* and *y* axes show the LT in hours and values of scale sizes in

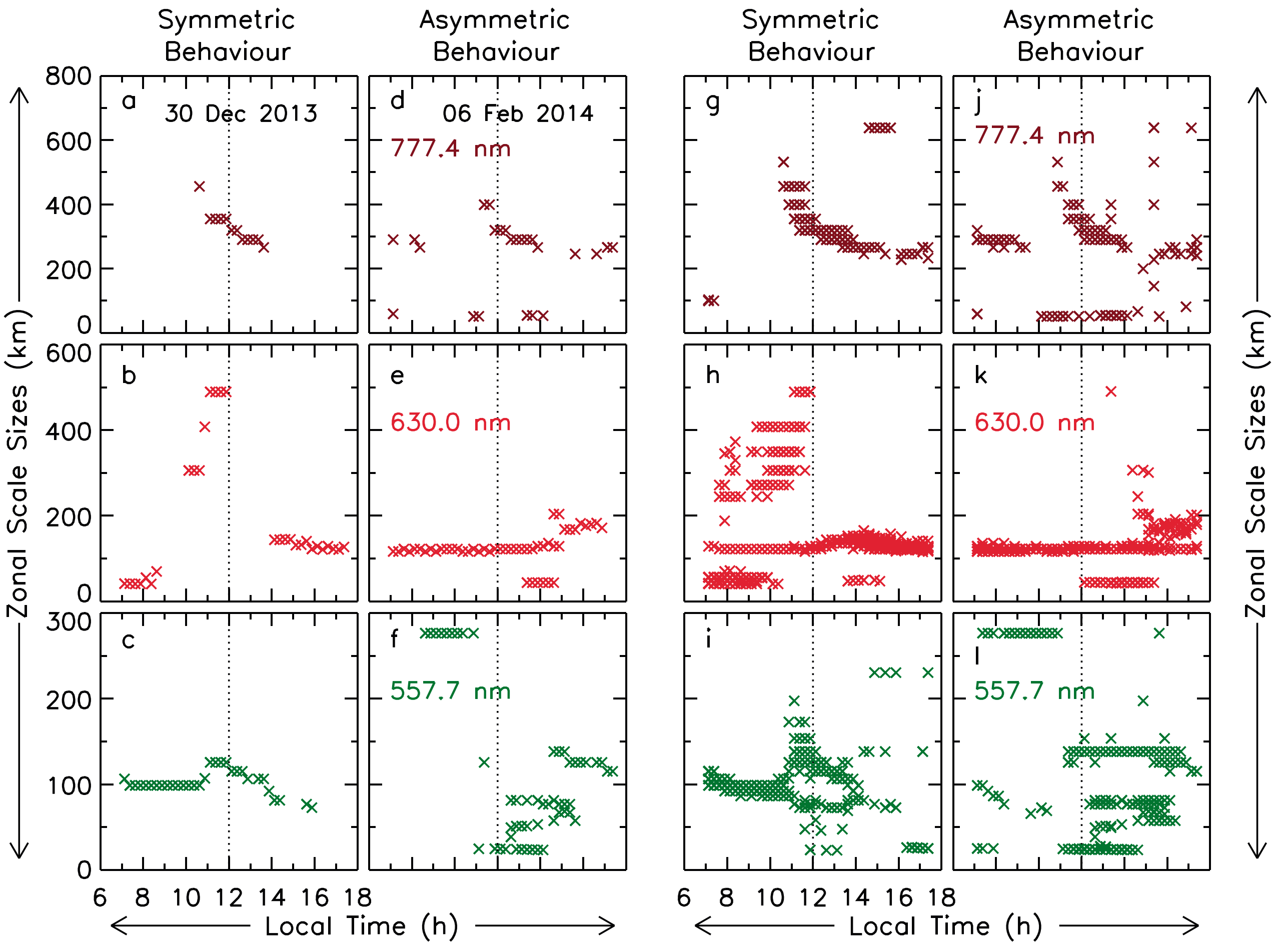

Figure 5. Diurnal distributions of the significant zonal scale sizes on two sample days (a–c) with symmetric and (d–f) with asymmetric diurnal emission intensity patterns are shown. Diurnal distributions of the significant scale sizes are collated for all the days with (g–i) symmetric and (j–l) asymmetric diurnal emission intensity patterns in all the three wavelengths. Significant differences may be noted in the scale sizes between the days with symmetric and asymmetric diurnal patterns in emission intensities.

kilometres. Notable contrast exists for the values of zonal scale sizes and their diurnal behavior obtained between the days with symmetric/asymmetric diurnal pattern in dayglow emission intensities at all the three wavelengths. The diurnal behavior of zonal scale sizes has been shown for only one sample day each for symmetric/asymmetric diurnal pattern in Figures 5a–5f. However, it was noted that all the other days showed almost similar behavior as characterized by the symmetric/asymmetric diurnal behavior. Therefore, we have overlaid the diurnal distribution of the significant GW scale sizes obtained for all the days with respect to symmetric/asymmetric diurnal patterns in Figures 5g–5i and 5j–5l, respectively. It is striking that the pattern of the diurnal distribution of scale sizes is (i) remarkably similar within the days with symmetric or asymmetric diurnal pattern and (ii) distinctly different when compared with one type to another in zenith emission intensity pattern.

Table 1 includes summary of the diurnal distribution of zonal scale sizes on both the type of days (either with symmetric/asymmetric diurnal emission intensity pattern in all the three wavelengths). The contrast is apparent in terms of the magnitudes of the zonal scale sizes and the times at which they exist at a given emission wavelength between the two types of diurnal emission intensity patterns. The dashed line corresponds to the nonavailability of significant scale sizes within the observational window of this experiment. As mentioned above, the ranges of integrated EEJ strengths (*A*) values on the days (considered for Figures 5g–5l) with symmetric/asymmetric diurnal emission intensity pattern are 64–196/124–295 nTh. This points to the important role of the EEJ strength in all these days.

At the emanation altitude of 777.4 nm emission, on all the days (either with symmetric or asymmetric diurnal emission intensity pattern), waves with scale sizes greater than 200 km were present, mostly during noon which seem to be decreasing gradually toward afternoon hours (Figures 5a, 5d, 5g, and 5j). However, on the days with asymmetric diurnal emission intensity pattern, larger- and smaller-scale sizes of around 300 and 50 km are also seen in the forenoon and noon hours (Figures 5d and 5j), which are absent on the days with symmetric diurnal emission intensity pattern (Figures 5a and 5g). From Figures 5b and 5h it is clear that at 230 km altitude, on the day with symmetric diurnal emission intensity pattern, larger-scale sizes (>200 km) are present only during forenoon hours and seem to be increasing toward noon time with around 500 km on some days. It is possible that the scale sizes are increasing in magnitudes in the afternoon hours and going well beyond the spatial extent of 600 km possible in the present experiment. Waves of scale sizes >200 km and ~50 km are present during forenoon hours on the days with symmetric diurnal emission intensity pattern (Figures 5b and 5h), whereas these are absent on the days with asymmetric diurnal emission intensity pattern (Figures 5e and 5k). The presence of waves with smaller-scale sizes of around 120 km is clearly noticeable on the days of both types of diurnal emission intensity pattern (Figures 5h and 5k). At 130 km altitude scale sizes of GWs of around 100 km are seen in forenoon which increase during noon time and then gradually decrease with time on the days with symmetric diurnal pattern (Figure 5i). Contrary to this, on the days with asymmetric diurnal pattern, larger-scale sizes of around 270 km are present during forenoon hours. Also, on the days with asymmetric diurnal pattern, the spread in the values of significant scale sizes is clearly seen during afternoon (Figure 5l). The 557.7 nm dayglow emission has contributions from both lower thermosphere and higher above (*F* region). The lower altitude contribution is mostly affected by the wave activities from the mesosphere/lower thermospheric regions, while the higher one gets affected by equatorial electrodynamics as well. Hence, on the days with asymmetric diurnal pattern, as the equatorial electrodynamics is stronger, the *F* region contribution to the OI 577.7 nm dayglow could be significant and time varying, which could give rise to the observed values of multiple zonal scale sizes during afternoon hours.

Even though the three dayglow emissions considered in the present work emanate from different altitudes and have different production mechanisms, the broad pattern of presence of waves with larger-scale sizes in the forenoon/noon hours of a day with symmetric diurnal pattern (Figures 5g–5i) and of relatively smaller-scale sizes in the afternoon on days with asymmetric diurnal pattern (Figures 5j–5l) is clearly noticeable, especially for 630.0 nm dayglow emission intensities. It is to be emphasized here that the days with symmetric and asymmetric diurnal pattern in zenith intensities are irregularly spaced in the duration of December 2013 to March 2014. Thus, it is striking to note that in spite of these belonging to different months, the diurnal distributions in the zonal scale sizes on all the days with symmetric diurnal pattern follow a similar configuration. Similar is the case for days with asymmetric diurnal pattern as well. This indicates that the neutral wave dynamics is mainly influenced by the strength of the equatorial electrodynamics and follows a broad order in the upper atmosphere.

As has been shown above, optical dayglow emissions over low-latitude regions are sensitive to the equatorial electrodynamics and display zonal variations. On the days with symmetric diurnal pattern of the dayglow emission intensities, the time periods of waves in a separation of 3°–8° in longitudes are found to be coherent. Contrary to this, on the days with asymmetric diurnal pattern in the zenith intensities the coherency in time periods over these longitudinal separations is poor. Moreover, the diurnal distribution of the zonal scale sizes of GWs also shows differences with respect to these two types of diurnal emission intensity patterns. Such contrasting behavior of time periods and scale sizes implies a clearly different behavior in the neutral wave dynamics on these two types of days. To further investigate the behavior of the wave dynamics, information on the propagation characteristics of the waves at each altitude has been obtained. In order to do that, the power of the statistically significant scale sizes of GWs at a given time is selected by centring a band-pass filter at the peak of the dominant scale size with widths of 22, 40, and 50 km for 557.7, 630.0, and 777.4 nm, respectively. Inverse Fourier transform is carried out on the selected scale sizes to obtain the corresponding intensity modulations. The positions of crests/troughs as seen in the emission intensities are laid one-next to the other as a function of time to be able to track the movement of the wave. This procedure to obtain the keogram by tracking the modulations in intensities with time is explained in detail in *Pallamraju et al.* [2016]. The keogram analyses have been carried out on the days in which all the three dayglow emissions show a common type of diurnal pattern (i.e., either symmetric or asymmetric). Figure 6 shows the

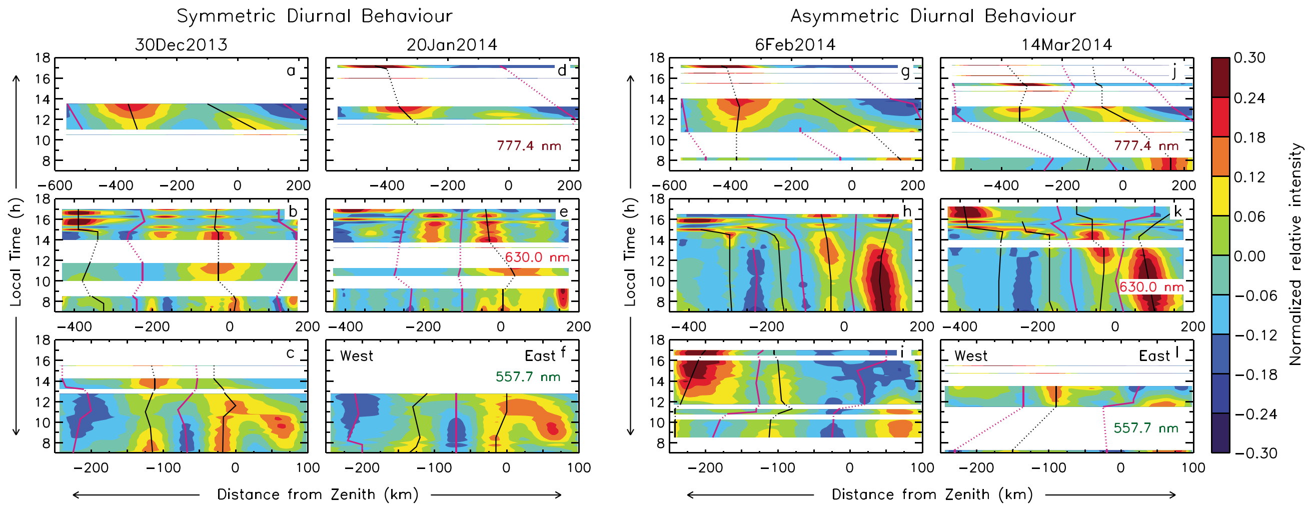

Figure 6. (a–l) Contours of the normalized relative dayglow intensity variations obtained using band-pass filter centred at the dominant scale sizes on four sample days that were considered for periodgram analyses (in Figure 2) are shown. The values of the normalized relative intensity are shown in the bar on the right-hand side. Figures 6a–6f/Figures 6g–6l show symmetric/asymmetric diurnal dayglow emission intensity pattern in all the three emission wavelengths. Contrasting characteristics in the zonal propagation of waves can be seen the days with symmetric/asymmetric diurnal pattern.

keograms on four sample days that were considered for periodgram analyses shown in Figures 2, 3, and 5. The *x* and *y* axes show the zonal distance from zenith in kilometer and LT in hours, respectively. The differing extents in zonal distances covered at each emission wavelengths may be noted. Positive/negative values of the distance correspond to the eastern/western directions with respect to the zenith. The normalized relative intensity is shown as contours, and their values are represented by the color bars on the right-hand side of the figure. The gaps in the figures at some times are due to the absence of statistically significant scale sizes in the GWs at those times as seen from the wave number spectral analysis. To follow the propagation of waves, black/violet lines have been drawn (to aid the eye) that join the crests/troughs with respect to time. The dotted lines are drawn to show the most probable movement of the GWs with time when the power of the scale sizes is found to be below the FAL.

On days with symmetric diurnal pattern, westward movement of the zonal component of GWs is seen at the altitude of 777.4 nm dayglow emission (Figures 6a and 6d). At 230 km (emission height of 630.0 nm dayglow) and 130 km (altitude of 557.7 nm dayglow emissions), no significant movements of the crests and troughs are noticed. They seem to follow a standing wave type of pattern throughout the day (Figures 6b and 6c). On the second day as well, such standing wave type of pattern in the waves is clearly noticed (Figures 6e and 6f). A uniform pattern of waves without any significant zonal movement of the wavefronts on the days with symmetric diurnal pattern indicates to a systematic and uniform behavior in the dynamic processes over large spatial extent and the absence of zonal differences within the spatial coverage possible in this experiment. On the days with asymmetric diurnal pattern, thermospheric neutral waves at 777.4 nm emission altitude show a westward propagation (Figures 6g and 6j) similar to the days with symmetric diurnal pattern. The behavior of the GW propagation at the top most layer of the *F* region as measured by OI 777.4 nm dayglow emission seems to be mainly westward on all the days, most probably due to the existence of strong daytime westward winds at this altitude. At 230 km altitude, the crests/troughs toward east of zenith move eastward and those toward the west move westward (Figures 6h and 6k). This kind of movement of waves in 630.0 nm emission was seen on other days as well, as reported in one of our earlier works [*Pallamraju et al.*, 2016]. The cause for such behavior is under investigation. On the days with asymmetric diurnal pattern, the waves at 130 km altitude show an eastward propagation (Figures 6i and 6l). It is interesting to note that the movement of the crests and troughs is significantly different after 13 LT at both the emission altitudes of 630.0 and 557.7 nm dayglow emissions. Moreover, at different longitudinal regions the gradients of the change in propagation direction of the waves are also different. This type of spatially varying direction of propagation of waves in forenoon and afternoon clearly indicates to the different nature of the processes and dynamics that are prevalent at the respective longitudes.

4. Discussion

The neutral wave dynamics in the thermosphere show different behavior on the days with symmetric/asymmetric diurnal pattern in the optical dayglow emission intensities. Analyses of the data obtained over a large spatial distances show significant differences in terms of (i) the existence/nonexistence of coherent time periods, (ii) dissimilar diurnal distribution of the zonal scale sizes, and (iii) varying propagation characteristics of the zonal wavefronts on the days with symmetric/asymmetric diurnal pattern. All these distinct features confirm the existence of longitudinal variations in wave dynamics in the thermosphere in smaller (3°–8°) longitude spatial extent. The magnetic declination angles and magnitudes of magnetic field strengths do not vary within the zonal separations considered in this study. Hence, the differences in the zonal component of the neutral thermospheric waves as seen in the optical dayglow emissions at multiple wavelengths are most likely due to the differences in the equatorial electrodynamic processes along the respective longitude sectors. Changes in the magnitudes and directions of the thermospheric neutral wind, if any, can also bring about such small-scale zonal variations of the wave dynamics. Moreover, the effect of localized wind shears in bringing about change in the wind structure and thereby affecting the waves cannot be neglected, especially for the lower altitude emissions at 557.7 nm. During December/January when equatorial electrodynamics is weaker [*Karan et al.*, 2016], the coherency in GW time periods were found to be more, indicating the absence of longitudinal variations in the 3°–8° longitudes. On the other hand, during March, the equatorial electrodynamics is stronger and the coherent GW time periods along these longitudinal separations are observed less frequently suggesting to a possible existence of longitudinal differences in the neutral wave dynamics. This could be due to stronger wave activities during equinoxes. In this background it is striking to note that the diurnal pattern in the zenith OI optical dayglow emission intensities, which are a part of the overall upper atmospheric system indicates as to whether longitudinal differences exist or, not.

These new results presented here hold lot of promise on various aspects of the coupling of atmosphere that vary as a function of time. In this work we have considered only the days when all the emission intensities showed a common type (i.e., either symmetric or asymmetric) of diurnal pattern. However, there are days in which a couple of emission wavelengths show symmetric/asymmetric diurnal pattern while the remaining one shows an opposite behavior. Characterization of the dayglow emission intensity data on these days will provide information on the nature of intercoupling among thermosphere at different altitudes. Further, small-scale variations in the wave features could also be due to structures in the density distribution over space, which can vary with time. Also, there are cases when the distribution of the scale sizes on the days with symmetric/asymmetric diurnal pattern showed a behavior similar to that on the days with asymmetric/symmetric diurnal pattern. These days are found to be relatively geomagnetically active among all the days considered and, hence, are not included in the present work. This indicates a positive response of low-latitude thermospheric neutral GWs to the geomagnetic activities. Further, it is to be kept in mind that in this study the focus had been on the zonal component of the GWs. However, GWs are three dimensional in nature with different projections in zonal, meridional, and vertical directions [*Pallamraju et al.*, 2016]. In this case, for zonal propagation, when the zonal scale sizes are seem to be varying with time, it is also possible that the direction of propagation is changing. For that investigation near-simultaneous information of dayglow variations along both zonal and meridional directions is required. Such data were acquired in campaign mode and the results of which will be presented separately.

For the sake of completeness, we have looked at results, if any, of smaller-scale size zonal variation in the published literature. Many of the all-sky measurements reported in the literature [e.g., *Shiokawa et al.*, 2009; *Taylor et al.*, 1995; *Nakamura et al.*, 1998; *Makela et al.*, 2013] do not show the existence of longitudinal differences. This is probably because the all-sky images of the nighttime ionosphere over low- and equatorial-latitudes are dominated by the significant feature of the movement of plasma bubbles (with greater occurrence in high solar activity and during equinoxes), and the smaller-scale feature, if any, are masked. During geomagnetic disturbances the zonal variations could be due to shears in the zonal plasma flow in the equatorial- and low-latitude regions [e.g., *Sekar et al.*, 2012] or due to prompt penetration electric field [*Basu et al.*, 2001; *Chakrabarty et al.*, 2015]. However, in this work we present the results on the existence of longitudinal differences in equatorial electrodynamic processes during geomagnetic quiet periods. The lower thermospheric/mesospheric emissions of OI 557.7 nm in the nighttime is governed mainly by the lower atmospheric forcing with waves of different scale sizes moving in different directions [e.g., *Taylor et al.*, 1995].

To the best of our knowledge, no result exists in the literature that describes a longitudinal difference as presented in this work.

In the present study the longitudinal differences within 3°–8° separations present in the daytime seem to be mainly due to zonal differences in the EEJ strengths. As the equatorial electric field is electrostatic in nature (i.e., $\vec{\nabla} \times \vec{E} = 0$), any changes in the value of $\vec{E}$ at certain longitude give rise to changes of $\vec{E}$ at other longitudes around the globe so as to maintain the $\int \vec{E}.dl = 0$ condition. Thus, the possibility of existence of changes in the EEJ strengths in such small separations seems to be the cause of longitudinal variations observed in this study. The fact that the integrated EEJ strengths play a distinct role in influencing the diurnal emission intensity pattern in the dayglow as shown in Figure 4 adds credence to this conclusion arrived at. To the best of our knowledge, these experimental results that suggest to the possible existence of dissimilarities in the equatorial electric fields in the daytime in such short separations of 3°–8° longitudes are first of their kind. Information as revealed in the present experiment has great potential in forming inputs to regional- and global-scale dynamical models.

5. Conclusion

Optical OI dayglow emission intensities were obtained over a large FOV along the zonal direction from a geomagnetic low-latitude station. Periodgram analyses were carried out on the dayglow emission intensity variability obtained in the west, zenith, and east directions to investigate the periodicities in them. The presence/absence of coherent time periods in these three directions suggests to a common/different source driving the wave features indicating the nonexistence/existence of longitudinal differences in the wave features within this spatial extent. From the zenith intensity measurements it was found that the coherent time periods are present/absent on the days with symmetric/asymmetric diurnal dayglow emission intensity pattern. The nonexistence of coherent time periods on the days with asymmetric diurnal pattern was attributed to the stronger equatorial electrodynamics, which seems to show variations even within an ~3° longitudinal separation. This gives a clear and broader picture of the coupling processes between equatorial electrodynamics and off-equatorial neutral wave dynamics. Moreover, the gravity wave features in terms of zonal scale sizes and propagation directions also show different behavior on the days with symmetric and asymmetric diurnal dayglow emission intensity pattern. The high spatiotemporal resolution measurements at three optical dayglow emissions emanating from different altitudes revealed, for the first time, that there exist longitudinal differences of the equatorial electrodynamic processes in as small a separation as 3° in longitude. Such longitudinal differences observed over such short separations in the neutral wave features and electrodynamic processes over low-latitude thermosphere provides new insights into the understanding of the intricacies of the upper atmospheric dynamical processes regionally as well as globally.

Acknowledgments
The optical dayglow data used in this work were obtained by Physical Research Laboratory and can be made available on request. The logistic support with regard to operation of MISE provided by T. Vijaya Lakshmi and her team at the Jawaharlal Nehru Technological University in Hyderabad, India, is duly acknowledged. The hourly EEJ data can be obtained from the website of Indian Institute of Geomagnetism. This work is supported by the Department of Space, Government of India.

References

Abdu, M. A., J. A. Bittencourt, and I. S. Batista (1981), Magnetic declination control of the equatorial F-region dynamo electric field development and spread-F, *J. Geophys. Res.*, *86*, 11,443–11,446, doi:10.1029/JA086iA13p11443.

Basu, S., et al. (2001), Ionospheric effects of major magnetic storms during the International Space Weather Period of September and October 1999: GPS observations, VHF/UHF scintillations, and in situ density structures at middle and equatorial latitudes, *J. Geophys. Res.*, *106*(A12), 30,389–30,413, doi:10.1029/2001JA001116.

Chakrabarty, D., D. Rout, R. Sekar, R. Narayanan, G. D. Reeves, T. K. Pant, B. Veenadhari, and K. Shiokawa (2015), Three different types of electric field disturbances affecting equatorial ionosphere during a long-duration prompt penetration event, *J. Geophys. Res. Space Physics*, *120*, 4993–5008, doi:10.1002/2014JA020759.

Chandrasekhar, N. P., K. Arora, and N. Nagarajan (2014), Characterization of seasonal and longitudinal variability of EEJ in the Indian region, *J. Geophys. Res. Space Physics*, *119*, 10,242–10,259, doi:10.1002/2014JA020183.

England, S. L., S. Maus, T. J. Immel, and S. B. Mende (2006), Longitudinal variation of the E-region electric fields caused by atmospheric tides, *Geophys. Res. Lett.*, *33*, L21105, doi:10.1029/2006GL027465.

Hajkowicz, L. A. (1991), Global onset and propagation of large scale travelling ionospheric disturbances as a result of the great storm of March 13 1989, *Planet. Space Sci.*, *39*, 583–593, doi:10.1016/0032-0633(91)90053-D.

Hocke, K., and K. Schlegel (1996), A review of atmospheric gravity waves and travelling ionospheric disturbances: 1982–1995, *Ann. Geophys.*, *14*, 917–940, doi:10.1007/s00585996-0917-6.

Immel, T. J., E. Sagawa, S. L. England, S. B. Henderson, M. E. Hagan, S. B. Mende, H. U. Frey, C. M. Swenson, and L. J. Paxton (2006), Control of equatorial ionospheric morphology by atmospheric tides, *Geophys. Res. Lett.*, *33*, L15108, doi:10.1029/2006GL026161.

Karan, D. K., D. Pallamraju, K. A. Phadke, T. Vijayalakshmi, T. K. Pant, and S. Mukherjee (2016), Electrodynamic influence on the diurnal behavior of neutral daytime airglow emissions, *Ann. Geophys.*, *34*, 1019–1030, doi:10.5194/angeo-34-1019-2016.

Kelley, M. C. (2009), *The Earth's Ionosphere: Plasma Physics & Electrodynamics*, vol. 96, 152 pp., Academic Press, San Diego, Calif.

Laskar, F. I., D. Pallamraju, B. Veenadhari, T. Vijaya Lakshmi, M. Anji Reddy, and S. Chakrabarti (2015), Gravity waves in the thermosphere: Solar activity dependence, *Adv. Space Res.*, *55*, 1651–1659.

Lomb, N. R. (1976), Least-squares frequency analysis of unequally spaced data, *Astrophys. Space Sci.*, *39*, 447–462.

Makela, J. J., D. J. Fisher, J. W. Meriwether, R. A. Buriti, and A. F. Medeiros (2013), Near-continual ground-based nighttime observations of thermospheric neutral winds and temperatures over equatorial Brazil from 2009 to 2012, *J. Atmos. Sol. Terr. Phys.*, *103*, 94–102.

Moffett, R. J. (1979), The equatorial anomaly in the electron distribution of the terrestrial F-region, *Fundam. Cosmic Phys.*, *4*, 313–391.

Nakamura, T., T. Tsuda, H. Miyagawa, Y. Matsushita, H. Fukunishi, Y. Takahashi, and Y. Yamada (1998), Propagation directions of gravity wave patterns observed in OH CCD images during SEEK campaign, *Geophys. Res. Lett.*, *25*, 1793–1796, doi:10.1029/98GL01064.

Pallamraju, D., J. Baumgardner, and S. Chakrabarti (2000), A multiwavelength investigation of the Ring effect in the day sky spectrum, *Geophys. Res. Lett.*, *27*, 1875–1878, doi:10.1029/1999GL010961.

Pallamraju, D., J. Baumgardner, and S. Chakrabarti (2002), HIRISE: A ground-based high-resolution imaging spectrograph using echelle grating for measuring daytime airglow/auroral emissions, *J. Atmos. Sol. Terr. Phys.*, *64*, 1581–1587.

Pallamraju, D., S. Chakrabarti, and C. E. Valladares (2004), Magnetic storm-induced enhancement in neutral composition at low latitudes as inferred by O(1D) dayglow measurements from Chile, *Ann. Geophys.*, *22*(9), 3241–3250.

Pallamraju, D., U. Das, and S. Chakrabarti (2010), Short- and long-timescale thermospheric variability as observed from OI 630.0 nm dayglow emissions from low latitudes, *J. Geophys. Res.*, *115*, A06312, doi:10.1029/2009JA015042.

Pallamraju, D., F. I. Laskar, R. P. Singh, J. Baumgardner, and S. Chakrabarti (2013), MISE: A multiwavelength imaging spectrograph using echelle grating for daytime optical aeronomy investigations, *J. Atmos. Sol. Terr. Phys.*, *103*, 176–183.

Pallamraju, D., J. Baumgardner, R. P. Singh, F. I. Laskar, C. Mendillo, T. Cook, S. Lockwood, R. Narayanan, T. K. Pant, and S. Chakrabarti (2014), Daytime wave characteristics in the mesosphere lower thermosphere region: Results from the Balloon-borne Investigations of Regional-atmospheric Dynamics experiment, *J. Geophys. Res. Space Physics*, *119*, 2229–2242, doi:10.1002/2013JA019368.

Pallamraju, D., D. K. Karan, and K. A. Phadke (2016), First three dimensional wave characteristics in the daytime upper atmosphere derived from ground-based multiwavelength oxygen dayglow emission measurements, *Geophys. Res. Lett.*, *43*, 5545–5553, doi:10.1002/2016GL069074.

Raghavarao, R., P. Sharma, and M. R. Sivaraman (1978), Correlation of Ionization anomaly with the intensity of the electrojet, *Space Res.*, *18*, 277–280.

Raghavarao, R., R. Sridharan, J. H. Sastri, V. V. Agashe, B. C. N. Rao, P. B. Rao, and V. V. Somayajulu (1988), The equatorial ionosphere, in *World Ionospheric/Thermospheric Study*, *WITS Handbook*, vol. 1, edited by C. H. Liu and B. Edwards, pp. 48–93, SCOSTEP Secretariat, Univ. of Illinois, Boulder, Colo.

Raghavarao, R., L. E. Wharton, N. W. Spencer, H. G. Mayr, and L. H. Brace (1991), An equiatorial temperature and wind anomaly (ETWA), *Geophys. Res. Lett.*, *18*, 1193–1196, doi:10.1029/91GL01561.

Raghavarao, R., W. R. Hoegy, N. W. Spencer, and L. E. Wharton (1993), Neutral temperature anomaly in the equatorial thermosphere—A source of vertical winds, *Geophys. Res. Lett.*, *20*(11), 1023–1026, doi:10.1029/93GL01253.

Richmond, A. D., and S. Matsushita (1975), Thermospheric response to a magnetic substorm, *J. Geophys. Res.*, *80*(19), 2839–2850, doi:10.1029/JA080i019p02839.

Sagawa, E., T. J. Immel, H. U. Frey, and S. B. Mende (2005), Longitudinal structure of the equatorial anomaly in the nighttime ionosphere observed by IMAG/FUV, *J. Geophys. Res.*, *110*, A11302, doi:10.1029/2004JA010848.

Sekar, R., D. Chakrabarty, and D. Pallamraju (2012), Optical signature of shear in the zonal plasma flow along with a tilted structure associated with Equatorial Spread F during a space weather event, *J. Atmos. Sol. Terr. Phys.*, *75-76*, 57–63.

Sharma, P., and R. Raghavarao (1989), Simultaneous occurrence of ionization ledge and counterelectrojet in the equatorial ionosphere: Observational evidence and its implications, *Can. J. Phys.*, *67*, 166–172.

Shiokawa, K., Y. Otsuka, and T. Ogawa (2009), Propagation characteristics of nighttime mesospheric and thermospheric waves observed by optical mesosphere thermosphere imagers at middle and low latitudes, *Earth Planets Space*, *61*, 479–491, doi:10.1186/BF03353165.

Scargle, J. D. (1982), Studies in astronomical time series analysis. II. Statistical aspects of spectral analysis of unevenly spaced data, *Astrophys. J.*, *263*(2), 835–853.

Solomon, S. C., and V. Abreu (1989), The 630.0 nm dayglow, *J. Geophys. Res.*, *94*(A6), 6817–6824, doi:10.1029/JA094iA06p06817.

Sridharan, R., D. Pallamraju, V. V. Somayajulu, A. Taori, D. Chakrabarty, and R. Raghavarao (1999), Imprint of equatorial electrodynamical processes in the OI 630.0 nm dayglow, *J. Atmos. Sol. Terr. Phys.*, *61*, 1143–1155.

Sunda, S., and B. M. Vyas (2013), Local time, seasonal, and solar cycle dependency of longitudinal variations of TEC along the crest of EIA over India, *J. Geophys. Res. Space Physics*, *118*, 6777–6785, doi:10.1002/2013JA018918.

Taylor, M. J., M. B. Bishop, and V. Taylor (1995), All-sky measurements of short period waves imaged in the OI(557.7 nm), Na(589.2 nm) and near infrared OH and O2(0,1) nightglow emissions during the ALOHA-93 campaign, *Geophys. Res. Lett.*, *22*, 2833–2836, doi:10.1029/95GL02946.

Tinsley, B. A., A. B. Christensen, J. Bittencourt, H. Gouveia, P. D. Angreji, and H. Takahashi (1973), Excitation of oxygen permitted line emissions in the tropical nightglow, *J. Geophys. Res.*, *78*(7), 1174–1186, doi:10.1029/JA078i007p01174.

Upadhayaya, A. K., and V. Singh (2002), Effects of temperature dependence of reaction $N_2(A^3\Sigma_u^+) + O$ on greenline dayglow emission, *Ann. Geophys.*, *20*, 2039–2045.

Witasse, O., J. Lilensten, C. Lathuillere, and P. L. Blelly (1999), Modeling the OI 630.0 and 557.7 nm thermospheric dayglow during EISCAT-WINDII coordinated measurements, *J. Geophys. Res.*, *104*(A11), 24,639–24,655, doi:10.1029/1999JA900260.

Zhang, S. P., and G. G. Shepherd (2005), On the response of the O(1S) dayglow emission rate to the Sun's energy input: An empirical model deduced from WINDII/UARS global measurements, *J. Geophys. Res.*, *110*, A03304, doi:10.1029/2004JA010887.